Visualisation of Nanoslurries and Hybrid Nanomaterials

Manahil Kadhim

Thesis submitted to the University of Nottingham for the degree of Doctor of Philosophy

June 2019

Abstract

The use of nanomaterials has become increasingly important in the past 50 years in applications such as transport, health and catalysis. Prior to usage either individually or in combination with polymers, these nanomaterials must be tested for quality, such as stability, or for different properties - such as total refractive index (RI), concentration and solubility in different solvents. Traditional techniques, such as transmission electron microscopy (TEM), can be expensive and time-intensive. A novel and low-cost technique involving the use of a digital camera (Logitech HD Pro C920), an iPad (Apple) and a computer to characterise the aforementioned properties of nanomaterials has been developed. The images were taken in clear glass cuvettes against different background colours (red, blue and green) and patterns (striped, lettered and dotted). This was done to reveals variations in the RI, colour intensity, concentration and settling rates after processing of images using MATLAB. Results indicated that, in the case of Fe_2O_3 (iron (III) oxide) nanoparticles prepared at temperatures ranging 200-400°C, accurate settling rates were obtained and quantified during 5 h. This was evidenced by an increase in the mean pixel value (which represents the degree of settling) after 5 h for samples formulated at 300°C and above. Similarly, the RI values increased in correlation with the concentration of sucrose in the solution and was evidenced by an increase in the quantified letter areas. Furthermore, a high initial pixel value of the red channel was obtained before decreasing in correlation with an increase in Nigrosin blue dye concentration (in ppm) exhibiting sensitivity to concentration. Conversely, the blue channel value revealed the reverse trend. In conclusion, an accessible, simple and cost-effective system has been developed to calculate multiple properties of different types of solutions.

Acknowledgments

I would like to express my deep and sincere gratitude to my supervisor, Professor Edward Lester, whose encouragement, supervision and support from the first day of my research and during the long journey thereafter undeniable.

I am grateful to my supervisor, to the University of Nottingham and the department of Chemical Engineering for providing me the opportunity to undertake a Ph.D.

I would also like to acknowledge the help and support of my colleagues and core supervisors, Miquel Gimeno-Fabra and Thomas Huddle, for their precious guidance throughout my first and second years.

Special thanks are due to Promethean Particles, for sharing their expertise, materials and equipment - especially Sean Butterworth, who is a pioneer in his field of research and was a great asset for guidance and advice.

Thanks are due to all the lovely people I met during my time at the University of Nottingham, without whose support and encouragement it would have been very hard to continue during the difficult periods.

I would like to express my especial gratitude to my two brothers and sister for their continuous support and encouragement, and to my family, both close and far, who, even though they are scattered all over the world, kept in touch with all their support and encouragement.

I also give my loving thanks to my parents, Fouad Kadhim and Manahil Hussain. I would not have reached this point without their unconditional love and support.

Finally, appreciation to my husband for his endless kindness and patience; he never stopped believing in me, never stopped taking care of me, and now also Maria, our happy daughter, who was born during the hard times to spread happiness and light in our life.

Table of Contents

List of Figures

List of Tables

Nomenclature

AIC	analysing image colours
AIL	analysing image letters
ASR	analysing settling rates
CHS	continuous hydrothermal synthesis
DI water	deionised water
FB	full blue background
FB-B	full blue background-blue only channel
FB-G	full blue background-green only channel
FB-R	full blue background-red only channel
FG	full green background
FG-B	full green background-blue only channel
FG-G	full green background-green only channel
FG-R	full green background-red only channel
FR	full red background
FR-B	full red background-blue only channel
FR-G	full red background-green only channel
FR-R	full red background-red only channel
FW	full white background
HSP	Hansen solubility parameters
HSV	hue, saturation, value colour space
IPA	isopropanol
MAC	MATLAB analysis code

MS	metal salt
nm	nanometre
NPs	nanoparticles
RED	relative energy difference
RGB	red, green, blue colour channels
RI	refractive index
ROI	region of interest
RST	relative sedimentation time
ScW	supercritical water
SD	standard deviation
TSC	total solid contents
VIS	visual imaging system

Chapter 1: Introduction and Literature Review

1.1 Introduction

Over the last 20 years, Nottingham has had considerable success with the use of hydrothermal and solvothermal technologies in the synthesis of nanoparticle dispersions, using both bench and pilot scale continuous hydrothermal synthesis (CHS) rigs. This thesis introduces a new device to support this technology which is focussed on a characterisation method that is accessible, quick and effective. The concept is to use an image analysis system to provide rapid characterisation of the products directly from the rig. These characteristics can then provide initial conclusions about the physical properties and overall behaviour of a nanoparticle dispersion. This system aims to provide a more systematic and quantitative analysis of products whilst saving time and effort. This characterisation method can also predict the stability of a nanoparticle dispersion as well as other properties (such as transparency and colour variations) under different production conditions.

Research to fully understand the behaviour of nanodispersions immediately after leaving the Nottingham CHS rig and during storage (akin to shelf life behaviour) is of paramount importance to optimise the produced dispersions. Furthermore, successful scaling up to a pilot plant requires the products to be reliable for use in industry.

The visual imaging system (VIS) has been invented to be specifically used with the Nottingham CHS rig outlet stream to instantaneously and continuously monitor and evaluate the stability of the produced dispersions. Thus, the behaviour of the formulations can be estimated and this process also acts as quality assurance over time by checking the consistency and reliability at regular intervals during a production run. For example, taking samples every 5 minutes will allow comparisons to be made, which will indicate any changes during operation – such as the first sample not settling and the second sample settling after 15 minutes. This may signify either that no particles have been formed in the unsettled sample (it is simply the precursor solution) or the sample is a stable nanoparticle dispersion; the second sample, on the other hand, may have undergone agglomeration due to possible changes in pH, the conversion rate or reaction temperature. This provides a rapid indicator that a run is unreliable and inconsistent formulations are produced during the course of this run.

Although visual observation by naked eye remains the widely employed method by scientists, the VIS would allow visualisations to be analysed and quantified.

The stability of a system has been evaluated by simple methods, mainly by monitoring the sedimentation behaviour of dispersions in different liquids.

The properties and factors that result in the settling or sedimentation of particles dispersed in liquids have been a fundamental research focus for decades (Jamison et al., 2008). It is highly important to understand the influence of external liquid forces that cause the nanoparticle to change in motion, especially when considering processing these nanodispersions for different industrial applications. Both the liquid and the interfacial area surrounding the dispersed particles have a vital effect on the sedimentation behaviour of particles on the nanoscale (Hiemenz and Rajagopalan, 1997).

The forces acting against particle settling are buoyancy, thermal diffusion and viscous drag. Particle mass versus its cross section can change the default assumption that the larger particles fall faster than small particles (Abbott and Holmes, 2013). The size of particles, therefore, has a significant effect on stability. For small or fine particles, the cohesive forces between particles become more dominant than gravitational forces (Parteli et al., 2014).

The VIS has proven to be a simple tool to quantitatively determine the settling time based on particle size and the properties of the dispersing medium.

1.2 Literature Review

1.2.1 Introduction to Nanotechnology

While nanoparticles (NPs) have always existed in nature and their use evidenced throughout time, the real era of nanotechnology was arguably first launched on December 29th, 1959, by the eminent physicist, Richard Feynman, in his speech "*There's Plenty of Room at the Bottom*", in which he discussed the potential of manipulating and controlling individual atoms and molecules on a small scale (Feynman, 2012). Since then, the field of nanotechnology has seen exponential growth – particularly in the last four decades, as more and more techniques to study and analyse particles have become introduced. The field of nanotechnology can be defined as the synthesis, study, utilisation and manipulation of particles on the nanoscale, with at least one dimension less than 100 nm; where a nanometre is described as one billionth (10^{-9}) of a metre (Allaker and Ren, 2008).

This miniaturisation of particles offers unique properties, which are different to those exhibited by the traditional bulk scale material. In fact, two principal factors play a key role in enhancing the properties of nanomaterials: increased relative surface area and quantum effects (Bhushan, 2010). Therefore, particle reactivity, strength and magnetic, optical and electronic characteristics can be improved at the nanoscale. As a result, nanoparticles have garnered diverse applications (shown in Figure 1.1).

As depicted in Figure 1.2, the surface area of particles increases dramatically as the particle size decreases from bulk material to nanoscale particle. Thus, a greater proportion of atoms are found at the surface, compared to those embedded within the materials. For example, a particle sized 30 nm contains 5% of its atoms on its surface, at 10 nm 20% of its atoms and at 3 nm 50% of its atoms (Chaturvedi et al., 2012).

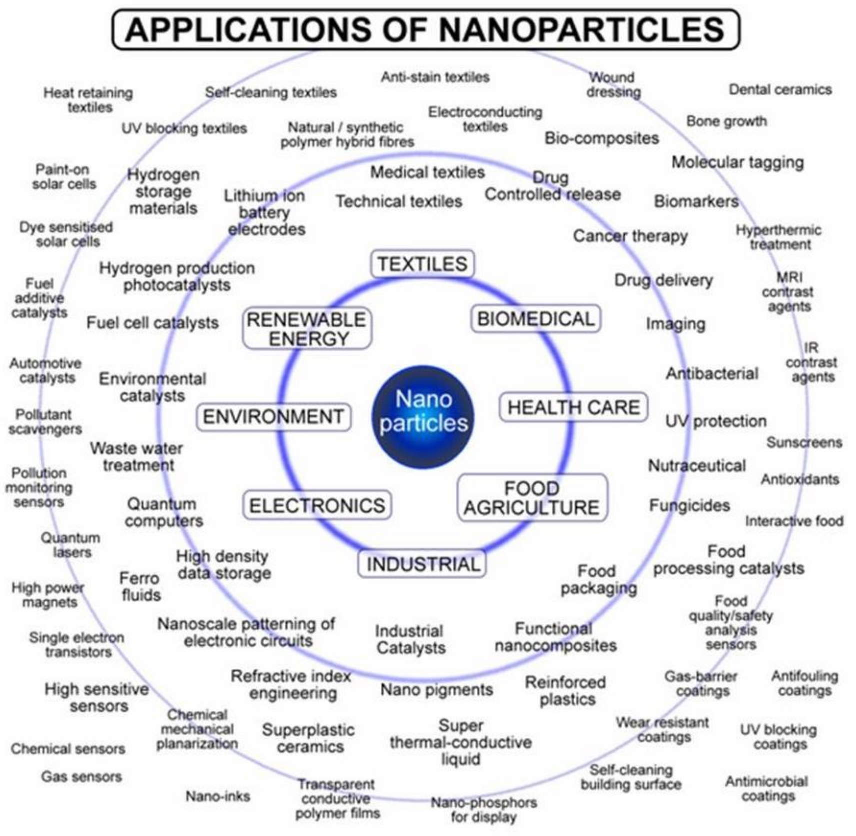

Figure 1.1 Applications of nanoparticles in different fields (Tsuzuki, 2009)

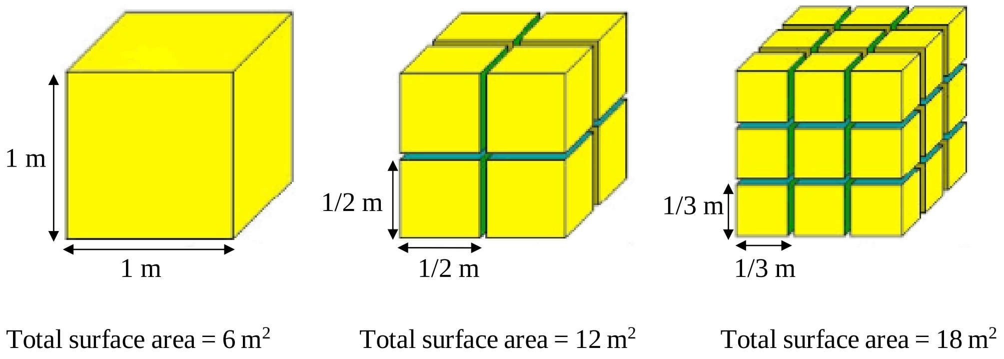

Figure 1.2 The increase in the relative surface area with smaller particle size (from left to right). (Image adapted from (NanoSense, 2006).

As catalytic chemical reactions occur at surfaces, the increase in surface area to volume ratio in nanoscale materials leads to enhanced catalytic activity of nano-catalysts compared to those exhibited by the equivalent bulk scale material (Zhao et al., 2011, Yetter et al., 2009, Kim et al., 2006, Abou El-Nour et al., 2010). This results in higher efficiencies or rates of conversion for smaller mass materials. Moreover, this reduces costs and any detrimental effect on the environment. TiO2 nanoparticles are a prime example of the advantages of nanoparticles in catalytic applications; they are shown to be more effective than the materials of the same mass but that are made up of larger particles in the photocatalytic decomposition of contaminants (Loryuenyong et al., 2013).

Moreover, smaller particles of 10 nm were found to exhibit super-paramagnetic behaviour. This phenomena seen in magnetic nanoparticles is due to the large proportion of atoms at the particle surface (Willard et al., 2004).

1.2.2 The Synthesis of Inorganic Nanomaterials

The properties of nanomaterials, including size, morphology, purity, crystallinity and surface area, are crucial to their function and application. These properties of any type of nanoparticle are, in turn, largely determined by the manufacturing route used to synthesise them. Thus, the method of manufacture is a highly significant factor in determining the characteristics and properties of the nanomaterial product. Each method of synthesis has its advantages and limitations, with the suitability depending on the target material or application. Generally speaking, the methods of nanoparticle production are divided into two main categories: *top-down* approaches and *bottom-up* approaches. *Top-down* methods involve the breakdown of larger particles (microscale or bulk scale) into smaller ones (nanoscale) without atomic-level control. The most common examples of this destructive process for nanoparticle production are mechanical milling, anodisation and lithography. Magnetic nanomaterials and others used for electrical and pharmaceutical applications have been produced using such methods (Sampathkumaran et al., 2011, Chen et al., 2010, Hallmann et al., 2011, Laaksonen et al., 2011). In this technique, the length of time of milling and the milling speed are the key determinants of the structure of the final product (Basa et al., 2008). However, this method suffers from inherent disadvantages that limit its industrialization. For instance, there is no consideration of particle size distribution, particle size or morphology, and, in some cases, this method can be time-intensive with some processes taking up to several hours (Thuan et al., 2009). This thesis will only focus on the constructive, synthetic *bottom-up*, approach – in particular, the chemical ‘build up’ of nanomaterials using principles of molecular recognition.

1.2.2.1 Solid state reactions

In sold state reactions, solid reactants, such as simple metal oxide or carbonate, are mixed and then heated at high temperatures (700-1000 °C) either in air or another gas flow of choice (Sohrabnezhad and Valipour, 2013). Reports have described the use of solid state reactions to produce CuO (Sohrabnezhad and Valipour, 2013) and Si3N4 (Dasog and Veinot, 2012), among other materials. The precursors are generally cheap and the technology is scalable; however, these reactions have the disadvantage of being energy-intensive and producing dry powders, which can pose health risks if inhaled (Zhao et al., 2019, Nel et al., 2006).

1.2.2.2 Vapour-phase methods

Vapour phase synthesis is the most commonly practiced method of producing metal and metal oxide nanoparticles. These approaches, such as spray pyrolysis, involve a liquid feed – a metal precursor dissolved in a solvent - which is mixed with a carrier gas (e.g. nitrogen) and nebulised, or atomised to produce droplets, into a furnace at high temperatures – typically >800 °C (Thiebaut, 2011). The high temperature leads to solvent evaporation and enable the metal precursors to undergo a chemical reaction to yield products that are deposited onto a substrate. This method has reportedly been used to synthesise coatings and films, GaN (Ogi et al., 2009) and TiO_2 (Figgemeier et al., 2007) nanoparticles and other materials. Although this method is typically cheap, relatively easy to run and produces particles with a narrow size distribution, its energy-intensive nature is a drawback. In addition, as with solid state reactions, products of vapour phase reactions are typically nanopowders and these must be handled with care.

1.2.2.3 Liquid-phase methods

Liquid phase synthesis is advantageous over the vapour phase method in that it does not require an expensive energy source and the reaction can take place at relatively low temperature. The wet route of manufacturing nanomaterials will be highlighted in this thesis as an example of it is the hydrothermal synthesis of nanomaterial, which will be used in this work. Thus, liquid phase processes will be described in more detail.

1.2.2.3.1 Co-precipitation

Co-precipitation is a simple and convenient technique for producing metal oxide nanoparticles with controlled composition. Typically, solutions are created by dissolving the starting materials (usually metal salts) in a solvent. The aqueous metal salts are then mixed, or added dropwise, at ambient or raised temperatures, to a base which acts as a precipitating agent. The product is a co-precipitated powder which elutes out of the solution. Co-precipitation is a widely used technique for the synthesis of ferrite nanomaterials (Rahman et al., 2013) (Amiri and Shokrollahi, 2013) and, in some cases, the process is performed in an inert atmosphere (Lu et al., 2007). While the method benefits from its simplicity, it has been shown that the particle size, morphology and composition of the product heavily relies on the type of precursor used, the pH and the reaction temperature. Furthermore, particles produced by co-precipitation are hindered by a wide particle size distribution as this process does not involve a typical short nucleation phase, followed by a slow growth period – which is what confers a narrow size distribution (Lu et al., 2007).

1.2.2.3.2 Microemulsion

Microemulsion is carried out in a thermodynamically stable system containing two immiscible liquids - usually water and oil - and an amphiphilic surfactant (Fanun, 2008). A solution of metal salt dissolved in water and small droplets of oil (such as heptane) are stabilised by the surfactant. Oil droplets can also be stabilised in the water, depending on the ratio of each in the mixture. The exact droplet size can be manipulated by altering different parameters but remains within the nanometre scale. The reactions of particle synthesis take place within the drops, which act as 'nanoreactors'. The size of the droplet thus limits the size of the final particle (López-Quintela et al., 2004). The issues with this technique mainly relate to finding the right combination of surfactant and oil; nevertheless, the microemulsion method has been successfully utilised to synthesise $BaTiO_3$, $CaCO_3$, CeO_2, ZrO_2, and SnO_2, among other materials (Ganguli et al., 2008). The method has the advantage of finely controlling particle size, distribution and shape. However, the reaction mechanisms enabling the control of particle size and size distribution remain to be fully understood, limiting the applicability of this method somewhat.

1.2.2.3.3 Sol-gel

Sol-gel methods have been used extensively for many years for the synthesis of metal oxides nanoparticles (Bezzi et al., 2003, Senthilkumaar and Selvi, 2008, Isasi-Marín et al., 2009). Typically, a soluble chemical (metal salt or alkoxide) is carefully reacted so that clusters of the insoluble particle are formed, which gradually over time develop into a 'gel' network – a matrix of solid nanoparticles dispersed in a liquid phase. Through centrifugation, filtration or evaporation, the nanoparticles can then be isolated to yield the product. Low reaction temperatures and a highly controllable environment allow for more controlled growth of nanoparticles, compared to the cruder solid state methods. As a relatively cheap, straightforward method that creates highly homogenous particles of fine-tuned size and size distribution, sol gel remains one of the most popular methods of synthesising nanoparticle today.

However there are some disadvantages to this technique, such as the need for templates, which can be costly and need to be removed after synthesis (Liou et al., 2010, Lester et al., 2013). Moreover, this process is associated with low crystallinity and purity and requires post-synthesis steps (such as calcination and milling steps) (Hakuta et al., 1998). The high cost of sol gel processes (including for equipment, precursors or running costs) coupled with low yield and long reaction times also signifies that, even if the method produces extremely high quality nanoparticles, there is little to no potential of scaling up the technology to a commercial or industrial level (Tighe et al., 2013).

Conversely, hydrothermal synthesis has been demonstrated to allow greater control of the composition and morphology of products. Furthermore, the requirement for additional processing steps is minimal and the products are dispersed in water, rather than as a nanopowder, making this the preferential method for nanomaterial synthesis.

1.2.3 Hydrothermal Synthesis of Nanomaterials

Hydrothermal synthesis is generally defined as the use of aqueous solvents with high temperature and high water pressure to dissolve and recrystallise materials that, under ordinary temperature and pressure (<100 °C, <1 atm) conditions, are relatively insoluble (Yang et al., 2014). This method allows a high degree of flexibility in terms of the experimental design, is cost-effective, environmentally benign and utilises widely available precursors with good control over reaction parameters. All this facilitates the formation of products with controllable characteristics and high crystallinity, usually without the need for any post-synthesis steps. Moreover, as the main reaction medium for this method is water (rather than noxious solvents), the technology attracts a lot of scientific and commercial interest as sustainable, green technology. Increasing efforts in research devoted to hydrothermal synthesis has generated a wide range of nanomaterials which can be produced via this route (Aksomaityte et al., 2013, Clark et al., 2017, Lester et al., 2013, Hobbs et al., 2009b).

1.2.3.1 Supercritical water (ScW)

When considering a mixture of liquid and vapour at equilibrium conditions it is notable that when the temperature is increased, the liquid phase becomes less dense due to thermal expansion; thus, increasing the pressure would increase the density of the gas phase. As the pressure and temperature are elevated, a point is reached at which there is no longer a distinction between the two phases; in a pressure-temperature phase diagram, this is called the “critical point”. The critical point of water (T_c=374 °C and P_c=22.1 MPa) is the point of the highest temperature and pressure at which its vapour and liquid coexists in equilibrium (Figure 1.3). Above this point, there is no noticeable difference between the two phases. At pressure and temperature conditions higher than the critical point, however, water becomes supercritical (LaGrega et al., 2010).

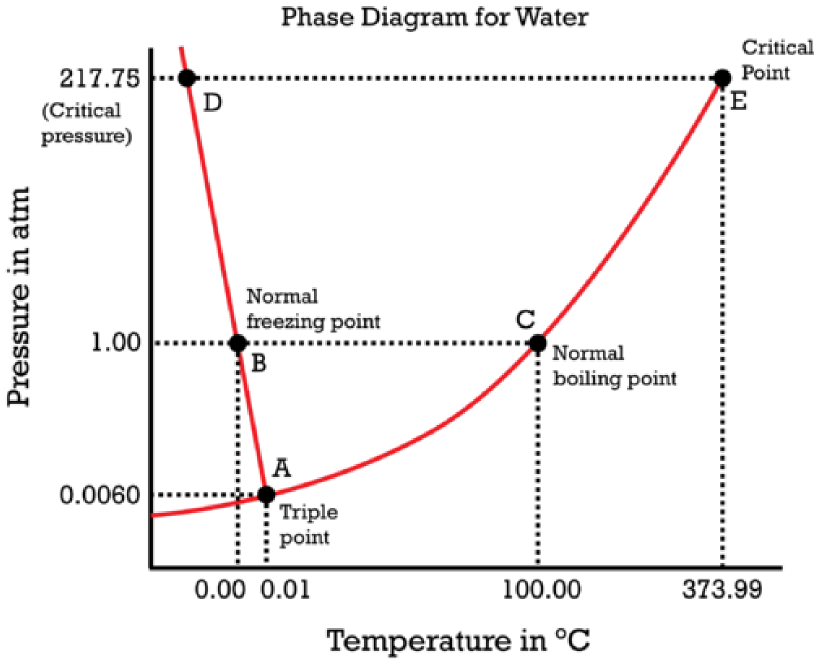

Figure 1.3 Pressure-temperature phase diagram showing the triple point, normal boiling point and critical points of water (Kamler and Soria, 2012).

ScW is another phase under which the physicochemical properties of the mixture range between gas and liquid. ScW's solvation power is perhaps the most exploited property of this mixture. Changes in chemical and physical properties of water, upon reaching its supercritical state, have a tremendous effect on its solvation power (Weingärtner and Franck, 2005). For example, ionic salts that are dissolved in a water at ambient conditions become less soluble at supercritical conditions. Due to this principle, and other chemically attractive properties of ScW, it has been increasingly used in recent years as a reaction medium for the production of nanoscale metals and metal oxides (Dunne et al., 2015).

The properties of water at ambient conditions are mainly dictated by hydrogen bonding, which allows water to support the ionisation of salts and to dissolve poorly organic substances. At supercritical conditions, however, the number of hydrogen bonds present in water is about one-third of that in water at normal conditions (Cochran et al., 1992). This leads to a decrease in the dielectric constant and an increase in the dissociation constant, K_w – which measures the breakdown of water molecules to H^+ and OH^- ions (Lester et al., 2006). Figure 1.4 shows the density, dielectric constant and ion products of water at 24.0 MPa. All properties suffer abrupt changes in the proximity of the critical point of water; exceeding this point causes the water properties to remain constant, without detectable changes.

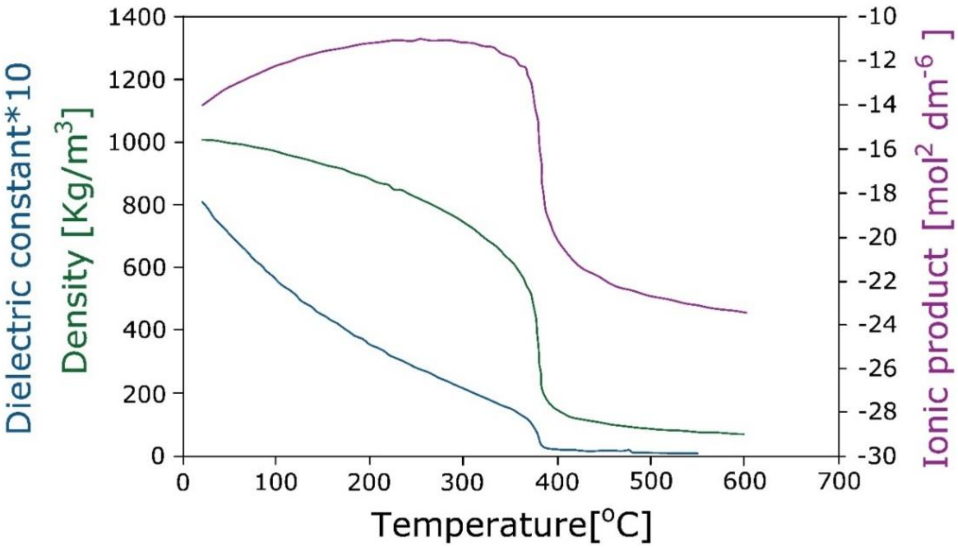

Figure 1.4 Changes in the properties of water with increasing temperature at 24 MPa. (Adopted from (Kritzer et al., 1999).

1.2.3.2 Formation of metal oxide in ScW

In the early 1990s, the Arai and Adschiri group were the first to take advantage of the unique properties of ScW – namely the reduced dielectric constant and ready dissociation to H^+ and OH^- – for the synthesis of metal oxide particles in a continuous manner, including different morphologies of aluminium oxide, cobalt oxide, magnetite, nickel oxide and titania (Adschiri et al., 1992). This research was extended, making remarkable contributions to the field of continuous ScW synthesis of nanomaterials, which included detailed optimisation of reaction conditions for tunable product composition, morphology and functionality (Byrappa and Adschiri, 2007).

In ScW hydrothermal synthesis of metal oxide nanoparticles, the reagent stream – which typically consists of an inorganic metal salt (ML_x) – is brought into contact with a separate stream of water, which is pre-heated to a near critical or supercritical state. The high K_w value and concentration of OH^- species in near-critical water leads to the immediate hydrolysis of the metal salt, without the addition of any base. Then, the metal hydroxide proceeds to precipitate as metal oxides through a dehydration step, which results in the formation of metal oxide nanoparticles – as shown by the following equations (Adschiri et al., 2000, Adschiri et al., 2001):

$ML_x + xOH^- \rightarrow M(OH)_x + xL^-$ Hydrolysis step

$M(OH)_x \rightarrow MO_{x/2} + x/2H_2O$ Dehydration step

These metal oxide nanoparticles are then carried further downstream through an additional heating zone to promote growth (Dunne et al., 2015).

1.2.3.3 Other reactions in ScW

The properties of ScW described in Section 1.3.1 make it a ‘solvent of interest’ for applications other than the hydrothermal synthesis of nanomaterials.

Reactions conducted in ScW are divided into degradation and synthesis reactions (Al-Duri et al., 2008, Caramazana-Gonzalez et al., 2017). Degradation in ScW involves complete oxidation and efficient elimination of aqueous waste by a process known as supercritical water oxidation (ScWO) (Bermejo and Cocero, 2006). Due to the non-polar nature of ScW, it becomes completely miscible with organic compounds, such as alkanes and aromatics (as well as permanent gases, like oxygen) allowing it to transport molecules more effectively (Brunner, 2009). As a green technology, ScWO is significantly advantageous over other conventional treatment processes and even certain modern processes, such as wet air oxidation and incineration (Al-Duri et al., 2015). Other notable degradation reactions include gasification of biomasses for production of light gases – particularly methane, hydrogen, carbon dioxide and carbon monoxide. As with ScWO, the unique properties of ScW act as potentially useful features for the application of ScW to gasification media (Marrone and Hong, 2009).

ScW has also reportedly been used for the extraction of cellulose nanocrystals (CNCs) by supercritical water hydrolysis. Again, compared to any other established processes, this technology is beneficial due to its greenness, continuous availability in nature and potentially significantly higher energy efficiency (Novo et al., 2015). Recently, a combination of the two opposed processes, synthesis and destruction, carried out in ScW has been reported in a one stage reactor for hazardous waste oxidation and in-situ nanoparticle formation. This led to enhanced oxidation efficiency and the potential economic benefits of combining the two processes together was thus deemed to be significant (Al-Atta et al., 2018).

1.2.4 Continuous-flow Hydrothermal Reactors

For the purpose of hydrothermal synthesis of nanoparticles, continuous methods are shown to have the potential to provide a wide range of nanoparticles on the commercial scale. Continuous systems use pumps to drive reactants through a heated, pressurised pipework reactor system. Hence, these systems are renowned for their high reaction rates and very short residence time (< 1 min) (Fang, 2010). Moreover, continuous systems allow more control over experimental parameters, such as temperature, pressure, concentration of reactants and residence time; this is important as these paremetrs exert a direct effect on the product characteristics, such as particle size, size distribution, morphology and crystallinity (Lester et al., 2012, Sue et al., 2006).

It is generally understood that the way the metal salt and the ScW streams are mixed within continuous hydrothermal reactors plays an key role in determining the quality and yield of the product (Blood et al., 2004, Takami et al., 2012). As such, several groups have built and experimented with different mixer/reactor designs to optimise hydrothermal synthesis of nanomaterials. Early work on hydrothermal synthesis used a T-piece fitting to mix the reagent flows, as a simple reactor design (Adschiri et al., 2000). In many cases, the T-piece was placed upright with the ScW feed entering through the side arm and the cold metal salt flowing down; the bottom arm of the T-piece in turn formed the product outlet (as shown in Figure 1.5). While this simple reactor configuration is a readily available part, allows rapid heating of precursor streams and has proven successful for the synthesis of a variety of materials, it is unfortunately prone to blockages as a result of particle build-up in the metal salt feed arm.

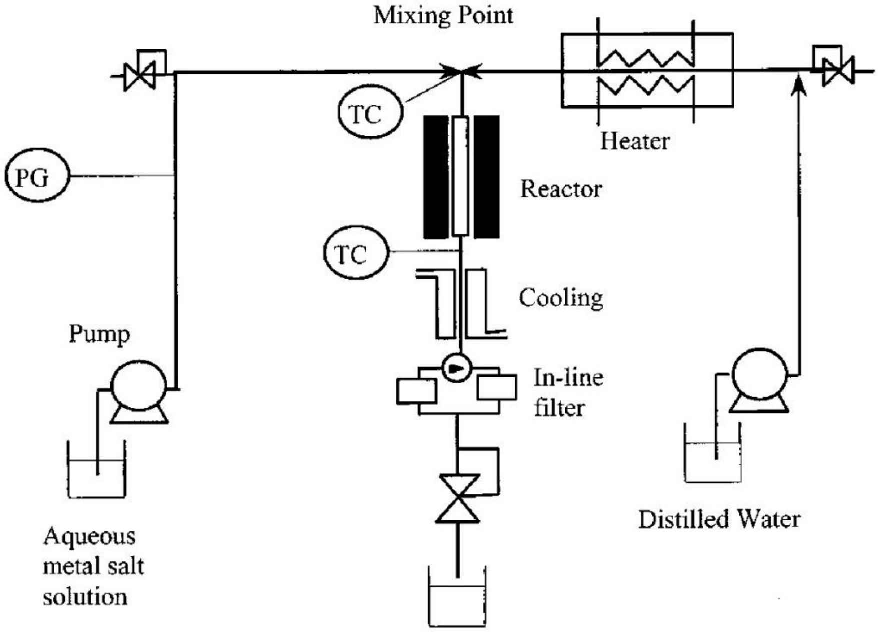

Figure 1.5 Schematic diagram of the apparatus typically used for continuous hydrothermal synthesis of nanoparticles (Adschiri et al., 2000).

Previous studies at the University of Nottingham were conducted to apply a new modelling technique to develop and optimise the above process, as well as highlight any inconsistencies in the mixing dynamics within a T-piece reactor (Blood et al., 2004). The physical modelling method is based on the absorption of light by a dyed solution, which is used to quantify the mixing pattern of two modelling fluids in a Perspex modelling reactor at ambient conditions. Modelling fluids, methanol and sugar water (with densities of 0.79 gcm^{-3} and 1.178 gcm^{-3}, respectively) were carefully selected as analogues for low-density ScW and the higher density cold stream. The mixing regime was physically recreated using modelling fluids in a Perspex modelling reactor. The Reynolds numbers for the ScW and aqueous metal salt streams entering the ScW system were used to calculate the corresponding flow rates in the pseudoreactor. This was shown to be a powerful visualisation technique, as ScW cannot be directly visualized due to the process conditions not permitting the use of transparent reactors (Huddle et al., 2017). The experimental results (depicted in Figure 1.6) indicated that T-piece reactor geometry would lead to poor mixing conditions and suffer undesirable issues. These issues, including back mixing, stagnant zones and fluid partitioning, were shown to arise due to the difference in the densities of the modelling fluids, which induce strong buoyancy forces and turbulent macro-mixing. This, in turn, results in particle build up and blockages – a problem regularly observed in ScW reactors.

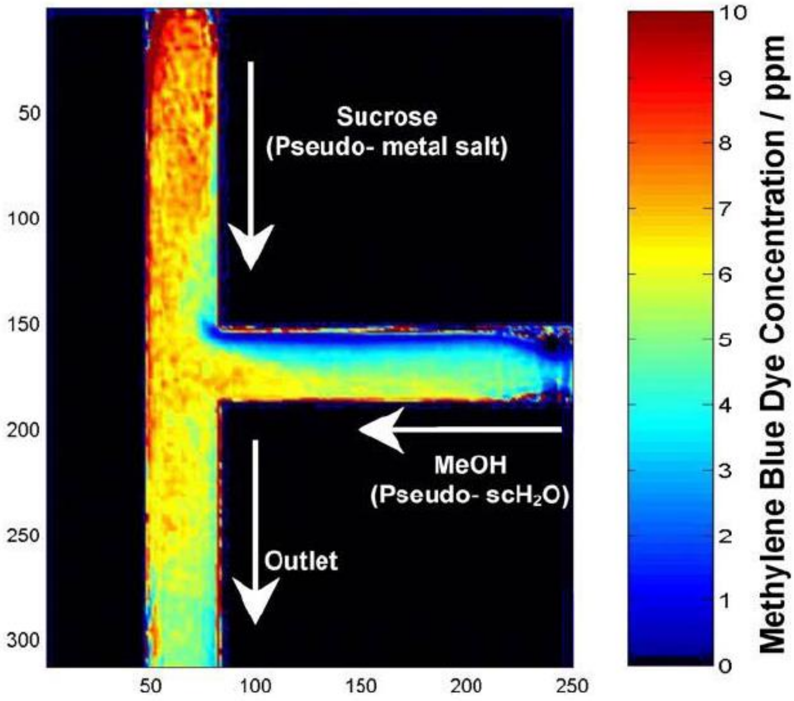

Figure 1.6 Results of the physical modelling studies on the mixing dynamics of the T-piece mixer (Blood et al., 2004).

Later, the physical modelling results were confirmed by computational fluid dynamics (CFD) simulations (Sierra-Pallares et al., 2011) and, more recently, by a neutron beam, which was used to visualise the mixing behaviour of ScW and room-temperature water in a T-mixer (Takenaka et al., 2013). Neutrons are effectively scattered by hydrogen atoms and exhibit high permeability in heavier elements, such as Fe, Cr, and Ni. Therefore, neutron radiography can be used to detect differences in the water density in a stainless-steel reactor. The use of this technique represented a major breakthrough in the field and the researchers have since shown that it is possible to use this form of radiography to observe flow arrangements within the reactor. The results (Figure 1.7) indicated the importance of buoyancy forces due to the density difference between two fluids, as proved by findings from physical modelling studies.

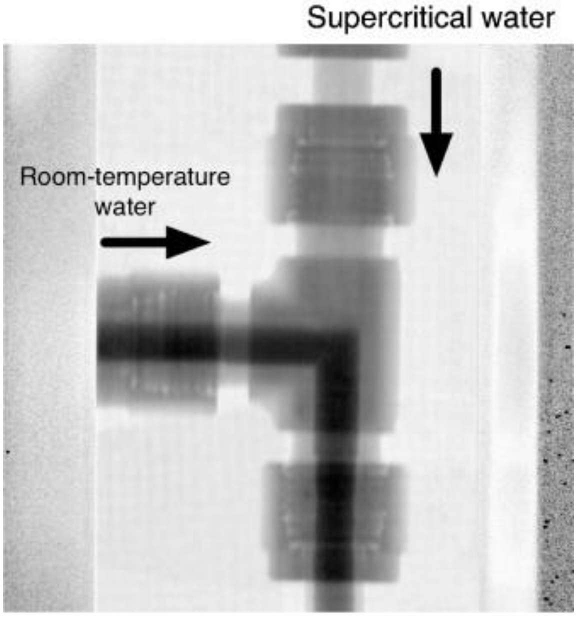

Figure 1.7 The internal structure and water flow in the T-piece reactor, visualised using neutron radiography (Takami et al., 2012).

Continuing from the work of Blood et al., researchers at the University of Nottingham used physical modelling images, combined with CFD results, to assess the best possible design for a ScW reactor. As a result of these investigations, a novel counter-current mixing reactor design was patented (Lester and Azzopardi, 2009). This reactor exploited strong buoyancy forces to induce turbulent mixing and prevented the unwanted mixing conditions associated with the more basic T-piece reactor.

1.2.4.1 Counter current mixing reactor

The physical modelling and CFD simulations revealed that the difference in density between the two modelling fluids was a phenomenon of the T-reactor. It was suggested that the key to achieving uniform mixing within the mixing point, and thus optimising the reactor, was to exploit this difference in density between the two fluids. Five principles were considered of greatest importance for designing the 'ideal' ScW hydrothermal synthesis reactor:

1. Achieving ideal and uniform mixing of the reactants in and downstream of the mixing zone. Homogeneous mixing is essential for the formation of small particles.

2. Ensuring minimal (if any) heating of the inlet precursor stream before the mixing point to prevent premature deposition of metal salts in the pipes leading to the reactor.

3. Enabling instant and rapid heating of the precursor upon contact with superheated water feed to induce supersaturation.

4. Creating strong downstream eddies to prevent any particle accumulation on the reactor surface.

5. Ensuring a short average residence time to minimise subsequent particle growth and, thus, produce relatively uniform particle sizes with a narrow particle size distribution.

The application of these principles led to the development of the novel reactor design, termed the 'counter-current mixing reactor'. This in-house laboratory-scale reactor was used for the work described in this thesis.

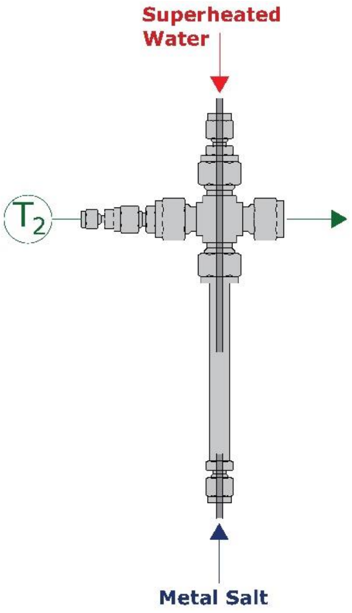

Figure 1.8 The counter-current mixing reactor used for the synthesis of nanoparticles in this thesis. The cold aqueous metal salt flows upwards from the base of the reactor and mixes counter-currently with a superheated water stream.

The counter-current mixing reactor design is depicted in Figure 1.8: a tube-in-tube configuration was constructed using Swagelok® high pressure fitting and the process works as follows: preheated water is fed downward through the thinner inner tube (of 1/8" diameter, with a wall thickness of 0.028") and a cool metal salt stream is fed counter-currently into the outer tube (of 3/8" diameter, with a wall thickness of 0.065") (Lester et al., 2006). Mixing and nanometal oxide particle formation occurs at the interface, following which the product travels upwards and leaves via the side branch of the reactor, before being cooled at the heat exchanger. Since the development of this innovative reactor, a wide range of nanomaterials have been successfully produced and include metal oxides such as Co3O (Lester et al., 2012), TiO2 (Caramazana-Gonzalez et al., 2017), Fe2O3 (Dunne et al., 2015), ZrO2:Eu3+ (Hobbs et al., 2009a), metals such as Ag (Aksomaityte et al., 2013), phosphates such as hydroxapatite $Ca_{10}(PO_4)_6(OH)2$ (Lester et al., 2013) and metal organic frameworks such as ZIF-8 (Munn et al., 2015).

The equipment set-up used to conduct the experimental work was constructed in-house at the University of Nottingham for the continuous production of nanoparticles. A process flow diagram representing the ScW CHS rig equipped with a counter-current mixing reactor is provided in Figure 1.9. All system components, including the counter-current reactor, tubing and fitting were constructed entirely from 316L stainless steel (Swagelok). Pressure within the system was maintained by a back pressure regulator (BPR, Pressure Tech, UK). Temperature was monitored and recorded using Picolog software connected to a personal computer.

For nanoparticle formation experiments, an organic material solution was introduced into the system at a pre-set flow rate of up to 10 $mLmin^{-1}$, using a Gilson HPLC pump equipped with a 25 SC pump head. The stream flowed through a check valve before entering the counter current reactor from the inlet at the base as an upward flow, without any preheating.

Meanwhile, a DI water stream (sometimes containing hydrogen peroxide) was pumped into the system, at a maximum flow of 20 $mLmin^{-1}$, using a Gilson HPLC pump equipped with a 25 SC pump head. This proceeded to flow through a check valve before flowing through a pressure relief valve and piezoelectric pressure transducer, which in turn was connected to a digital pressure monitor. The stream passed through an analogue pressure gauge, before entering a 6m length of 1/4" tubing coiled around an 2KW electric heater. A thermocouple within the heater block acted as a feedback control. After the heater, the water feed flowed past a thermocouple, before entering the top of the reactor as a down flow.

Upon exiting the reactor, the solution product, including any particles formed during the synthesis process, was partially cooled via a primary vertical cooling loop. The product then flowed through a T-shaped union at which a thermocouple was mounted on the perpendicular port, allowing the initial cooling temperature to be monitored. The product was subsequently cooled by a counter current heat exchanger, which reduced the temperature to ambient. The product stream then continued to flow through a pressure relief, before passing through the BPR and resulting in the collection of the product at ambient pressure.

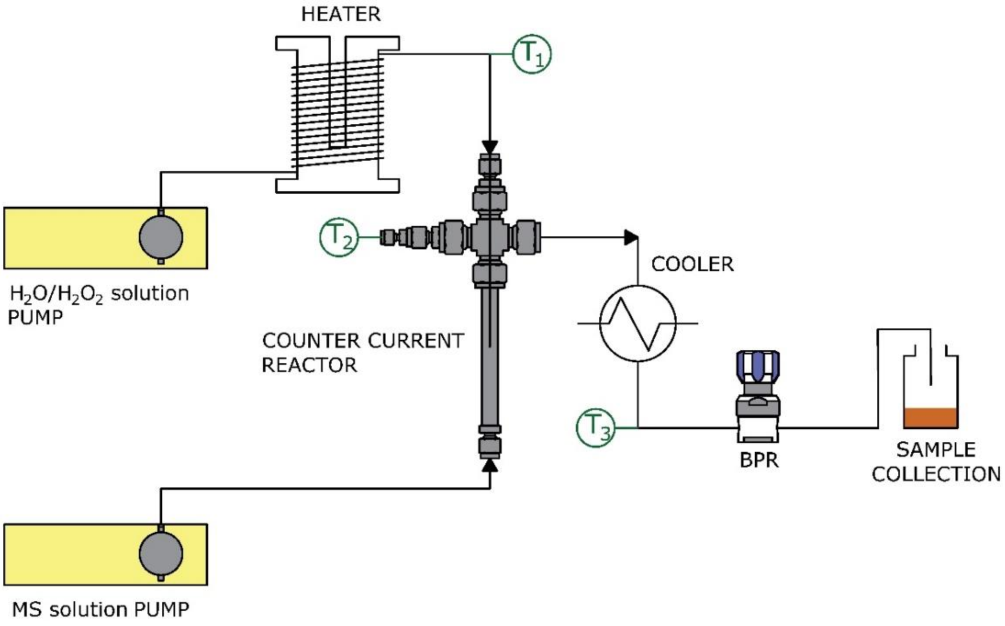

Figure 1.9 Simplified flow diagram of the CHS rig. T1 measures immediately after the heater; T2 is the post-mixed flow; and T3 is the temperature of the flow before the BPR.

1.2.4.2 Advantages of the counter current design

The counter-current mixing reactor contains a stream of ScW feed flowing down the internal pipe before colliding with the cold metal salt feed. This is an important feature of the reactor as ScW is buoyant and tends to rise – a behaviour that was revealed by physical modelling (Blood et al., 2004). In the scenario of an upright T-piece reactor with the heated water feed entering through the side arm and the cold metal salt flowing down, the water was shown to rise into the top arm of the T. By flowing upwards, the metal salt feed became heated, causing the nucleation of particulates. Thus, the cold metal salt feed in the counter-current mixing reactor is pumping upwards, representing another good feature; the cold flow is approximately four times more dense than the superheated fluid and the counter-current geometry, therefore, ensures the metal salt stream is not heated prior to mixing, as this could cause precipitation of the salt and, in turn, blockage.

Generally, the nucleation process of continuous hydrothermal synthesis has an average reaction time of just a millisecond; however, this time can vary depending on the material. The counter-current reactor design also offers the ability to heat the post-mixed flow with the help of a band heater attached to the reactor external wall.

Unlike other reactor designs for hydrothermal synthesis of nanoparticles, the counter-current mixing reactor combines the mixing device and the reactor into one entity, which promotes instant and rapid heating of the precursor stream and, thus, short residence times.

1.2.5 Destabilisation of Nanoparticle Dispersions and Current Challenges in Stability Characterisation Methods

As stated in Section 1.2.1, the benefits and applications of nanomaterials are vast. However, maintaining a stable nanoparticle dispersion that is monodisperse (i.e. shows minimal or no change in particle size and size distribution with time) is a known challenge. Furthermore, the available characterisation methods for detecting instability in dispersions lack many important features, such as reliability, cost-effectiveness and accessibility. The following sections shed detail on these challenges and describe the most commonly used instrumentations for stability evaluation, as well as their limitations.

1.2.5.1 Dispersion stability

Constructing a novel end-product of a desired function using nanoparticles can only be achieved if the nanoparticles are stable within their dispersing medium. Stable dispersion can be effectively incorporated in the intended material, such as a polymeric matrix, to produce nanomaterials of different functions. Thus, maintaining a nanosized, homogeneous and stable dispersion throughout the formulating and processing stages is the most important and currently the main challenge when working with nanomaterials (Shqau, 2005, Mori, 2015).

As a particle decreases in size, a greater proportion of atoms can be found at its surface, compared to bulk or larger particles. Consequently, surface energy and reactivity increase with decreasing particle size (Nanda et al., 2003, Hanemann and Szabo, 2010). This has profound effects on stability, as smaller particles tend to be less stable due to their relatively increased surface area to volume ratio; thus, they can coagulate more easily into agglomerations to reduce their surface energy. The mechanism by which the particles coagulate determines whether a soft or hard agglomeration occurs

(Nichols et al., 2002). Soft agglomeration (e.g. flocculation) is governed by Van der Waals and other physical particle interactions and is usually reversible by applying mechanical mixing or simple agitation. Conversely, hard agglomeration (e.g. coalescence) of particles can be irreversible and is formed when particles are bonded together by sinter necks or other strong chemical bonds (Tsantilis and Pratsinis, 2004, Hanemann and Szabo, 2010).

Since many novel applications rely on the nanosize and large surface area of particles, agglomeration can be problematic – examples for this are fluorescence, photocatalysis, magnetism and ultraviolet absorbency (Kim et al., 2014). Nanomaterial used in applications that can be adversely affected by the presence of agglomerations include: coatings, where this would impede the mechanical properties (Parida et al., 2011); antibacterial agents, where this would affect transport and biological activity (MacCuspie et al., 2011); and transparent protective films for transparent plastics, where resultant opacity would reduce the desired optical transparency (Chantarachindawong et al., 2012). For this reason, rigorous efforts throughout the history of nanoformulations have been made to suppress agglomeration using different methods either during formulation or post-production. Using treatments, such as stabilising agents (with the right compatibility and stoichiometry), the right solvent (or mix of solvents) as a dispersing medium (with consideration to the solvent's viscosity and density) or simple mechanical mixing or sonication were some of the methods employed, with consideration of the potential toxicity and environmental impact of treatments.

The destabilisation in dispersions can take several forms, such as creaming or sedimentation, and these mainly result from particle migration. Coalescence or flocculation can also occur due to increasing in particle size (Buron et al., 2004).

1.2.5.2 Methods used for evaluating dispersion stability

As discussed earlier, obtaining stable dispersions by controlling and maintaining the particles size and size distribution with time plays an important role in preserving novel or favourable characteristics in engineered nanomaterials. This is important for satisfying the continually expanding market requirement for different nanoparticle applications, such as in sensors, drug delivery systems, diodes, data storage materials and photovoltaic cells (Mori, 2015). Thus, it is particularly important for formulators to analyse the dispersion stability and investigate its physicochemical quality before incorporating nanoparticles into different products (Buron et al., 2004).

The methods described in this section measure or characterise certain destabilisation phenomena in particle dispersions. For example, electron microscopy instruments can reveal the particle size increase from the formation of agglomerates, while UV-visible spectroscopy and turbidity measurements can be used for assessing stability by monitoring sedimentation with time.

1.2.5.2.1 Naked eye observation

The simple method of observing by eye has been used in several studies to witness destabilisation in dispersions, which leads to phase separation (namely sedimentation or creaming), and any manifestation of instability due to particle migration or increase in size. However, this is not a reliable, accurate or a quantifiable method of observation. Moreover, the naked eye takes a longer time to detect the beginnings of any destabilisations, compared with technological methods, such as the Turbiscan (Mengual et al., 1999a).

1.2.5.2.2 UV-visible spectroscopy

In this method, ultraviolet (UV) light and visible light are shined through a sample. When exiting the sample, light will possess a different intensity from that before it is passing through the sample. This is due to the absorption, reflection or scattering of part of the passing light – depending on the properties of the interaction medium. The UV-visible spectroscopy instrument is able to perform measurements by detecting and recording the intensities of incident radiation (I_o), the transmitted radiation (I) from the sample and the transmittance (T), which is determined by the Lambert's Law ($T= I / I_o$).

Additionally, the absorbance is calculated based on the Beer-Lambert relation ($A= k. c. l$); where A is the absorbance, k is the extinction coefficient, c is sample's concentration and l is the length of the radiation that passes through the sample (Agilent, 2000).

To monitor the stability of a dispersion, the change in transmittance with time is measured by using the rate measurements/kinetics mode in the UV-visible spectrophotometer, whereby any increase (e.g. due to particles sedimentation) or decrease (e.g. due to particle flocculation/coalescence) in the transmitted light intensity can be recorded as a function of time at a fixed wavelength.

The use of UV-visible spectroscopy for stability evaluation of nanoparticle systems or dispersions has been reported in numerous studies (Mudunkotuwa and Grassian, 2010, Xu, 2018); these included measurement of the sedimentation rate, which indicates the occurrence of destabilisation due to particle agglomeration. Stable dispersions can also be evidenced using this technique; such samples can generate a sharp absorption peak in the UV-visible absorbance spectra at a certain wavelength – the more homogeneous the distribution of particles in the dispersion, the sharper the absorption peak (Sathiya and Akilandeswari, 2014).

The disadvantage of performing stability analysis using this method is that the radiation beam strikes only a limited area of the analysed dispersion. Thus, only one spot of the sample can be analysed each time. This can make it difficult to identify whether full or partial sedimentation occurs and where the clear, partially clear or agglomeration layers are located.

1.2.5.2.3 Electron microscopy

Both types of electron microscopy (EM) – scanning electron microscopy (SEM) and transmission electron microscopy (TEM) – have been used for stability studies by showing the presence of agglomerates and, thus, confirming any flocculation or coalescence in a sample (Klang et al., 2012). These phenomena indicate instability of dispersions, as mentioned earlier. Thus, EM commonly accompanies other methods of evaluating stability to confirm the causes of certain dispersion behaviours (Sun et al., 2012).

Due to the high resolution and contrast of EM imaging, it is possible to determine the size, shape and composition of agglomerates and even of particles at the lower limit of the nanoscale, as well as detecting whether a formulation is mono- or polydisperse. Furthermore, EM images can identify materials caused instability, which can result based on the type or concentration of the material, by (for example) observing the presence of intermolecular bridging (Chen and Elimelech, 2007).

The disadvantages of SEM and TEM, however, are complicated sample preparation – including dilution of concentrated dispersions, drying (Kuo and Wen, 2008) or the need to using cryogenic techniques for accurate investigation of nanoemulsions (Klang et al., 2012). Furthermore, TEM measures only a small drop of sample, which may not accurately represent the qualities of the full dispersion. Additionally, certain polymers and organic materials are not visible using TEM (Preetz et al., 2010).

SEM, on the other hand, is only able to measure solid samples; these must be prepared to fit into a specialised chamber of 10 cm diameter. Moreover, some organic materials can become significantly damaged when exposed to the SEM high-voltage electron beam.

The principles of EM and sample preparation for the work in this thesis will be discussed in Chapter 2.

1.2.5.2.4 Zeta potential

The zeta potential is an essential parameter affecting a dispersion’s stability, especially for aqueous systems; it is a measure of the mean charge developed at the ‘effective surface’ of charged particles in contact with an ionic solution (Figure 1.10). This can cause a repulsion or attraction between particles, depending on the strength of the charge (MalvernPanalytical, 2019). The Zetasizer instrument (Malvern Panalytical Ltd) has been widely used to measure this value (Pelin et al., 2009, Dubey et al., 2010, Sathiya and Akilandeswari, 2014, Preetz et al., 2010) and was used for the work in this thesis. The zeta potential measurement will be discussed in more detail in Chapter 2.

To describe the principles behind the zeta potential, a positively charged particle is given as an example in Figure 1.10. In this case, negative ions from the surrounding medium are attracted and strongly bind to the particle to form the stern layer. This is followed by the diffuse layer, where less tightly connected ions can be found. Both layers form the electrical double layer that includes the slipping plane, which defines the new boundary of the particle. The zeta potential is the potential at this boundary.

Thus, the zeta potential is an indicator of the stability of particles in a dispersion. The usual rule of thumb is that dispersions of > +30 mV or < -30 mV of zeta potential magnitude are “charged” and will resist flocculation via electrostatic repulsive forces; thus, they are considered to be stable. Factors affecting the zeta potential are the solution pH, type, the concentration of ions in the solution and its conductivity (Bhattacharjee, 2016).

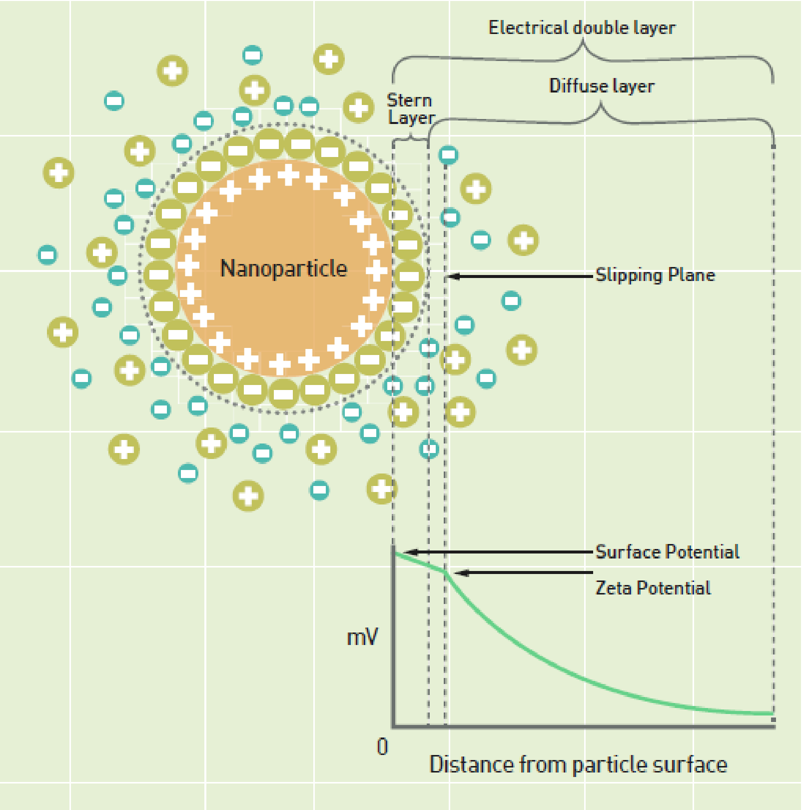

Figure 1.10 The origin of the zeta potential of a charged particle in an ionic solution (MalvernPanalytical, 2019).

Using the zeta potential technique to analyse the stability of dispersion has many advantages; for instance, samples can be easily introduced into the instrument and data is generated rapidly. Furthermore, the number of materials required to be tested to improve sample stability is greatly reduced, thereby also reducing the duration and cost of measurements. However, careful sample preparation is essential as the zeta potential is easily influenced by small changes in pH, the type and concentration of the ions in the medium surrounding the particles and the presence of surfactants.

1.2.5.2.5 Dynamic light scattering

Dynamic light scattering (DLS) principles have also been exploited for colloidal stability studies using particle size analysis. The most frequently used instrument for the DLS technique is the Zetasizer Nano-ZS (Malvern Panalytical Ltd), the operation of which will be discussed in Chapter 2.

The method used to determine the stability of dispersions is monitoring variation in the mean hydrodynamic diameter and the polydispersity index (PDI) of particles with time (Chen and Elimelech, 2007, Yuan et al., 2008, Kuo and Wen, 2008). This variation is the result of several factors, such as the type and the concentration of an added stabiliser or surfactant, the type and pH of the dispersion medium and the formulation temperature (Wang et al., 2014). Maintaining particle size for a longer time indicates a stable dispersion (Weir et al., 2012, Bai et al., 2017).

The DLS instrument is compact, table-top and integrated for both particle size and zeta potential measurements. Additionally, this technique is non-invasive and provides detailed information from the analysed data (Bhattacharjee, 2016).

However, there are limitations to the DLS technique using the Zetasizer Nano-ZS instrument. First, because particle size is a measure of the intensity of scattered light by particles of any size and shape, reliable size measurements are only obtainable if the particles in the dispersing medium are highly stable (i.e. with no evidence of agglomeration or sedimentation with time). Furthermore, polymer layers or other materials attached to the particle surface are added to the calculated particle size. In addition, dispersions must be highly diluted to be suitable for DLS measurements, which may alter several parameters of the original formulation (e.g. the size of particle by possible agglomeration or changes in pH, viscosity and RI). Thus, the initial formulation can be inaccurately represented by the diluted version (Lerche, 2002).

1.2.5.2.6 Turbidimetry

The most effective and frequently used instrument for colloidal stability assessment is the Turbiscan™, manufactured by Formulaction Inc. (Mengual et al., 1999a, Mengual et al., 1999b, Lemarchand et al., 2003, Yuan et al., 2008, Celia et al., 2009, Liu et al., 2011, Kim et al., 2014, Sun et al., 2019). This instrument utilises multiple light scattering techniques to characterise dispersion stability with time. The principle behind this method is as follows: near-infrared radiation (wavelength = 880 nm) is shined onto a sample placed inside a transparent glass cell. The light, along with the transmitting (T) and backscattering (BS) light detectors, are placed onto a mobile head that moves up and down to scan the entire height of the sample in the cell (usually 55 mm) (Figure 1.11, left). The emerged light from a sample, after undergoing scattering multiple times by various dispersion entities (such as droplets in emulsions, solid particles in dispersions or bubbles in gas), is captured by backscattering and transmission detectors for analysis by the instrument (Figure 1.11, right). The obtained data is interpreted using Turbiscan™ software and parameters, such as the particle average diameter (d) and volume fraction (φ), can be quantified using the formula: $BS = f(d / \varphi)$ (Formulaction, 2019).

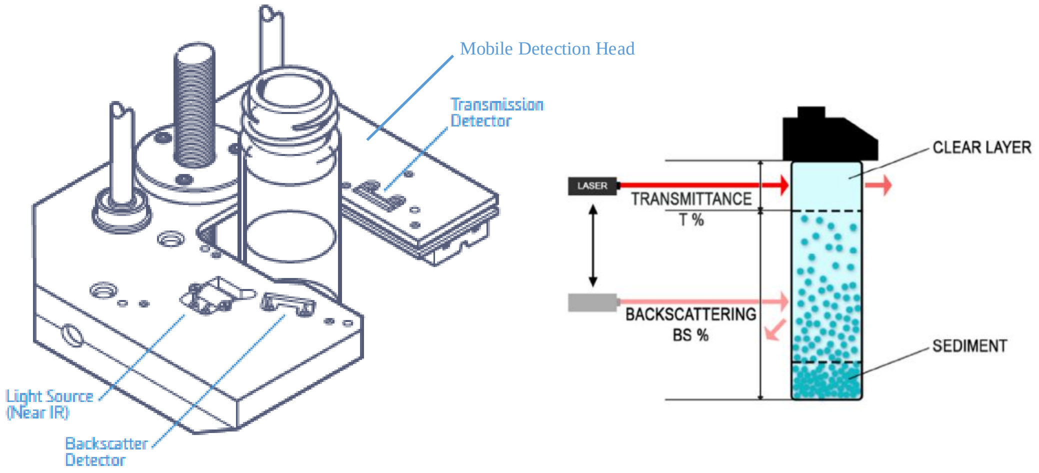

Figure 1.11 (Left) The main parts of the mobile head of the Turbiscan™ instrument (Formulaction, 2019) and (right) a schematic of light interactions with an unstable dispersion in the measurement cell (Matusiak and Grządka, 2017).

The advanced technology of the Turbiscan™ instrument (i.e. its ability to scan the entire sample vertically at user-defined periods) enables it to detect and accurately characterise multiple destabilisation phenomena, such as coalescence, flocculation, sedimentation and creaming, by monitoring variations in the particle size and concentration with time. Furthermore, all measurements can be carried out on original concentrated dispersions, without the need to alter the formulation (e.g. by dilution).

Some of the aforementioned methods were used for the work in this thesis to support the findings generated by the novel VIS system. Relevant experimental details will be described in Chapter 2.

1.3 Research Objectives and Scientific Contribution

The importance of formulating stable nanodispersions in order to maintain their desired characteristics is cardinal for a reliable production of novel end-products and has been highlighted throughout this chapter. The key factors affecting dispersion stability, along with a number of remediations, have also been described.

The starting point of ensuring stable dispersion is establishing a reliable technique for formulating nanodispersions. Thus, the merits of the University's CHS rig, equipped with the in-house patented counter-current mixing reactor, have been discussed in detail in this chapter. The specialised design of this reactor has been associated with improved chemistry at the mixing zone of the metal salt and ScW streams, as well as shortened residences time of reactants. This has the advantages of producing ultrafine particles with sizes that are at the small end of the nanoscale.

The CHS rig has proved viability, reproducibility and sustainability in the production of a wide array of nanoparticles with many desirable characteristics, such as high crystallinity, narrow size distribution, controlled shape and composition, as well as improved purity in both the lab and pilot scales. However, destabilisation of nanodispersions produced in this rig can still occur. Thus, improvements to this technology are constantly made by testing new materials and optimising the generated formulations to satisfy the rise in industrial and commercial demand.

As particle properties and stability determine the performance of the end-product application, it is always important for formulations to be characterised using suitable methods. To achieve this, a characterisation instrument should always accompany the continuous production of dispersions to reveal any issues with stability that may occur in real time. The most frequently used methods for dispersion stability evaluations were, therefore, reviewed in this chapter (Section 1.2.5.2). Unfortunately, as mentioned, these methods share either one or more of the following drawbacks: they are too costly, are not readily accessible, require long operation times and significant efforts for adequate sample preparation and involve alteration of the original sample formulation. This is also coupled with the individual limitations of each instrument. These disadvantages can, therefore, cause unwanted delays in measuring the stability of a sample, which increases the risk of the physical properties of the sample changing in the process. Developing a device that can be readily available to easily and effectively measure destabilisation is, therefore, of the utmost importance. Filling this gap in nanoparticle characterisation was the motivation for this PhD work and inspired the invention of the VIS at the University, which aims to fulfil the above goal. The VIS system will be described in Chapter 3.

The main aims of this work are:

1. To design, construct and develop a device (the visual imaging system; VIS) that can characterise the stability of different particle dispersions.

2. To investigate whether the VIS is easily accessible, reliable and can provide rapid data acquisition and interpretation, using a simple image analysis principle, of particle dispersions obtained using the University of Nottingham's CHS rig.

3. To validate the VIS characterisation results by comparing them with the results obtained using commercial instruments.

4. To evaluate the usefulness of the VIS in providing information about other physical properties of nanoparticle dispersions, such as transparency and colour variations.

5. To investigate the potential of VIS to simplify and improve the methods used to select the best solvent for maintaining dispersion stability (Hansen solubility parameters; HSP).

Ideally, the outcome of this research would help formulators in the colloidal and nanodispersion production sectors to evaluate the quality of the produced dispersions using a simple, cost-effective and accessible optical technique that is based on the concept of image analysis. This should help provide a rapid, systematic and quantitative evaluation of the characteristics of the products. The information to be gathered from this technique includes changes in physical appearance, such as colour, opacity and transparency, as well as the main function of the instrument – which is detecting and quantifying the destabilisation phenomena in a dispersion by monitoring the dispersion over time.

Compared to other techniques used in the characterisation of colloidal systems, the VIS is an improvement as it:

1. Offers multiple functions at the same time.
2. Is simplistically designed by including an iPad, a webcam and a computer. This make it relatively cheap to operate, easily constructed and readily accessible.
3. Uses the image analysis principle for data acquisition and analysis, which enables simple and rapid characterisation of multiple sample properties.
4. Can measure the stability of highly concentrated dispersions.

1.4 Thesis Structure

This thesis is composed of seven chapters, evolving in line with the research development: from theory to application.

Chapter 1: An introduction to the general purpose of the current research work and a review of the importance of nanomaterials and nanotechnology. The traditional routes for nanomaterial manufacturing are described, with specific emphasis on hydrothermal synthesis of nanoparticles using the CHS rig. The techniques used to characterise the physical properties and stability of dispersions are reviewed, followed by a brief introduction to the purpose behind the development of the VIS in Nottingham.

Chapter 2: The characterisation techniques utilised to confirm the observations and accuracy of the findings by the VIS are detailed.

Chapter 3: The methods employed to validate the novel instrument, by exploring different designs and image analysis concepts using MATLAB, are presented.

Chapter 4: The use of the VIS to assess the stability of titania dispersions, produced by the CHS rig, at different conditions is reported. Additionally, the stability of comparable batches of titania dispersions after integration into polymeric matrix was investigated to further confirm the VIS results.

Chapter 5: The use of the VIS to investigate several properties of different iron oxides, such as transparency, turbidity, colour and stability, at different formulation conditions is detailed.

Chapter 6: The calculations of HSP using VIS for the prediction of dispersibility of nanoparticles in several solvents are presented.

Chapter 7: Summarised conclusions and potential future directions are provided.

Chapter 2: Experimental Protocol

This chapter details the characterisation techniques used to confirm observations made during the validation stage of the VIS and samples stability evaluations. The underlying principles, generated information and operation conditions will be described for each instrument.

All the materials presented in this thesis were formulated using the Nottingham CHS rig.

2.1 NPs Formulation using the CHS Rig

The nanoparticles generated in this project were synthesised using the CHS rig developed by Lester and Azzopardi (Lester et al., 2006, Lester and Azzopardi, 2004), as reported in Chapter 1. The rig arrangement is shown in Figure 2.1.

This reactor is based on the 'counter-current mixing reactor' configuration, as shown in Figure 2.1 (c). This reactor consists of two pipes: one is inside the other to enable counter-mixing of the metal salt precursor (which is pumped at room temperature upwards) with a stream of heated water (which is pumped at sub- or supercritical conditions downward through the inner, smaller diameter pipe). This produces dispersions of nanoparticles through rapid hydrolysis and dehydration of the metal salt to the corresponding metal oxide. This design ensures not only uniform mixing of the reactants but also minimises the residence time of the products at the reaction point, preventing further crystal growth (Lester and Azzopardi, 2004). A back pressure regulator (BPR) is used to control the pressure either manually or pneumatically from a computer. A temperature control regulator is located above the pumps to set the water stream temperature. The process pressure and temperatures are monitored and recorded using the PicoLog software.

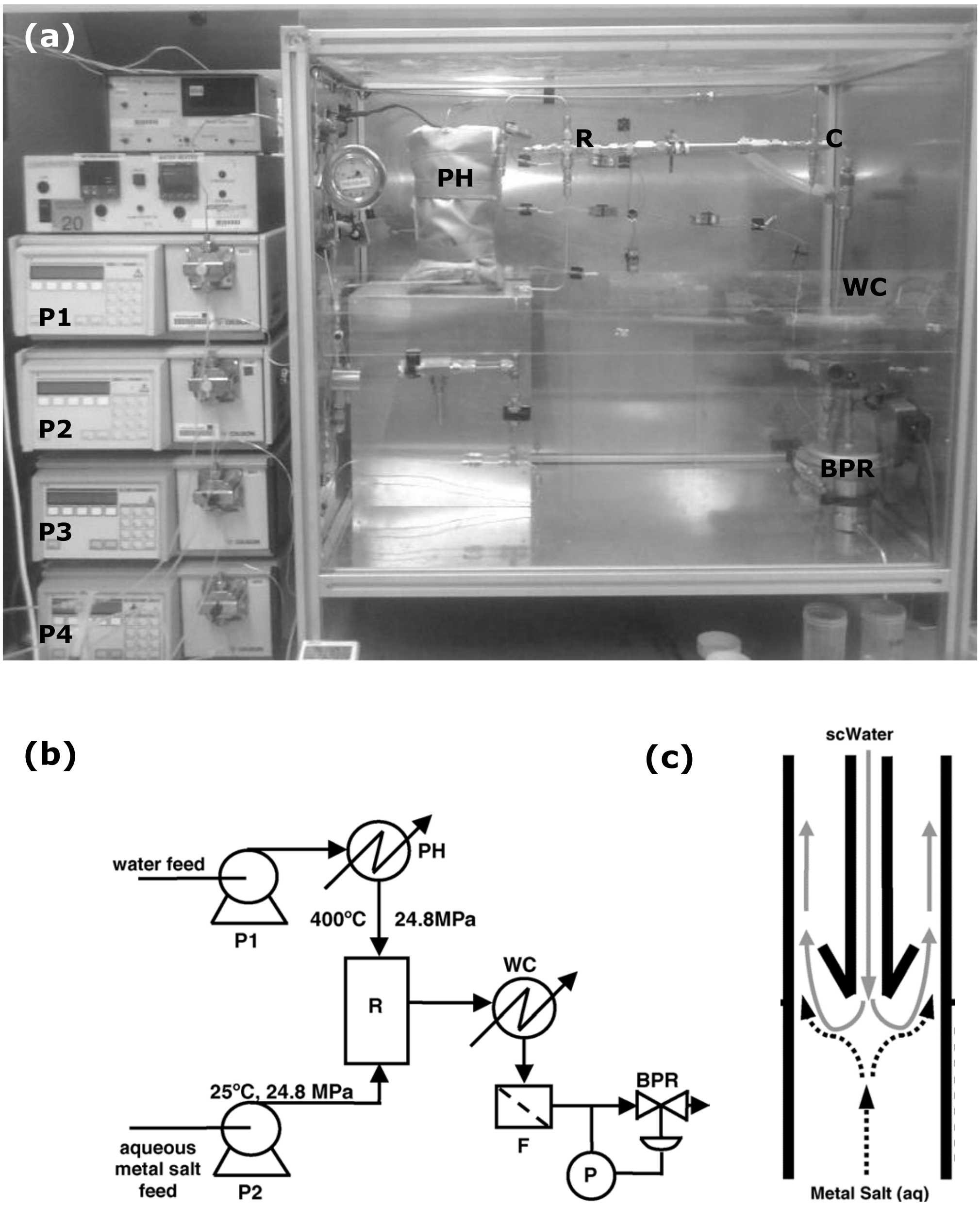

Figure 2.1(a) The CHS rig, where P1 - P4 are Gilson® HPLC pumps, PH is the preheater, R is the counter-current mixing reactor, C is the capping point, WC is the water cooler and BPR is the back pressure regulator. (b) Continuous supercritical reactor flow diagram of the main parts and the arrangements by which the ScW and the metal salts are introduced into the reactor (R) with an example of a condition used. (c) The counter-current mixing reactor. (Figure adapted from (Lester et al., 2006).

In this system, there is also the possibility of using a capping point ("C" in Figure 2.1, a), which allows for post-synthesis modifications of the particles, such as adding surfactants, polymers or other metal salts. In this thesis, however, the capping agents were introduced as part of the metal salt solution before the reaction, in line with the earlier experiments carried out by co-workers (Elbasuney, 2012).

2.2 Dynamic Light Scattering (DLS)

Dynamic light scattering is a technique used to estimate the particle size and size distribution. The instrument used for DLS analysis is a Zetasizer Nano-ZS (Malvern Panalytical Ltd), which is fitted with a 632.8nm wavelength He-Ne laser and can measure particle of sizes ranging from 0.3nm to 10µm. The instrument also measures the particle hydrodynamic size, which is "*the size of a hypothetical hard sphere that diffuses in the same fashion as that of the particle being measured*", using Malvern's Non-Invasive Back Scatter (NIBS) technology (MalvernPanalytical, 2019). This is achieved by exploiting the continuous Brownian motion of particles interacting within the solvent – which corresponds to the translational diffusion coefficient. Larger particles diffuse slower than smaller ones and this motion causes the laser light beam in the DLS instrument to be scattered at different intensities, depending on the particle size (very small particles tend to absorb light and scatter very little light, which is difficult for the DLS to detect). The resulted fluctuation in the intensities of the backscattered beam are then recorded and analysed using the DLS cumulants analysis to calculate the hydrodynamic particle diameter, using the Stokes-Einstein correlation (Equation 2.1) – which relates the diffusion coefficient and the diameter of the particle (Oriekhova and Stoll, 2014).

$$\mathbf{d(H) = kT/3\pi\eta D} \qquad \text{Equation 2.1}$$

Where d(H) is the particle hydrodynamic diameter, D is the translational diffusion coefficient, k is Boltzmann’s constant, T is the absolute temperature and η is the viscosity of the fluid.

The polydispersity index (PDI) is also an important factor, recorded alongside the particle size measurements; it is a width parameter that can show how broad the particle size distribution is (the range of small to large particle sizes) and whether large agglomerations are present in the sample. A PDI larger than 0.7 indicates a very wide-ranging particle size distribution and signifies that inaccurate DLS results will be obtained (Hunter, 2001).

The temperature is also an important parameter, as it affects the accuracy of the DLS results due to its relationship with the viscosity of the solvent that, in turn, directly affects the velocity of the Brownian motion (the translational diffusion coefficient, D) used to determine the particle size in the DLS.

DLS measurements were applied to the experiments in Chapters 4 and 5; cuvettes made of disposable 12mm o.d. square polystyrene (part number: DTS0012) were filled with a minimum 1 mL of sample for accurate size calculations and placed inside the Zetasizer Nano-ZS instrument. The Zetasizer software was then used to obtain the data for each sample. It is important to specify the solvent package used for the samples before running the software for the accuracy of the produced data. The dispersant in all cases was water with a 0.89 cP viscosity at 25 °C. For each sample, the software provided three measurements in order to calculate the standard deviation.

2.3 Zeta Potential

The zeta potential (ζ) was also measured using Zetasizer Nano-ZS, exploiting Malvern's M3-PALS technique provided by this instrument – which is a development of the Laser Doppler Velocimetry (LDV) technique. This can overcome the electroosmosis effect which occurs on the measurement cell wall and enables the user to measure the electrophoretic mobility of particles in the sample, which is important to calculate the ζ using the Smoluchowski approximation (Equation 2.2).

$$\boldsymbol{\zeta = \eta/\varepsilon\, U_e} \qquad \text{Equation 2.2}$$

Where, ζ is the zeta potential, U_e is the electrophoretic mobility, η is the viscosity and ε is the dielectric constant.

Electrophoretic mobility is a measure of the velocity of particles travelling towards the opposite charge electrodes of a cell after applying an electrical field through the sample. The intensity of the scattered beam passing through the cell, which represents the speed distribution of particles, is then recorded and the data was obtained using Zetasizer software (MalvernPanalytical, 2019).

The zeta potential technique was applied in Chapters 4 and 5; samples, which were prepared according to the methodology described in the respective chapters, were loaded into specialised cells that are fitted with electrodes for zeta potential measurement. These cells were made from disposable folded capillary (U-shape, part number: DTS1060) and were introduced into the instrument to obtain the measurements produced by the Zetasizer software.

2.4 Electron Microscopy

Electron microscopy (EM) utilises the electrons that either pass through a sample (transmission EM; TEM) or are refracted from the sample surface (scanning EM; SEM) to generate images. These types of EM can be used to study materials in the low nano-/microranges, with TEM showing a higher resolution at higher magnifications. In addition, the x-rays diffracted by the samples can be used to quantify the sample composition (Energy Dispersive X-Ray or EDX).

2.4.1 SEM

In this thesis, the NP dispersion in titania-epoxy nanocomposites was analysed using a JEOL WINSEM JSM-6400 scanning microscope. High-resolution images of the back-scattered electron (BSE) were obtained using 10kV accelerating voltage and x1000 magnification to obtain a 60 μm scale. Each image was collected after 30 frame x-ray mappings. Elemental analysis was achieved with the EDX attached to the SEM instrument.

2.4.2 TEM

TEM is a microscopy imaging technique that uses electrons as a source to provide very high-resolution images down to the scale of several Angstroms. The configuration of the TEM system is given in Figure 2.2. An electron beam generated by an electron gun travels through the sample material and the transmitted electrons hit a screen located at the bottom of the microscope to form a projection of the sample, where parts may appear darker than others depending on the density of a material. Thus, particle size and morphology can be determined based on the difference in contrast of the transmitted electrons. The transmitted electrons then generate an image of the particle, which is shown either on a fluorescent screen or a monitor.

In this work, TEM was used for the characterisation of metal oxide nanoparticles produced via hydrothermal synthesis in order to assess their morphology and size. TEM micrographs were obtained using JEOL 2000 FX TEM at an accelerating voltage of 100 kV (using higher energy might cause the magnetic iron oxide particles to attract and stick to each other to form aggregates). The grid used was copper mesh with graphene oxide on a lacy carbon film. The tested samples were prepared by adding 10 drops of DI water to one drop sample. After a gentle shake, the samples were added to the copper grids to be introduced to the TEM instrument.

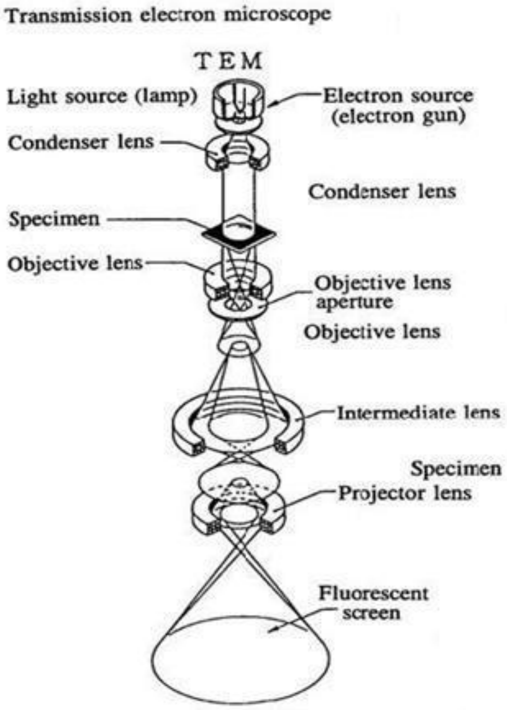

Figure 2.2 The basic layout of a transmission electron microscope (Warwick, 2018).

2.5 pH and Conductivity Measurements

pH and conductivity measurements were very helpful in the characterisation of the colloidal behaviour of particle dispersions. For this, the suspensions were analysed using the JENWAY 3540 pH-conductivity meter. The meter was regenerated and calibrated using pH buffers spanning the pH range of interest (pH4, 7 and 10) prior to experimentation. Following this, appropriate cleaning and maintenance was conducted as per the manufacturer's instructions to ensure accurate readings for each experiment.

2.6 X-Ray Diffraction (XRD)

This technique is used to determine the phase composition, crystalline size and structure of a solid sample. As illustrated in Figure 2.3, an X-ray beam of a known wavelength (λ) is fired at the target material, which then interacts with the electrons of the atoms on each crystal plane. As a result, the x-rays are scattered from the atoms and collected by the detector component of the equipment. The crystal solid in which the atoms are arranged in a periodic array (in long-range order) can produce a diffraction pattern that contains information about the atomic arrangement within the crystal. However, amorphous materials lacking a long-range atomic order cannot produce such a diffraction pattern. During analysis, an x-ray beam is directed at the target material from a range of incident angles. As the rays hit the material, they are diffracted by the lattice structure of the crystal. The sample is fixed and the detector rotates to measure the intensities of the diffraction peaks at each angle. Thus, the intensity at each angle depends on the orientation and the distance between the parallel planes of atoms. Braggs law calculates the angle where constructive interference from x-rays scattered by the parallel planes of atoms will produce a diffraction peak.

$$\mathbf{n\lambda = 2d\sin\theta} \qquad \text{Equation 2.4}$$

Where n is an integer, λ is the wavelength of the x-ray, d is the spacing between diffracting planes and θ is the incident angle between the x-ray source and the sample.

The diffraction pattern obtained for every crystalline phase is unique, as the position and spacing of the atoms within the crystal lattice, and the spacing between the crystal planes, are specific to the material. Thus, each crystal structure yields signal peaks of different intensities at differing angles of 2θ. A diffraction pattern can, therefore, act as a 'fingerprint' for a given substance. In addition to this phase identification, diffraction patterns may also yield information on the crystallite size. Crystallites smaller than 120 nm create broad diffraction peaks and this can be used to quantify the average crystallite size of nanoparticles, using the Scherrer Equation 2.5.

$$\mathbf{D} = \frac{\mathbf{k\lambda}}{\boldsymbol{\beta}\ \mathbf{cos}\boldsymbol{\theta}} \qquad \text{Equation 2.5}$$

Where D is the crystallite size, K is the Scherrer constant, which takes into account the shape of the crystal, λ is the x-ray wavelength, β is the full width of the peak at half maximum (FWHM) in radians and θ is Bragg's angle.

In this work, XRD analysis was carried out on the dried metal oxide nanoparticles, which were obtained by freeze-drying with liquid nitrogen under low temperature vacuum (-54°C). The analysis was completed using a Bruker D8 Advance system (Bruker AXS, Germany) through CuK radiation (λ=1.54056 A) in a 2θ range between 15° and 75°. The Scherrer method, assuming Gaussian peak broadening, was used to calculate the crystallite size of metal oxide nanoparticles.

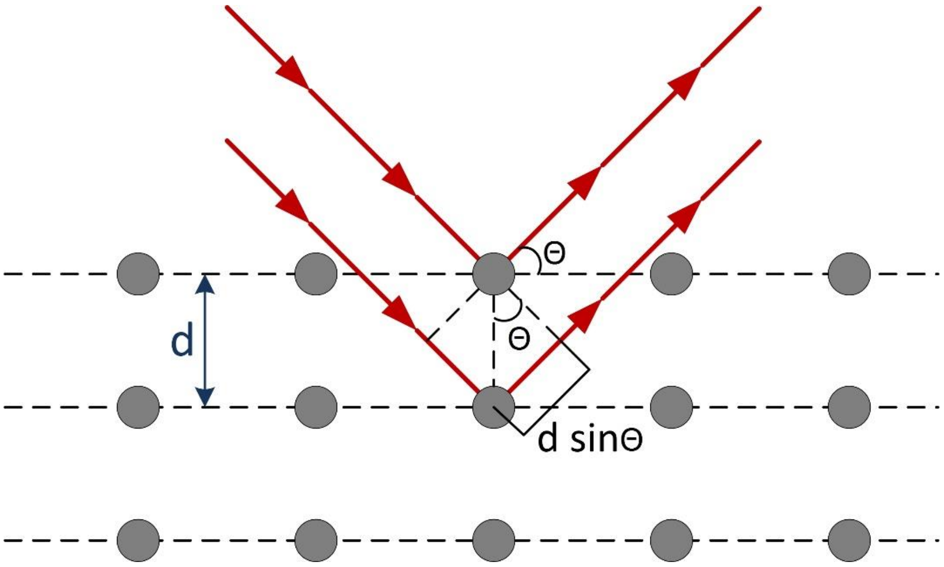

Figure 2.3 The principle of XRD analysis.

Chapter 3: The Visual Imaging System Design, Validation and Calibration

3.1 Introduction

In this chapter, the novel visual imaging system (VIS) constructed at the University of Nottingham is introduced, the procedures used to validate and calibrate it are described and examples of the possible measurements obtained using the system are demonstrated. The approaches employed to validate and define the limits of the system include: exploring different designs; testing materials of different properties; and utilising various image analysis techniques using MATLAB.

Three designs, termed VIS-1, VIS-2 and VIS-3, were evaluated in terms of convenience based on specific requirements. The VIS-1 is composed of a single, relatively large, glass vessel with attached acetate paper of various characteristics. It also contains a light pad, which is used as a source of white light (Section 3.2.1). The VIS-2 (Section 3.2.2) consists of multiple glass cuvettes loaded into a semi-circular holder, which is designed to overcome imaging issues related to camera optics. The final design (VIS-3) is comprised of multiple glass cuvettes placed on a straight holder and an iPad as the source of light and characters (Section 3.2.3). The validation and calibration steps also required solutions of various densities, colours and nanoparticle dispersions. Finally, because the data is acquired using the concept of image analysis, the contribution of MATLAB to capturing and analysing the images will be described.

The system is simple, cost-effective, accessible and can be easily assembled. It is particularly useful for initial characterisations of a variety of samples, which can be easily carried out prior to undertaking more complex characterisation methods. As described in Chapter 1, such methods generally require booking, complicated sample preparation and user training.

The VIS can be used to evaluate the following parameters (as will be shown in Chapters 3, 4, 5 and 6).

1- Transparency/opacity

2- Colour

3- Stability of dispersions

4- The compatibility between particles and different solvents, using Hansen solubility parameters (HSP)

3.2 The VIS Designs

The VIS designs were fully carried out in this work, ensuring minimal use of parts and amounts of solution and a maximum number of possible measurements.

Table 3.1 The specifications of the components used in the VIS designs.

	Make and Model	Dimensions (Height x Width x Depth) mm	Technical Specifications	The VIS Design
Cam	Logitech® HD Pro C920	(43x94x71) mm	▪ Max Resolution: 1080p/30fps - 720p/30fps ▪ Focus type: autofocus	VIS-1, VIS-2 and VIS-3
Light screen	MiniSun® LED LightPad	(260x350x8) mm	▪ Energy Saving LED Technology. ▪ Produces Bright and Even White Light.	VIS-1 and VIS-2
iPad (used as projector only on max brightness)	iPad Air (MD796B/A)	(170x240x7) mm	▪ Resolution: 2048x1536 ▪ Capacity: 64 GB ▪ 9.7 in (diagonal) display ▪ Anti-reflective coating on display	VIS-3
Computer	Gigabyte Technology Ltd. (B250M-DS3H)	Standard	▪ Processor Intel(R) Core (TM) i7-7700 CPU @ 3.60GHz ▪ RAM 32 GB ▪ Operating system 64-bit ▪ Windows 10	VIS-1, VIS-2 and VIS-3

A summary of the specifications of each of the components of the three VIS designs is shown in Table 3.1.

3.2.1 The VIS-1 (glass vessel and light pad)

3.2.1.1 System configuration

The VIS-1 is composed of a transparent glass vessel (170 x 240 x 26 mm dimensions and ~800 ml capacity). An image depicting letters of varying sizes or a colour swatch were positioned behind the vessel containing the solution (sample) of interest (Figure 3.1).

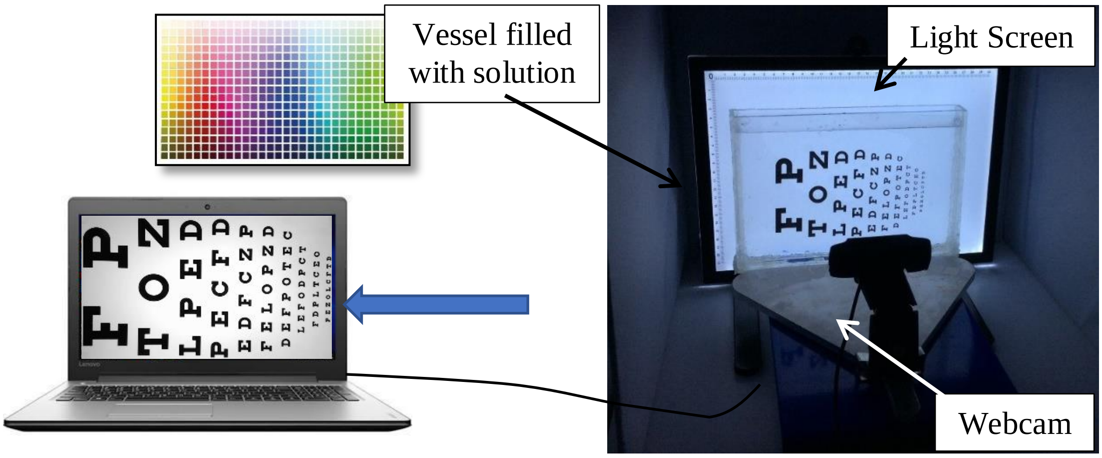

Figure 3.1 Setup of the VIS-1 using a Snellen chart attached to the glass vessel. The inset represents the colour swatch option, which can be interchanged with the Snellen chart.

The system was placed inside a white box to minimise interference with external light during sample alterations. A light pad (MiniSun® LED LightPad) was used as the white light source to provide sufficient and uniformly diffused light for systematic results. A webcam (Logitech® HD Pro C920) used to capture the images was affixed to a base facing the vessel and connected to a computer, through which images were captured using a MATLAB code (Section I.1-I.2, Appendix I).

3.2.1.2 System Calibration and validation

Calibration of the VIS-1 was carried out using digital image analysis and correlation of data with outputs from commercial instruments, or well-known systems, depending on the property required to be measured. For example, in measuring concentrations using the letters (Section 3.2.1.2.1), the measured variable is the letter distortion value (the variation in letter area or perimeter) in the acquired images of different solutions. This is attributed to the change in the refraction angle of light in dense liquids or nanoparticle dispersions and was calibrated using refractometer data. The calibration of the VIS-1 was carried out following the procedure described in Sections 3.2.1.2.1 and 3.2.1.2.2.

3.2.1.2.1 Validation using refractive index (RI) measurements

In these experiments, liquids with RIs that are known to vary significantly with their concentrations were used to demonstrate the ability of the VIS-1 to show that distortion of characters in the images is detectable (and thus measurable), resulting in different distortion values generated by different liquids or concentrations. Distortion of the images was quantified and analysed using MATLAB for each letter. The measured distortion values were then correlated with the RI values of each sample for calibration and validation.

3.2.1.2.1.1 Materials and methods

For VIS-1 analysis using the Snellen chart, known volumes of acetone, ethanol, glycerol, methanol, 2-propanol and sucrose solutions were added to water at different concentrations (0 wt.%, 10 wt.%, 20 wt.%, 30 wt.%, 40 wt.%, 50 wt.% and 60 wt.%). The chemicals were purchased from Fisher Scientific Ltd, except for sugar, which was bought at the supermarket.

RI data for the investigated concentrations was generated as previously described (Haynes, 2011-2012), whereby the measurements were conducted at 20°C and 589 nm wavelength for the sodium D line. Figure 3.2 show an example images acquired for liquids of different RIs.

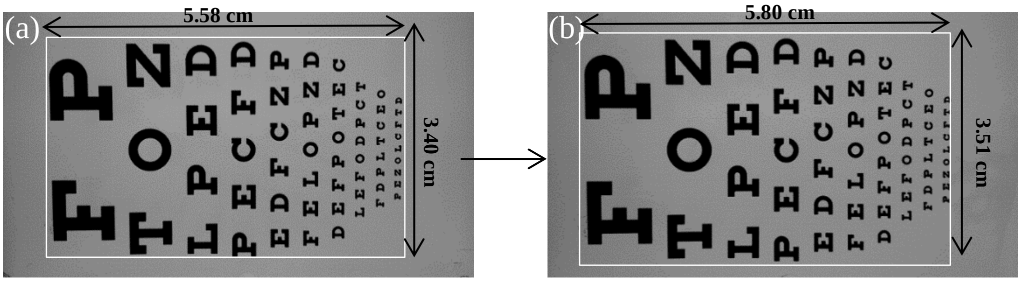

Figure 3.2 The VIS-1 images for (a) an empty vessel and (b) 60 wt.% IPA in H_2O. A stretch in the image can be seen by eye after addition of the liquid.

In Figure 3.2 (b), the image for 60 wt.% IPA in H_2O is larger by 0.22 cm in length and 0.11 cm in height compared to the image for the empty vessel (Figure 3.2 (a)). This indicates that the solution containing IPA/H_2O causes a distortion of the image containing letters due to its larger density. The concept behind this is that refraction occurs when light passes through the medium in the vessel. The light pad shines light uniformly onto the vessel, where some of the light radiations become absorbed by the letters while others are transmitted through the transparent glass. The transmitted light is then refracted at specific angles, depending on the density of the solution measured and the RI of each medium. Snell's Law (Pedrotti et al., 2007) describes the relation of the angles of incidence and refraction and the velocity of light travelling through two mediums, as shown in Equation 3.1.

$$\frac{V_i}{\sin\theta_i} = \frac{V_r}{\sin\theta_r} \qquad \text{Equation 3.1}$$

The relation in the form of RI is given in Equation 3.2.

$$n_i \sin\theta_i = n_r \sin\theta_r \qquad \text{Equation 3.2}$$

Where V is the velocity of light in a medium, θ is the angle of travelled light, n is the RI and i and r are the incidence and refraction, respectively. As depicted in Figure 3.3, light is refracted at a higher angle from the surface separating the two mediums when travelling from a low to a high RI medium – this is because the velocity of light decreases in the latter. Thus, as the $n_{glass} > n_{IPA\_60wt.\%} > n_{water} > n_{Air}$, IPA with 60 wt.% concentration causes a greater refraction compared to pure water. Conversely, the empty vessel has uniform light spread across it, except for the transparent glass areas where some refraction occurs.

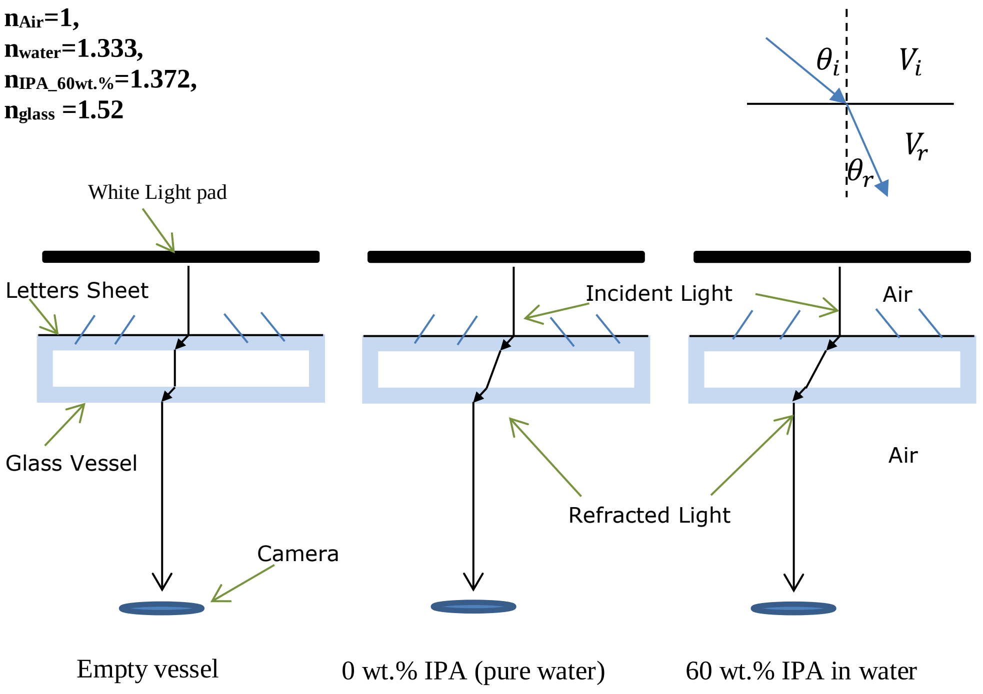

Figure 3.3 Top view of the vertical plane in the VIS-1 setting showing the degree of refraction for different fluids. RIs measured at room temperature and the visible light wavelength range are shown. The vessel path length is 2.6 cm.

The system must remain low-cost, accurate and efficient to implement, taking no longer than a few hours for a full experiment.

An analysis of the imaging situation is shown below. For flat planar layers of finite thickness (i.e., slabs) of a given RI (the sample fluid), an objective (the display) that is imaged through the slab will appear closer as the RI of the slab increases. This can be easily demonstrated using an ABCD matrix treatment (Haus, 1984).

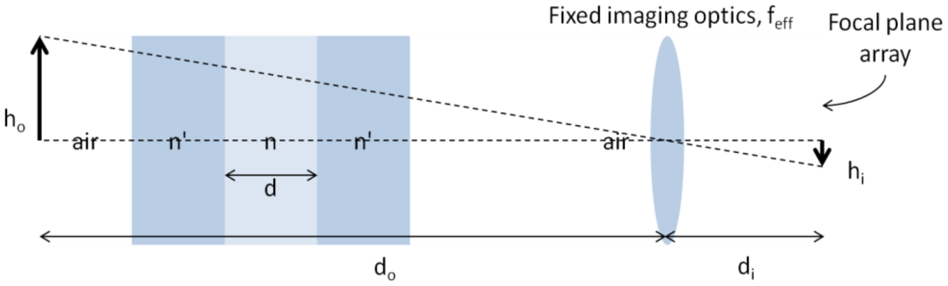

Figure 3.4 Setup for analysing the effect of fluid RI, n, in a vessel with transparent walls of RI, n', and vessel a width of d. An object of size h_o is being imaged by a fixed optical system with an effective focal length f_{eff} with respect to the focal plane array, where the image size is h_i. The object and image distances are d_o and d_i, respectively.

As shown in Figure 3.4, propagation through a slab that is composed of and surrounded by the same RI on both sides (e.g., for Figure 3.4, n=n' means no refraction occurring as the fluid-vessel interfaces) has the ABCD matrix of:

$$\begin{pmatrix} 1 & d \\ 0 & 1 \end{pmatrix}$$

For propagation through a slab of material surrounded on both sides by vessels walls of a different RI (n≠n'), the ABCD matrix is as follows:

$$\begin{pmatrix} 1 & 0 \\ 0 & \frac{n}{n'} \end{pmatrix}\begin{pmatrix} 1 & d \\ 0 & 1 \end{pmatrix}\begin{pmatrix} 1 & 0 \\ 0 & \frac{n'}{n} \end{pmatrix} = \begin{pmatrix} 1 & d \\ 0 & \frac{n}{n'} \end{pmatrix}\begin{pmatrix} 1 & 0 \\ 0 & \frac{n'}{n} \end{pmatrix} = \begin{pmatrix} 1 & d\left(\frac{n'}{n}\right) \\ 0 & 1 \end{pmatrix} = \begin{pmatrix} 1 & d_{eff}[n] \\ 0 & 1 \end{pmatrix}$$

In this way, an effective optical thickness of the slab d_{eff} is defined. If that same slab's RI changes from n to n+Δn, the effective optical thickness, d_{eff}, changes by Δd_{eff}:

$$\Delta d_{eff} = d_{eff}[n+\Delta n] - d_{eff}[n] = d\left(\frac{n'}{n+\Delta n}\right) - d\left(\frac{n'}{n}\right) = dn'\left(\frac{-\Delta n}{n(n+\Delta n)}\right)$$

$$\Delta d_{eff} = -dn'\left(\frac{\Delta n}{n}\right)\left(\frac{1}{n+\Delta n}\right)$$

$$\Delta d_{eff} n + \Delta d_{eff} \Delta n = -d\left(\frac{n'}{n}\right)\Delta n$$

$$d\left(\frac{n'}{n}\right)\Delta n + \Delta d \Delta n = -\Delta d_{eff} n$$

$$\left(\frac{\Delta n}{n}\right) = -\frac{\Delta d_{eff}}{d\left(\frac{n'}{n}\right) + \Delta d_{eff}} \qquad \text{Equation 3.3}$$

Thus, if the system is calibrated when the slab is at RI, n, then the subsequent fractional change in RI Δn is given in Equation 3.3 (in terms of the change in the effective optical slab thickness Δd_{eff}, the physical slab thickness (vessel contents thickness) d, and RI of the vessel walls n', respectively).

A relationship between the image size change Δh_i and the effective optical change in object position Δd_o must be established. To do this, the following assumptions are made:

1. The imaging optics of the camera are fixed.
2. The imaging optics of the camera are aberration-free.
3. The imaging optics of the camera can be represented by a single thin lens.

4. The changes in RI are such that the image position, relative to the effective thin lens that comprises the imaging system, is fixed. This is equivalent to assuming that the image position remains within the depth of focus and is justified by the fact that images taken with the camera are always in focus for objects over a wide range of distances.

Using these assumptions and the geometry of Figure 3.4 for the main ray, it is clear that:

$$h_i = -\frac{d_i h_o}{d_o}$$

In cases where the image size will change by Δh_i because of a change in the effective optical object position Δd_o:

$$h_i + \Delta h_i = -\frac{d_i h_o}{d_o + \Delta d_o}$$

$$\Delta d_o = -\frac{d_i h_o}{h_i + \Delta h_i} - d_o$$

$$\Delta d_o = \frac{h_i d_o}{h_i + \Delta h_i} - \frac{h_i d_o + \Delta h_i d_o}{h_i + \Delta h_i}$$

$$\Delta d_o = -\frac{\Delta h_i d_o}{h_i + \Delta h_i} \qquad \text{Equation 3.4}$$

Combining Equations 3.3 and 3.4, and considering the change in effective optical thickness of the slab in Equation 3.3, also changes the effective optical object distance (i.e. $\Delta d_o = \Delta d_{eff}$) – the relationship between the image size change and the RI change in reference to a calibrated set of images and sizes:

$$\left(\frac{\Delta n}{n}\right) = -\frac{1}{1 - \left(\frac{h_i + \Delta h_i}{\Delta h_i d_o}\right)\left(\frac{n'}{n}\right)d} \qquad \text{Equation 3.5}$$

Using Equation 3.5, a measured feature size change can be used to determine the average change in RI over the feature.

3.2.1.2.1.2 Analysing image letters (AIL)

A MATLAB code (Section I.3, Appendix I) was scripted to investigate the average pixel values in the region of each letter (in a Snellen chart) for each of the variably concentrated solutions (Figure 3.5). This allowed the determination of threshold values.

A threshold of 20-256 pixels was chosen in order to select all the pixels comprising the letters, while ignoring any variation in pixel values resulting from the backlight gradient and random noise. B (0) → W (256), BW= W>20.

The code then returns information for each letter, including the locations and areas that were altered due to different solution concentrations. Typical data returned for each letter is illustrated below in Figure 3.5.

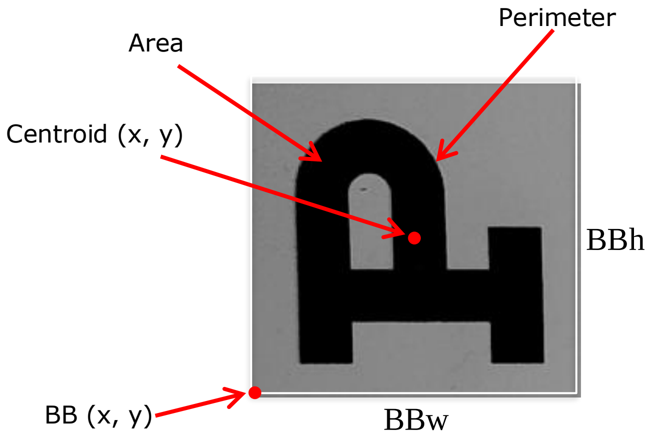

- Centroid (x, y).
- Letter Area (pixel^2).
- Boundary box, BB (x, y).
- Boundary box width, BBw.
- Boundary box height, BBh.

Figure 3.5 Letter area deducted from the Snellen chart to illustrate MATLAB scripting.

3.2.1.2.1.3 Results and discussion

The MATLAB coding outputs for the Snellen chart use data from each solution of a different concentration and different RI. This is primarily done to demonstrate the validity of the VIS-1 for analysing such solutions. The solutions used were acetone, ethanol, glycerol, methanol, 2-propanol and sucrose.

Quantification was carried out by analysing the captured images of the letter distortions (variations in letter areas or perimeters) in each solution of a different concentration. The changes in the letters area, perimeter, number of pixels, centroid location, BB, BBw and BBh were all measured using the MATLAB code described in Section 3.2.1.2.1.2. The results were then compared with the RI data for the same concentrations. This provided calibration data for VIS-1 by correlating the image variables (e.g. letter area) with the RI values.

To illustrate the above, the results for sucrose and 2-propanol are shown below. Data was obtained by analysing the largest P letter area (only one element) from the produced images for each concentration (see Figures 3.6- 3.14).

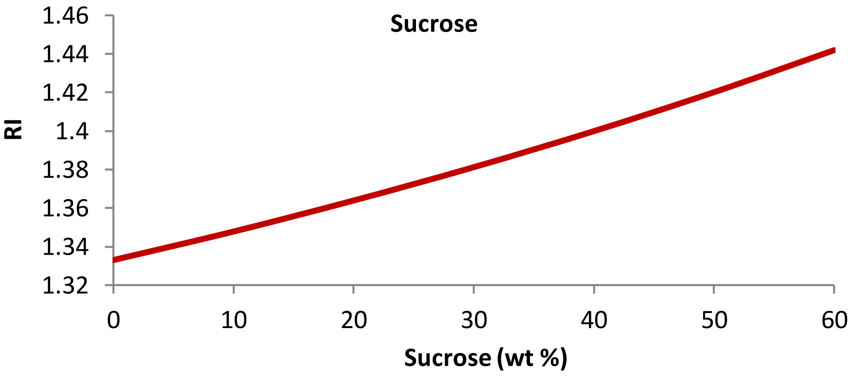

Figure 3.6 Sucrose RI values for different solution concentrations, showing a linear relationship; the RI values increase in proportion to the increase in concentration (Haynes, 2011-2012).

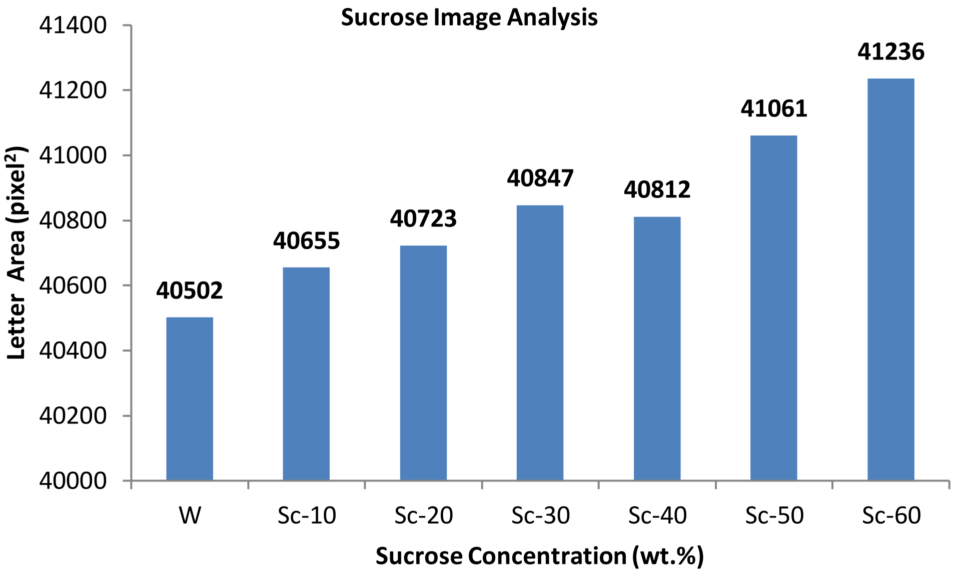

Figure 3.7 Sucrose image analysis using the VIS-1. W represents the water-filled vessel (Sc-0 wt.%) and Sc is sucrose at different concentrations (10-60) wt.%. An increase in the letter area with increasing concentration is seen for all cases, except for Sc-40. This aberration is due to a change in the vessel position during a switch in the solutions.

As can be seen in Figure 3.7, increasing the concentration of a solute dissolved in water results in an increase in the overall density of a solution. In return, the distortion values measured using the VIS-1 change, which is expressed here by the increase in the area of a letter in the captured images, in comparison to the same parameter for the imaged vessel containing only water. The increase in the letter area for a specific solution concentration was quantified in proportion to the initial sucrose concentration (0; Table 3.2). This correlation confirms the relationship between the RI and the concentration, as shown in Figure 3.6.

Table 3.2 The percentage increase in the area of the letter P with the increase in the concentration of sucrose.

Sucrose wt.%	% Increase in P Area
0	0
10	0.38
20	0.55
30	0.85
40 (VIS-1 error)	0.77
50	1.38
60	1.81

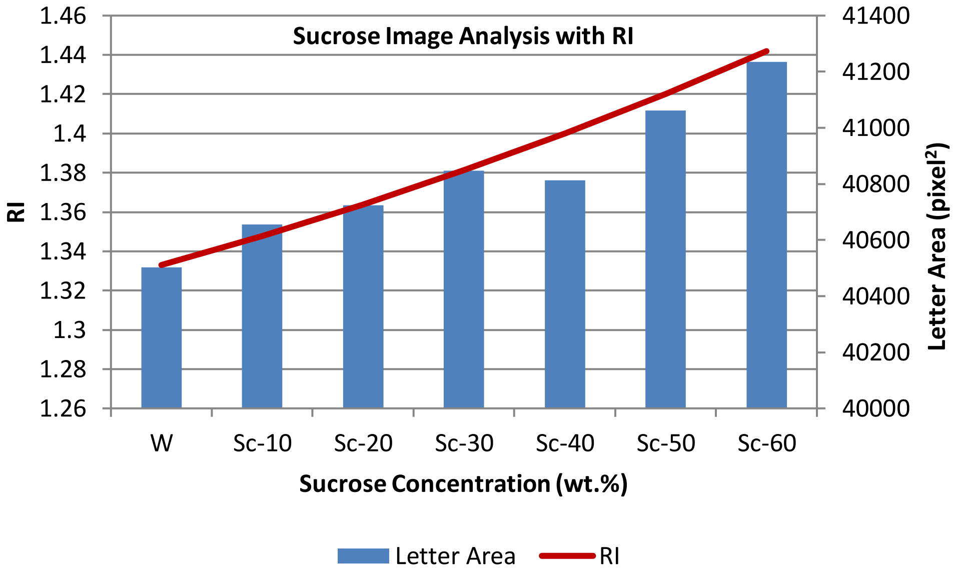

Figure 3.8 Sucrose image analysis using the VIS-1 correlated with the RI data. W represents the water-filled vessel (Sc-0 wt.%) and Sc is sucrose at different concentration (10-60) wt.%. An increase in the letter area with increasing RI is seen.

The plot in Figure 3.8 demonstrates the proportional relationship between the letter area and the RI, proving that this method can replace a refractometer to determine the concentration under the investigated experimental conditions.

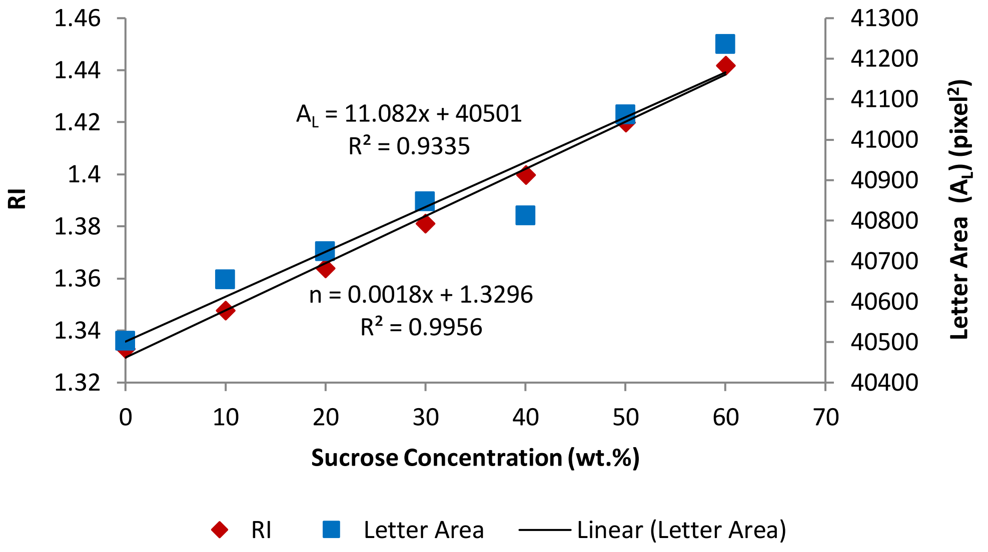

Figure 3.9 Linear correlations of the RI, the letter area and the sucrose concentration, where A_L is the letter area and x is the concentration.

The relationship between A_L and RI, shown in Figure 3.9, validates their similar correlation to concentration – as the two sets of data are equally linear, except for the instrumental error seen at the 40 wt.% sucrose concentration. Thus, with the new plans to make the VIS-1 more stable to minimise this error (as will be explained in the following sections), this correlation successfully validates the VIS-1. Moreover, by producing database calibrations of A_L versus concentration for different solutions and NPs dispersions, unknown concentrations of solutions can be determined using this method. In the next section, the same procedure using sucrose is applied to IPA to confirm the method's applicability to different materials.

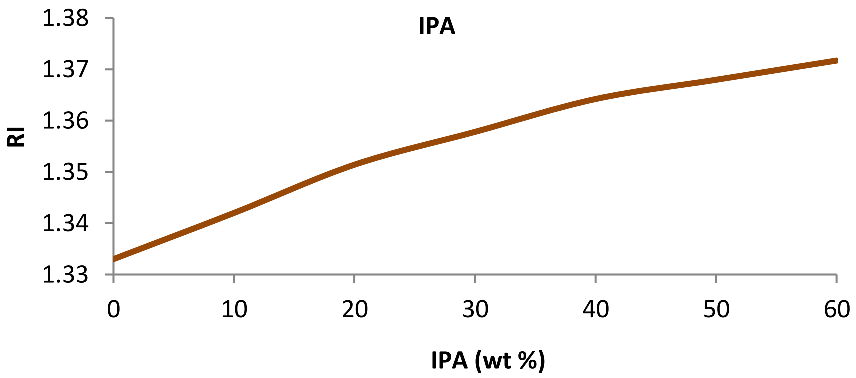

Figure 3.10 Plot of IPA in water versus RI values for different concentrations. Results indicate a directly proportional increase in RI values with increasing concentration (Haynes, 2011-2012).

The RI curve increases linearly up to the 20 wt.% concentration, after which it becomes more convex with increasing IPA concentration (Figure 3.10).

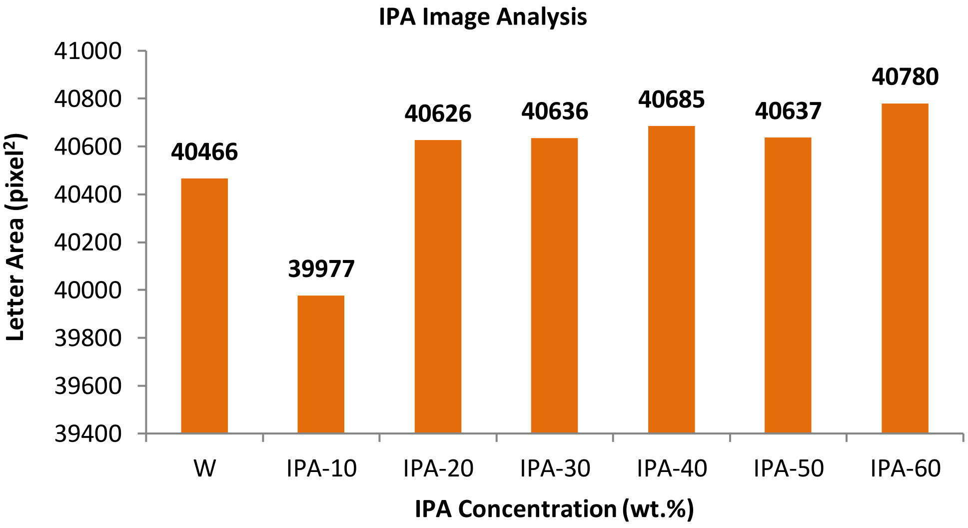

Figure 3.11 IPA image analysis using the VIS-1. W represents the water-filled vessel (IPA-0 wt.%) and IPA is isopropanol at different concentrations (10-60) wt.%.

A trend towards an increase in letter area with increasing concentration can be seen, except for IPA-10 and IPA-50. This aberration is due to a change in the vessel position during a switch in the solutions. The tendency of the letter area to increase with increasing solution concentration is also notable in the case of IPA (Figure 3.11). However, this trend was less pronounced compared to sucrose (for example, at 60 wt.% the increase in P area is 1.81% for sucrose and 0.78% for IPA, compared the value of P area of water). The SD in the P area in the water image from both the sucrose and IPA measurements was 0.06%. Thus, the VIS-1 system proved its sensitivity to solutions with slightly varying concentration-dependent RIs – with IPA as an example (the RI increase for 60 wt.% IPA from the initial value of 2.9% (Figure 3.10) and 8.2% for sucrose (Figure 3.6)).

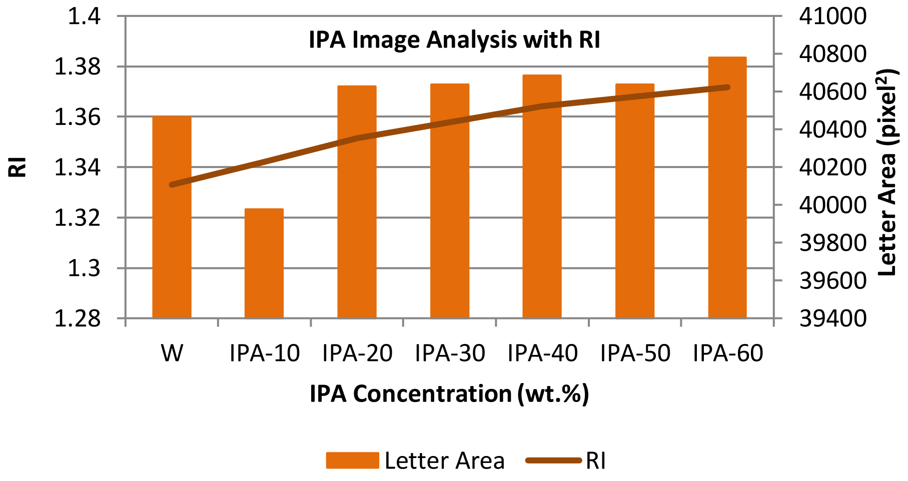

Figure 3.12 IPA image analysis using the VIS-1 correlated with the RI data. W represents the water-filled vessel (IPA-0 wt.%) and IPA is isopropanol at different concentrations (10-60) wt.%. An increase in letter area with increasing RI can be seen.

Theoretically, the VIS-1 should using the same analogue as a refractometer and the curves of “RI versus concentration” and “letter area versus concentration” conform to each other (Figures 3.8 and 3.12).

To provide evidence of reproducibility, three images were taken for each concentration. Each image was taken at a gap of 30 seconds and the triplicates reproducibility was recorded for the largest P letter area for sucrose and IPA of 10 wt.% respectively, as seen in Table 3.3 and Figure 3.13 (a and b) below.

Table 3.3 Standard deviation data of the P area for 10 wt.% sucrose and IPA.

Sample at 10wt.%	**P area in Image 1**	**P area in Image 2**	**P area in Image 3**	**SD**	**%Uncertainty**
Sucrose	40655	40630	40662	40649±17	0.04%
IPA	39977	40009	39962	39982.67±24	0.06%

The captured images, each at an interval of 30 seconds, provide reproducible results with a very small deviation of 0.04% and 0.06% of sucrose and IPA at 10 wt.%, respectively. In future work, other parameters could be adjusted, such as increasing the intervals between captured images, changing the solution of a particular concentration and capturing a number of images on different days. These will nullify any possible confounding factors, such as changes in environmental lighting and subsequent positioning and concentration errors.

(a)

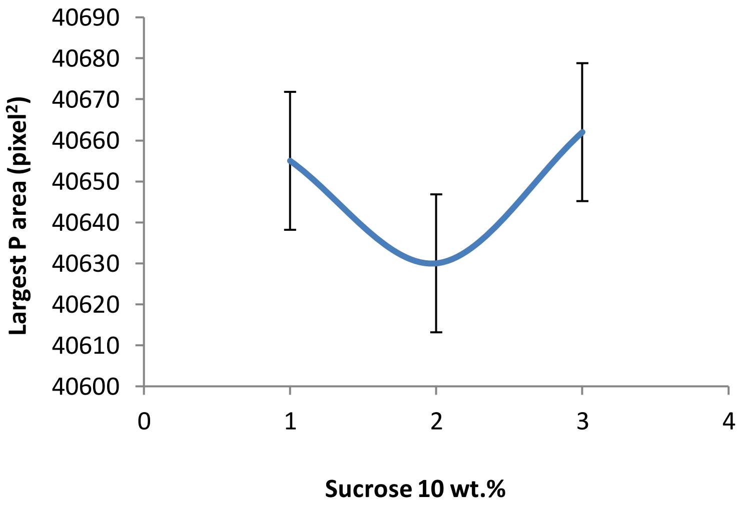

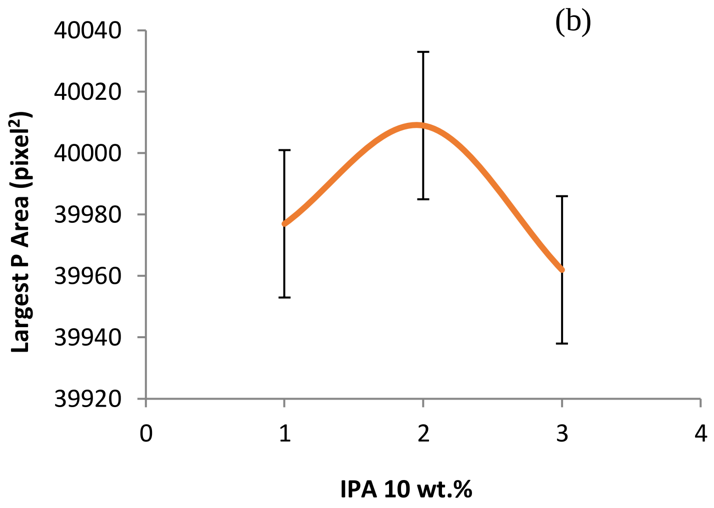

Figure 3.13 Evidence of reproducibility by taking images of the same sample at 30 seconds intervals (a) for sucrose and (b) for IPA, both at 10 wt.%.

The slight deviation between the three images captured at 30 sec intervals is shown in Figure 3.13 (a and b) and must result from changes in environmental light as vessel position and solution concentration remained fixed during image capture.

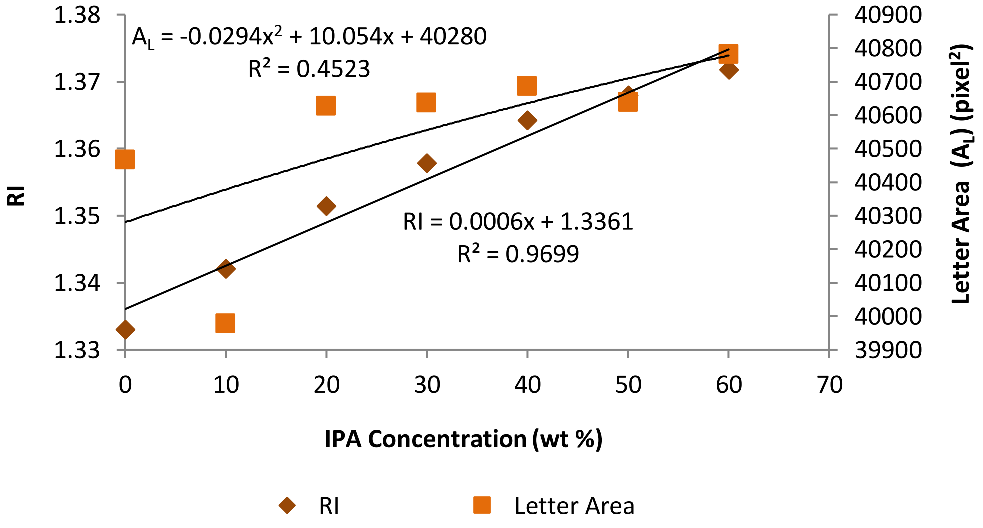

Figure 3.14 Correlation between, RI, letter area and IPA concentration.

The data in Figure 3.14 exemplify vessel position error that can occur when the solutions are changed.

3.2.1.2.2 Colour evaluation

3.2.1.2.2.1 Materials and methods

For analysis using the colour swatch in the VIS-1, known volumes of Nigrosin blue, red, green and orange dye solutions were prepared in water at different concentrations: for Nigrosin blue, 0 PPM, 5 PPM, 10 PPM, 15 PPM, 20 PPM, 25 PPM, 30 PPM by wt; and for all other food dyes, 0 wt.%,0.025 wt.%, 0.05 wt.%, 0.10 wt.%, 0.15 wt.%, 0.20 wt.%, 0.25 wt.%, 0.30 wt.%, 0.35 wt.%, 0.40 wt.% and 0.50 wt.%). The dyes were purchased from supermarkets, except for Nigrosin (Fisher Scientific Ltd). The NP dispersions were supplied by Promethean Particles Ltd and diluted to different total solid contents for investigation.

Images of the vessel filled with the samples were acquired after ensuring that the solutions covered the entire colour swatch area. This way, interactions of the sample with all available colours can be analysed. The same amount of each sample was added each time using a volumetric cylinder to ensure accuracy between concentrations.

Any changes in solutions were monitored by varying the image capture duration. In this section, three images per sample were acquired in 30 second intervals. It should be noted that the acquisition duration can be increased to 1 hour or more to account for any environmental changes.

3.2.1.2.2.2 Analysing image colours (AIC)

A MATLAB code (Section I.4, Appendix I) was developed to observe the change in the mean pixel values (red, green and blue (RGB)) for each colour square in the colour swatch, under different colour dye concentrations.

In the MATLAB code, 0 indicates no channel (R, G or B) in the selected area, while 256 indicates full or pure colour (e.g. in the RGB code settings):

Pure red	256, 0, 0
Pure green	0, 256, 0
Pure Blue	0, 0, 256

Other colours are numbered in the range between pure red, green and blue. For example, green, which is near the blue region, will have a large value for the green and less for the blue and red colours.

3.2.1.2.2.3 Results and discussion

1. Imaging dispersions

It is possible to investigate the colour interactions in NPs dispersions of different colours, determine the concentration of NPs in a solution and evaluate the transparency of dispersions by quantifying the red, green or blue intensity values as a proportion of a values obtained from a transparent solution (such as pure water). Some of the above theoretical applications are investigated in the next sections with different samples.

- ***Zirconia (ZrO_2) NP solutions of varying particle sizes***

This section focuses on observation and calibration using dispersions of different particle sizes (Figure 3.15).

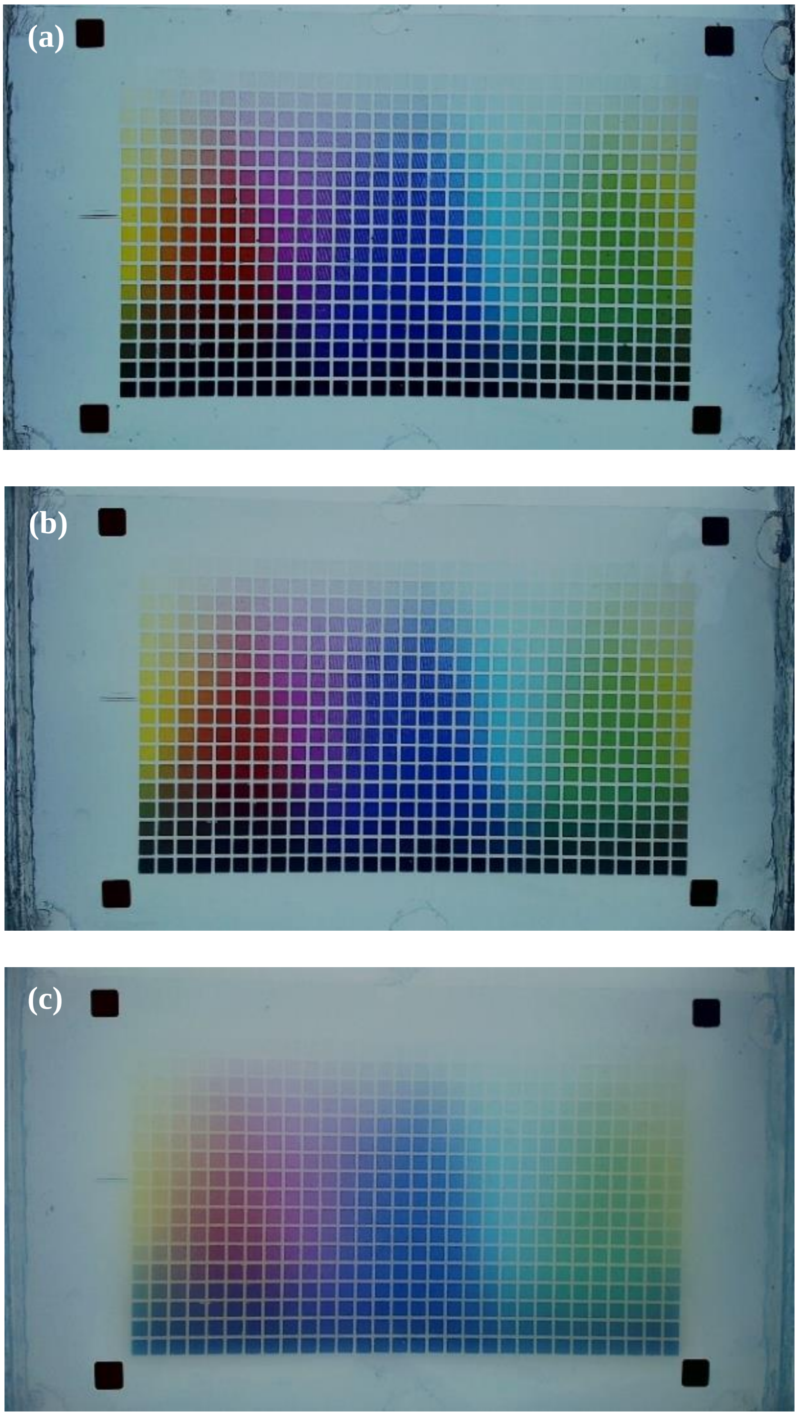

Figure 3.15 The VIS-1 images of ZrO_2 dispersions with particle sizes of (a) 40 nm, (b) 70 nm, and (c) 150 nm, showing an opacity increase with increasing particle size. It can be noted that the colour swatch becomes less visible at a 150 nm particle size.

- ***TiO_2 NP solutions (130 nm particle size) of different concentrations***

Aqueous TiO_2 nanoparticle solutions of a 130 nm mean size, prepared at 12 different concentrations (0.019 wt.% TSC – 0.2295 wt.% TSC), were measured using the VIS-1 system to observe any changes to the colour swatch (Figure 3.16).

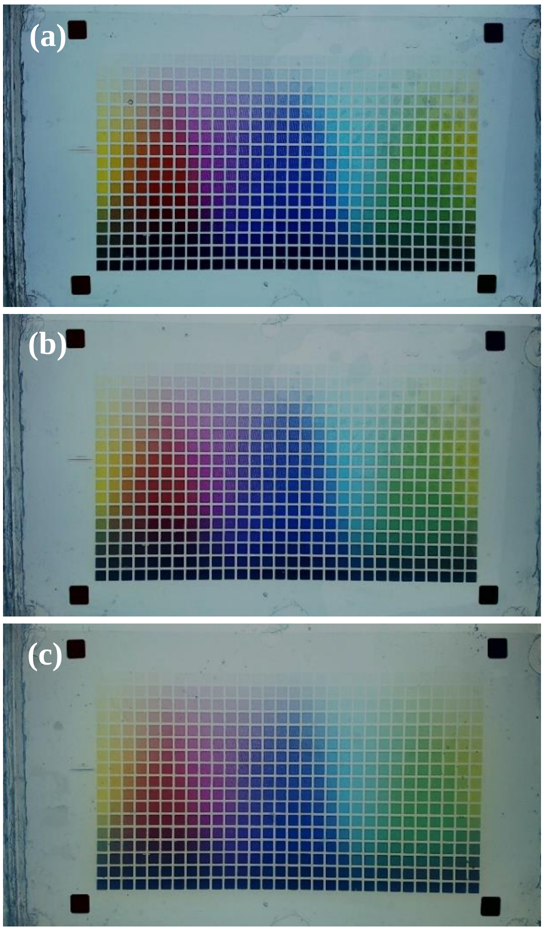

Figure 3.16 The VIS-1 images of TiO_2 dispersions of (a) 0.019 wt.%, (b) 0.1339 wt.%, and (c) 0.2295 wt.%, showing a slight decrease in the visibility of the colour swatch with increasing concentration.

2. Measuring liquids of different colours

The first trial used Nigrosin blue dye, as shown in Figure 3.17.

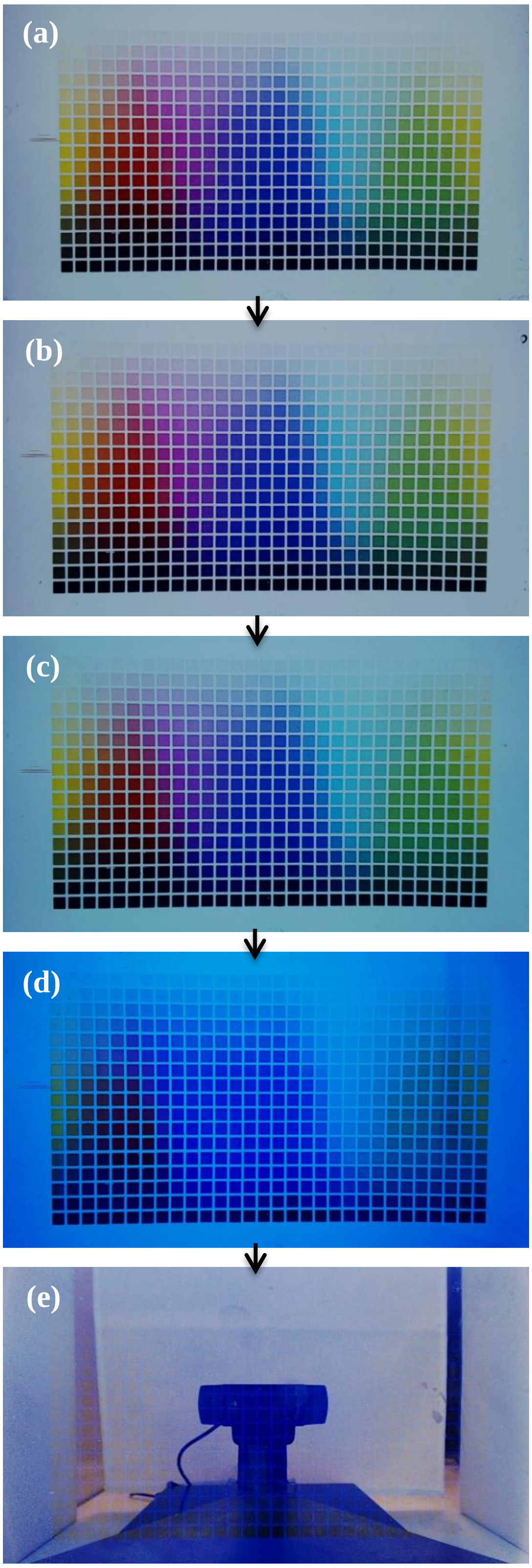

Figure 3.17 The VIS-1 images for: (a) empty vessel, (b) water only, (c) 5 PPM Nigrosin dye, (d) 25 PPM Nigrosin dye, showing the variation in swatch colours from highly visible to a poorly visible (a-d, respectively), and (e) 30 PPM Nigrosin dye.

The same VIS-1 settings were used for this method; however, the Snellen chart was in this case replaced with a colour swatch and the photos were captured in colour, instead of greyscale by the MATLAB code (Section I.2, Appendix I), to evaluate colour variations at different dye concentrations.

A limitation of using Nigrosin dye is that VIS-1 cannot measure a concentration greater than 25 PPM with this configuration, as when the sample becomes too dark it acts as a mirror – causing the camera to record an object's reflection (Figure 3.17, e).

The method shown in Figure 3.17 was used to measure variations in RGB intensity values for colour swatch image analysis, with the increase in dye concentration observed in the following section.

Each image was run separately using MATLAB code (Section 3.2.1.2.2.2) and RGB values were calculated for each region of interest (ROI). The ROI for each square had to be as close to the centre as possible, for a total of 510 squares (Figure 3.18).

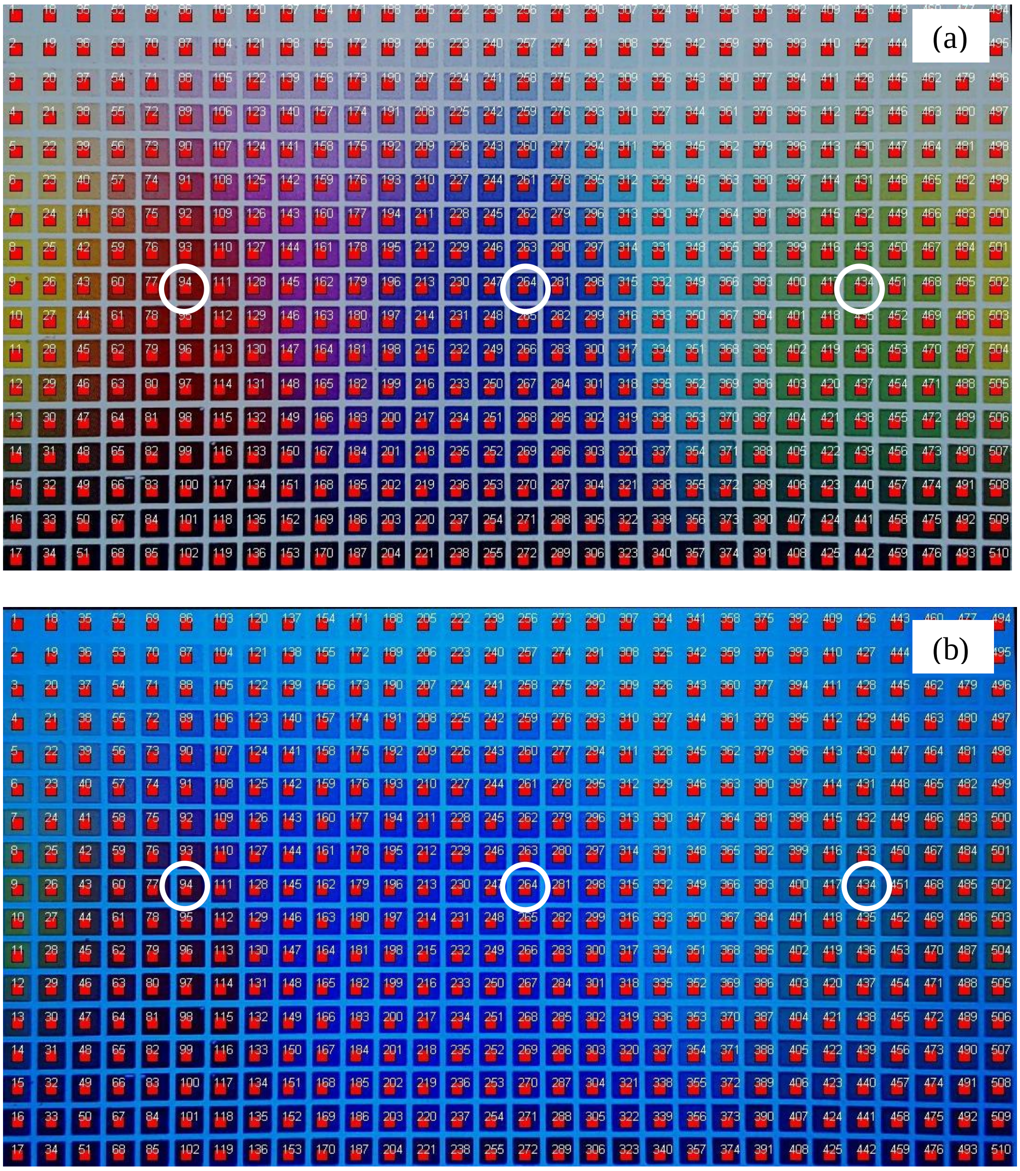

Figure 3.18 The analysed segment of an image of a colour swatch vessel filled with (a) water and (b) Nigrosin 25 PPM at ROI value=0.35.

The occasional deviation of the ROIs from the centre was due to camera lens distortion, positioning of the vessel and additional errors arising from slight shifts of the ROI position between concentrations. As an example, ROI-179 may shift slightly to a more blue area (to the right) at a 10 PPM Nigrosin concentration compared to the same ROI in a 5 PPM concentration. Moreover, the ROI areas were set to be smaller than the original colour square area in order to prevent interference from the margins of the squares. Thus, RGB analysis can be conducted under different scenarios (in Figure 3.19).

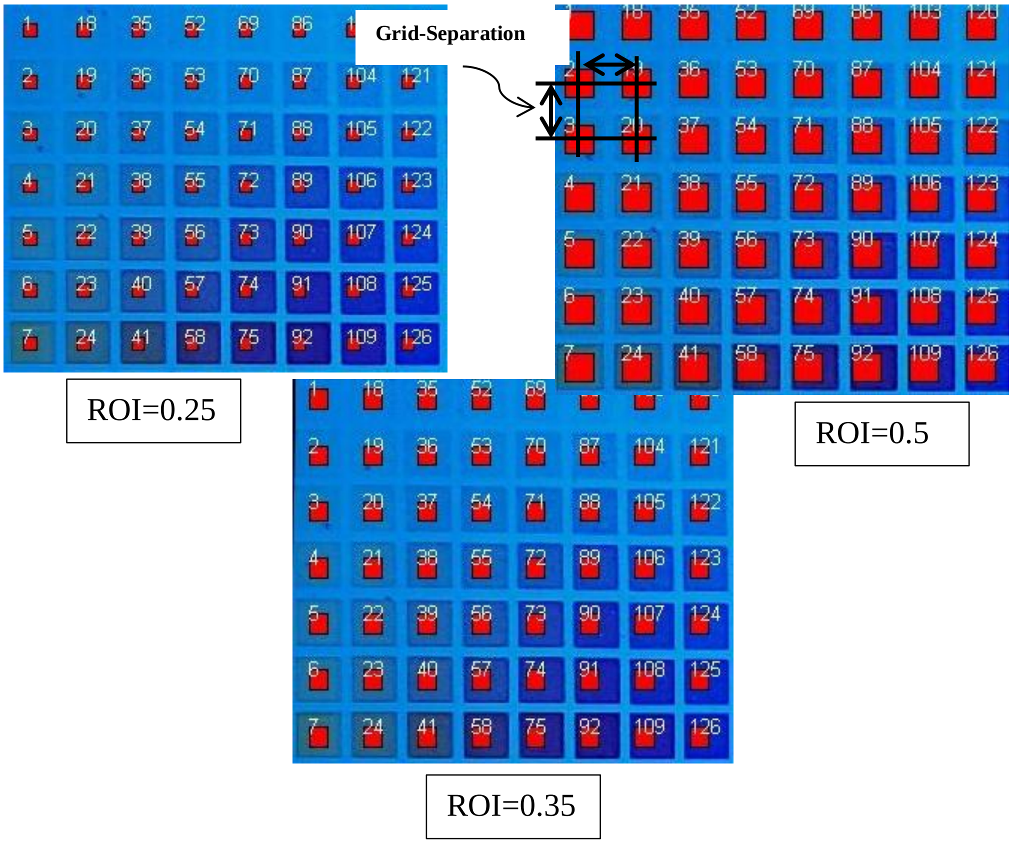

Figure 3.19 Choosing the most reliable scenario to calculate RGB values.

As can be seen in Figure 3.19, a ROI=0.5 can be used here; however, the same result may not be obtained for all other samples due to any of the errors mentioned above. The results, therefore, may not be reproducible and require smaller ROIs to minimise value deviations between samples. The SDs in the RGB values from the three ROIs (0.25, 0.35 and 0.5) taken from square 92 in the Nigrosin blue (25 PPM) sample are shown in Table 3.4.

Table 3.4 RGB values for ROI-92 for all the ROI values (shown in Figure 3.19).

ROI Value	**Red Value**	**Green Value**	**Blue Value**
0.25	28	27	158
0.35	28	27	157
0.5	27	25	155
SD	27.7±0.6	26.3±1.2	156.7±1.5

The ROI value is arbitrary as a user-defined parameter determining the size of an analysis area as the ratio of the grid separation distance (see Figure 3.19).

Previous work (Kohl et al., 2006) has shown that a digital image of a yellow sample (of any different concentration) can be used to estimate the absorbance of the complementary colour (blue) by obtaining the image's blue value at a specific position with respect to concentration. In turn, the image's blue values decrease inversely to the concentration of the sample, conforming to the absorbance data obtained by the authors using UV-visible spectrophotometry and the Beer-Lambert law. However, the RGB image analysis system generates one value for each channel. Therefore, a linear relationship between absorbance and concentration can only be obtained from one-component samples of complementary colours of red, green or blue. For other coloured samples, this method would have to be replaced by UV-visible spectrophotometry.

In the current work, another concept was used to quantify the interaction of light with a sample; this involved using a swatch of many colour shades and digitally measuring the interaction of these shades with the sample. A sample concentration can be deduced using the variation of the RGB values with the colour intensities of a sample. Figure 3.20 shows the variation of RGB values (0-256) with the different colour concentrations of a blue dye. The blue dye is in clear contrast with the differently coloured squares of the swatch, which is recorded for the red, green and blue pixels of the ROI using the captured image for each concentration.

The RGB values chosen for demonstration and those used in Figure 3.20 were taken from the ROIs in the colour squares containing the highest RGB values. These were regions 94, 434 and 264 for the red, green and blue colours, respectively, as indicated by the white circles in Figure 3.18. As the dye colour used here was blue, the highest value was for blue at 207, recorded in the blue square (ROI-264) in a sample of 25 PPM Nigrosin blue dye concentration (Figure 3.20, c). In all the selected regions of interest (Figure 3.20, a, b and c), a general trend towards increasing blue and decreasing red and green values was observed with increasing blue dye concentration. Conversely, the highest red intensities generated values of 111 in ROI-94 in the 0 concentration sample, decreasing by 23.4 % at the lowest concentration (5 PPM). This intensity decreased by 69.4 % at 25 PPM, while the green intensity remained virtually constant for all concentrations (Figure 3.20, a). Similarly, the green intensity generates the highest value in the green square (ROI-434) when the blue dye concentration is 0, decreasing by 32.8 % at the highest blue dye concentration (Figure 3.20, b). The red and green data curves were almost constant when analysing the blue square (ROI-264) for the blue dye interaction with the sample; and the blue value by the final concentration was the highest (Figure 3.20, c) amongst the three ROIs presented here. Conversely, the percentage of variation is the lowest (ROI-94: 89.4 %, ROI-434: 59.3 % and ROI-264: 23.7 %). This is explained by the fact that the blue value was already high for blue ROI-264.

(a)

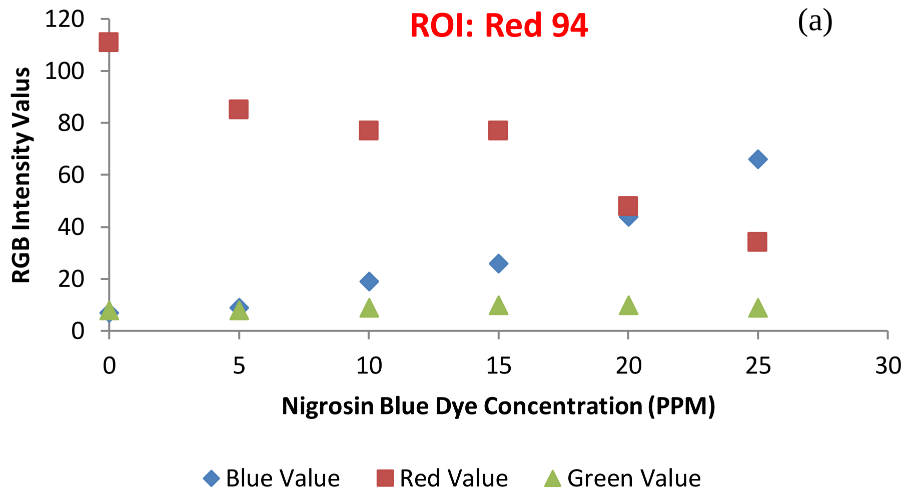
ROI: Red 94
RGB Intensity Valus
0
20
40
60
80
100
120
0
5
10
15
20
25
30
Nigrosin Blue Dye Concentration (PPM)
Blue Value
Red Value
Green Value

(b)

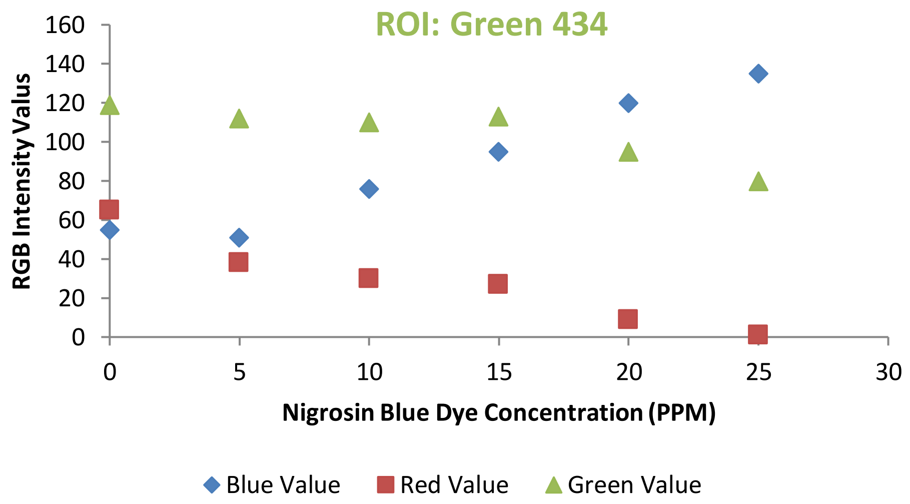
ROI: Green 434
RGB Intensity Valus
0
20
40
60
80
100
120
140
160
0
5
10
15
20
25
30
Nigrosin Blue Dye Concentration (PPM)
Blue Value
Red Value
Green Value

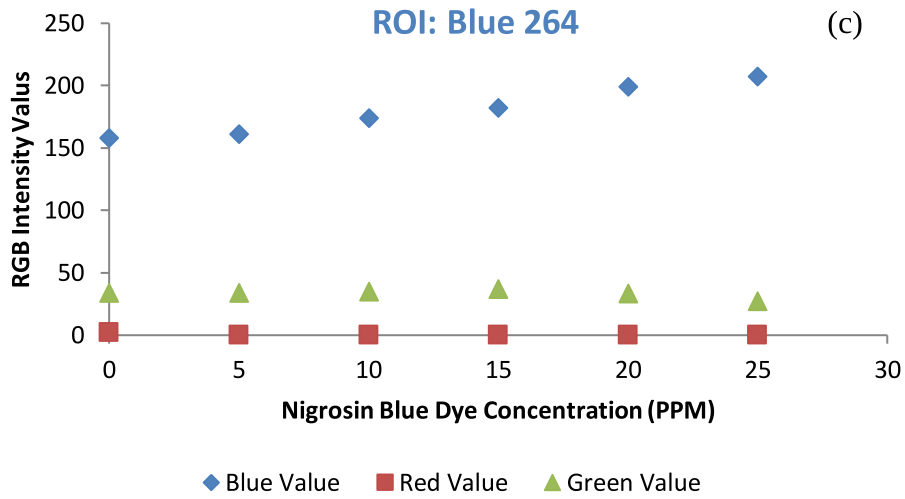

Figure 3.20 ROI red, green and blue value variations at different Nigrosin blue colour dye concentrations.

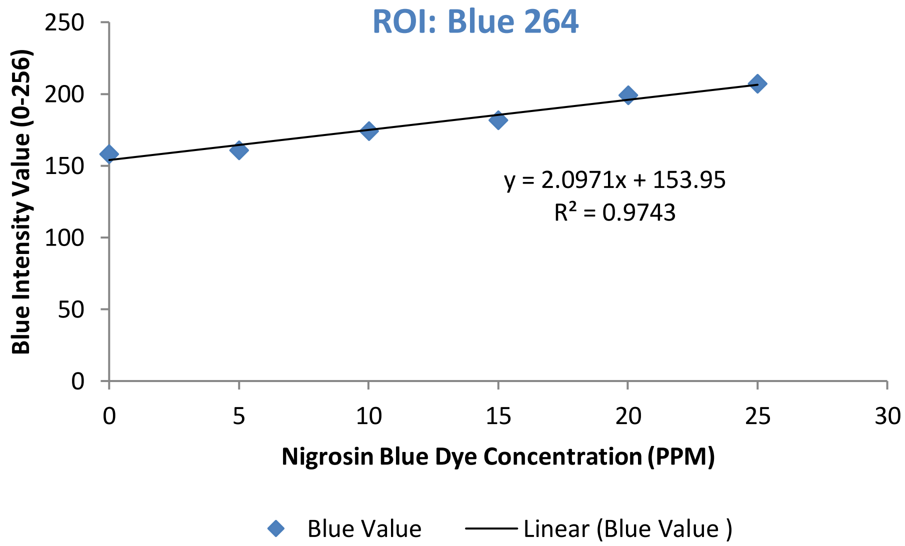

Figure 3.21 Plot of blue intensity versus blue dye concentration for blue ROI-264.

For example, determining an unknown concentration of a Nigrosin blue dye would use the linear relationship obtained in Figure 3.21 of the most affected ROIs for the relevant sample.

The following issues arose during the validation experiment with the glass vessel, which were due to slight changes in vessel positioning during solution changeovers – despite efforts to minimise this by:

1. Drawing marks at the base of the vessel and the plate for positioning the vessel against and only filling the vessel with solutions once in its required position.
2. Gluing the Snellen chart and colour swatch acetate papers onto the vessel with silicone.

To solve the above problem, a new approach involved affixing four reference points onto the vessel to frame the image. A new MATLAB code was then scripted in an attempt to obtain more accurate results, as will be described in the next section.

3.2.1.2.3 Reference point calibration for identifying position errors

For this calibration, a MATLAB code (Section I.5, Appendix I) was written to obtain the actual change/distortion in the acquired images caused by different solutions, whilst accounting for changes in the camera's or vessel's position.

The first stage of the calibration was designed to correct for imaging errors due to the positioning of the VIS-1 camera and vessel. This was done using a "feature matching" algorithm in MATLAB to match an image to a supplied reference image through image geometric image distortion. The process for feature matching image adjustment is as follows:

1. An ideal reference image is acquired and manually adjusted (stretching and skewing) so that the grid of colour squares appears as uniform and undistorted as possible with equal spacing.

2. An image is selected for analysis. Both this image and the reference image are converted to greyscale.
3. The "detectSURFFeatures" algorithm is used to analyse both the selected image and the reference image, recording the positions of distinct common features in both images (Figure 3.22).
4. Based on the relative positions of the common features in the two images, MATLAB is used to calculate the "estimated geometric transform" matrix of vectors, which enables most accurate geometric transformation of the image to the reference image.
5. The estimated geometric transform matrix is then applied to the image.

To achieve the above, four square stickers were attached to the front of the glass vessel, to provide an ideal reference point for matching of common image features. Attaching these to the front of the vessel meant that filling it with solution (which reduces the visibility of the colour swatch squares) did not affect the stickers.

The calibration was first carried out for an empty glass vessel with the colour swatch attached to it. Square colour stickers were affixed to the corners of the tray at maximally similar distances. The images of the different vessel positions were then taken with VIS-1 (Figure 3.22).

- Running the MATLAB position code for the original images (Figure 3.22, left) revealed any changes, with respect to the reference image, in position as lines and average numbers (Figure 3.22, right).

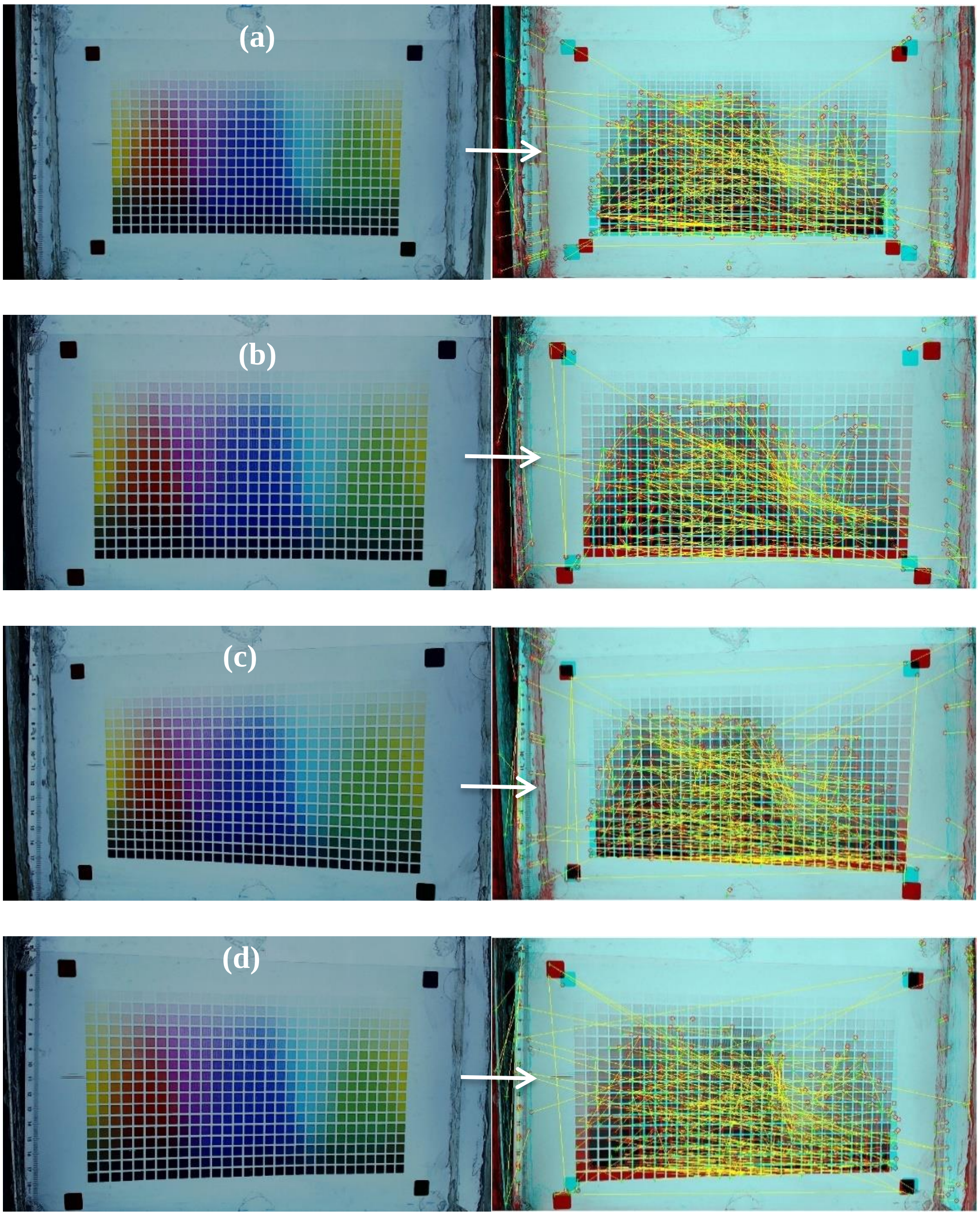

Figure 3.22 The VIS-1 images taken of vessel positions for calibration: a and b are far and close vessel positions, respectively; c and d are right and left angled vessel positions, respectively.

The next steps of the VIS-1 development aimed to minimise the error by using the following strategies:

1. Clipping and bolting the instrument components, such as the camera and the base.
2. Manufacturing a suitable holder for the vessel.

3. Capturing images in a small, dark room, away from movements.
4. Enhancing the clarity of the glass used for the vessel.

3.2.2 The VIS-2 (multiple cuvettes, semi-circular cuvette holder and a light pad)

3.2.2.1 System configuration

In this configuration (Figure 3.23), the VIS-2 is composed of 14 cuvettes in a metal holder designed to enable arrangement of the cuvettes in a semi-circular fashion, so as to minimise the inherent concavity (the cuvettes were narrow in the middle and inclined at the edges. This unwanted effect of camera optics would be intensified in images if the cuvettes were lined up in a straight line.

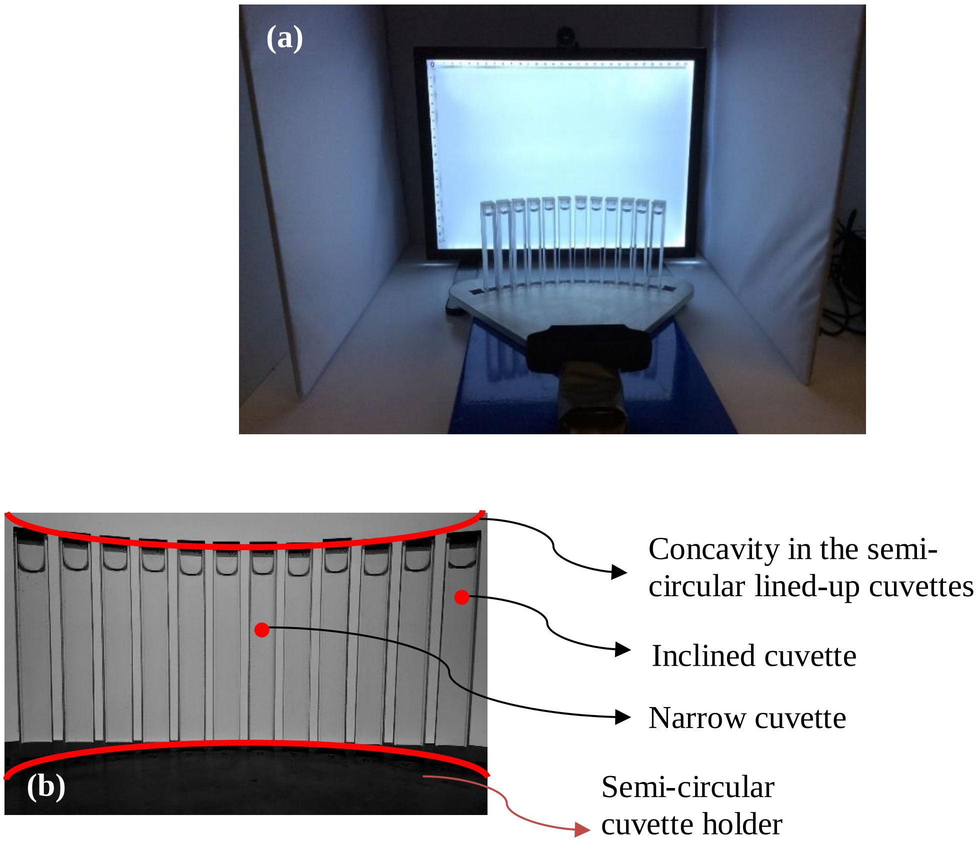

Figure 3.23 a) The VIS-2 setup and b) an image produced using the VIS-2 with the semi-circular cuvette holder design.

3.2.2.2 Analysing settling rates (ASR)

In this section, MATLAB image analysis was applied to the measurement of settling rates in dispersions against a fully white background.

First, images of cuvettes containing only water were acquired and used as a reference for investigating the sedimentation rates of various dispersions (Figure 3.24, left). Then, the images were converted to greyscale, so that the cuvettes containing water would give the “lightest” possible appearance. Dispersions that create opacity in the cuvette (compared to water) appeared darker in contrast after converting to grayscale, even if the dispersions were white in the original images.

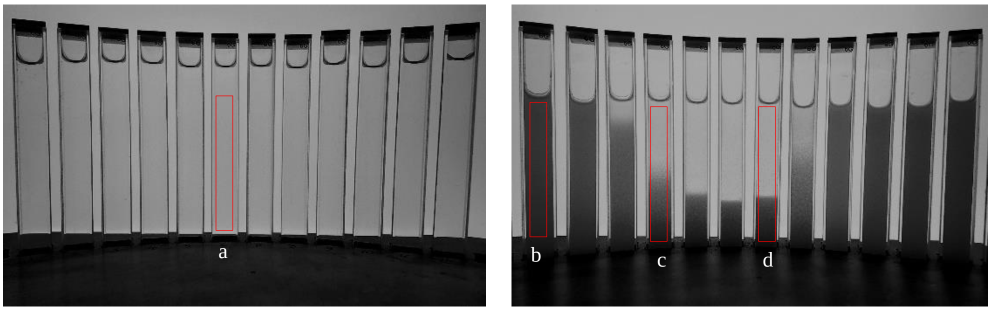

Figure 3.24 VIS-2 images for water (left) and TiO2 NP solutions (right). The red rectangles indicate regions of interest.

ROIs were defined in the MATLAB script (Section I.6, Appendix I) for each of the cuvettes. These regions were rectangular, of equal size, and were placed entirely within the sample contained in each cuvette (ensure no overlap with the meniscus of the fluid). The degree of settling was quantified in each image by calculation of the mean pixel value within these ROIs.

Since a cuvette containing water would give the highest possible mean pixel value within a ROI (cuvette ‘a’ in Figure 3.24), a pixel value of 255 represents white and 0 represents black. This also represents the highest possible degree of settling – i.e. what would be observed if the dispersion were to sediment completely below the ROI.

Conversely, the first image acquired during a settling experiment, where the least degree of sedimentation had occurred, resulted in the lowest mean pixel value for the ROI (cuvette ‘b’ in Figure 3.24). As sedimentation progressed, the calculated mean for pixel values within each ROI increased to a maximum of that for the background (the cuvette containing water).

A significant limitation of this crude approach to quantifying the degree of settling is that it does not account for “settling gradients”, which are sometimes observed. For some particle species, the level to which the particles have sedimented within the aqueous sample remains distinct – for which cases this approach is suitable. However, for other species, a gradient is often observed, which means the average pixel value approach may result in multiple scenarios to produce an identical result. For example, comparing the cuvettes labelled ‘c’ and ‘d’ in Figure 3.24 shows two visibly different scenarios. However, in cuvette ‘d’, the level to which the particles have settled is relatively distinct and, in cuvette ‘c’, there is a gradient of lightness across the area where a distinct level is observed in cuvette ‘d’. Consequently, the mean pixel values calculated for the two cuvettes may appear very similar, even though the states of sedimentation in the cuvettes are visibly different. In this case, a second-generation code is needed to account for and quantify any gradients observed and to allow for an accurate distinction between these scenarios.

The mean pixel values for each ROI in each image are outputted into excel sheets and plotted for comparison between samples. The plots are used in the sedimentation rates measurements, as will be shown in Chapter 4.

3.2.3 The VIS-3 (multiple cuvettes, a straight cuvette holder and an iPad)

This system design was modified to include a straight cuvette holder instead of a semi-circular so as to facilitate the integration of an iPad as a source of light and characters. Cuvette slots at the margins of the holder (3 on each side) were rotated at specific angles (12°, 16° and 21° from the holder centre to the holder edges) to eliminate the appearance of "dark cuvette walls" that block visibility of iPad-generated characters. This design can occupy 10 cuvettes at a time.

This upgraded design enables the user to extract and quantify more parameters easily, such as variations in colour intensity, transparency and turbidity of a solution undergoing changes in properties (e.g. density and concentration) simultaneously. This has been achieved by using different backgrounds at the same testing run to extract such information, and the easiest way possible to use the required backgrounds is by displaying them through a device where the display timing, type, design and the number of backgrounds can be manipulated and varied in real time. Here the iPad proved to be optimal for displaying multiple backgrounds at once. In turn, the straight cuvettes holder was designed to be of the same length as the iPad so that all samples would fit against the iPad screen. The implementation of this design will be reported in Chapters 5 and 6.

3.2.3.1 Backgrounds used in the VIS-3

1- Dense and sparse letters in black and white

Using multiple letter analysis facilitates measurement of different parameters from different locations in the sample image. For example, monitoring variations in areas of consecutive letters are useful to systematically reveal any changes in samples properties over time (e.g. due to a destabilisation). Moreover, obtaining the letter from different image locations can be used to quantify other sample properties, such as transparency and consistency, which is applicable to stable samples. Furthermore, one can also conduct a comparison between these letter areas in the same sample at different locations (Figure 3.25, b).

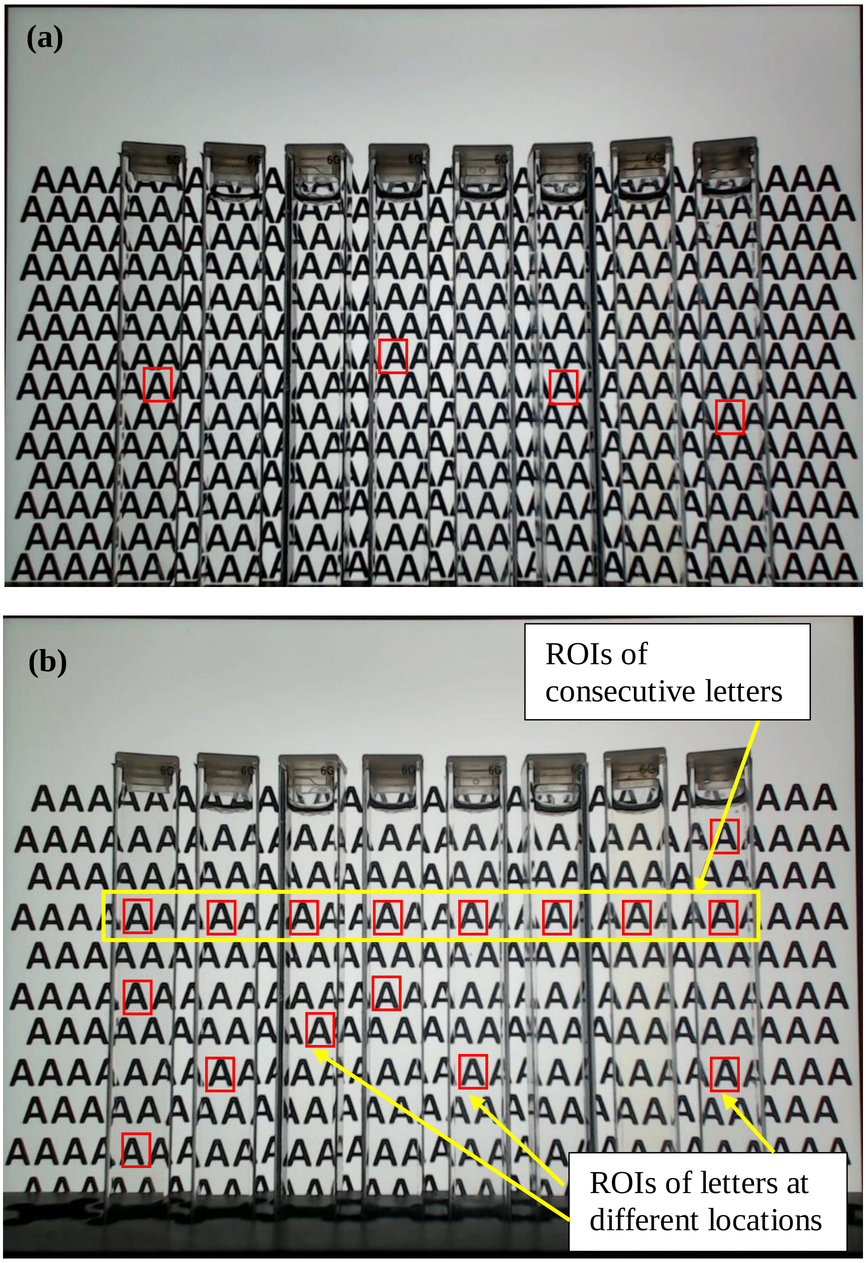

Figure 3.25 (a) dense letter and (b) sparse letter background configurations. Letters in the red squares indicate the ROIs.

The dense letter configuration (Figure 3.25, a) was difficult to analyse with MATLAB as the letters appeared overlapped. During analysis, a well-defined ROI, where the letters were not blocked by the walls of the cuvettes and there was enough space between the letters, was not possible in this case. To overcome this issue, the background was redesigned to create sufficient space between letters for easy detection. This was achieved using the sparse letter configuration (Figure 3.25, b).

2- Thin and thick vertical lines in black and white

The aim of using the line background was to monitor the distortion of these shapes with addition of different solutions or dispersions over the entire sample (Figure 3.26). Quantifying the average thickness, area and perimeter of lines within the ROI of a sample and compare these parameters with the ROI value of a reference (water) sample gave an estimation for the characteristics of the sample. For particle dispersions, it is suggested that the larger the perimeter value, the larger the possible particle size (due to agglomeration) or the more turbid the dispersion (with high total solid content) – as will be demonstrated in Chapter 5. As previously stated, with line analysis, the ROI is quantified for the full sample in the cuvette, which provides more general results than with letter analysis (which measures specific areas of a sample).

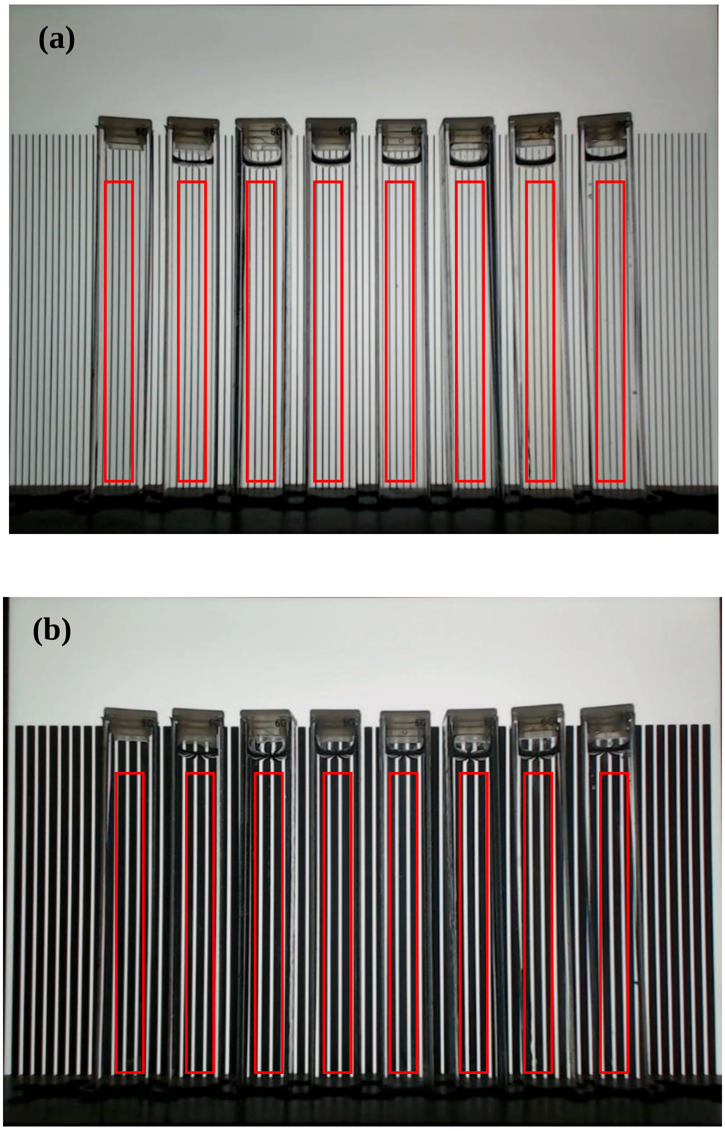

Figure 3.26 (a) Thin lines and (b) thick line backgrounds. Red rectangles indicate the ROIs.

The line designs were further amended so that only one line was contained within each cuvette, which was easier for MATLAB processing.

3- Coloured horizontal lines, squares and circles

Using coloured shapes can provide an estimation of the variation in a sample's colours by measuring the RGB channel values. For example, a red solution produces a higher red channel value than green or blue for any of the coloured shapes in the acquired images, as discussed in Section 3.2.1.2.2.3.

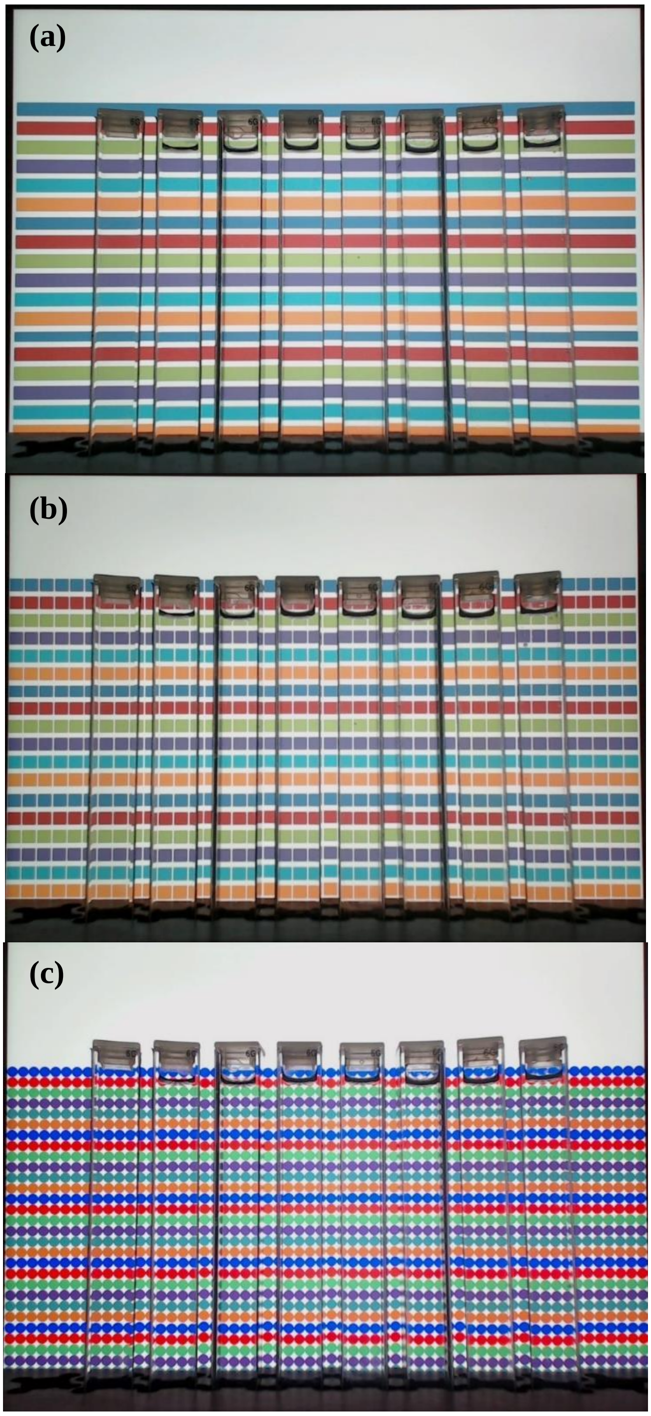

Figure 3.27 Backgrounds of different shapes and colours; (a) horizontal lines, (b) squares and (c) circles.

Using backgrounds of different shapes and colours enables extraction of multiple parameters at the same time – such as the RGB values, areas and perimeters – against a single background.

4- Filled backgrounds (white, red, green and blue)

These backgrounds were specifically designed to measure settling rates in dispersions, as well as the changes in colour with increasing the sample concentration or modification of the dispersion medium.

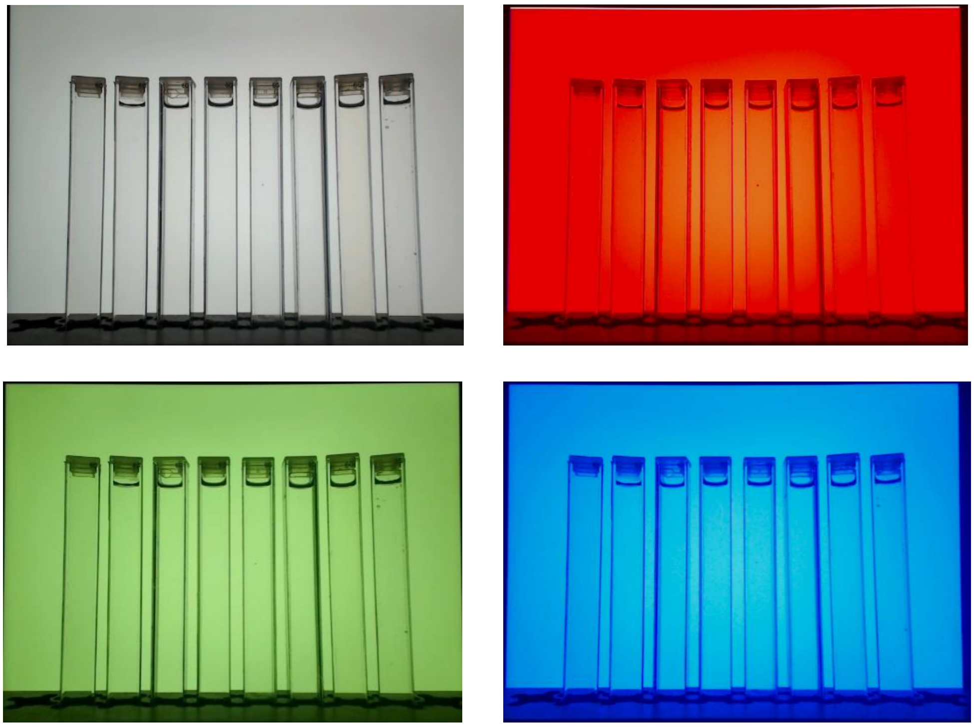

Figure 3.28 The VIS-3 images of filled white, red, green and blue backgrounds.

3.2.3.2 MATLAB analysis code (MAC)

In this section, a full description of the process of acquiring data is provided.

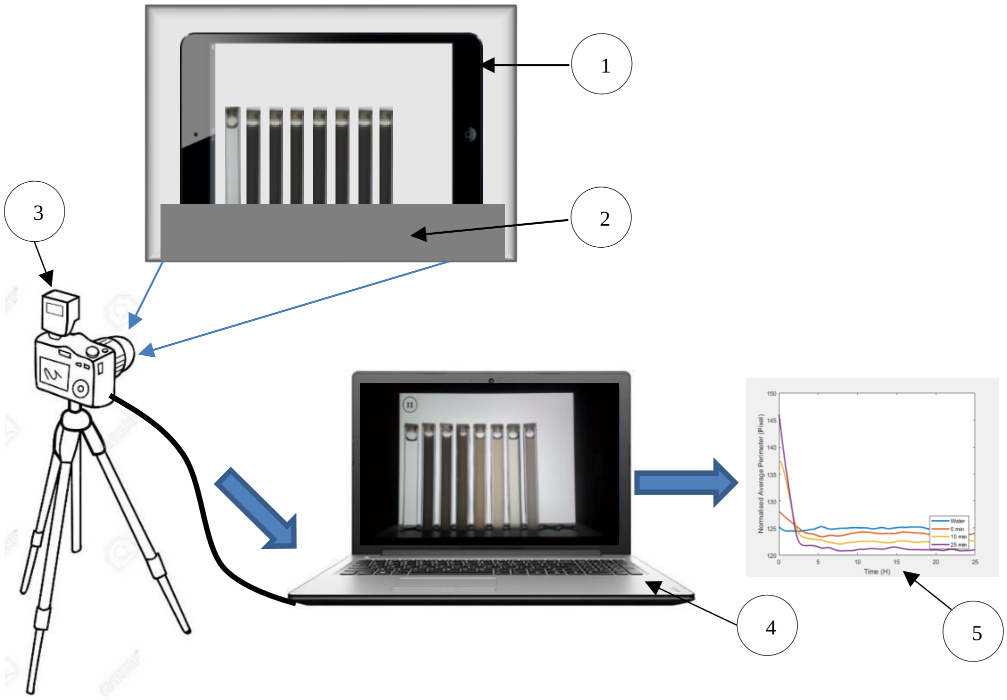

Figure 3.29 Schematic showing the VIS-3 components; 1) iPad fitted into the base, 2) cuvette holder, 3) webcam, 4) computer with MATLAB installed and 5) sample measurements.

MAC has six main components, as illustrated in the block diagram below.

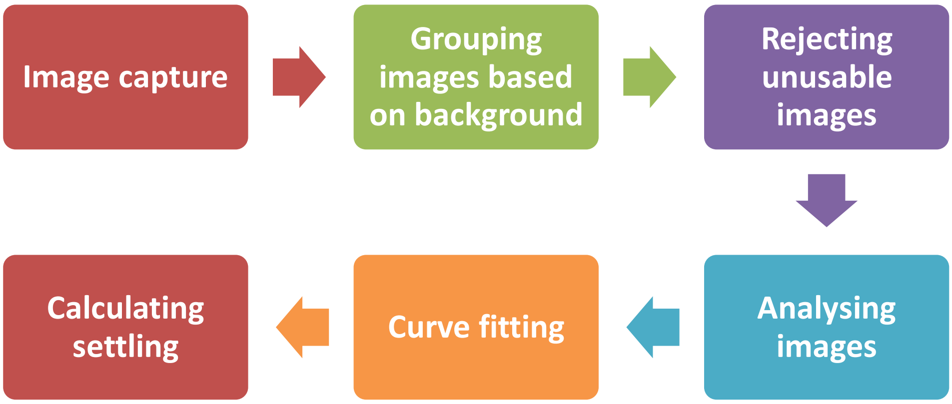

Figure 3.30 Main components of MAC.

3.2.3.2.1 Image capture

In the first stage of MAC, images capturing component captures the photos of the cuvettes affixed in front of an iPad that keeps displaying a sequence of backgrounds. The backgrounds change every 5 seconds, while the code captures images every 1 second, generating more than one image of the same background within the 5 sec time period. The reason for this is to produce extra images in case some are unusable. The code stores the images in tiff format of size 1920 x 1080 to ensure high quality; an example is shown below. The images are sequentially saved by serial number and the time of capturing in a separate Excel file. The index (number) of the cell in the time file corresponds to the serial number of the image captured at that time (Figure 3.32). In the figure, the capture time of image ‘10’ (0.007161 hour) is stored in cell number 10. The MATLAB code for image capturing can be found in Section I.2 (Appendix I).

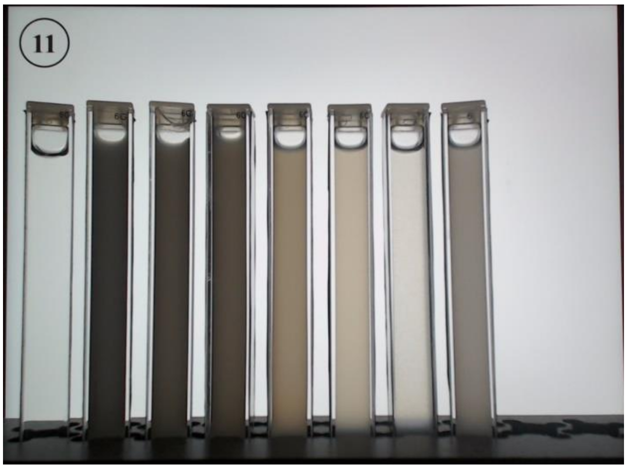

Figure 3.31 An example of the captured images.

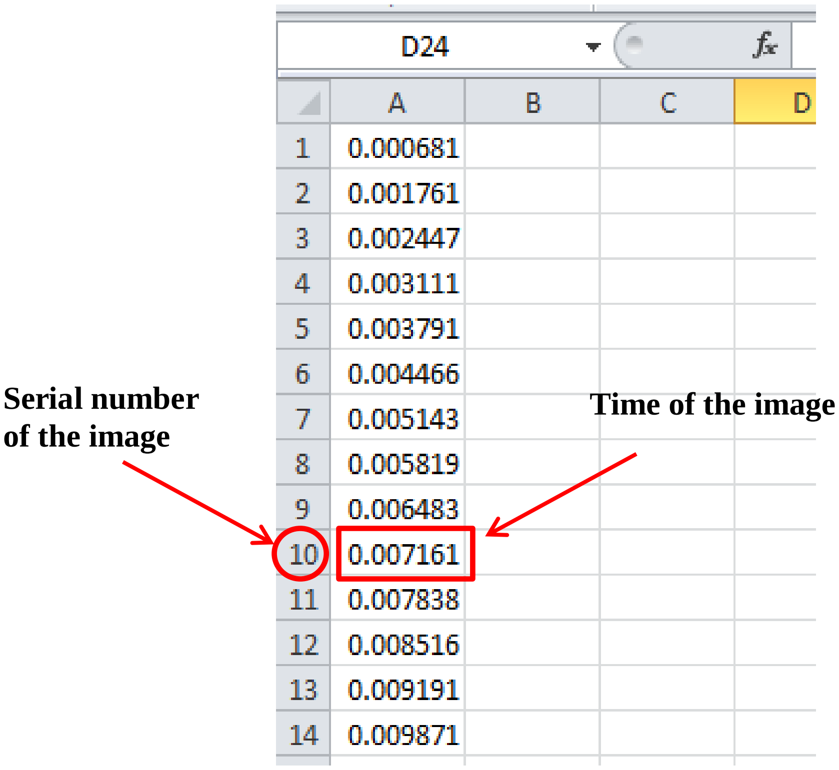

D24

	A	B	C	D
1	0.000681			
2	0.001761			
3	0.002447			
4	0.003111			
5	0.003791			
6	0.004466			
7	0.005143			
8	0.005819			
9	0.006483			
10	0.007161			
11	0.007838			
12	0.008516			
13	0.009191			
14	0.009871			

Serial number of the image

Time of the image

Figure 3.32 Determining the time of capture.

3.2.3.2.2 Grouping images

It was previously pointed that that the iPad continuously changes its display and all images, of all backgrounds, are captured and stored in one group. To ease the process of image analysis, the images were first grouped based on the background, which was done by labelling backgrounds with numbers (later optimised to symbols). Then, a deep learning-based neural network was used to classify (group) the images by background. The MATLAB Deep Learning Toolbox was used to build the deep neural network (Figure 3.33) and the MATLAB code for background classification is shown in Section I.7 (Appendix I).

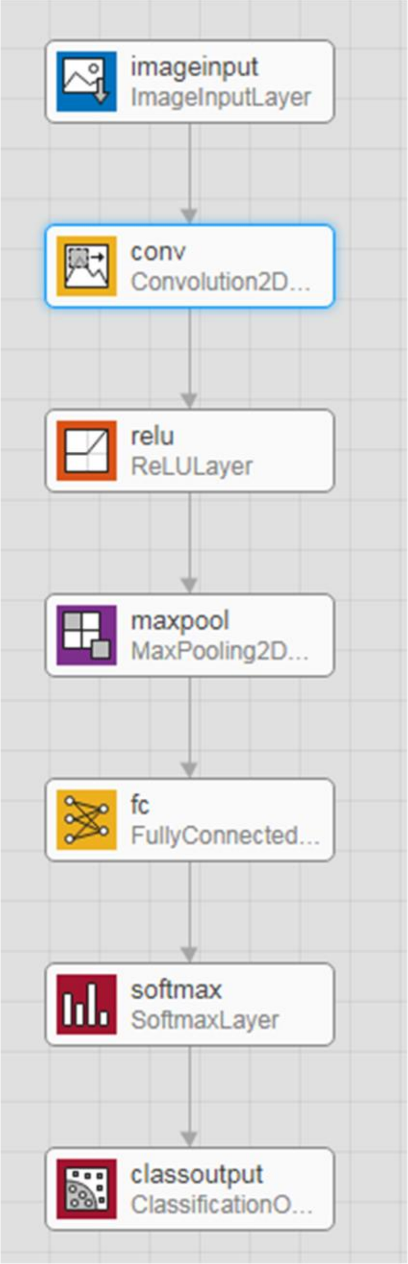

50 x 50 x 1

5 x 5 x 1 x 100

Pool: 2,2

Stride: 2,2

11 x 52900

Figure 3.33 Deep Neural used for grouping images based on background.

Following the above, patches of identification symbols were collected from 1000 images: 100 for each background, as shown in Figure 3.34. The patches were then labelled based on background from which they were collected. Finally, the collected patches and labels were used to train a neural network via deep learning in MATLAB. The trained classifier can achieve an overall accuracy of 99.9%. The classifier makes separation of the images quite easy, fast, and automatic. MATLAB training code was shown in Section I.8 (Appendix I).

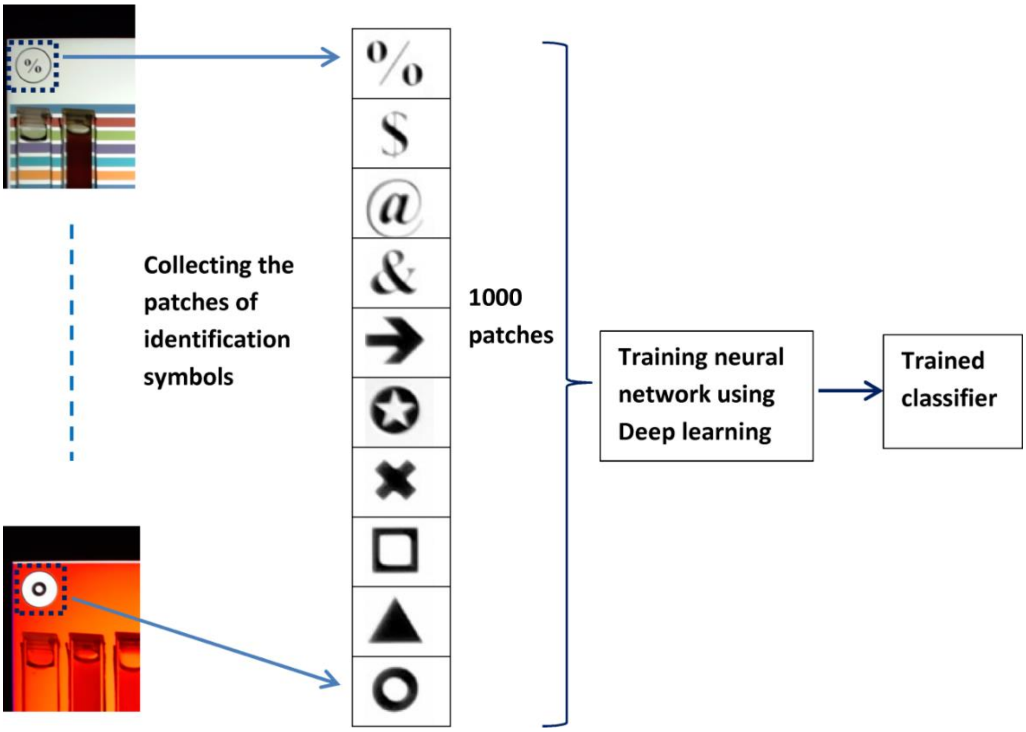

Figure 3.34 Training image classifier.

3.2.3.2.3 Rejecting unusable images

The proposed system relies on a low-cost webcam to capture images throughout experiments. In addition, the images are captured at intervals that are less than 2 seconds, requiring a high-speed camera. While the webcam was capable of this, some images were over- or underexposed, or became corrupted, as shown sample images in Figure 3.35.

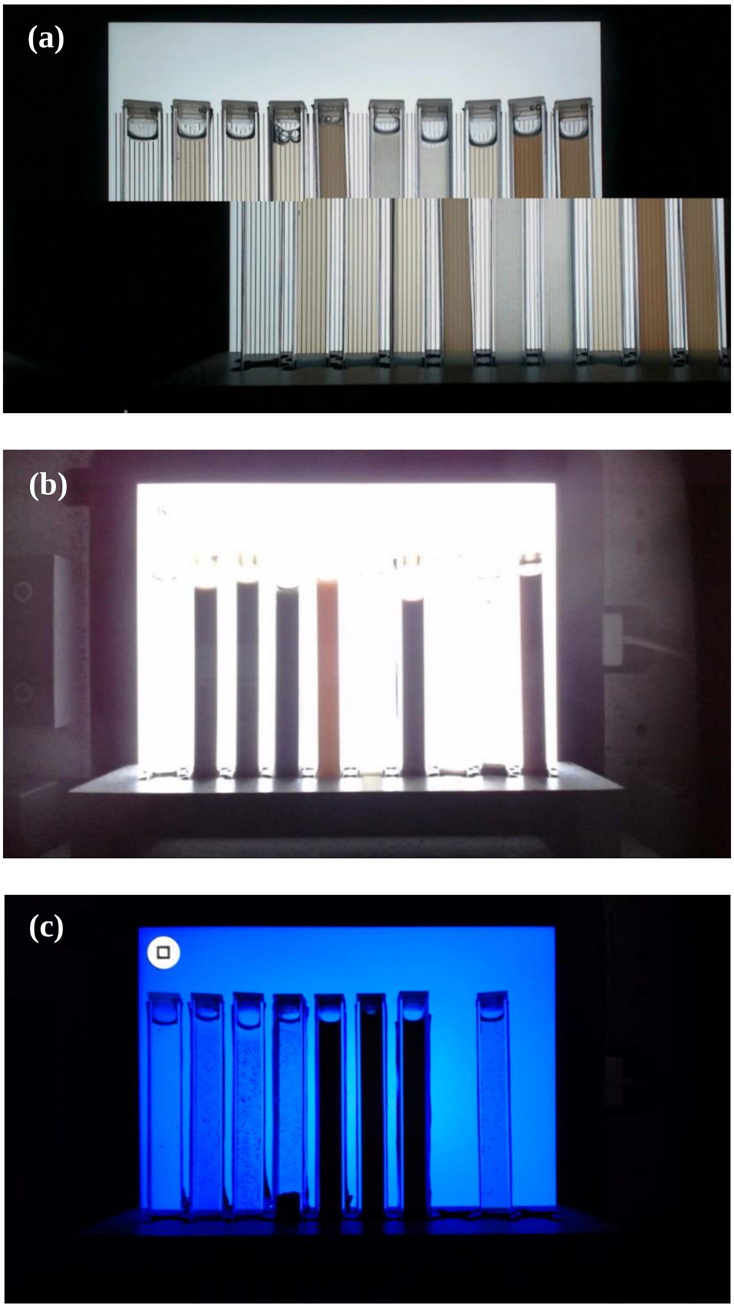

Figure 3.35 Examples of unusable images: (a) corrupted, (b) overexposed and (c) underexposed.

The above images were excluded from analysis; this was done using MAC, which exploits the fact that the area of an image representing a cuvettes containing water should have the same pixel intensity in all images throughout the experiment. Thus, MAC can scan all images to pick out images with higher or lower values compared to the reference image, effectively reading them as ‘unusable’ and eliminating them from further analysis. Suitable images, on the other hand, were collected and saved in a separate location for analysis. The MATLAB code for extracting optimum images is shown in Section I.9 (Appendix I).

3.2.3.2.4 Analysing the images

This is the core component of MAC as it conducts all analysis-related operations (see block diagram in Figure 3.36). The function of this part is described in the next flowchart (Figure 3.38). The subcomponents of the image analysis part are presented in the next sections.

1. Entering experiment details

In this initialisation part, the code asked the user to enter the details of each experiment, such as the name of the experiment, the date and the maximum number of cuvettes, as shown in Figure 3.37. This information was used to generate the Excel file containing the extracted data under the same name as the experiment. The maximum number of cuvettes as important for selecting the ROI inside each cuvette, for which reason it was also recorded. The MATLAB code for implementing this part of the analysis is given in Section I.10 (Appendix I).

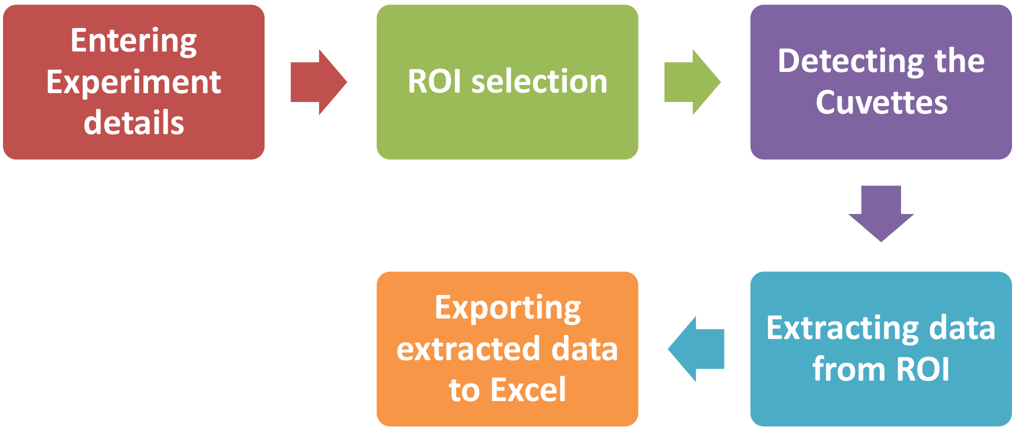

Figure 3.36 Block diagram of the analysis part of MAC.

2. ROI selection

To ensure accuracy of data extraction, the ROI from each cuvette was manually selected. This step is done using a selection tool that allows the user to define the ROI manually as shown in Figure 3.39. A custom MATLAB code was written for this purpose. The tool asks the user to define the ROI by drawing a rectangle inside the cuvette using the mouse. Then, the tool makes sure that all ROIs are of the same size and vertically aligned as in Figure 3.40. The user needs to do ROI selection only once for each experiment and the data associated with the selected ROI (which essentially defines ROI), is stored as a text file in case the user wants to repeat the analysis. The MATLAB code for the selection tool is given in Section I.11 (Appendix I).

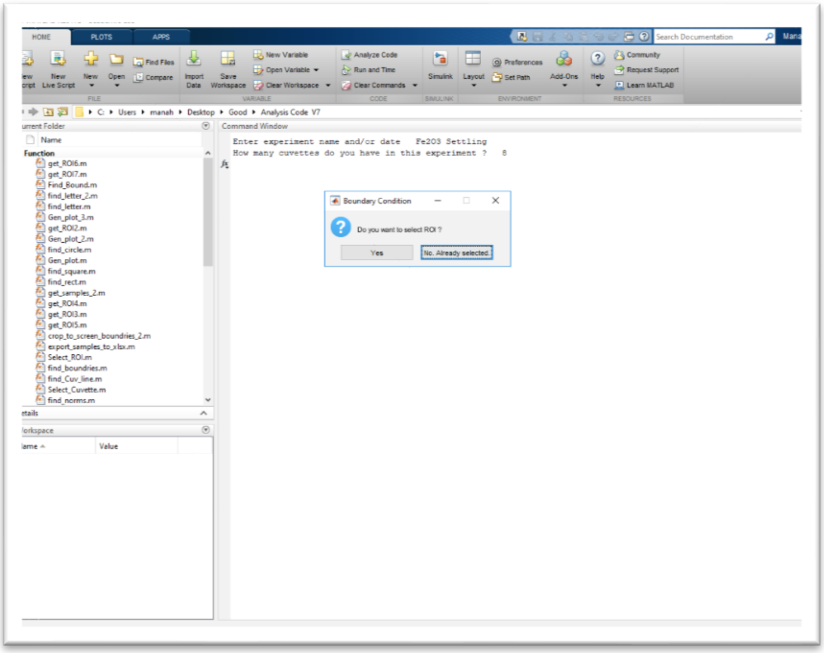

```
Enter experiment name and/or date   Fe2O3 Settling
How many cuvettes do you have in this experiment ?   8
```

Do you want to select ROI ?

Figure 3.37 The first step of analysis is initialisation.

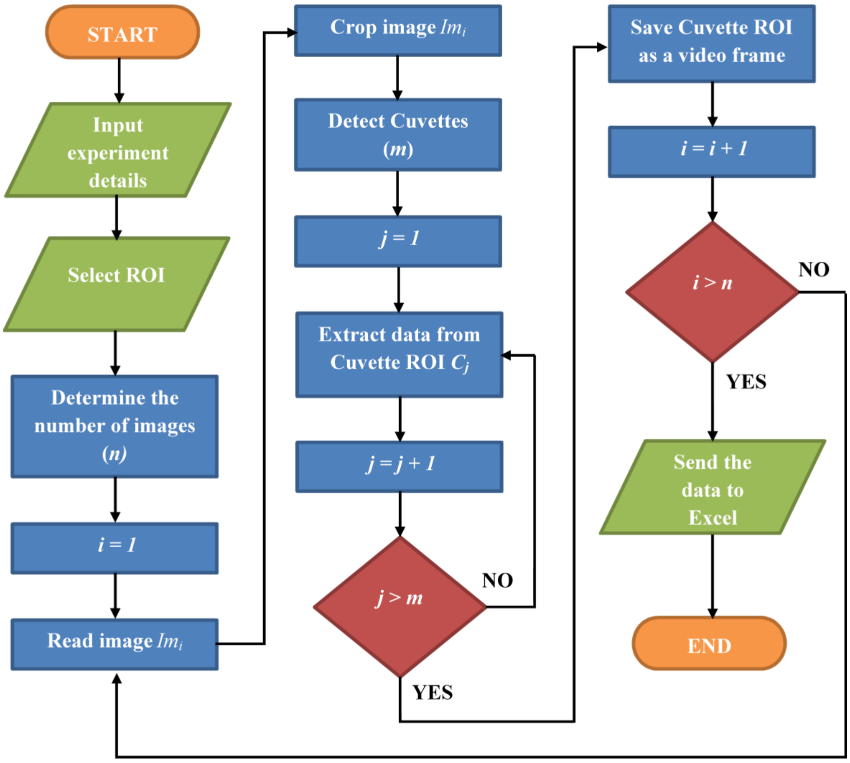

Figure 3.38 Flowchart of the analysis part of MAC, where *i* is image index, *n* is the number of images, *j* is an index of the cuvette and *m* is a number of cuvettes.

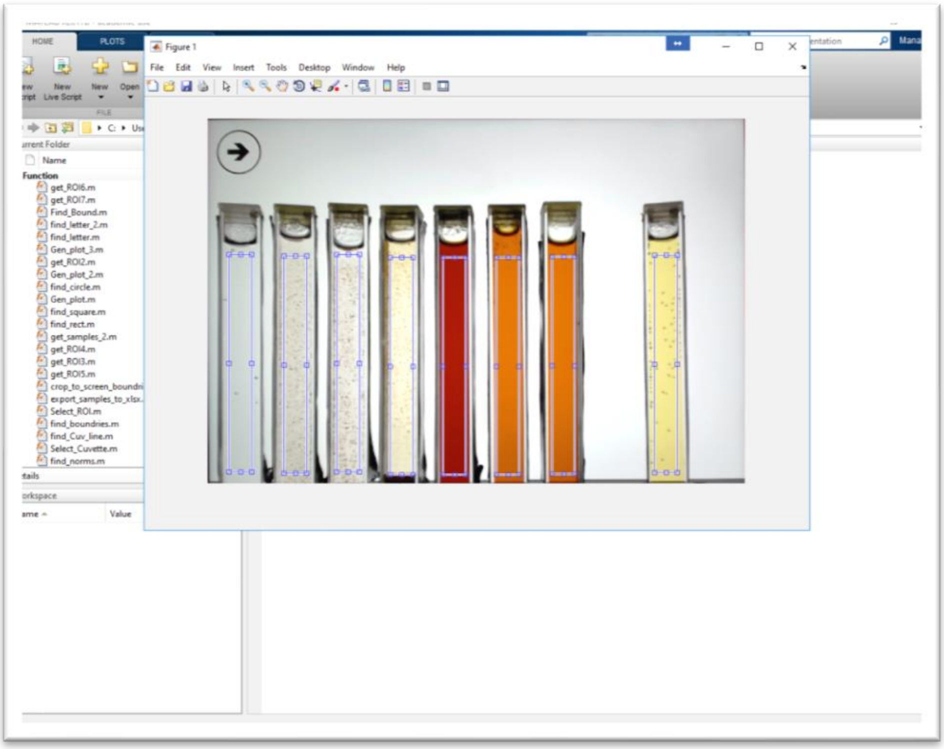

Figure 3.39 ROI selection using the manual selection tool.

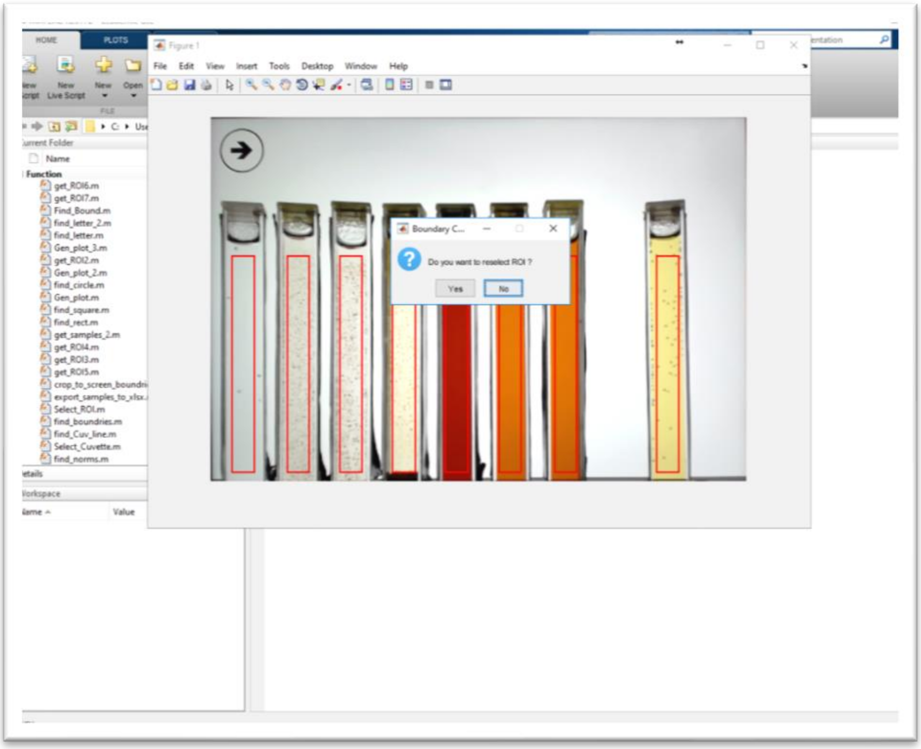

Do you want to reselect ROI ?

Figure 3.40 The selection tool ensures that all ROIs are of the same size and perfectly aligned.

3. Detecting the cuvettes

Due to the nature of the experiments, not all cuvettes were ready at the beginning of each experiment; thus, they were placed in front of the iPad one by one. This required MAC to detect the cuvettes in every single image, for which a special function was developed; this cut out an area of the image to be processed, which contained the top part of the cuvettes (Figure 3.41, a). In the figure below, the top parts of 5 cuvettes appear. It means that the function must detect 5 cuvettes. Then, the cut-out area (Figure 3.41, a) is converted into HSV colour space and only the V channel was used for the next step. In fact, different colour spaces have been tested, and only the V channel generated the best results. The purpose of this step was to highlight the cuvette tops and make them very different than the background. In other words, the pixel values that belong to the cuvettes' tops were darker than the background pixels. Following this, the pixels in the V channel were summed in the vertical direction, as shown in Figure 3.41 (b). As the cuvette tops were darker than the background, summing the pixel values vertically reflected the existence of the cuvette pixels (as shown in Figure 3.41, b). The resultant signal was thresholded to yield bins, as demonstrated in Figure 3.41 (c) – with the number of bins corresponding to the number of cuvettes. The MATLAB code for cuvette detection is shown in Section I.12 (Appendix I).

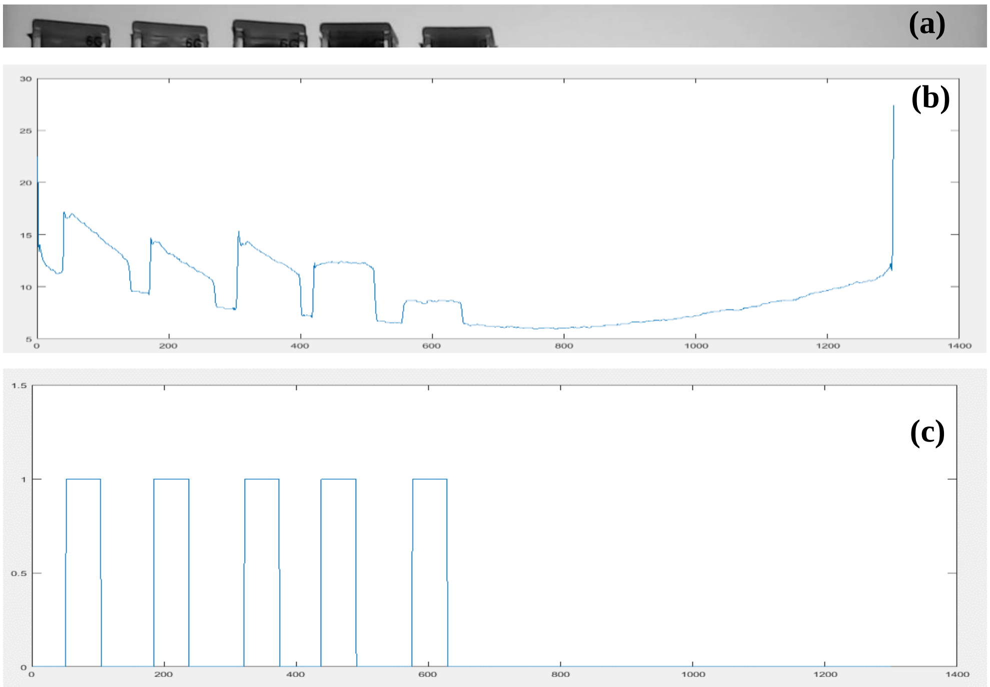

Figure 3.41 Detecting the cuvettes to analyse samples based on the selected ROI.

4. Extracting data from ROIs

After detecting the number of cuvettes in an image, MAC cut out the ROI of each cuvette using the ROI data defined earlier in Number 2. Then, based on the background in the image, MAC extracted the necessary data. A custom MATLAB code written for this purpose can be found in Section I.13-I.15 (Appendix I). For example, if the background was ‘white’, MAC calculated the average intensity of the ROIs after converting them into greyscale. The average intensity was calculated by summing all pixel values inside the ROI and dividing this by the number of pixels inside the ROI. The same thing was done for coloured backgrounds; however, here, instead of converting the image into greyscale, the average intensity was calculated for each of the RGB channels separately. If the background was ‘thin strips’, then the MAC calculated the thickness and perimeter of every single strip for all ROIs. It is, however, worth noting that MAC had to detect the strips first by converting the ROIs into binary images, followed by 'blob' analysis. This analysis is used also to detect thick strips, letters, circles and squares in the other corresponding backgrounds and is carried out using a MATLAB function, called 'regionprops'. This function extracts information that describes the blobs, which can be strips, letters, circles or squares. For the current experiments, only the area and perimeter of the blobs were extracted. MAC also concatenates the extracted ROI's to generate a video, where each frame contained truncated ROIs from a specific image (as shown in Figures 3.42 and 3.43). The resulting video provided a few-second sequence of the entire experiment.

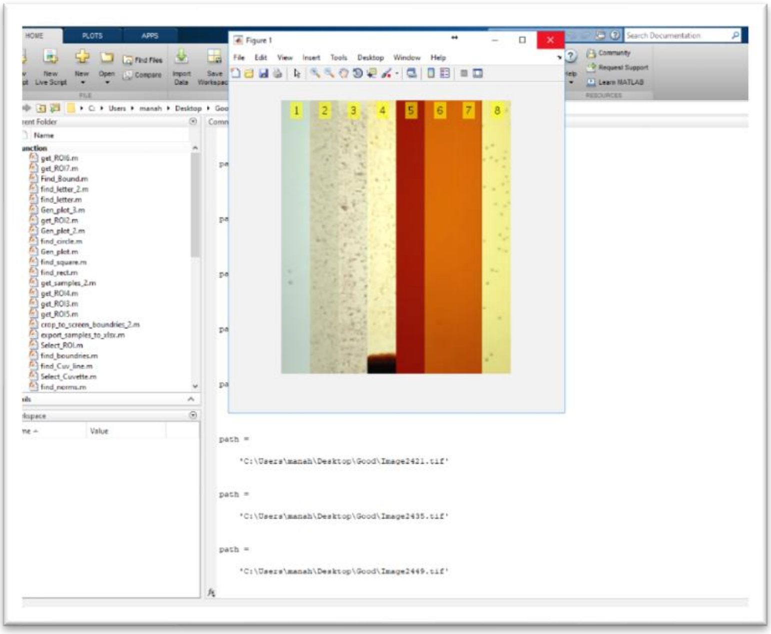

```
path =

    'C:\Users\manah\Desktop\Good\Image2421.tif'

path =

    'C:\Users\manah\Desktop\Good\Image2435.tif'

path =

    'C:\Users\manah\Desktop\Good\Image2449.tif'
```

Figure 3.42 Analysing the images: extracting average intensity from ROIs.

5. Exporting the extracted data to Excel

MAC exported all extracted data into an Excel file using the MATLAB function 'actxserver'; the data was combined into tables and saved as Excel templates, where it was plotted against time. In addition, MAC generated the colour distance map as shown in Figure 3.44. It is worth mentioning that the data was filed in Excel according to background; for example, a white background generated a single Excel file, whereas a coloured background generated three Excel files, one for each channel (R, G, and B). The MATLAB code for exporting data into Excel is shown in Section I.16 (Appendix I).

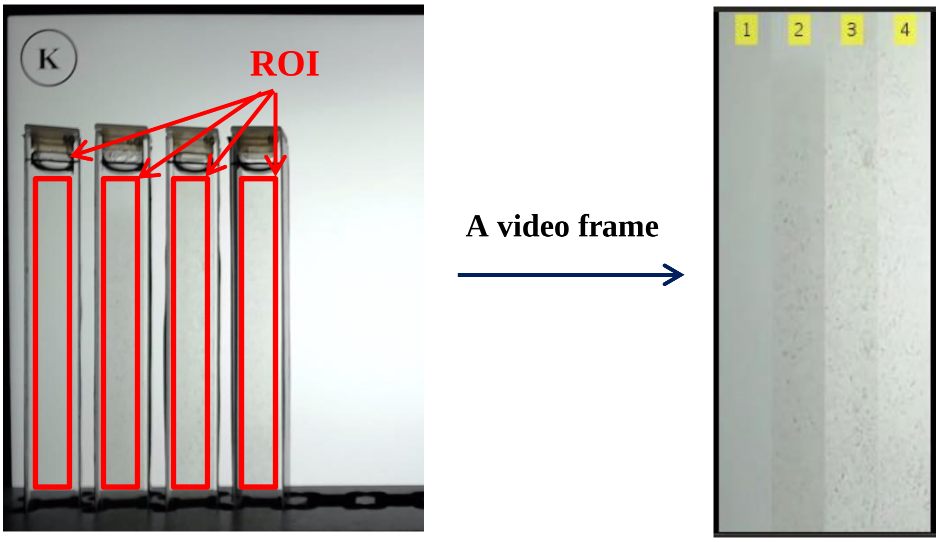

Figure 3.43 Concatenating ROI to form a video frame.

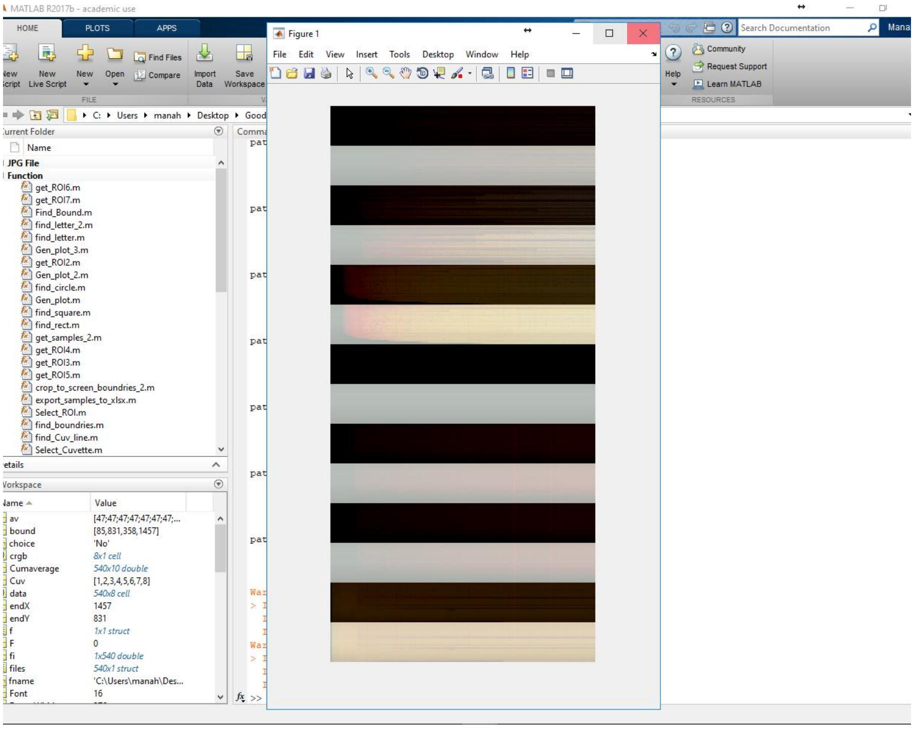

get_ROI6.m
get_ROI7.m
Find_Bound.m
find_letter_2.m
find_letter.m
Gen_plot_3.m
get_ROI2.m
Gen_plot_2.m
find_circle.m
Gen_plot.m
find_square.m
find_rect.m
get_samples_2.m
get_ROI4.m
get_ROI3.m
get_ROI5.m
crop_to_screen_boundries_2.m
export_samples_to_xlsx.m
Select_ROI.m
find_boundries.m
find_Cuv_line.m
Select_Cuvette.m

ame	Value
av	[47;47;47;47;47;47;47;...
bound	[85,831,358,1457]
choice	'No'
crgb	8x1 cell
Cumaverage	540x10 double
Cuv	[1,2,3,4,5,6,7,8]
data	540x8 cell
endX	1457
endY	831
f	1x1 struct
F	0
fi	1x540 double
files	540x1 struct
fname	'C:\Users\manah\Des...
Font	16

Figure 3.44 Generating a colour distance map.

3.2.3.2.5 Curve fitting

Due to the quality of the camera, the plots in the Excel templates demonstrated noise in the form of ripples, as shown in Figure 3.45 (a). As such plots are difficult to analyse, curve fitting was used to smooth out the plots (Figure 3.45, b). For this purpose, a custom MATLAB code was written to include a MATLAB curve fitting function (fit), as shown in Section I.17 (Appendix I).

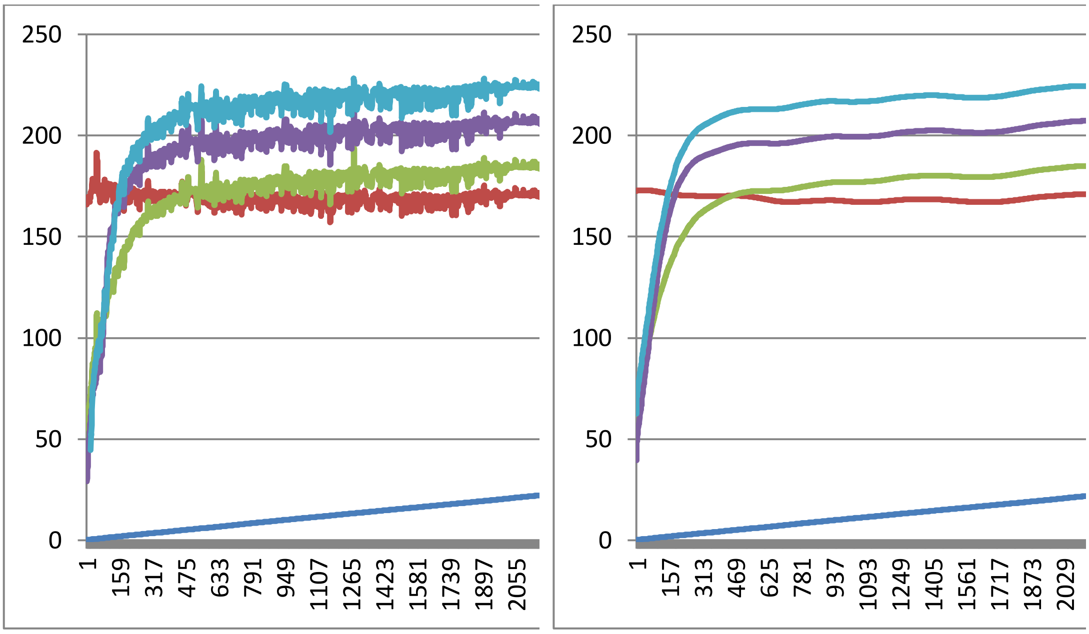

(a) **(b)**

Figure 3.45 Smoothing out plots using curve fitting: (a) the original plot and (b) after curve fitting.

3.2.3.2.6 Calculating settling time

The final step of MAC was to calculate the settling time – which is the time taken for the plot to reach a steady value, as shown in Figure 3.46. For this purpose, a custom MATLAB code was written and used the ‘stepinfo’ function to calculate rise time, settling time and other step-response characteristics, as shown in Figure 3.47. The settling time is the time that it takes for the error ($|\ y(t)\ - y_{final}\ |$ between the response $y(t)$ and the steady-state response y_{final}) to fall to within 2% of y_{final}. The settling time calculation code is shown in Section I.18 (Appendix I).

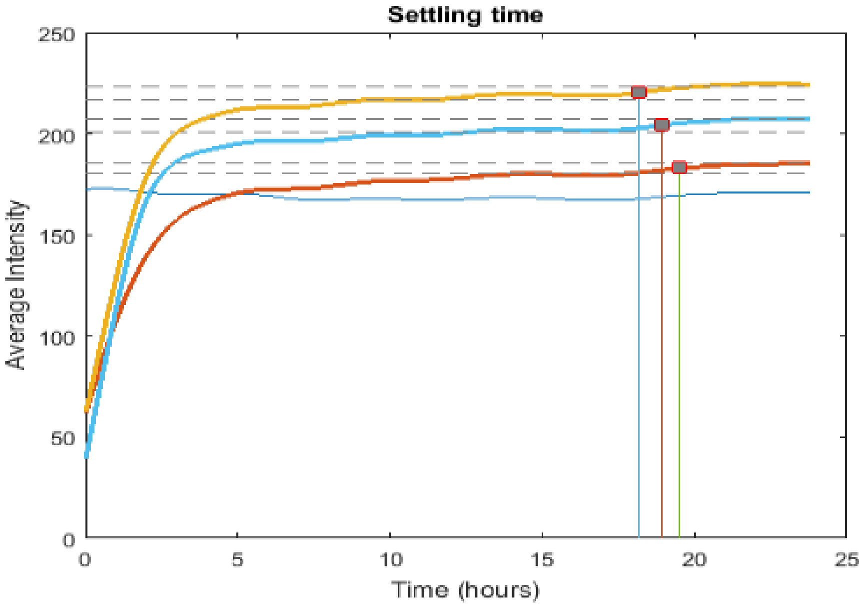

Figure 3.46 Calculating settling time by detecting the steady state at the end of settling.

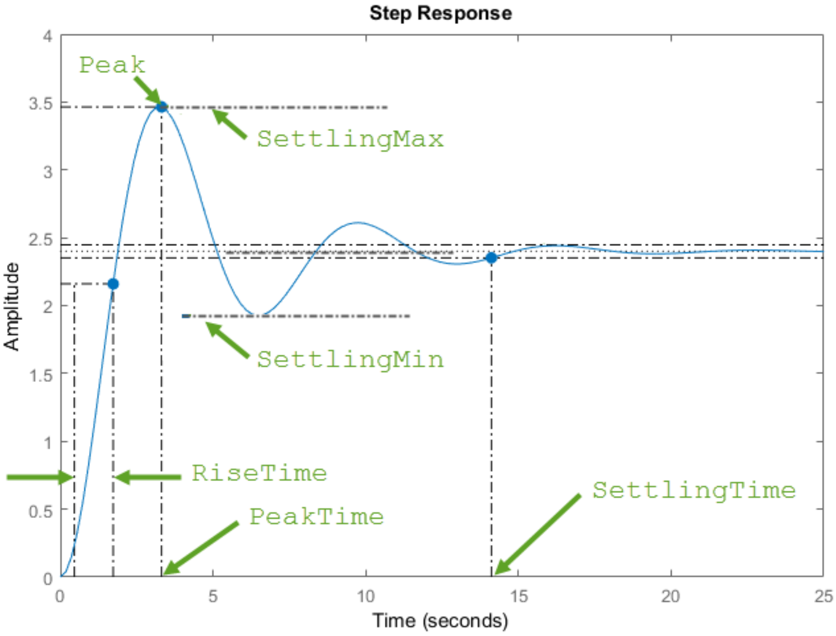

Figure 3.47 Calculating step-response characteristics using the MATLAB function ‘stepinfo’.

MAC was also used to obtain Hansen Solubility Parameters (HSP) by outputting an Excel sheet that tabulates the calculated settling time, relative settling time and the grading estimate (based on the relative settling time value), as described in Chapter 6. The MATLAB code implementing HSP analysis is provided in Section I.19 (Appendix I).

3.3 Summary of the VIS Designs

A summary of the components, measurement options and types of MATLAB image analyses used in each VIS design is presented in Table 3.5.

Table 3.5 Summary of the components and functions of the three VIS designs.

	The VIS-1	**The VIS-2**	**The VIS-3**
Sample container types and dimensions (Height x Width x Depth) mm	Glass Vessel (170x240x26) mm	Rectangular Glass Cuvettes (100x10x10) mm	Rectangular Glass Cuvettes (100x10x10) mm
Number of samples	1	14	10
Source of light	Light Pad	Light Pad	iPad
Source of Characters	Acetate paper	-	iPad
Measurement types	Concentration, Colour, and Transparency	Settling rate	Concentration, Colour, Transparency, Turbidity and Settling rate
MATLAB processing codes	AIL and AIC	ASR	MAC
Chapters where designs were used	3	4	5 and 6

Although VIS-1 allowed for several measurements to be taken (Table 3.5), such as sample concentration from a calibration curve (as described in Sections 3.2.1.2.1.3 and 3.2.1.2.2.3), a large amount of solution was required for these measurements. In addition, there was difficulty attaching and interchanging backgrounds (letters and colour swatch) made from acetate paper without shifting the precise positioning of each sample. This had caused inaccuracy and errors in the obtained measurements. This, therefore, led to the development of the VIS-2, which enabled use of multiple cuvettes and as little as 10 ml of sample for each measurement. Furthermore, with the VIS-2 up to 14 different samples could be simultaneously evaluated (Chapter 4). However, as this configuration did not use acetate paper backgrounds, it was only possible to measure dispersion settling rates. Finally, the VIS-3 was developed as a combination of the two prior designs. Notably, the ability to switch between multiple backgrounds displayed on an iPad allowed multiple measurements to be taken. In addition, smaller sample amounts were required. The sample parameters measurable by VIS-3 are colour, transparency, turbidity and settling rates (Chapter 5). Moreover, the validation procedure conducted for both VIS-1 and VIS-2 facilitated measurements using the VIS-3, as all designs followed the same principle of image analysis. The VIS-1 was, therefore, only used for validation in this thesis.

3.4 Conclusions

Each iteration of the VIS system enabled improvement towards an optimal configuration. A future design could incorporate automatic vials shaker, which would be turned off just before commencing image capturing, and also automated cuvette filling during imaging.

- The first developed system (the VIS-1), which used a Snellen chart and a colour swatch attached to a relatively large vessel, was successfully used to determine concentrations of a known solution using letter development. Furthermore, the interaction of a sample of a certain colour with different colours within the colour swatch was visualised and quantified digitally. However, small differences in the position of the glass vessel were often shown to skew measurements – particularly when modifying the vessel between configurations. It was important to account for these differences during image analysis in order for the results to be comparable; the MATLAB code was subsequently scripted to account for these differences using several approaches. Furthermore, during the first stage of the VIS-1 validation, the analysis focused on changes in letter areas and locations and, for colour swatches, the same was true for variations in the colour squares. The next stage focused on overcoming vessel position errors. The initial plan was to conduct multiple, repeatable experiments to assess the uncertainty margins by determining cumulative error. However, at that stage of VIS-1 development, this was not feasible due to the occurrence of errors from three main sources; measurement letter area, vessel position and sample concentration. Thus, even by maintaining one of the above variables constant in a repeated experiment, it would not be possible to control the other two. This led to the decision to solve the above issue by changing the configuration of the setup and developing MATLAB coding to obtain accurate results from good quality images in a simplified manner so as to characterise any sample.

- The final design (the VIS-3) was more successful as errors from sample shifting were eliminated, the sample volume was minimised and the ability to test several samples at the same time was introduced. Nevertheless, invalid images were sometimes produced due to the quality of the used camera. This led to the development of MATLAB coding (MAC) to extract and analyse the best groups of images, as described in the previous sections.

General limitations

- High sample concentrations were sometimes not possible due to opacity, which prevented the visibility of characters for detection by the VIS. Thus, to provide the exact limitation, calibration data must be conducted for set of samples to determine the highest concentration can be detected by the VIS. Moreover, the concentration of the solutions corresponds to the weight loading or total solid content, in the case of NP dispersions.

- It is not possible to determine the composition of a solution without developing an extensive look-up-table that would recognise a series of optical behaviours (and guess the possible composition).

- The concentration of the different solutions can only be determined by knowing sufficient information about the measured sample. For example, the particle size (for NP solutions), type of solvent, as well as other properties such as density, must be measured in advance. The NP solution must also be stable and lacking sedimentation or agglomeration to ensure that the results are reproducible.

Chapter 4: Stability Evaluation of TiO_2 Dispersions in Polymers and using the VIS-2

4.1 Introduction

As stated in Chapter 1, agglomeration of nanoparticles, whether in their dry or wet form, as produced or dispersed in a polymeric matrix, presents a key challenge in nanotechnology. A solution to this issue can only be achieved by improved understanding of nanoparticle dispersion behaviour in different mediums and under different conditions. Particle size, morphology and functionality are known factors affecting the quality of a dispersion and its dispersibility into a polymeric matrix.

As the main aim of this thesis was to evaluate the dispersions produced by the Nottingham CHS rig using efficient approaches (Chapter 1), the resultant TiO_2 formulated dispersions (among others) were used in this chapter. Moreover, these dispersions showed a high level of destabilisation during production and with ageing. The stability of TiO_2 dispersions was investigated using two approaches; first, by evaluating their behaviour after integration into polymers and, second, by directly investigating the dispersions as produced by the CHS rig and after modification. The second approach involved the VIS-2, as described in Chapter 3.

4.2 Materials and Methods

TiO_2 dispersions in aqueous solution, formulated from different precursors using the CHS rig (Chapter 2), were tested for stability either in in their dry polymeric state (Section 4.3.1) or as wet dispersions using the VIS-2 (Section 4.3.2). In general, the dispersions were produced in a way so that comparable batches of titania from different precursors and modified titania were formed. The resulting dispersions were evaluated for stability immediately post-production or after modification via chemical or mechanical methods – which were considered to improve colloidal stability (Pashley and Karaman, 2005). These products were then characterised using SEM, TEM, XRD and DLS, among other methods.

4.2.1 Titania (TiO_2) NPs from TIBALD

Titanium (IV) bis (ammonium lactato) dihydroxide (TIBALD) [Aldrich, 50 wt. % in H_2O] (Figure 4.1) and hydrogen peroxide (H_2O_2) solution were used as precursors for the production of TiO_2 NPs.

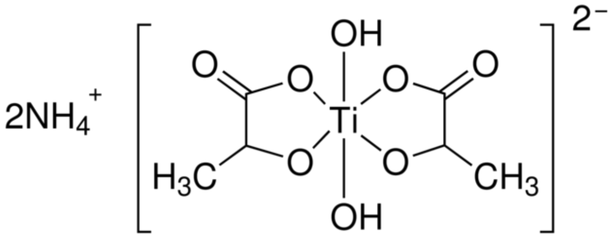

Figure 4.1 Chemical structure of TIBALD.

The conditions for this experiment were as follows:

- 0.1 M TIBALD (58.8 g in 1 L H_2O) was pumped through the metal salt (MS) stream upwards, with a pumping rate of 10 mL/ min.

- 5% H_2O_2 in DI water was pumped through the water stream downwards, with a pumping rate of 20 mL/ min.

The reactor was set to the supercritical conditions of 400 °C and 240 bar.

The above amounts and reaction conditions were kept in line with previously optimised protocols at the University of Nottingham (Elbasuney, 2012).

The product was collected and the total solid contents percentage (TSC %) was evaluated to be 0.294 wt.%.

4.2.2 Titania (TiO_2) NPs from TIPO

Titanium (IV) isopropoxide (TIPO) [Aldrech, 97 wt. %] (Figure 4.2) was dissolved in 2-propanol [$(CH_3)_2CHOH$, Aldrech] (IPA) and used as a precursor to produce the TiO_2 NPs.

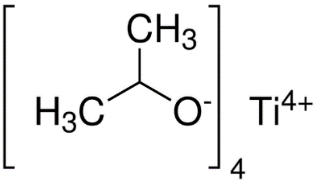

Figure 4.2 Chemical structure of TIPO.

The conditions for this experiment were as follows:

- 0.1 M TIPO (29.4 g in 1 L IPA) was pumped through the metal salt (MS) stream upwards, with a pumping rate of 10 mL/ min. IPA was used here instead of DI water as TIPO is insoluble in H_2O (TIPO condenses and precipitates in H_2O, which can cause reactor blockage).

- DI water was pumped through the water stream downwards, with a pumping rate of 20 mL/ min.

The reactor was set to the supercritical conditions of 400 °C and 240 bar, at which the reaction occurs in the counter-current mixing reactor.

4.2.3 Modified Titania (TiO_2DDSA) NPs from TIPO

TIPO and dodecenylsuccinic anhydride (DDSA) (Figure 4.3) were dissolved in IPA and used as a precursor to produce the TiO_2DDSA NPs.

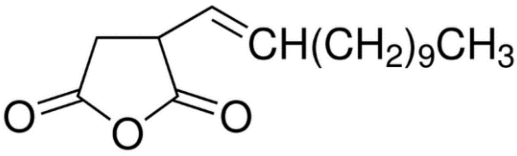

Figure 4.3 Chemical structure of DDSA

The conditions used were:

- 0.1 M TIPO and 0.01 M DDSA (29.4 g TIPO and 3 g DDSA in 1 L IPA) were mixed and pumped through the metal salt (MS) stream upwards, with a pumping rate of 10 mL/min.
- DI water was pumped through the water stream downwards, with a pumping rate of 20 mL/min.

The possible mechanism by which the DDSA carboxylate groups attached to the titania NPs via hydrogen bonding are illustrated in Figure 4.4 (Neouze and Schubert, 2008).

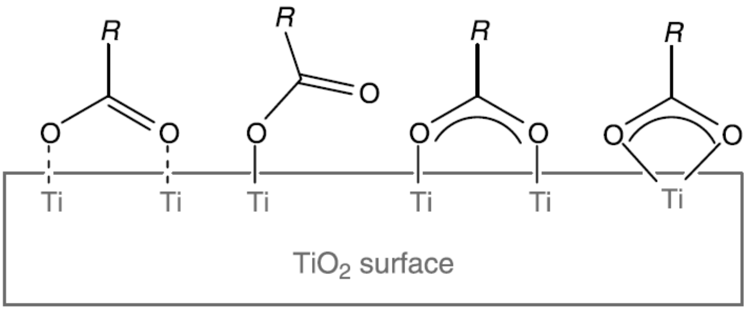

Figure 4.4 Adsorption mechanism of DDSA carboxylate ligands on titania nanoparticles (Neouze and Schubert, 2008).

A comparison experiment to assess the ring-opening conditions of DDSA under increased heat was carried out in a round bottom flask. In this method, 10 g of DDSA (n=226.4 g/mol) and 0.68 g of DI water (n=18 g/mol) were placed in a 250 mL round bottom flask, fitted to a condenser. The solution was heated to 95 °C with 600 RPM stirring on a hot plate. DDSA required 24 hrs under these conditions to successfully ring-open (Figure 4.5).

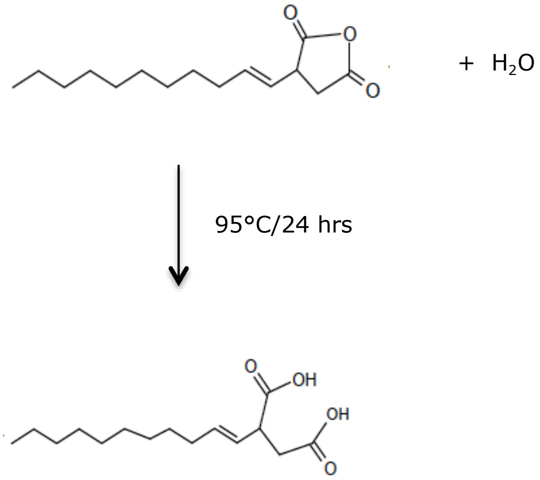

Figure 4.5 Schematic illustrating the DDSA ring-open mechanism.

Many batches of modified NPs were produced. Some of the products were used in the solution collected from the rig under VIS-2 observations. Other batches were extracted with xylene (Figure 4.6); the organic-NP layer was collected, centrifuged, freeze-dried and used for the dispersion study with epoxy-nanocomposites (as described in Section 4.3.1). Extraction with xylene was carried out by adding xylene to the suspension of NPs at a 5:1 ratio. The mixture was placed into a separating funnel, shaken and left overnight to separate. Two layers were then obtained (xylene layer at the top and water at the bottom of the funnel). The DDSA-modified nanoparticles were successfully extracted onto the organic layer and this was also used to qualitatively assess whether the NPs had been successfully modified.

Figure 4.6 TiO_2DDSA NPs after extraction into xylene.

4.2.4 Commercial Titania NPs (P25)

Dry titania NPs of 25 nm size were purchased from Degussa and used with the polymer and was larger than the particles produced by the CHS rig (Section 4.3.1).

4.2.5 Titania-epoxy Nanocomposites

Epoxy resin [bisphenol-A (epichlorohydrin)] was used as a hosting polymer along with a cross-linking agent (triethylene tetramine), both purchased from Struers (Figure 4.7).

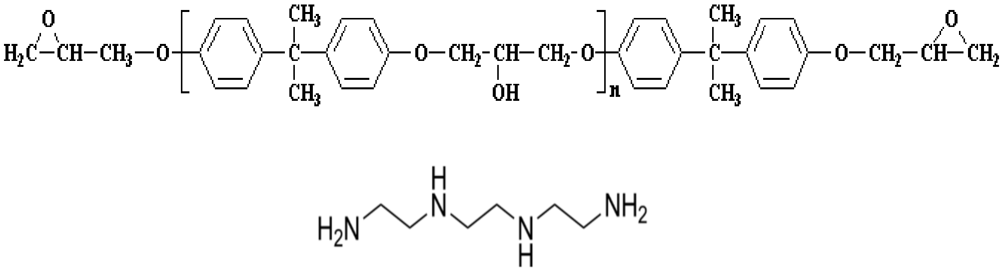

Figure 4.7 The chemical structures of epoxy and triethylene tetramine.

Two types of (dry) titania nanoparticles were used for the dispersion study with epoxy resin: 25 nm-sized titania (commercially known as P25) produced by Degussa and TiO_2DDSA NPs produced using the CHS rig (Section 4.2.3).

Titania-epoxy composites were prepared using *in situ* polymerisation, as follows: the dried nanoparticles were added to epoxy resin and mechanically mixed at 1200 RPM for 1 hour to provide the required shearing force to separate the nanoparticles and break down any possible agglomerates. The cross-linking agent was added at the end of the mixing time. The prepared formulations were cast under vacuum (0.1 bar) into a circular mould for subsequent characterisation with SEM. Vacuum casting minimised the entrapped air bubbles and enabled the achievement of a compacted structure with minimum air voids. Figure 4.8 shows the mechanical mixing set-up and the vacuum casting unit.

Figure 4.8 Polymerisation by mechanical mixing (left) and vacuum casting (right).

P25- and TiO_2DDSA- epoxy nanocomposites were each produced at three different concentrations (1 wt.%, 5 wt.% and 10 wt.%), with respect to the amount of epoxy resin used. For example, to produce 4 blocks of the nanocomposites, the required resin mass was 33.3 g, to which a total of 4 g of cross-linking agent was added; this was then divided into 4 moulds (standard ratio from the manufacturer). Thus, a total amount of 0.33g of P25 powder was needed for a 1 wt.% NPs concentration.

4.3 Results and Discussion

Titanium dioxide NPs are widely used in composites to improve polymer properties, such as thermal stability and the refractive index for different applications (Convertino et al., 2007, Imai et al., 2009, Laachachi et al., 2005). In the first part of this work, titania was selected due to its low dimensionality (< 30 nm) and the ease with which it can be functionalised and dispersed into polymers.

The following observations from TEM, XRD and DLS have provided insight into the properties of the investigated systems.

Figure 4.9 shows TEM images of the commercially available titania P25. As can be seen, the average particle size did match with the expected ca. 25 nm and the particles were highly crystalline.

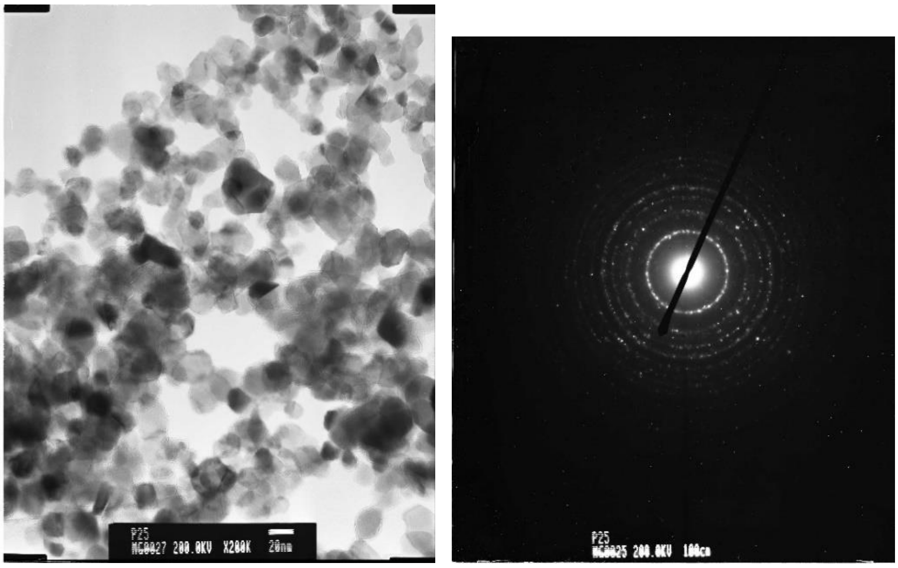

Figure 4.9 (left) TEM images for P25 and (right) their SAED pattern. Scale bar = 20 nm.

In comparison, the titania nanoparticles generated using the CHS were of an average particle size of ca. 4.4 nm (standard deviation SD = 1.3) when using TiBALD as a precursor and 7.0 nm (SD=1.5) when using TiPO (Figure 4.10).

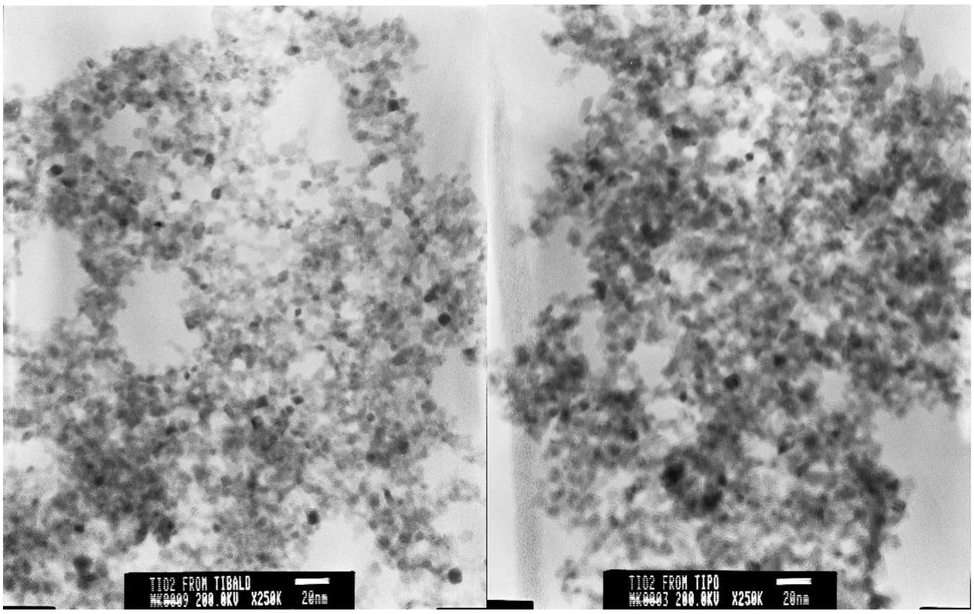

Figure 4.10 TEM images of the TiO_2 produced here from (left) TiBALD and (right) TiPO. Scale bars = 20 nm.

NP shape was seen to be almost the same when synthesised from both sources and corresponded to spherical nanoparticles. When modified with DDSA, the average particle size was 6.9 nm (SD=1.4), which was not significantly different from unmodified NPs produced using the same method (with CHS and TiPO as the source) under the same conditions. The layer of DDSA was not seen using TEM, as it is organic and remained mainly transparent. The product was, however, still highly crystalline (Figure 4.11). The particle sizes were calculated by measuring the diameter of 250^+ particles using Image J.

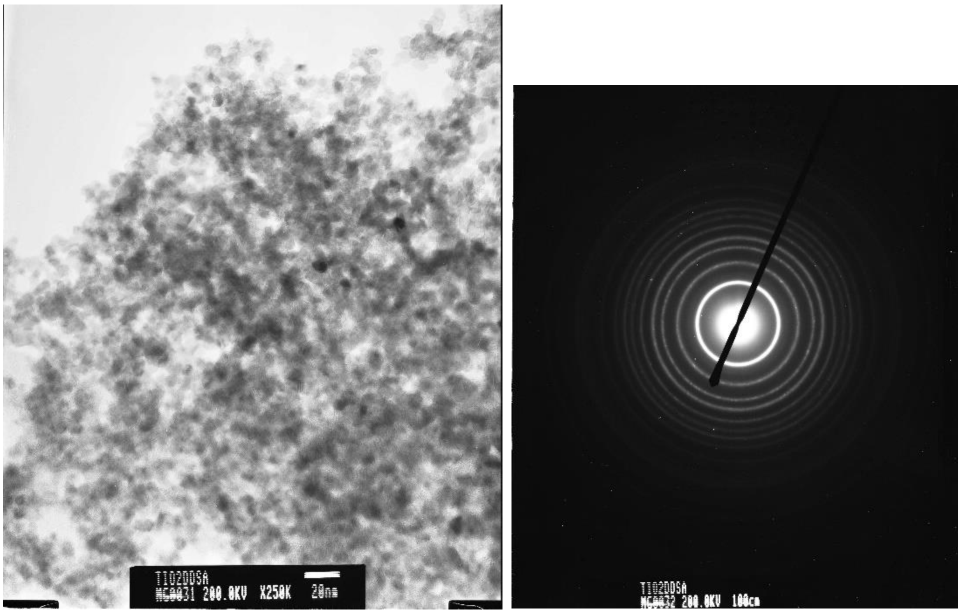

Figure 4.11 TEM images of TiO_2DDSA produced by CHS and their SAED pattern.

In all cases, XRD analysis showed that the products matched with the tetragonal titania anatase phase (ICDD-PDF-01-078-2486) and lacked any impurities or detectable organic residues (Figure 4.12).

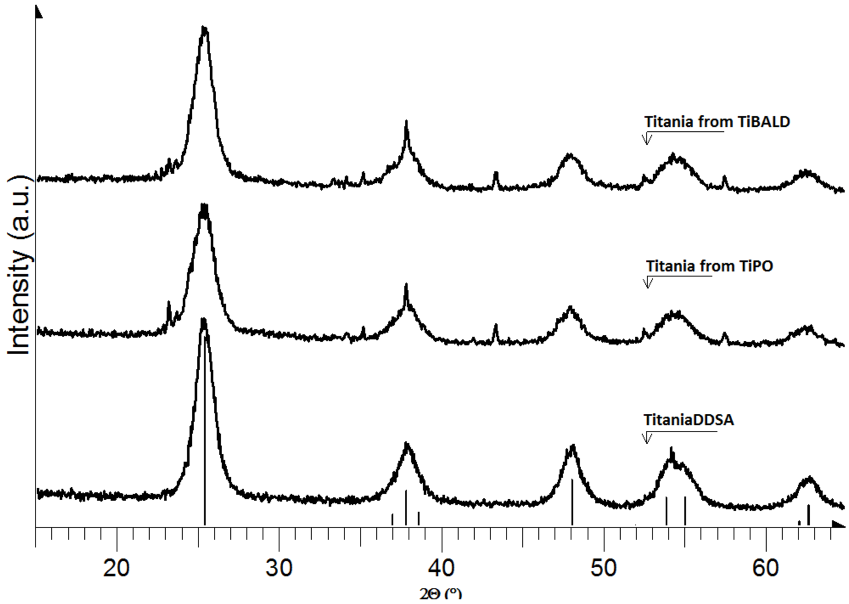

Figure 4.12 XRD patterns of the titania products presented in this report.

Dynamic light scattering (DLS) was also used to evaluate the NP size of the products of the CHS rig (colloidal titania from TIBALD and TIPO, as well as TiO_2DDSA from TIPO).

At first, readings were taken for the concentrated samples as produced from the rig. These solutions were, however, too concentrated for the recommended DLS values; hence, most of the scattered light resulted from the high concentration of the solution itself and from agglomeration of particles, which dominated over the smaller particles. Following this, samples were diluted to maximise the accuracy of the results and to detect smaller, individual particles. This was not the case with TiO_2 produced from TIPO, however, as no dilution of the sample was needed; this was either attributed to the size of NPs produced from TIPO or the high stability of the suspension. As can be seen in Figure 4.13, the detected particle sizes were still too large compared to those observed using TEM. This was explained by the constant movement of particles in the dispersion (e.g. during settling down). From DLS, the observed main particle sizes were approximately: 1700 nm from TiBALD, 120 nm from TiPO and 450 nm from TiO_2DDSA.

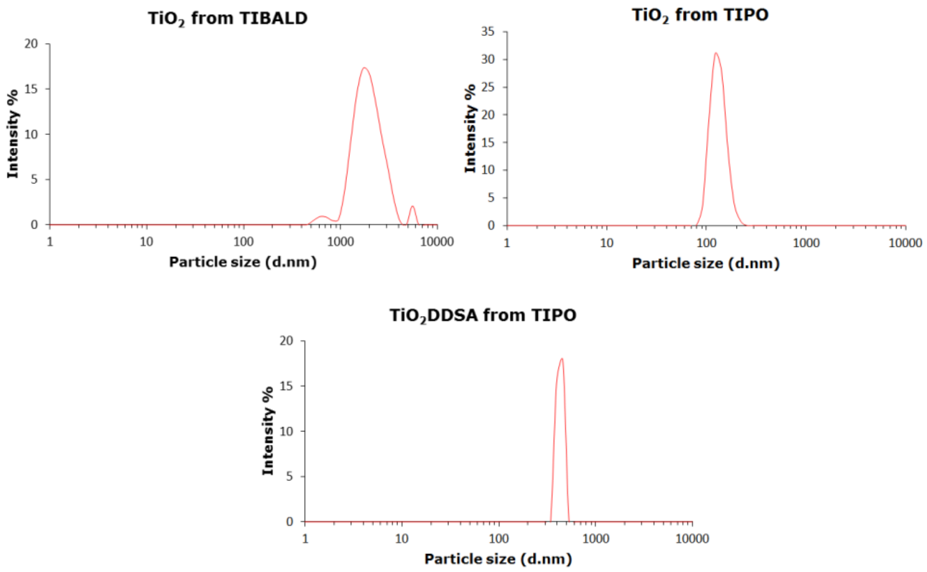

Figure 4.13 DLS results for titania samples.

4.3.1 Stability Investigations by Direct Integration into Polymers

TiO_2 NPs tend to be hydrophilic because of their polar group, for which reason they not readily interact with the organic compounds, such as polymers or organic solvents; instead they form poorly dispersed composites and unwanted large agglomerates in the polymeric matrix. It is suggested here that the TiO_2 NP modification using organic dispersants, such as DDSA, increases their affinity to the polymer and reduces the agglomeration – this is due to the steric stabilisation effect of the resultant "new" hydrophobic functionality.

The aim of this experiment was to observe whether the titania NPs could be successfully dispersed into a polymer matrix without affecting their low dimensionality (i.e. preventing agglomeration). This is the first step towards improving NP-polymer composites, which is currently one of the main aims in industry to improve products. For example, the particles must be less than 50 nm in diameter for optical applications (Holzmann et al., 2013, Liou et al., 2010). In this chapter, commercial titanium dioxide nanoparticles (P25) were compared to DDSA-modified titania obtained from CHS rig, as described in the methods (Section 4.2).

To make a comparison of the dispersion efficiency of NPs in the epoxy-nanocomposites before and after surface modification, SEM images were analysed using Image J software. SEM images previously obtained for each sample processed to a binary (black and white) threshold (example in Figure 4.14) and then the software quantified a range of particle sizes, including the agglomerates. A summary of the results corresponding to the quantified areas of free and agglomerated NPs was then obtained.

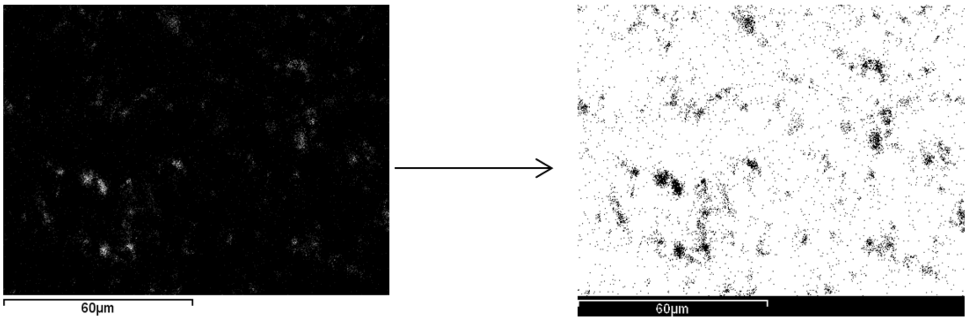

Figure 4.14 SEM map of epoxy-TiO_2DDSA 1 wt.% nanocomposites (left) converted to binary (right) in Image J.

The percentage area occupied by NP agglomerates was calculated as a proportion of the total polymer nanocomposite (PNC) area in the entire SEM image. For the three concentrations of nanoparticles used, the area occupied by the NPs was always larger when these contained DDSA (as shown in Table 4.1). This was due better dispersion of DDSA-NPs into the polymer matrix, a reduced tendency to agglomerate and, thus, occupation of a larger portion of the image. Furthermore, it is important to note that the size of the agglomerates formed was smaller than the particle sizes obtained for the unmodified P25 (Table 4.1). The individual size-distribution plots for this analysis can be found in Section II.1 (Appendix II).

Table 4.1 Agglomerate percentage area and sizes of titania dispersed in epoxy resins of different concentrations.

PNC Samples	**% Area**	**Av. Agglomerate Size (μm)**
P25_1 wt.%	8.13	1.6
TiO_2DDSA_1 wt.%	10.01	0.4
P25_5 wt.%	11.62	0.3
TiO_2DDSA_5 wt.%	13.07	0.3
P25_10 wt.%	24.28	2.5
TiO_2DDSA_10 wt.%	25.70	0.6

Figure 4.15 is an example of resin blocks loaded with (a) 1 wt.% P25 and (b) TiO_2DDSA, showing large agglomerates present with P25. EDAX (spot analysis of white agglomerates) also confirmed that these were mainly titania. Other elements were present in trace amounts, possibly a contamination from the sample preparation steps.

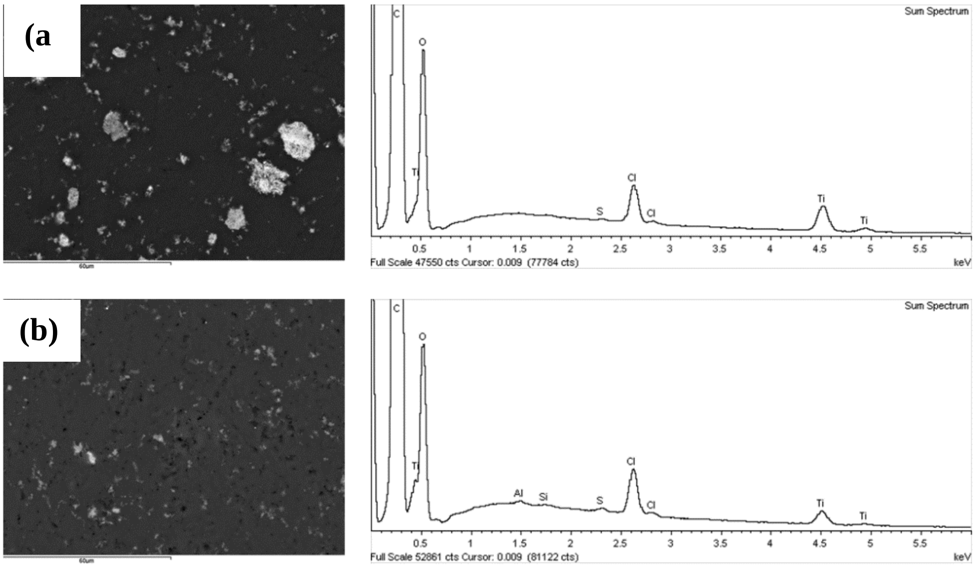

Figure 4.15 SEM micrographs of (a) P25-1 wt.% and (b) TiO_2DDSA-1 wt.% nanocomposites and their EDAX spectrum, which confirms the presence of titania.

4.3.2 Stability Evaluation using the VIS-2

In this section, observations of the stability of the four types of titania dispersions (i.e. TiO_2 from TiBALD, TiO_2 from TIPO, TiO_2DDSA from TIPO or P25) conducted by VIS-2 will be presented. This analysis was followed by in-depth studies using TiO_2 produced from TiBALD dispersions and the VIS-2. As discussed in Chapter 3, the configuration of this system allowed multiple samples to be monitored at the same time.

Figure 4.16 below shows the settling rate, measured over 10 hours, of the four types of titania. Dry P25 was dispersed in DI water, with a similar total solid content to that of TiO_2-TiBALD, and mechanically mixed for 1 hour. All the other three titania were formulated using the CHS rig, the same amounts of precursors and under similar conditions (as in Section 4.2).

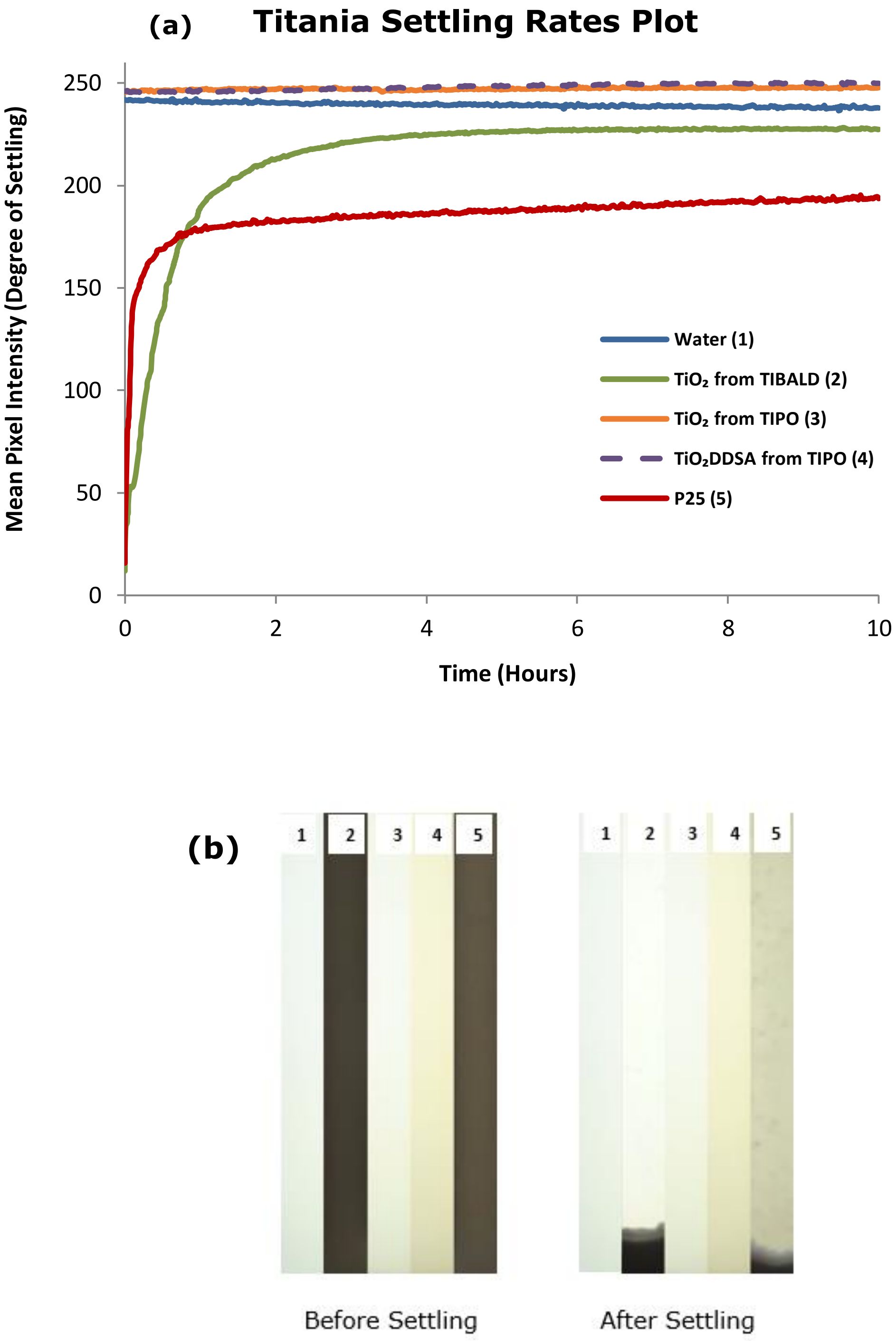

Figure 4.16 (a) Settling rate plot and (b) before and after images of the titania samples as they were loaded onto the VIS-2 setup. From left to right: water (1), TiO_2 from TiBALD (2), TiO_2 from TIPO (3), TiO_2DDSA from TIPO (4) and P25 (5).

In Figure 4.16 (a) and (b), P25 (5) was the fastest to settle (at about 0.82 hours), which may be due to its relatively larger particle size compared to other titania. TiO_2-TiBALD (2) was the next to settle, taking around 4.5 hours. TiO_2-TIPO (3) and

TiO_2DDSA produced from TIPO (4), on the other hand, were stable throughout the whole testing time – which is either attributed to their small particle size or the solvent used (IPA) making the suspension more stable compared to water. Moreover, the intensity values of the latter titania were close to that of water (1), indicating that they possess a degree of transparency as further confirmation of their stability.

Subsequently, the colloidal behaviour of the TiO_2 dispersion formulated from TiBALD was considered by varying the following parameters post-production:

- Changing the particles' surface charge (varying pH from 1-14 using buffer solutions of 1 M acetic Acid and/or 1 M NaOH);
- Increasing or decreasing the solution conductivity (varying electrolyte concentration using saturated NaCl solution);
- Adding a dispersing agent (Solplus™D540 from Lubrizol) at different concentrations (5%, 10%, 15%, 20%, 25% and 30 wt.% of TiO_2 NPs TSC %);
- Changing the mixing speed (7 manual inversions, homogenisation at 5,000 RPM and at 10,000 RPM for 5 min). The IKA T18 Digital Ultra Turrax® homogeniser was used.

The samples were then characterised according to the following parameters: pH and conductivity using a JENWAY 3540 pH and conductivity meter; zeta potential (ζ), particle size and particle size distribution using Zetasizer Nano-ZS; and settling rates using the VIS-2. All the instruments used were described in Chapter 2.

The VIS-2 image acquisition technique was used to produce the mean pixel intensity versus time plot using Matlab, conveying the sedimentation rates of TiO_2 dispersions. To achieve this, the TiO_2 dispersions were added to the cuvettes in order to monitor the settling behaviour. The filled cuvettes were then carefully placed in the provided slots in the metal guide base. Each cuvette was inverted once (in order to re-disperse the particles in solution) before it was placed into position in the metal guide. The settling of each sample was monitored, starting from the time each individual cuvette was placed into position in the metal guide; this avoided error in the recorded settling rates owing to the time taken to load all samples into position. For these studies, the Stokes equation was used to describe the relationship between average particle size and settling rate (Hunter, 2001, Cosgrove, 2010), which is given in Equation 4.1.

$$\boldsymbol{\nu = \frac{2}{9}\frac{(\rho_p - \rho_f)gr^2}{\eta}} \qquad \text{Equation 4.1}$$

where ν is the settling rate; ρ_p and ρ_f are the densities of particle and fluid respectively; g, is the acceleration due to gravity; r is the particle radius; and η is the viscosity of the fluid.

The samples were carefully introduced into the VIS-2 cuvettes to ensure, as far as possible, systematic results: the sample stock flasks were inverted twice before filling each cuvette to ensure the same solid contents in each cuvette; the 12 cuvette series were filled from left to right, ensuring the same sample level in all the cuvettes; and, finally, just before running MATLAB to capture the images, each pair of cuvettes was inverted once, as quickly as possible, from left to right and placed back in the metal guide. The glass cuvettes were 1x1 cm square in cross-section and 10 cm long, purchased from Starna Scientific.

The behaviour of the TiO_2 dispersions was studied for conventional colloid behaviour and then linked to observations of the sedimentation behaviour gained from the VIS-

2. The following section presents the results for the different TiO_2 dispersions, analysed using the VIS-2.

4.3.2.1 Studying the unmodified TiO2 dispersion

In this study, the pH, conductivity and particle size were measured and the results are shown in Table 4.2.

Table 4.2 The stabilisation study data for the unmodified TiO_2 dispersion.

pH	**Size (nm)**	**PDI**	**ζ (mV)**	**Conductivity (µs)**	**Di90 (nm)**	**Di50 (nm)**	**Di10 (nm)**
7.19	4190 ± 494.5	0.2	-13.4	3.1	3950	2850	2260

From Table 4.2, it can be seen that unmodifiedTiO_2 dispersion are of a very large mean hydrodynamic diameter (4190 nm), attributed to the agglomeration occurring at some point during or after preparation due to the low surface charge (identified by the low ζ value of -13.4 mV at pH 7.19). This facilitates van der Waals forces to hold particles together with weak bonds, reducing their diffusion speed – this results in a large hydrodynamic diameter, as measured by Zetasizer Nano-ZS (Orts-Gil et al., 2011). While the aim in high stable dispersions is to achieve highly optically transparent NP dispersions capable of maintaining stability with ageing, the lowest possible particle size in the nanometre range for high total solid contents is desired. Thus, the reported results indicate that the dispersion is unstable, which can be further confirmed by observations and destabilisation quantification using the VIS-2.

In spite of the low PdI, which indicates a narrow particle size distribution (as shown in Figure 4.17), the particles still showed undesirable agglomeration.

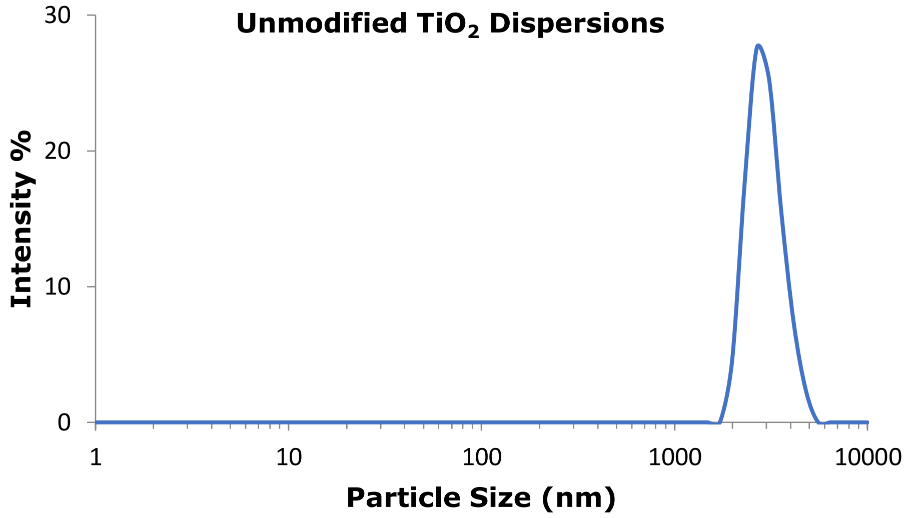

Figure 4.17 DLS readouts of particle size distribution, using intensity of scattered light, for unmodified TiO_2 dispersion. Average particle size of 4190 nm (0.2 PDI) is seen at 25°C.

Depending on the difference in densities between the particles and the dispersion medium, an unstable dispersion can demonstrate sedimentation, creaming or both – which can be due to the flocculation or coalescence of particles. These phenomena were obtained experimentally and simultaneously in previous studies by quantifying the clarity versus the extent of turbidity of a colloidal solution in terms of transmittance (transparent mediums) and the backscattering (opaque mediums) of light through a sample using Turbiscan™ instrument (Kim et al., 2014, Woo et al., 2007). The main difference between the Zetasizer Nano-ZS, instrument used for estimating colloidal stability, and the Turbiscan™ is that the latter can quantify samples without the need to dilute them (Mengual et al., 1999b). The Zetasizer Nano-ZS, on the other hand, can determine the zeta potential and estimate the surface charge of particles.

The VIS-2, meanwhile, uses image analysis to quantify the sedimentation rate of a solution by providing the mean pixel values within the ROI during a user-defined time period (as explained in Chapter 3). The images at 30 sec, 30 min, 1 h, 12 and 24 h, shown in Figure 4.18, are examples of images taken every 30 seconds for 1 day using the VIS-2; all acquired data for the unmodified TiO_2 dispersion, however, is presented in Figure 4.19. As depicted in Figure 4.19, ROI mean pixel values of all the cuvettes increased towards a higher value closer to the white pixel value (255) until a plateau was reached just after 8 h, following which no increase was observed – indicating full sedimentation occurring below the ROI value at that time. Thus, in this case, VIS-2 confirmed the presence of a clarity region in the cuvette by comparing the mean pixel value of reference cuvettes (which was 111.08 ± 0.05) and the maximum value of unmodified TiO_2 dispersion after full sedimentation (101.64 ± 2.35). This could confirm the presence of sedimentation rather than creaming, which was also visually observed in Figure 4.18. The average curve was generated to facilitate interpretation of data as the same sample was used in all cuvettes; nevertheless, the observed settling rate in cuvettes 4, 5, 6 and 7 (Figure 4.18, b) at 30 min is unexplained as it should have been the same as for the other samples.

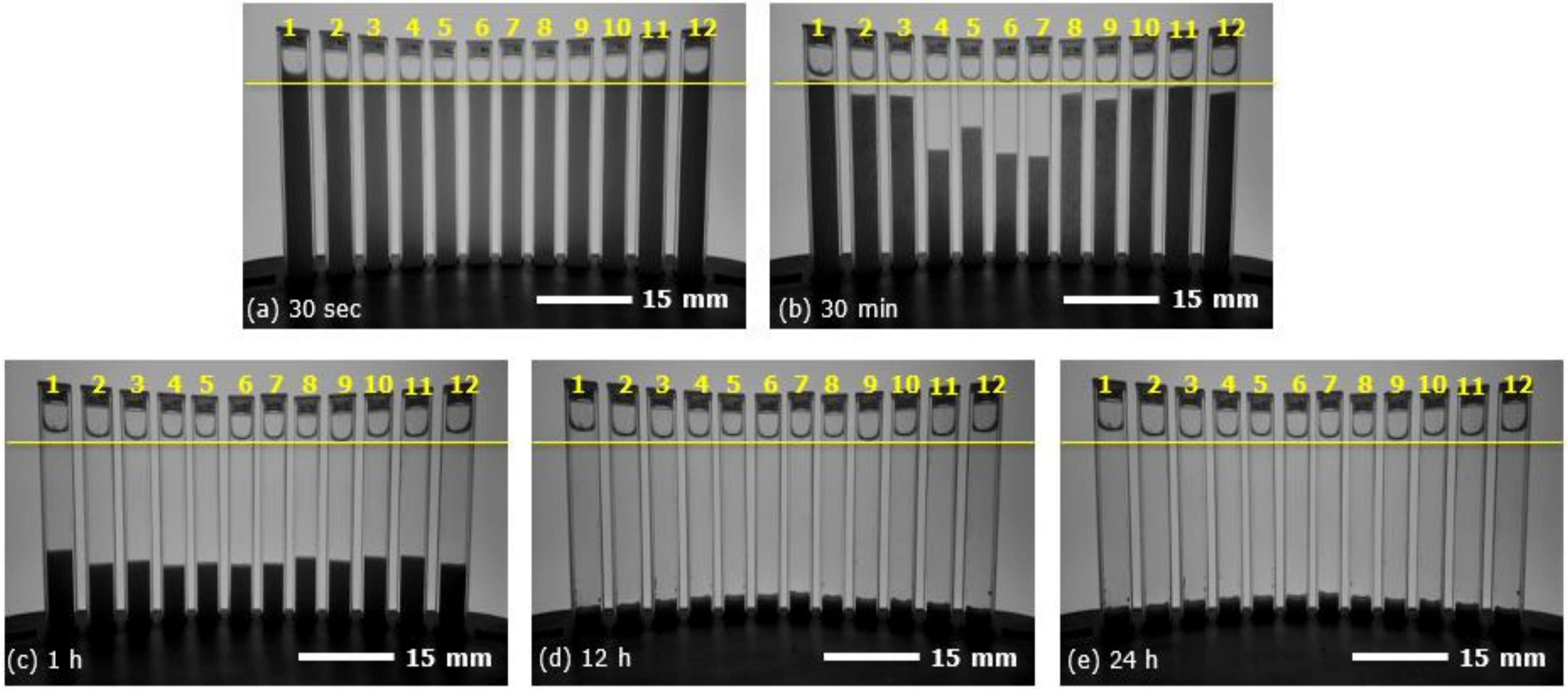

Figure 4.18 VIS-2 images of settling of unmodified TiO_2 dispersion (4190 nm average particle size, -13.4 mV ζ, pH 7.19 and 3.1 μs conductivity), where all the cuvettes were filled with the same solution for (a) 30 sec, (b) 30 min, (c) 1 h, (d) 12 h and (e) 24 h.

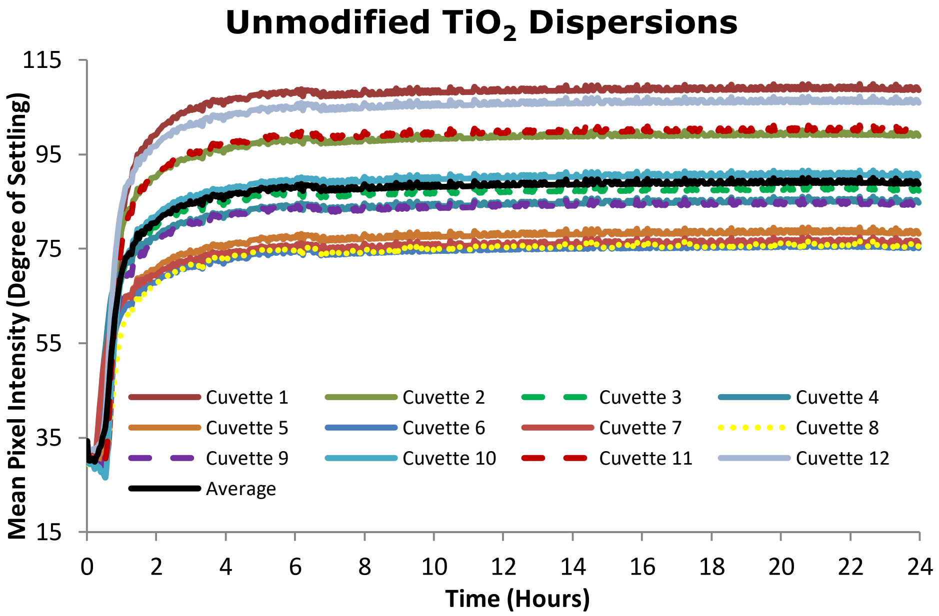

Figure 4.19 Settling rate of unmodified TiO_2 dispersion in the sample shown in Figure 4.18, obtained by recording the change in mean pixel intensity within the ROI from VIS-2 images every 30 seconds for 24 hours. The average value is represented by the black line.

Table 4.3 Settling distance (measured using ImageJ software) and change in mean pixel intensity over time for unmodified TiO_2 dispersion in 12 samples depicted in Figure 4.18.

Image no.	Time	Settling Distance from Liquid Surface/ in cm (Figure 4.18)	Mean Pixel Intensity (Figure 4.19)
1	30 sec	0	85.5
58	30 min	1.5	87.4
115	1 h	11.6	89.2
1384	12 h	15.6	105.3
2764	24 h	15.7	105.9

The values in Table 4.3 were further confirmation of the observations in Figure 4.18 and Figure 4.19. A sharp settling rate (0.856 x 10^{-3} cm/ s) could be seen in the first 30 min as a 1.54 cm distance of a clear sample was obtained. This was followed by a high increase in the sedimentation rate of up to 3.23 x 10^{-3} cm/ s in a 1 h period, which increased the distance between the original sample surface and the new nanoparticle suspension position to 11.64 cm.

The percentile values (D_i90, D_i50 and D_i10) for intensity-weighted particle size distributions are shown in Table 4.2 and represent the maximum particle size for a given intensity percentage – where D is the particle diameter; i is intensity; and 90%, 50% and 10% are the common percentiles used to describe the samples below this maximum particle size. Hence, D_i90 =3950 nm means that 90% of the sample included particle sizes below 3950 nm. In the same way, 50% of the sample contained particle sizes lower than 2850 nm and 10% of particle sizes below 2260 nm. This signifies that the particle sizes in the sample varied significantly, compared to the main particle size of 4190 nm and there was a wide particle size distribution as a result of large agglomerates or impurities.

Stokes Equation 4.1 was used to describe the sedimentation rate of the unmodified TiO_2 dispersion in water at 25 ^{o}C:

$$\boldsymbol{\nu = \frac{2}{9}\frac{(\rho_p - \rho_f)gr^2}{\eta}}$$

where $\rho_p = \rho_{\ TiO_2}$ = 4.23 g/cm^3; $\rho_f = \rho_{\ \mathrm{H_2O}}$ = 0.99704 g/cm^3; g = 980.665 cm/s^2; r^2 = (4190/2 nm)^2 = 4389025 nm^2 = 4.4 x 10^{-8} cm^2; and $\eta_{\ \mathrm{H_2O}}$ = 8.94×10^{-4} Pa. s = 8.94×10^{-4} kg/m. s = 8.94×10^{-3} g/cm.s.

Thus, from equation (1):

ν = 3.46 x 10^{-3} cm/s (average settling rate of the unmodified TiO_2 dispersion).

The settling rate calculated here is an average and not necessarily representative of all the sizes in the sample, given that the sample possessed a wide particle size distribution – each of a different velocity.

The samples remained opaque, even if highly diluted, with de-ionised water. Thus, attempts to improve the stability of the unmodified TiO_2 dispersion is discussed in the following sections.

4.3.2.2 Varying pH

To obtain the most stable system, TiO_2 dispersions were studied at different pH ranges and the sedimentation rates were observed for each pH.

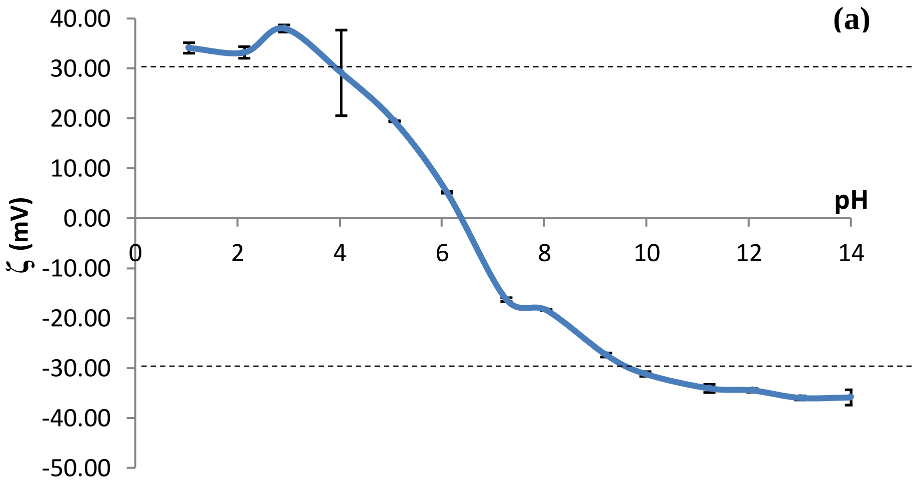

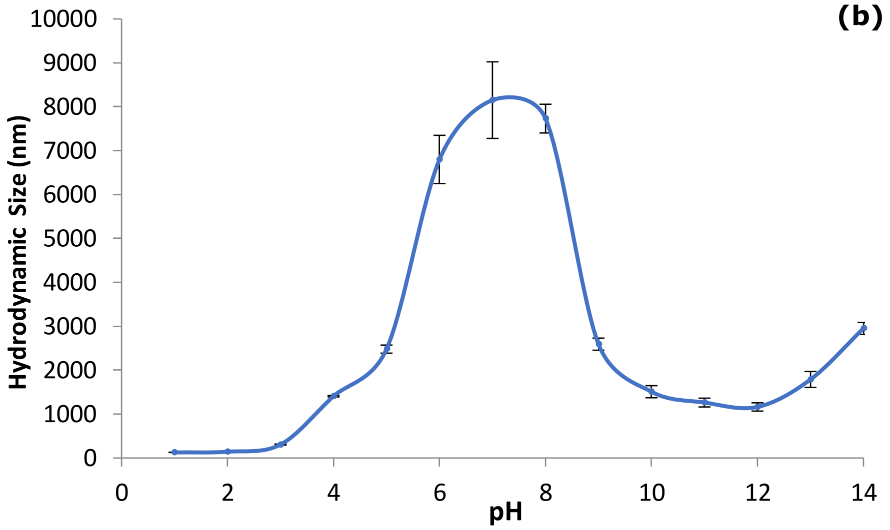

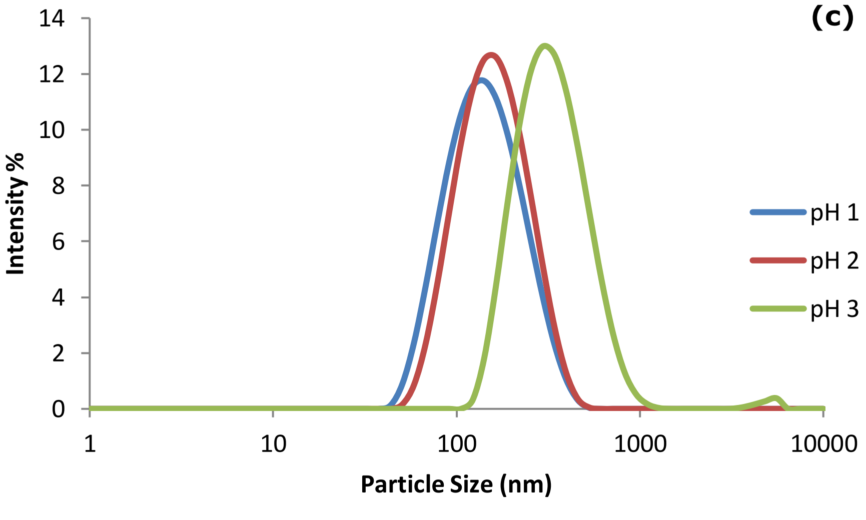

Figure 4.20 TiO_2 dispersions at pH 1-14 pH: (a) zeta potential values (the dotted lines bonded the most instable region), (b) hydrodynamic size distribution, and (c) particle size distribution of the most stable systems (i.e. at pH 1, 2 and 3).

Table 4.4 Stabilisation data of TiO_2 dispersions at varying pH.

Sample pH	**Size (nm)**	**PdI**	**ζ (mV)**	**Conductivity (µs)**	**Di90**	**Di50**	**Di10**
pH 1	127.4 ± 1.5	0.179	34.10	49.7	261	63.4	54
pH 2	143.5 ± 7	0.166	33.20	8.1	278	74.4	63.5
pH 3	306.7 ± 12.2	0.168	38.00	2.8	585	170	187
pH 4	1408 ± 16.1	0.205	29.10	2.3	2250	1350	1260
pH 5	2480 ± 91.7	0.176	19.40	3.0	3280	2190	1820
pH 6	6800 ± 549.6	0.188	5.18	3.5	5950	2230	1680
pH 7	8151 ± 872	0.435	-16.30	2.9	11200	4730	1.86
pH 8	7730 ± 327	0.213	-18.40	2.8	6230	4950	4560
pH 9	2593 ± 138.2	0.404	-27.40	2.8	2440	1580	1310
pH 10	1510 ± 137.6	0.391	-31.20	2.8	2810	1180	1490
pH 11	1263 ± 100.4	0.287	-34.10	2.8	2220	1080	1190
pH 12	116 ± 94.2	0.291	-34.50	3.1	2670	954	1370
pH 13	1788 ± 181.7	0.404	-36.00	5.2	2610	1350	1310
pH 14	2952 ± 137.1	0.725	-35.90	33.8	3030	2330	1890

The pH experiment results in Figure 4.20, a and Table 4.4 showed that the point of zero charge for TiO_2 NPs occurred at a a solution isoelectric point (IEP) of pH_{IEP} 6.6, which, as expected, lay within the pH_{IEP} 5-7 range reported for the TiO_2 NPs in aqueous solution (Fazio et al., 2008, Halmann, 1996). As confirmed by the ζ values in Figure 4.20 (a), the TiO_2 NPs surface charge changed to positive in acidic solutions with a pH lower than pH_{IEP} 6.6; the positive surface charge concentration increased gradually with increasing pH – except for the solution at pH 3, where a jump in the ζ value was observed. This was likely due to an experimental error. Conversely, a more negative TiO_2 NPs surface charge was obtained at pH> pH_{IEP} due to an increase in the dispersion's alkalinity by addition of a strong base (NaOH). Similarly, a gradual increase in the absolute ζ value with increasing pH was observed, with no significant difference in the last four pH values (Ahmad et al., 2014), (Vicent et al., 2011). Starting from the unmodified TiO_2 dispersion of a negative surface charge, as described in Section 4.3.2.1, the addition of concentrated acid neutralised the TiO_2 NPs surface charge, decreasing the solution pH until 1. At this point, a high surface positive charge was obtained. On the other hand, an increase in the initial negative surface charge concentration was seen with increasing pH of the TiO_2 dispersion. The lowest average particle size (127.4 ± 1.5 nm) was achieved at pH 1 (Figure 4.20, b and Table 4.4), followed by a slight increase in the average size at pH 2-3. This was followed by a sharp increase at pH 4, which became more gradual at subsequent pH values. The highest particle average sizes were obtained in the IEP region (pH 6-8), indicating the formation of large agglomerates with an average hydrodynamic size even larger than the particle size of the unmodified TiO_2 dispersion. This confirmed the fact that the system is of lowest stability at, and close to, the pH_{IEP} (Taguchi et al., 2011). The particle size distribution for the dispersions at pH 1, 2 and 3 of average particle sizes of 127.4 ± 1.5 nm, 143.5 ± 7 nm and 306.7 ± 12.2 nm, respectively, showed a narrow intensity distribution with the most average size values at about 261 nm, 278 nm and 585 nm for pH 1, 2 and 3 respectively (Figure 4.20, c and Table 4.4).

It is accepted that the ζ of values of ±30 and above indicate a stable suspension that does not agglomerate or sediment. As depicted in Figure 4.20 (a), the higher the pH, the more negative the ζ values and these were maintained here at about -34 ±2 mV at pH 10-14. Moreover, the closer the pH to the isoelectric point, the lower the absolute ζ values. Accordingly, the decrease in the average particle sizes of the unmodified TiO_2 dispersion at pH 1, 2 and 3 (from an initial 4190 nm) was attributed to the increase in ζ values – i.e. the particle surface charge increased, which in turn enhanced its repulsive force to dominate over van der Waals attractive forces, thereby preventing agglomeration.

The stability of the system was further assessed using VIS-2 and the sedimentation rates were quantified along using the Stokes equation to confirm that the VIS-2 correctly reflected the system behaviour shown from DLS results. A combination of images and digital settling rate data acquired directly from automated image analysis was necessary to demonstrate the VIS-2 application. As can be seen in the set of images in Figure 4.21 (b), the least stable systems were in the middle five cuvettes at pH 5, 6, 7, 8 and 9 and these quickly sedimented after 30 minutes. The settling rate for all pH values was quantified in Figure 4.22 by determining ROI mean pixel values every 30 seconds. The ROI showed an initial value of 60 for all pH ranges, following which this value increased towards the brighter pixel values. For pH 5, 6, 7, 8 and 9, the ROI mean pixel values similarly increased to 100, 93, 91.5,93 and 92 at 30 min and 97, 92, 96, 97 and 94.5 at 24 hours – indicating a very fast sedimentation in the 5-9 pH range. Complete settling was observed before the 30 min mark, as no change in the ROI values occurred after this time. The settling rates, calculated using the Stokes equation, were also the highest at pH 5-9 pH (Table 4.5) – consistent with the VIS-2 and DLS stability results. Conversely, at pH 1-2, the VIS-2 mean pixel intensity data

(Figure 4.22) showed that the ROI values remained close to the dark value, indicating that the NPs remained stable and did not sediment during the 24-hour period. The settling rates of these were the lowest at 3.20×10^{-6} cm/ s and 4.06×10^{-6} cm/ s. Conversely, at pH 11-12, the systems remained stable for up to 8 hours, displaying fairly constant ROI values, until the beginning of sedimentation after 12 hours and a resultant increase in ROI values.

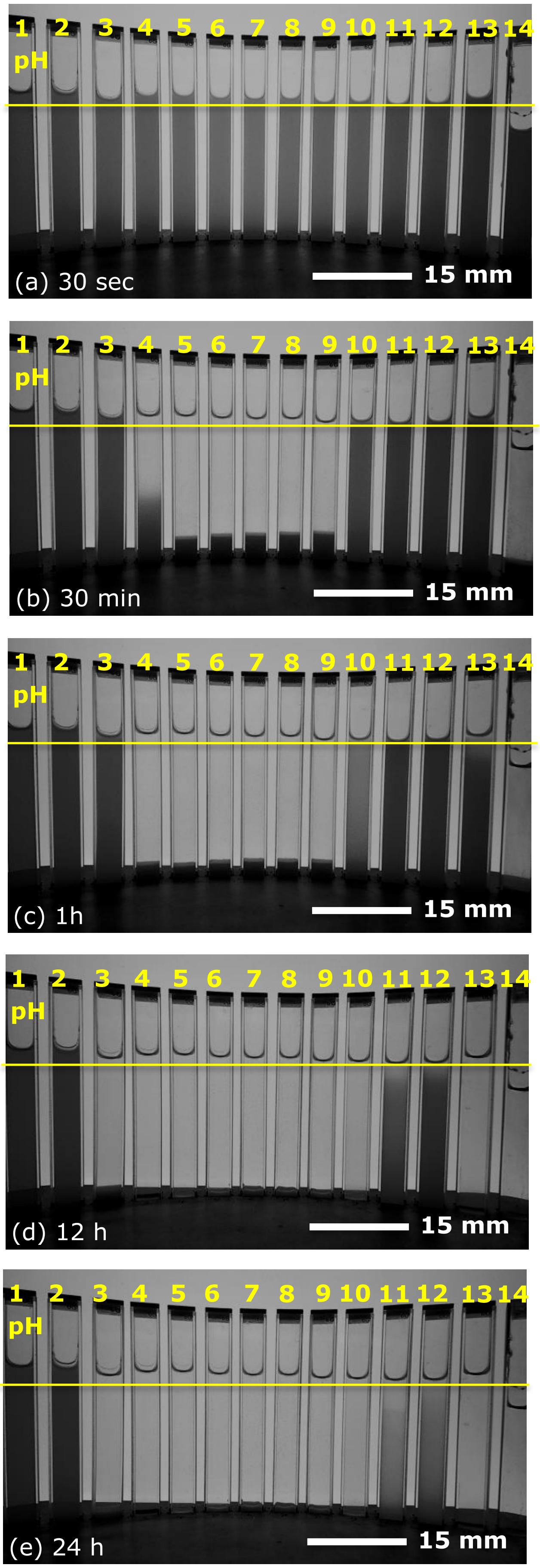

Figure 4.21 The VIS-2 images of TiO_2 dispersion settling at varying pH (pH 1-14 from left to right), after (a) 30 sec, (b) 30min, (c) 1h, (d) 12 h and (e) 24 h.

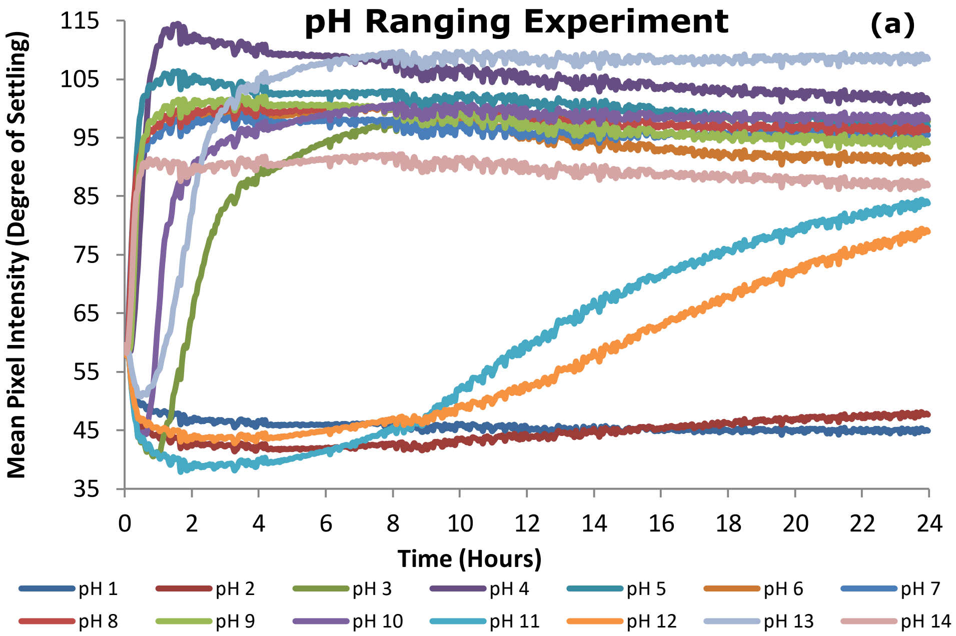

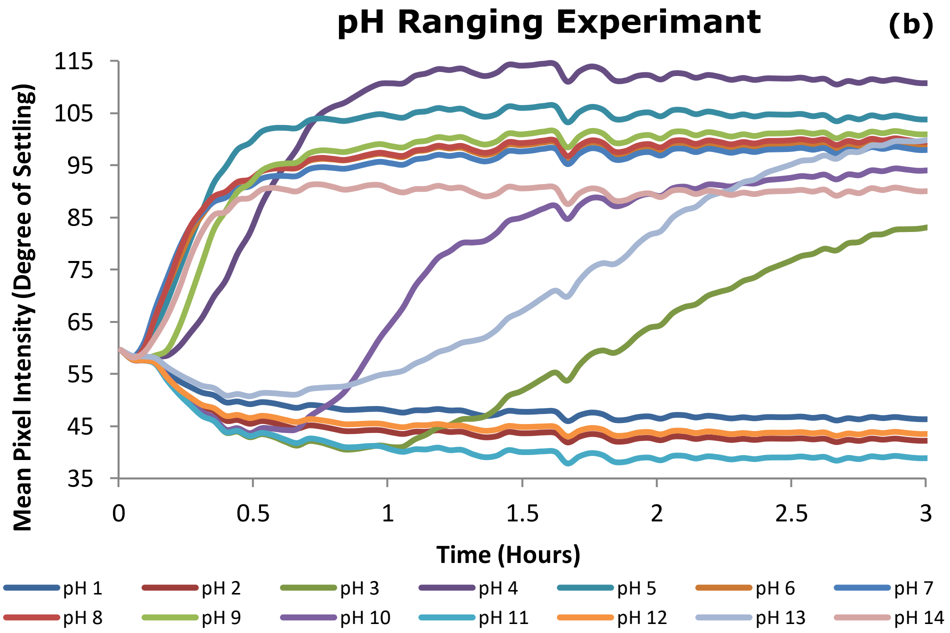

Figure 4.22 The VIS-2 settling rate of the unmodified TiO_2 dispersion at varying pH (a) within 24 hours and (b) within 3 hours.

Table 4.5 Settling rates in each cuvette in Figure 4.21 were obtained by applying Stokes Law to the TiO_2 dispersions at varied pH.

Sample pH	**Size (nm)**	**Size (cm)**	**r^2 (cm^2)**	**ν (cm/ s)**
pH 1	127.4	0.00001274	4.05769×10^{-11}	3.20×10^{-6}
pH 2	143.5	0.00001435	5.14806×10^{-11}	4.06×10^{-6}
pH 3	306.7	0.00003067	2.35162×10^{-10}	18.54×10^{-6}
pH 4	1408	0.0001408	4.95616×10^{-9}	3.90×10^{-4}
pH 5	2480	0.000248	1.5376×10^{-8}	12.12×10^{-4}
pH 6	6800	0.00068	1.156×10^{-7}	9.12×10^{-3}
pH 7	8151	0.0008151	1.66097×10^{-7}	13.08×10^{-3}
pH 8	7730	0.000773	1.49382×10^{-7}	11.78×10^{-3}
pH 9	2593	0.0002593	1.68091×10^{-8}	13.24×10^{-4}
pH 10	1510	0.000151	5.70025×10^{-9}	4.50×10^{-4}
pH 11	1263	0.0001263	3.98792×10^{-9}	3.14×10^{-4}
pH 12	1163	0.0001163	3.38142×10^{-9}	2.66×10^{-4}
pH 13	1788	0.0001788	7.99236×10^{-9}	6.30×10^{-4}
pH 14	2952	0.0002952	2.17858×10^{-8}	17.16×10^{-4}

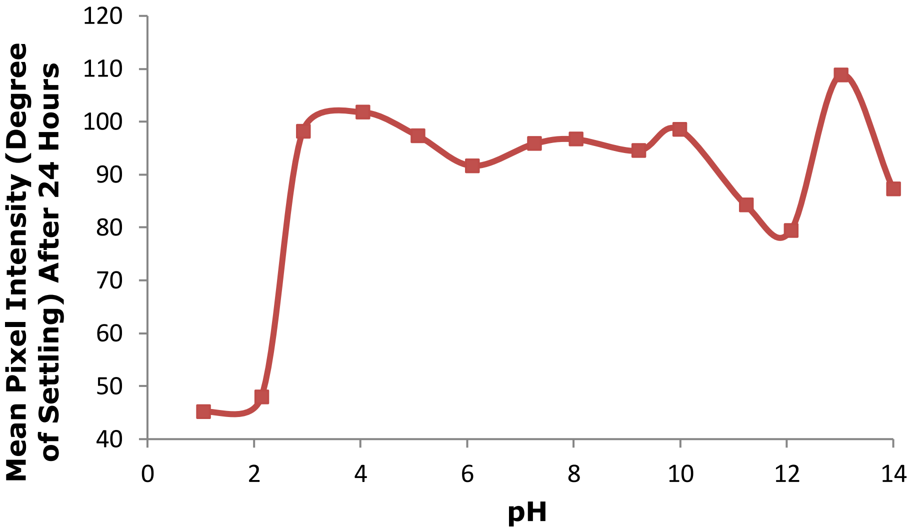

Figure 4.23 The mean pixel intensity of TiO_2 dispersions at varying pH obtained within 24 hours.

An example for the time-dependent change in settling rates with changing pH is shown in Figure 4.23.

Notably, UV-visible spectrophotometry was previously used to quantify the sedimentation rates for similar dispersion stability studies, by measuring the change in transmitted light with time (Mudunkotuwa and Grassian, 2010). However, as only one beam of incident light is introduced to the sample in this case, only one area of the sample was monitored. This may not be a reliable way of characterising system behaviour; in contrast, the VIS-2 is able to show a full image and quantify full system behaviour with time. For example, here the VIS-2 revealed system instability at pH 14 in less than 30 minutes, which may not be readily known from only the ζ value – unless other parameters, such as conductivity, are known.

4.3.2.3 Varying conductivity

The effect of changing the ionic strength of the sample was taken into consideration for the colloidal study and the results are shown in Figure 4.24 and Table 4.6 below.

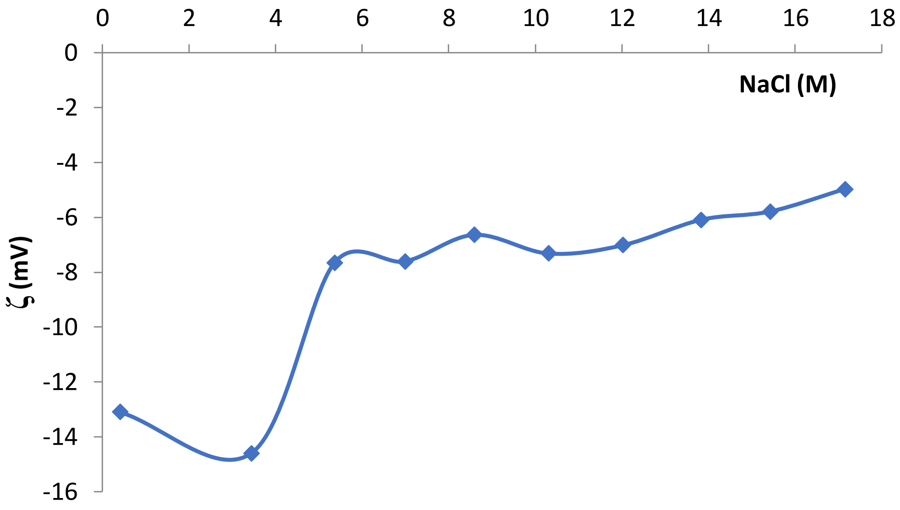

Figure 4.24 TiO_2 dispersions of varied electrolyte concentrations.

Figure 4.24 shows a general trend of increasing ζ with increasing electrolyte (NaCl) concentration, although there was an unexplained decrease in this value at several points. The more salt added, the lower the resulting surface charge was observed and this is due to electrostatic stabilisation. Primarily, all the obtained ζ values indicated that the system was not stable with all the tested electrolyte concentrations. However, the most stable sample was at ζ of -14.6 mV at 3.44 M NaCl. The data obtained is provided in Table 4.6.

Table 4.6 Stability of TiO_2 dispersions at varying electrolyte concentrations.

Sample NaCl concⁿ (M)	Size (nm)	PDI	ζ (mV)	Conductivity (µs)
0.41	7958	0.690	-13.1	12.0
3.44	5214	0.684	-14.6	60.2
5.36	5107	0.747	-7.67	81.0
6.98	6445	0.824	-7.61	94.0
8.59	4998	0.336	-6.64	107.2
10.30	3521	0.559	-7.32	116.6
12.01	5784	0.362	-7.02	121.0
13.83	6513	0.198	-6.09	133.0
15.42	5896	0.298	-5.79	138.9
17.15	4212	0.389	-4.97	122.1

There was no change in the pH value with any electrolyte concentrations, which remained equal to the pH of the unmodified TiO_2 dispersion (pH 7.2). The increase in conductivity confirmed the increase of the dispersion's ionic strength with increasing electrolyte concentration, while a fluctuation in the zeta potential value was observed; the largest values were recorded for the lowest conductivity, as illustrated in Table 4.6.

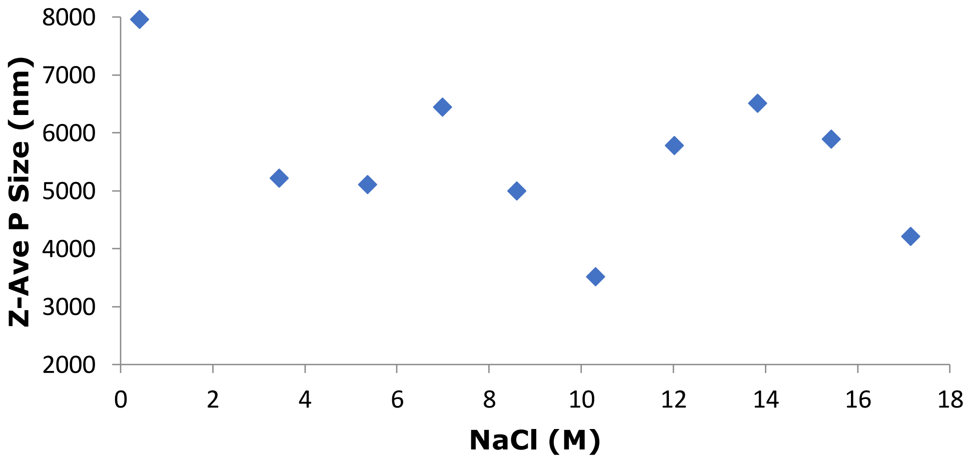

Figure 4.25 Particle size distribution at different electrolyte concentrations.

The maximum particle size (7958 nm) was obtained at the lowest electrolyte concentration (0.41 M), while the lowest particle size (3521 nm) was obtained at 10.3 M NaCl concentration (Figure 4.25). Only small changes in particle sizes were shown, with a deviation of 17.4 %. Ideally, increasing conductivity will decrease zeta potential by screening out the particle surface charge and prevent a repulsive force between particles – which would in turn promote agglomerates. Thus, accurate zeta potential measurements would be difficult due to the increase in conductivity inhibiting the electrophoretic mobility of particles, as demonstrated by the Smoluchowski approximation.

It was demonstrated in several studies that increasing the ionic strength of aqueous TiO_2 NP dispersions both decreases the zeta potential and the double layer thickness around the particle surface, thus increasing the mean hydrodynamic size of diffused particles (Jiang et al., 2009, Suttiponparnit et al., 2011). However, the results in Table 4.6 and Figure 4.25 showed the opposite situation. The theoretical assumption behind the phenomenon of obtaining the largest average particle size when the ionic strength is the lowest (at 0.41 M NaCl concentration) is that this size may be the product of several NPs that possess larger double layer thickness and are agglomerated together (as illustrated in Figure 4.26, a (left)).

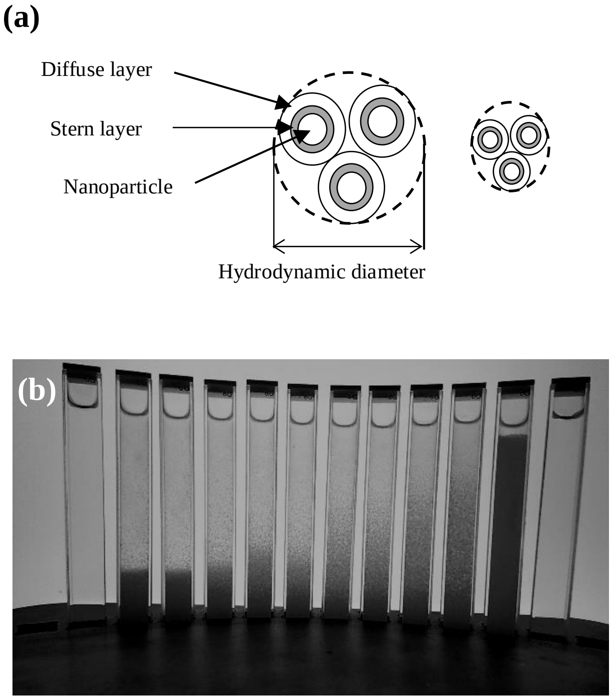

Figure 4.26 (a) Large and small nanoparticle agglomerations; (b) the VIS-2 image of addition of electrolytes at increasing concentrations, from left to right, within 30 min.

The VIS-2 image (Figure 4.26, b) shows a reasonable sedimentation rate with increasing average particle size. However, this contradicts the fact that increasing the solution ionic strength (with electrolytes) leads to an unstable dispersion; the sedimentation rate results were, therefore, not included in this section subject to further investigations.

The unstable system obtained here is because the TiO_2 dispersions were produced at high temperature and high shear which results in a low-quality and agglomerated product. Thus, increasing the ionic strength of the solution has little effect. It is also worth noting that not all the changes in this system could be accurately measured as the Zetasizer Nano-ZS instrument can only measure particle sizes up to 10 microns.

4.3.2.4 Adding a stabilising agent at varying mixing speed

Despite the fact that TiO_2 NPs are hydrophilic due to polar surface groups (which enables them to finely disperse in water), the large agglomerates obtained through the production process made it necessary to examine another approach to stabilising the solution and minimising the sedimentation rate. Thus, to develop the dispersion, the dispersions were stabilised using Solplus™D540 to eliminate particle agglomeration using steric stabilisation. Figure 4.27 shows the TiO_2 NP sizes (obtained using DLS) with added stabiliser at different concentrations and mixing speeds. In general, the most stable situation was achieved using a 10,000 RPM homogenisation system. This may have attributed to the brake in agglomeration by the vigorous mixing speed, allowing more stabiliser to attach at the particle surface. At this speed, the most stable sample was at 30 wt.% Solplus™D540 of the lowest particle size (449.4 nm) as it showed the largest absolute ζ value (26.9 mV) for the 30 wt.% stabiliser. However, a larger ζ value (-28.4 mV) was obtained using the inversion mixing system at 25 wt.% dispersant (Figure 4.28). The maximum particle size (2788 nm), achieved using inversion at 5 wt.% dispersant, was lower than the particle size of the unmodified TiO2 dispersion (4190 nm).

This was confirmed by comparing ROI values using the VIS-2 system and comparing settling rates between mixing methods (Figures 4.30, 4.32 and 4.34). The results demonstrated that the 10,000 RPM homogenisation achieved the slowest sedimentation rate, especially with added 30 wt.% Solplus™D540. The slower the sedimentation rate, the more stable is the sample.

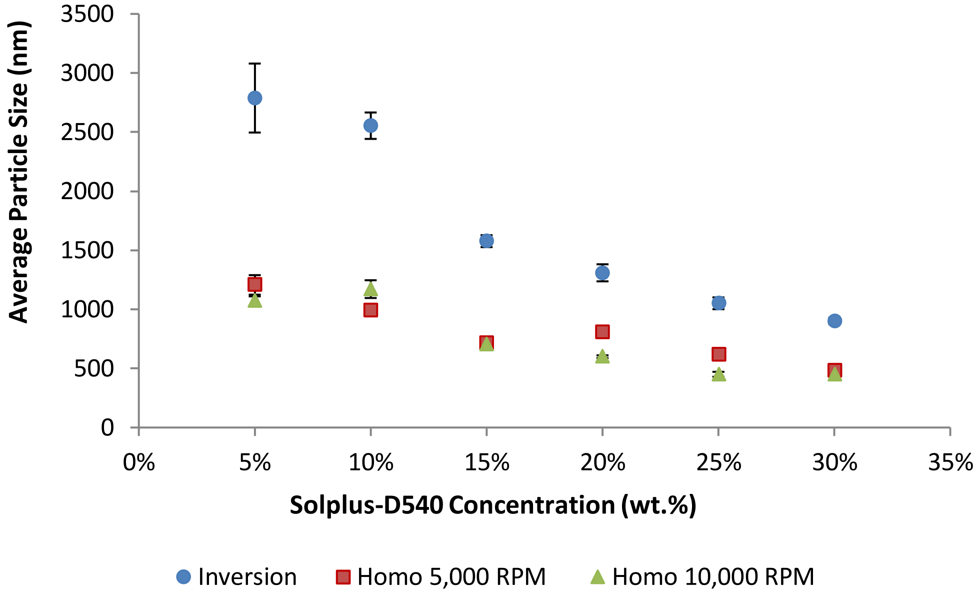

Figure 4.27 Particle size distribution of TiO_2 dispersions mixed using different methods with different added stabiliser concentrations.

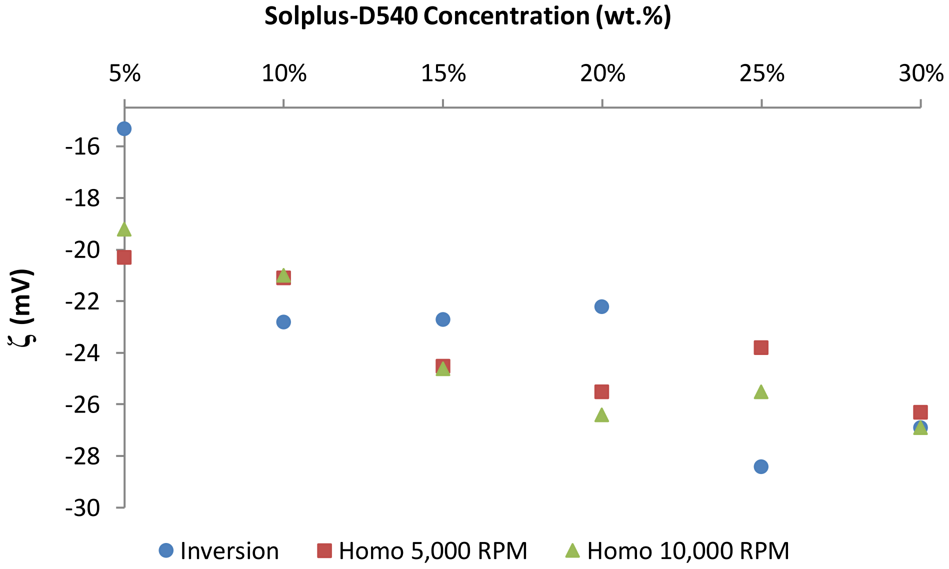

Figure 4.28 Zeta potential of TiO_2 dispersions at varied stabiliser concentrations and under different mixing conditions, showing a slight effect of varying mixing speeds on the ζ values.

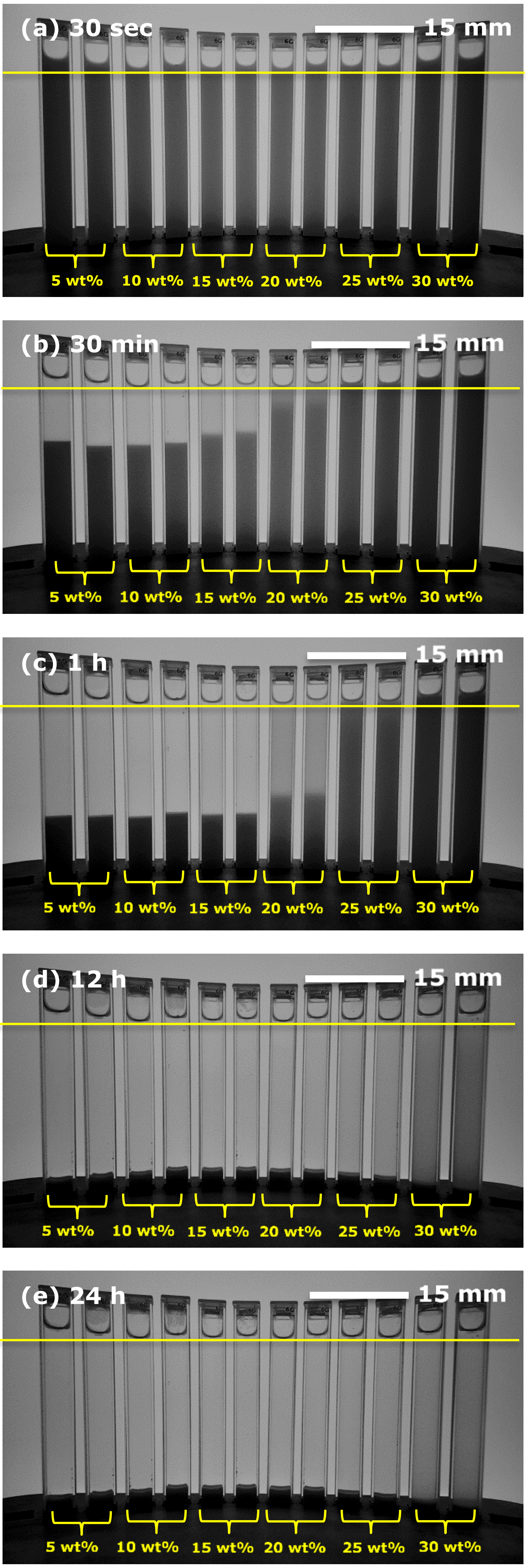

Figure 4.29 Inversion experiment: VIS-2 images of TiO_2 dispersion settling at varied Solplus-D540 concentrations (5, 10, 15, 20, 25 and 30) wt.% for each pair of cuvettes from, left to right, within (a) 30 sec, (b) 30 min, (c) 1 h, (d) 12 h and (e) 24 h.

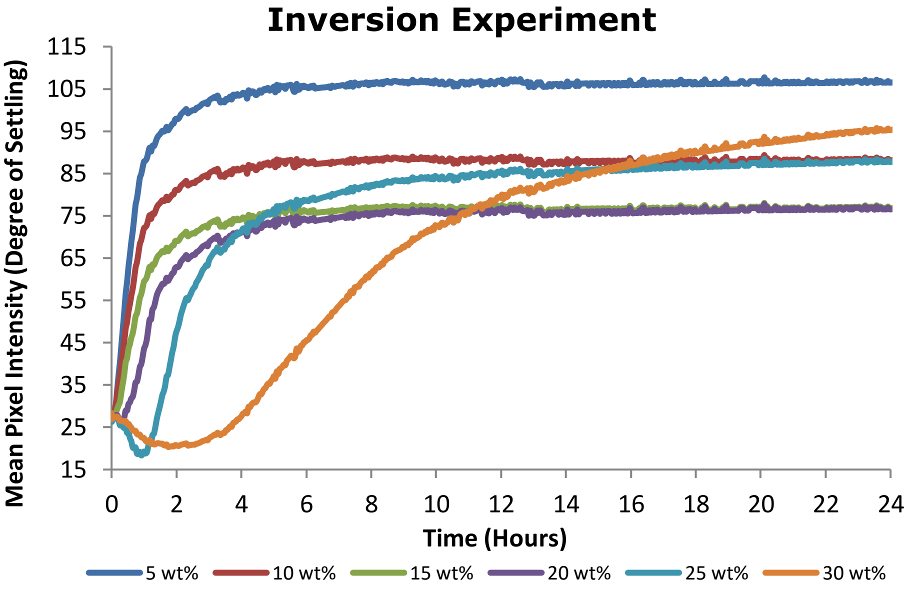

Figure 4.30 VIS-2 settling data plot for inversion experiments at different stabiliser concentrations.

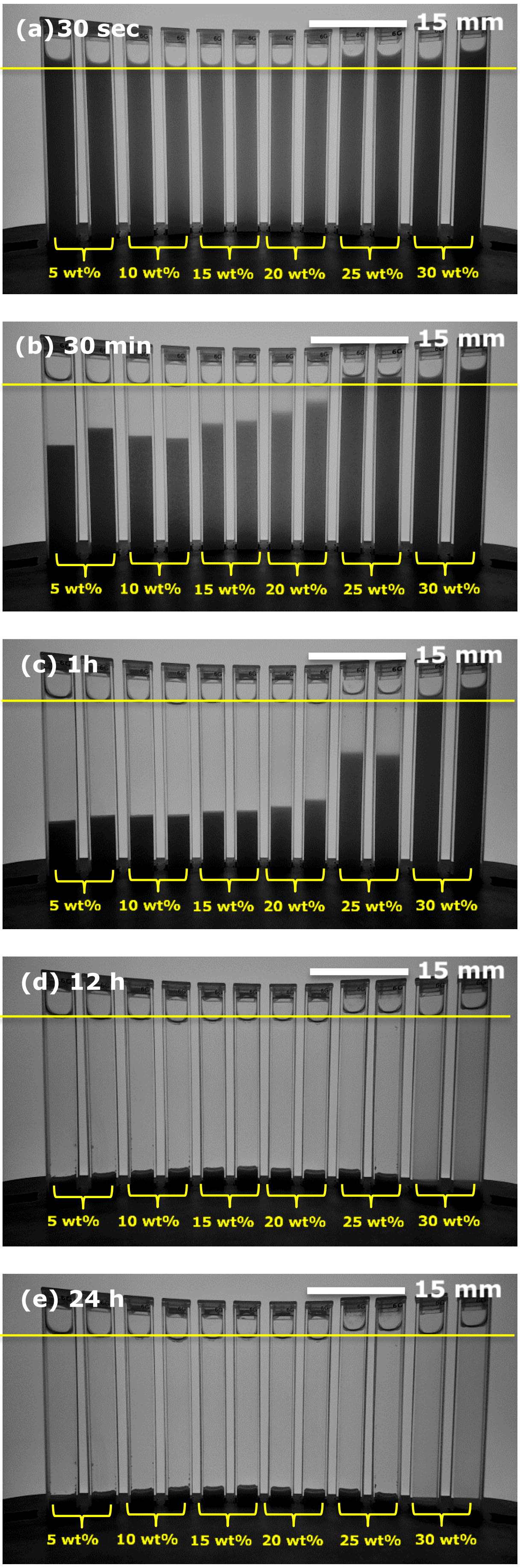

Figure 4.31 (5,000 RPM) Homogenising experiment: VIS-2 images of TiO_2 dispersion settling at varied Solplus-D540 concentrations (5, 10, 15, 20, 25 and 30) wt.% for each pair of cuvettes from left to right, within (a) 30 sec, (b) 30 min, (c) 1h, (d) 12 h and (e) 24 h.

With 5,000 RPM homogenisation speed, the 30 wt.% stabilised dispersion showed the least sedimentation, remaining fairly constant at the lowest mean pixel values for 1.5 hours (Figure 4.32).

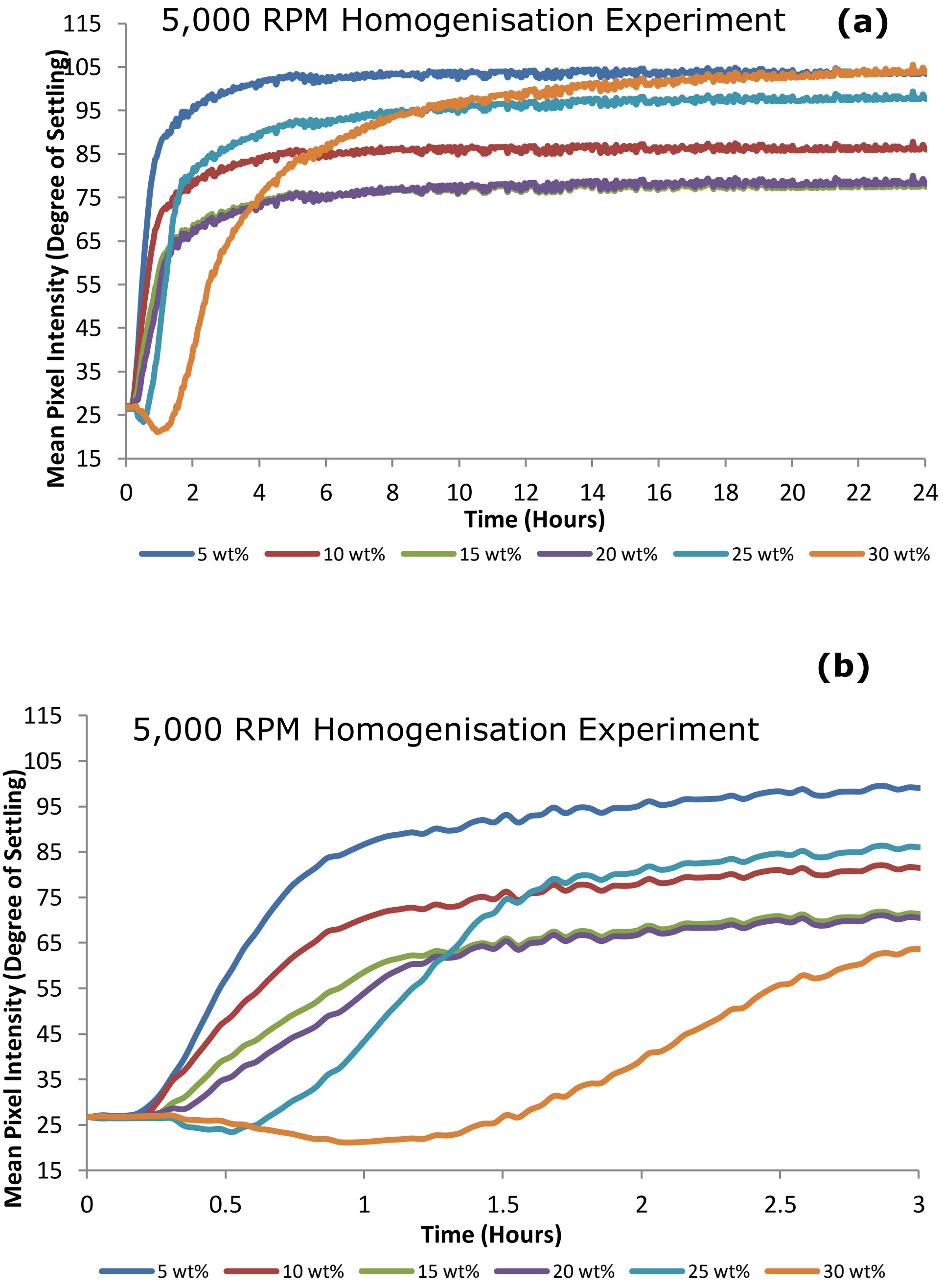

Figure 4.32 The VIS-2 plot for 5,000 RPM homogenisation at different stabiliser concentrations within (a) 24 hours and (b) during 3 hours.

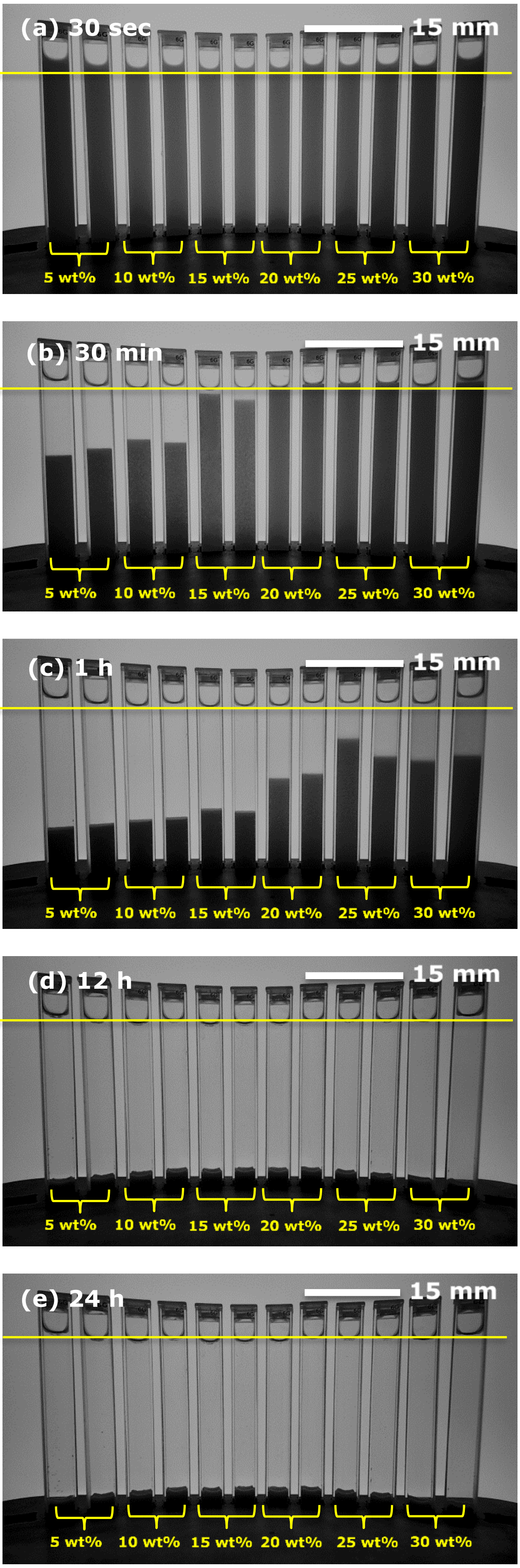

Figure 4.33 (10,000 RPM) Homogenisation experiment: The VIS-2 images of TiO_2 dispersion settling at varying Solplus-D540 concentrations (5, 10, 15, 20, 25 and 30) wt.% for each pair of cuvettes, from left to right, within (a) 30 sec, (b) 30 min, (c) 1h, (d) 12 h and (e) 24 h.

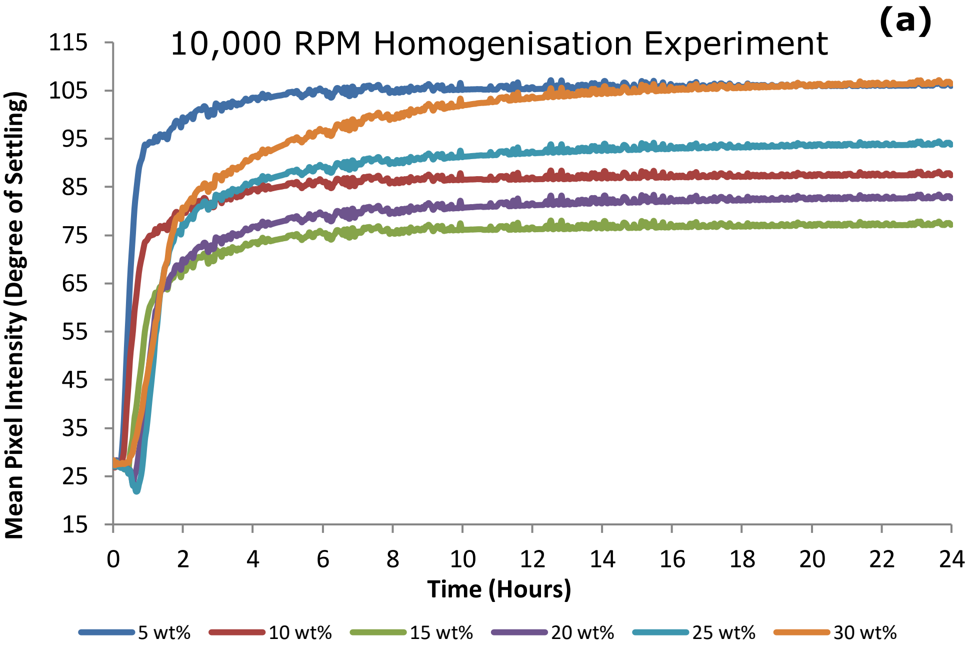

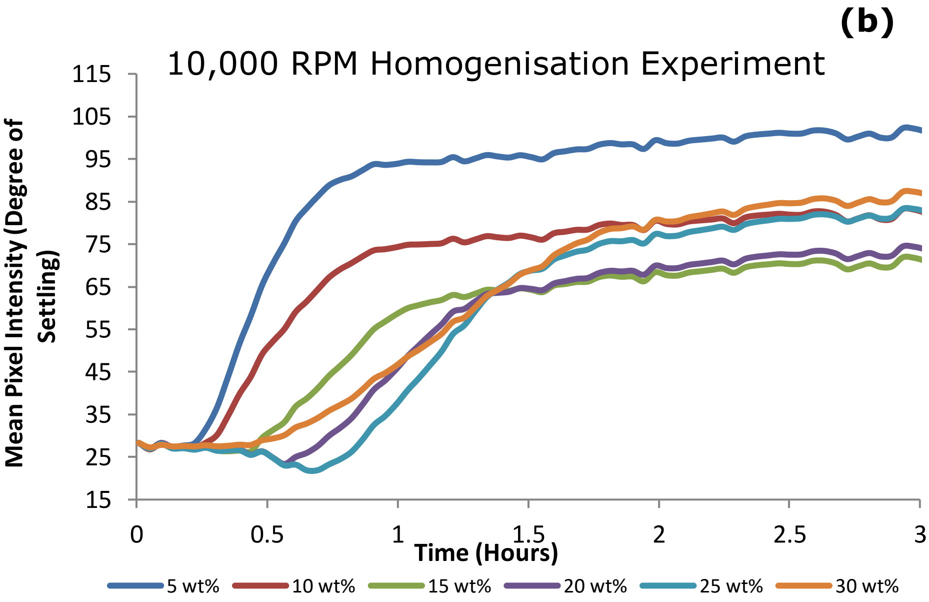

Figure 4.34 The VIS-2 settling rates data after 10,000 RPM homogenisation and at different stabiliser concentrations within (a) 24 hours and (b) 3 hours.

At 10,000 RPM mixing speed, the sedimentation rates were decreased with 15 wt.%, 20 wt.%, 25 wt.% and 30 wt.% stabiliser added.

4.4 Conclusions

Attempting to directly disperse nanosuspension systems into a polymer matrix, even with previous knowledge of particle size, led to some unsuccessful nanocomposites with poor nanoparticle dispersibility. This inspired the development of an efficient method of testing the stability of dispersions before proceeding with polymerisation. Not only does this save time, effort and cost, it is also good for the environment as it prevents disposal of waste and unsuitable materials. The VIS-2, used here, was shown to be a fast and cost-effective method for this purpose by quantifying different NP dispersions.

The four types of titania showed different settling behaviours, despite the fact that they all were all formulated the same way (similarly to the total solid content of P25); this can be explained by the difference in the precursors from which the materials were made of. TiO_2DDSA produced from TIPO showed high stability (Figure 4.16) and was better dispersed into epoxy (Figure 4.15) compared to the unmodified TiO_2 dispersion; nevertheless, it showed larger agglomerates (400 nm from SEM for the 1wt.% concentration) in its dry form (with epoxy) compared to its wet form (~7 nm from TEM), as confirmed with VIS-2.

Unmodified TiO_2 dispersions produced from TiBALD showed large agglomerates of 4190 nm particle size (from DLS technique) that caused instability and sedimentation in a short time. Consequently, the colloidal behaviour of aqueous TiO_2- TiBALD was quantified with varying pH values and conductivity; and also, by adding hydrophilic stabiliser at different concentrations and employing different mixing speeds.

From the pH 1-14 experiments, the most stable TiO_2 dispersions was obtained in the most acidic samples (pH 1 and 2) without any stabiliser, followed by the most basic samples (pH 11 and 12) – with the largest settling rate of 13.1 x 10^{-3} (cm/ s) obtained at pH 7, as per the Stokes equation. The use of a stabiliser agent and 10,000 homogenisation speed minimised nanoparticle size in the unmodified TiO_2 dispersion; the most stable sample was at 30 wt.% Solplus™D540, with the lowest particle size (449.4 nm) and the largest ζ value (-26.9 mV). This signified improved stability from the unmodified TiO_2 dispersion.

Chapter 5: Evaluating Stability and Different Physical Properties of Iron Oxide Dispersions using the VIS-3

5.1 Introduction

This chapter investigates the stability of different iron oxide dispersions and whether it is possible to differentiate between some materials, by exploiting some visual properties they possess such as colour and transparency, using the VIS-3.

Iron oxides dispersions tested in this thesis are formulated using continuous near-critical and supercritical hydrothermal conditions under a pressure of 240 bar. The dispersion properties were investigated by varying the composition and concentration of the starting materials and the process conditions. Two precursors were used, namely iron (III) nitrate nonahydrate at a fixed concentration (0.05 M) under varied temperatures (200, 300 and 400 °C) and ammonium iron (III) citrate at different concentrations (0.025, 0.05, 0.1, 0.2 M) and a fixed temperature (400 °C).

Although the main iron oxide phase to be produced from iron (III) nitrate under similar conditions is hematite, other iron oxide phases (e.g. magnetite, maghemite and ferrihydrite) might be present as by-products (de Tercero et al., 2014). Similarly, by using the same method and ammonium iron (III) citrate as a precursor, magnetite is the main iron oxide phase but might not be the only one in the resulted dispersion (Andersen et al., 2014, Jensen et al., 2014, Park, 2009). In addition, maghemite and magnetite are sometimes confused with each other in XRD results and need accurate techniques to confirm their presence as the main phases or by-product. This clarification is important because each phase might affect the dispersion properties differently. The phases are usually characterised by their crystal structures using XRD and Raman spectroscopy. Although XRD is a good tool to analyse hematite, it is not recommended for some other phases because magnetite and maghemite produce identical diffraction patterns. However, with Raman or Mössbauer spectroscopy, the latter two phases are distinguishable. It is worth noting that phase transitions likely occur during the drying process (e.g. by air- drying, freeze- drying or oven drying) in the preparation steps for characterisation using the above-mentioned methods.

5.1.1 The Functionality of the Iron Oxides

Iron oxide is a functional material selected to fulfil a specific function based on its catalytic properties (Schwartz, 1980). Over the years, and mainly in recent decades, applications have multiplied to include pigments and environmental adsorbents.

This situation has driven the development of various synthesis routes that allow the obtaining of controlled products tailored from other oxides and oxalic precursors by the hydrolysis of iron salts and the decomposition of chelates (Udo Schwertmann, 1991). Most often, the hydrolysis pathway is followed to obtain several forms of iron oxide.

The first form is FeO, which is an unsteady pyrophoric amalgam. This amalgam then transforms to Fe and Fe_3O_4. The structure of FeO is rock-salt type, meaning that iron atoms are octahedrally coordinated by oxygen atoms and vice versa (Acevedo-Sandoval et al., 2004).

The second form is magnetite. Magnetite (Fe_3O_4) is known as tri-iron tetroxide or ferric ferrous oxide and has a black colour. Its chemical formula can also be expressed as $Fe^{II}Fe^{III}_2O_4$ because of its 2:1 ratio. The amalgam has a different shape in which oxygen forms the cubic network of centred faces, leaving 32 octahedral and 64 tetrahedral spaces; the octahedral spaces are occupied by Fe^{2+} and Fe^{3+} ions, and the tetrahedral spaces are occupied by Fe^{3+} ions. Iron accounts for 72.4% by mass and oxygen accounts for 27.6% by mass. Figure 5.1 shows the structure.

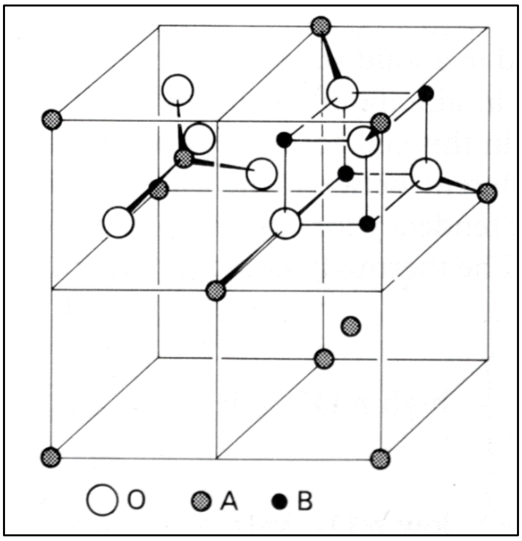

Figure 5.1 Normal spinel structure. It consists of A and B ions of a face-centred cubic O^{2-} lattice with A^{2+}. The structure occupies one-half of the octahedral holes and identical proportions of Fe^{2+} and Fe^{3+} ions (Shriver et al., 1994).

The third form is Fe_2O_3, which can be found in a diverse series of modifications, the most common modification consists of α forms and the second most common consists of γ forms (γ-Fe_2O_3). The most usual form is the hematite, which its chemical formula is α-Fe_2O_3 (70% Fe and 30% O). Hematite is a paramagnetic and electrical insulator, and the particles are shaped similar to hexagonal or octagonal platelets. Figure 5.2 shows the structure produced from Bragg and Claringbull (1965)

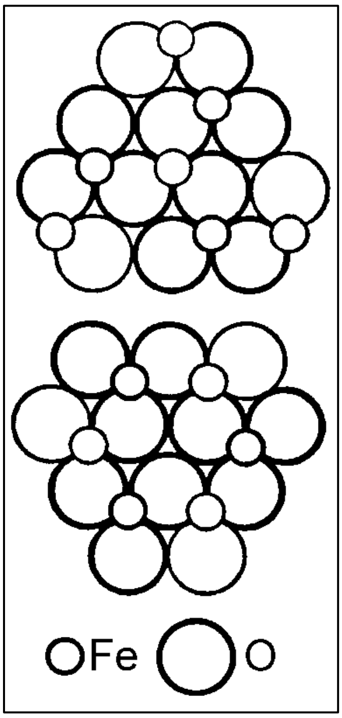

Figure 5.2 In the magnetite structure, it is possible to see a consecutive quantity of atoms. Two-thirds of the octahedral intervals in a cubic compact lattice of O^{2}- ions are packed with Fe^{3+} ions (Bragg and Claringbull, 1965).

γ-Fe_2O_3 can be obtained when Fe_3O_4 is oxidised, but to obtain it, the crystal structure must be cubic. When γ-Fe_2O_3 is heated *in vacuo*, it returns to Fe_3O_4. At the same time, when γ-Fe_2O_3 is heated in air, it converts into α-Fe_2O_3. All these conversions are possible because FeO, Fe_3O_4 and γ-Fe_2O_3 share a similar structure, which is a cubic-closed grid of O^{2-} ions.

However, γ-Fe_2O_3 can also grow with hydrothermal synthetic conditions by *in situ* total scattering and pair distribution function (PDF) analysis while using aqueous ammonium iron (III) citrate solutions. PDF is an analysis that provides information on a medium-range of inter-atomic distances (Lou et al., 2013).

Previous studies have suggested that this specific combination produces Fe_3O_4. Nonetheless, recent studies have proven that the final product is γ-Fe_2O_3. γ-Fe_2O_3

contains small nanocrystals (Dronskowski, 2001), and its magnetic performance depend on them. Therefore, it is critical to control the nanocrystals during synthesis.

One example of this procedure is the study performed by Jensen and co-workers (Jensen et al., 2014), in this study, the researchers used a solution that it was related to $[Fe(H_2cit)(H_2O)]n$ and possessed a corner-sharing octahedrally coordinated Fe^{3+} in a polymer-like structure associated by citrate molecules. After the hydrothermal treatment, nanoclusters (FeO_6) form immediately and the tetrahedrally coordinated iron ions are seen after seconds (<10 seconds at 320°C). The results of this study proved that distinguishing the crystalline steps is critical to understanding the inorganic hydrothermal synthesis.

Another advantage of using the hydrothermal synthesis method is that it is cost-effective and environmentally friendly (Byrappa and Adschiri, 2007), and the potential uses of this technology can be seen in many applications such as magnetic storage media (Lou et al., 2013) and medical imaging (Pankhurst et al., 2003).

5.1.2 Distinguishing between Formulated Iron Oxide Dispersions by their Different Properties (Colour Shades and Transparency)

Iron oxide dispersions can possess a range of colour shades that are caused by several parameters such as the dispersion’s most dominate particle size and morphology, crystal structure and orientation of the particles and the most abundant iron oxide phase which in turn is a function of the previous mentioned parameters (Jambor and Dutrizac, 1998). The colours of different phases as reported by (Jambor and Dutrizac, 1998) are as follows: hematite α-Fe_2O_3 is usually a bright red colour, magnetite (Fe_3O_4) is black, maghemite (γ-Fe_2O_3) is red to brown and ferrihydrite ($Fe_5HO_8.4H_2O$) is reddish brown. The colour property can be exploited to distinguish between all the above-mentioned four iron oxide phases using the VIS-3, but it was only possible to study the quantified colours for the most abundant iron oxide phases (i.e. hematite and magnetite) in the dispersions produced for the current work.

The main iron phases produced in this work are confirmed using the same method, conditions and precursors found in previous work (Adschiri et al., 1992, Edwards et al., 2005).

Furthermore, using the VIS-3, it was possible to quantify the transparencies of the different iron oxide dispersions formulated which correspond to the main particle size groups in the dispersion. Although transparency is a property for stable dispersions (i.e. not to be sedimented with time), it was possible to quantify the transparency values for some samples at the first moment they are introduced to the VIS-3 to enable comparison with other samples without sediment.

By using the supercritical water continuous hydrothermal synthesis method to formulate the dispersions tested in this work, the above parameters and in turn the iron oxide dispersion’s properties were easily tunable by changing the flow conditions and starting material composition such as the temperatures and precursor (metal salt) type and concentration. Other flow conditions such as metal salt concentration, water streams flow rates and mixing ratios have been investigated elsewhere (Lester et al., 2006, de Tercero et al., 2014).

By following the same method to produce iron oxide dispersions as previously accomplished using a CHS rig developed in Nottingham, the main iron oxide phases of hematite (Edwards et al., 2005) could be produced. Furthermore, hematite or magnetite were previously produced elsewhere using similar techniques (i.e. hydrothermal synthesis), precursors and conditions (Adschiri et al., 1992, Bremholm et al., 2009). Thus, hematite and magnetite dispersions produced from the CHS rig were investigated for their stability in water, and their characterisations for colour and turbidity using the VIS-3 are detailed in the following sections. XRD was conducted for some products to confirm the type of iron oxide formed. DLS and TEM techniques were used to investigate the effects of changing the temperature or precursors' concentrations on particle size, morphology and electrophoretic mobility.

5.1.3 Testing Stability by Settling Method using the VIS-3

The conditions (temperatures, pressures and precursors properties, compositions and concentrations) used with the CHS rig might not be the optimal or the desired conditions to produce nanoparticle dispersions (which have particle size ranges of 10–100 nm), because a product of larger size that are larger than the defined range for nanoparticles systems or agglomerated particles may be produced by the rig or the agglomeration may occur immediately after production or storage. Thus, the settling method and other methods with the aid of the VIS-3 have been employed to test the stability of particle dispersions immediately after coming out of the rig to 24 hours afterward, potentially realising the state of the solution instantly after production and what can occur to this solution after a period of time. This information can help in finding methods that maintain the desired solution properties after production. With the VIS-3, one graph for multiple samples can be produced to describe the change of sample behaviour with time, which makes it easier to observe samples with different properties directly after production. For example, if the settling occurs rapidly, this product is not desirable for certain applications. The settling can be determined by monitoring the settling curves with time. Moreover, the VIS-3 can determine whether a sample stops settling after a period of time while leaving some suspended particles to indicate that the sample has not completely sedimented. This state of dispersion can be quantified by obtaining a larger than the stable sample's mean pixel intensity value, in the settling curves, that is less than pure water's (the reference solution) value and remains constant with time. Consequently, it can be concluded that such system is bimodal with two particle size groups where the suspended particles might be in the nanometre region, as will be shown in the following sections.

5.2 Hematite (Fe_2O_3) Nanoparticles

5.2.1 Materials and Methods

5.2.1.1 Formulation with CHS rig

In this work, 0.05M Iron(III) nitrate nonahydrate [$Fe(NO_3)_3 \cdot 9H_2O$, Sigma Aldrich, ≥99.95% trace metals basis] (Figure 5.3) and DI water were used as precursors to produce hematite (α-Fe_2O_3) NPs.

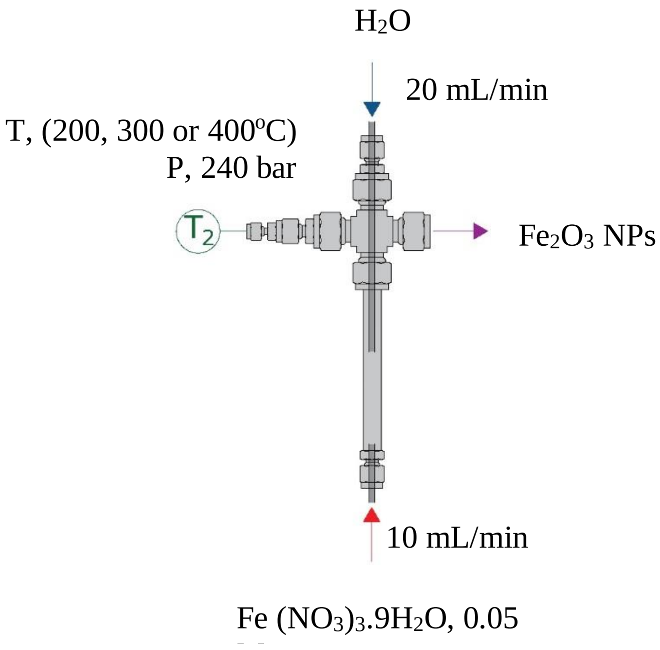

Figure 5.3 Supercritical reaction conditions for formulating hematite dispersions including the use of different formulation temperatures while fixing other parameters (i.e. mixing point pressure 240 bar, H_2O pumping rate of 20 mL/min downward through the water stream and metal salt with 10 mL/ min upward).

A precursor with a concentration of 0.05M was chosen, rather than higher concentrations, as the most feasible to run the CHS rig reliably (i.e. no tubing blockage might occur and no issues with back-pressure regulator cause the desired pressure to increase or decrease during each run), as had been tested in previous runs in Nottingham's rig.

Three runs were conducted with H_2O pumped through the water stream downward with a pumping rate of 20 mL/ min and metal salt precursor with 10 mL/min pumping rate, as shown in Figure 5.3 and Table 5.1.

Table 5.1 Reaction conditions for hematite dispersions synthesised using different temperatures while fixing other parameters. Temperatures and pressure sometimes undergo slight changes in values because of occasionally inconsistent performance of the CHS Rig.

Precursor	**Precursor Concentration (M)**	**Pressure (bar)**	**Metal Salt Stream Flow Rate (mL/ min)**	**DI Water Stream Flowrate (mL/ min)**	**Mixing Point Temperature (°C)**
$Fe(NO_3)_3 \cdot 9H_2O$	0.05	240	10	20	200
					300
					400

5.2.1.2 Introducing the products to the VIS-3

The dispersions formulated with the CHS rig were introduced to the VIS-3 directly after leaving the rig by filling the 10 mL cuvettes with 9 mL sample each as follows:

As illustrated in Figure 5.4, for only one background (the full white) that applies to all ROI images (a, b, c, d, e, f, g & h) in Figure 5.12, from the left to the right, the first cuvette is always filled with the main solvent used to produce the dispersions, where water in this experiment is used as a reference. Next, every two cuvettes are filled with similar solutions; The first solution was collected immediately after being produced from the rig, and the second was collected 5 min after being produced. These solutions are compared to quantify whether any variations might occur between the two consecutive batches as they are produced by the CHS rig.

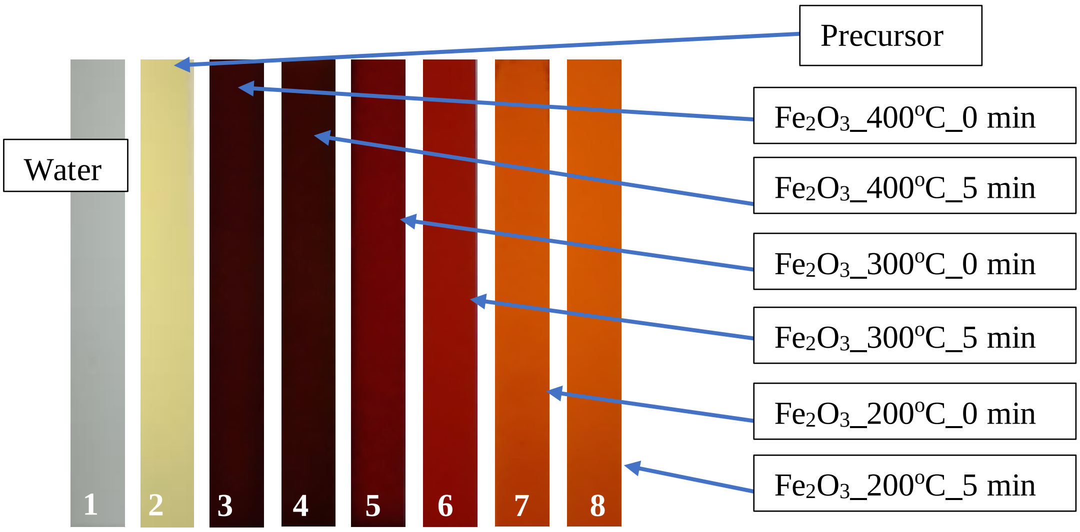

Figure 5.4 Samples at 0 hour at the VIS-3 running time. The times in the textboxes represent the times at which each sample formulated using the CHS rig.

The settling times in Table 5.5 and plots (Figures 5.8, 5.9, 5.10, 5.11 and 5.12) were calculated as a function of average pixel intensity in the full ROI in each cuvette by image analysing using MATLAB.

5.2.1.3 Analysing with TEM and DLS

TEM micrographs were used in addition to the DLS data to provide more accurate size measurements by distinguishing between and measuring the size of particles forming clusters or agglomerations and the size distribution. Compared to size calculation using TEM, the DLS technique generates the size of an equivalent sphere that has the same translational diffusion coefficient as the particle, usually giving a larger particle size than that by electron microscopy. In addition, TEM was used to gain extra information such as particle shape and crystallite state which cannot be observed with the current DLS technique. However, the trend of size with temperature can be confirmed using the DLS method and by investigating whether samples were electrostatically stabilised by obtaining zeta potential values to confirm the observation by the VIS-3 system. The DLS method uses the intensity of scattered light from particles to calculate the size distribution in a dispersion, and the presence of large contaminants or agglomerates can scatter light in higher intensities than that of smaller particles, potentially screening the intensity from the smaller particles; thus, using the DLS method is not suitable for the highly polydisperse samples (with PDI larger than 1). To overcome this limitation, sample dilution, filtration or purification sometimes is required in the sample preparation steps before measurements. Dilution can possibly change the original particle sizes because of possible agglomeration or changes in other sample properties (Lerche, 2002). Thus, in the current work, samples were analysed as they synthesised without any further treatment and were suitable for the DLS measurements.

TEM micrographs were obtained as described in Chapter 2. Then, the micrographs were processed using ImageJ software; particle size analysis was performed by measuring a minimum of 200 particles for each set of micrographs for samples at 200, 300 and 400 °C formulating temperatures.

Initially, a micrograph was loaded to the ImageJ software and calibrated so the resulted measurements are in nanometre rather than in pixels, which is the default measuring dimension in ImageJ. Then, by using the line tool, the lengths of each particle were measured by dragging a line across the longest distance through each particle with a well-defined boundary that can be detected. The results then were tabulated and exported to an Excel sheet for frequency analysis of each particle size for the three groups of samples.

5.2.2 Results and Discussion

Numerous studies have established, using the hydrothermal synthesis method to produce nanoparticles, that particle size generally increases with increasing reaction temperature (Andersen et al., 2014, Bremholm et al., 2009, Cabanas and Poliakoff, 2001, Edwards et al., 2005). This result is also the case with iron oxide dispersions produced in this work, as confirmed in the following sections.

In this work, dispersions at high temperature (400 °C) were considered not stable because of the large particles/ agglomerates formed that completely sedimented in the first half-an-hour of testing. In contrast, samples formulated at 300 and 200 °C with all other conditions fixed show a degree of transparency and colour that did not change with time, indicating that these dispersions are stable (Table 5.8).

The TEM results confirm the presence of particles with different sizes and size distribution, as illustrated in Table 5.2 and Figure 5.5. They show that the lower formulation temperature results in smaller particle sizes and narrower size distributions.

The results show that considerably larger particle size and broader size distribution can be obtained by increasing the temperature. Table 5.2 illustrates the means and standard deviations of the TEM data, showing, by the increasing values of mean and the relative standard deviation, how wide the spread in particle size distribution becomes when increasing the formulation temperature.

Table 5.2 The calculated mean and standard deviation of particle sizes using TEM data.

Temperature (°C)	**Mean particle size- with SD (nm)**
200	3.8 ± 0.9
300	26.5 ± 7

400	41.5 ± 11.8

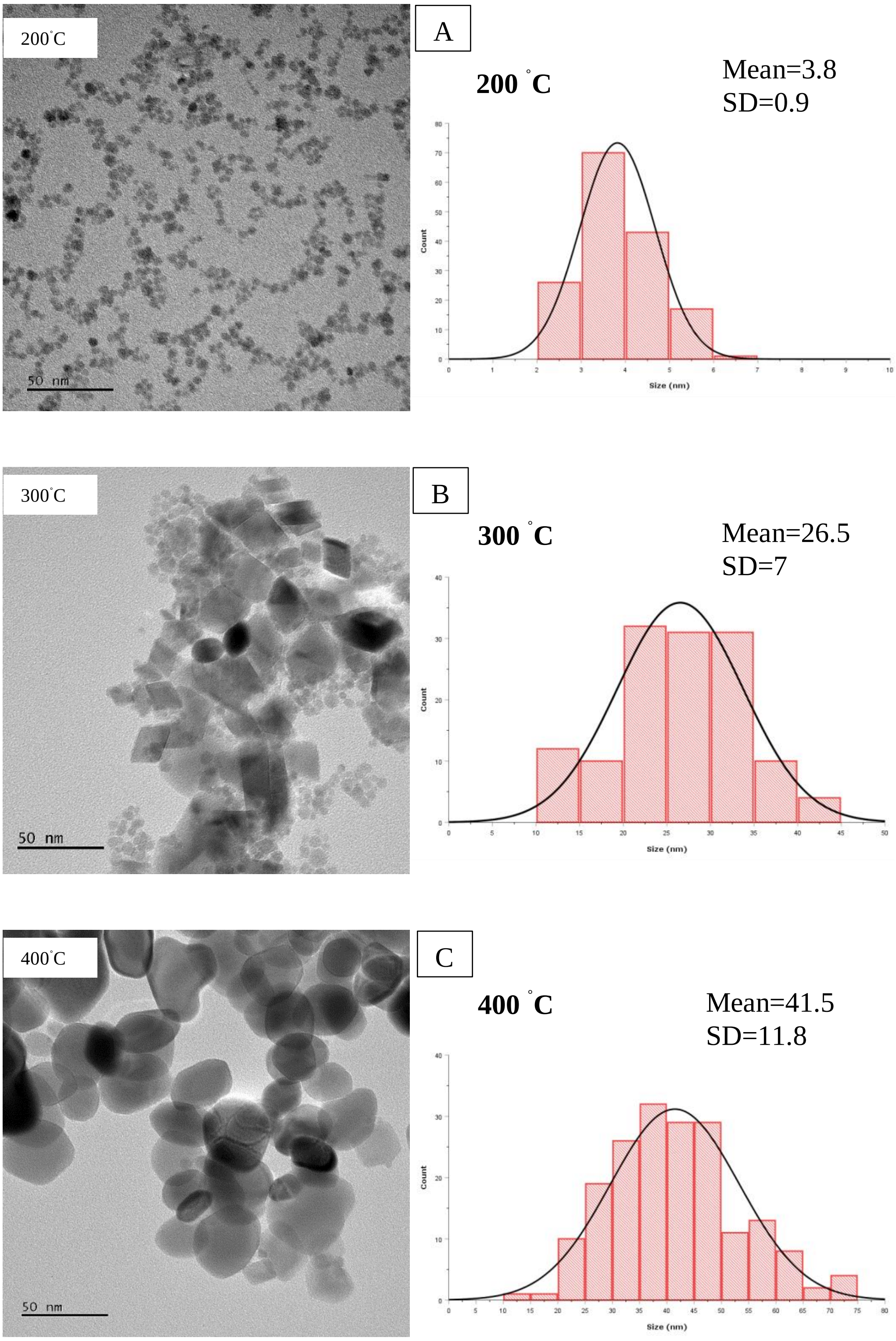

Figure 5.5 TEM images and corresponding size distributions of samples formulated at (A) 200 ˚C, (B) 300 ˚C and (C) 400 ˚C. Scale bars are 50 nm.

Furthermore, the micrographs (Figure 5.5) show a progression in crystallite nanoparticle formation from the least crystallite nanoparticle formation for samples at 200 °C to the highest crystallite nanoparticle formation at 400 °C iron oxide dispersions where the precursor's conversion is the greatest (Malinger et al., 2011). In addition, the micrographs clearly show the formation of rhombic to spherical (mostly at the sample fabricated at 400 °C) particle shapes.

Moreover, Figure 5.6 shows more particles at a lower TEM magnification; because the area surrounds the particles becomes clearer when moving from lower temperature to higher temperature, it can also be estimated that a higher formulation temperature leads to a higher conversion of the precursor. This relationship indicates that the precursor was highly consumed in the crystal growth during formulation with the higher temperatures (Hobbs et al., 2009a, Caramazana-Gonzalez et al., 2017). Furthermore, this conversion behaviour can confirm the findings from the VIS-3 images as they show dispersions with an orangish colour at 200 °C which is closer to the precursor colour, while samples formulated at 300 °C and 400 °C start with a darker colour and then become clearer by the end of testing duration, indicating the presence of larger particles that sedimented with time (Table 5.8).

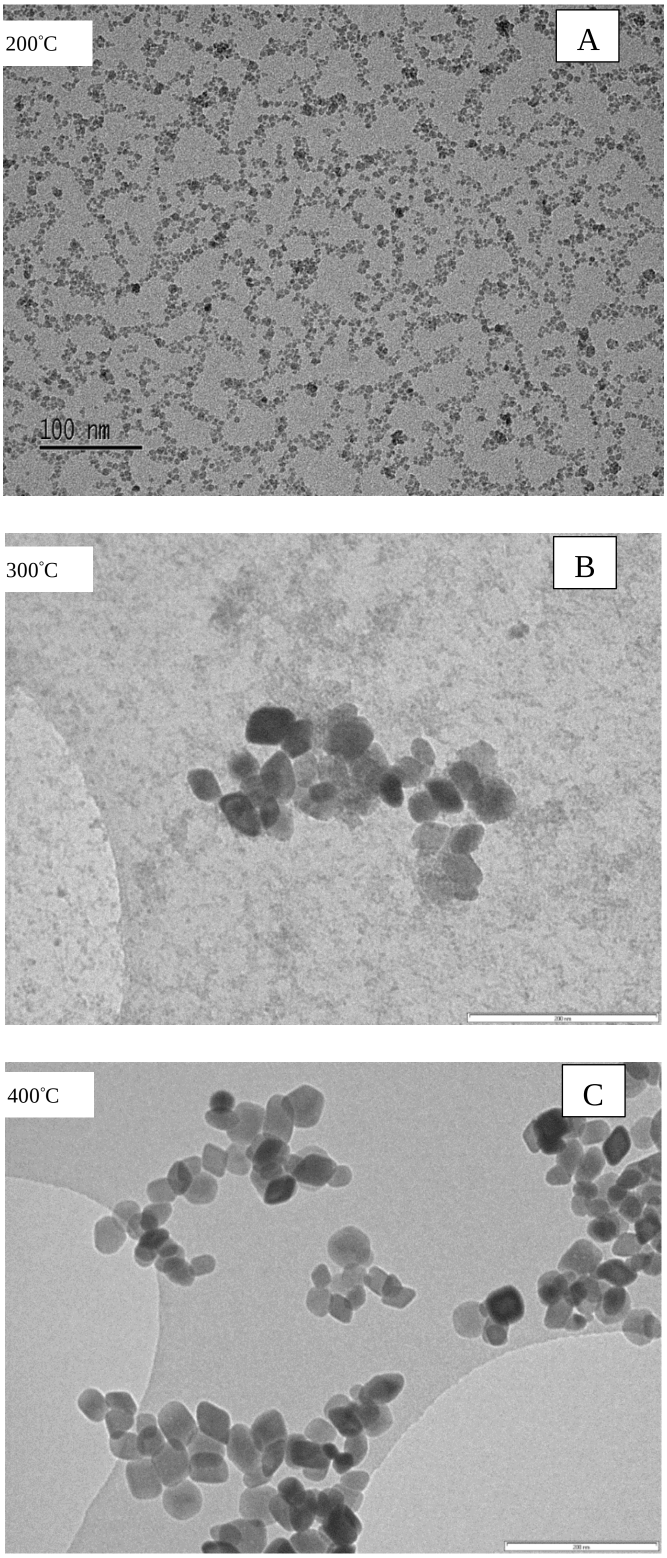

Figure 5.6 TEM micrographs to estimate precursor's conversion for samples formulated at (A) 200 ˚C, (B) 300 ˚C and (C) 400˚C. Scale bars are 200 nm except for the bar for the 200 ˚C sample is 100 nm.

DLS measurements show similar results to the TEM analyses; the particle size increases with increasing reaction temperature (Table 5.3).

Table 5.3 Data produced by DLS instrument including particle size and zeta potential.

T(°C)	**Z-Ave Size (nm)**	**PDI**	**Di90 (nm)**	**Di50 (nm)**	**Di10 (nm)**	**ζ (mV)**	**Conductivity (mS)**
200	150.3±12.1	0.368	360	169	89.8	37.8	10.2
300	2562±102.7	0.455	5130	3260	867	27.1	9.87
400	4044±294.5	0.205	5190	4020	3100	25	14.8

Based on the DLS technique's size calculations by the Zetasizer Nano series, the reported particle size is the scattered light intensity (weighted) mean diameter which is below the maximum size value; thus, a PDI (which is an estimate of the broadness of the size distribution) must always be reported along with the size to describe whether the size distribution is wide or narrow to give a clearer idea about the system being measured. PDI ranges from 0 to 1 in MALVERN DLS software with 0 indicating a monodisperse system and 1 indicating a highly polydisperse system. Values of PDI>1 indicate a highly polydisperse system that is not suitable for DLS measurements. Furthermore, as described in Chapter 4, reporting other particle size populations such as the median and the extremes of the intensity size distribution (Di10, Di50 and Di90) can show the extent of deviation from the main particle size that can be attributed to the presence of impurities, extra fine particles or large agglomerates. As shown in Table 5.3, intensity size distributions are dominated by the large particles with 90% of the distributions being 360, 5130 and 5190 nm for the 200 °C, 300 °C and 400 °C temperatures, respectively. In all cases, the 50% intensity distribution shows values that are the closest to the main particle sizes, indicating that 50 % of the sample intensity is related to the contribution of the scattered light by the main size particles.

The mean and standard deviation in DLS measurements were taken for three DLS samplings at three instants. The results shown in Table 5.3 are consistent with the results from TEM and show smaller particle sizes at lower temperature and that particle size increases with increasing temperature.

In addition, system stability status was determined by evaluating the zeta potential by estimating the electrophoretic mobility and applying the Smoluchowski approximation using a Zetasizer Nano series instrument.

From the zeta potential values (ζ) (Table 5.3), the stability of the dispersion can be estimated (the most stable system is the one with the ζ larger than ±30 mV, as described previously); the results show that samples synthesised at 200 °C are the most stable as they possess the highest ζ compared to others, with the least stable system at 400 °C. This observation agrees with the results from the VIS-3, as illustrated in the following section.

The XRD technique was used to confirm the presence of hematite that is expected to occur by the hydrothermal synthesis method using the iron(III) nitrate nonahydrate as the precursor and the proposed reaction conditions.

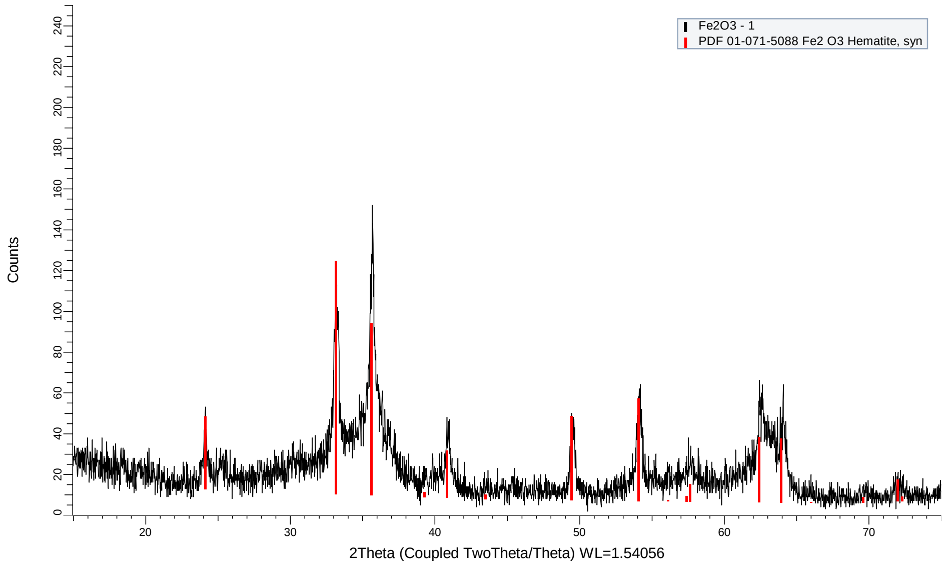

Figure 5.7 XRD pattern of hematite powder produced at 400 °C.

The XRD data collected from hematite powder is shown in Figure 5.7. The XRD patterns show that the crystalline phase of hematite was present. All peaks corresponding to the reference phase are present in the sample, confirming that hematite is the predominant crystal structure for the CHS rig sample. The mean crystallite diameter calculated using the Scherrer equation was 25.5 nm.

5.2.2.1 Stability studies using the VIS-3

Using the VIS-3 allowed the behaviour of several samples with varied formulation temperatures to be monitored by using the settling method to investigate the effect of changing in particle size with temperature on settling.

Figure 5.12 includes the before and after settling ROIs for all samples and include the same Figures (5.8, 5.9, 5.10, and 5.11) but with the end of settling indications added. The end of settling (settling time) was obtained directly by a MATLAB code (Section 3.2.3.2.6, Chapter 3) using the “curve analysis function” which calculates the point of time at which the settling rate starts to level off/plateau, which represents the point at which the settling ends. The settling time results are shown in Table 5.5.

The changes in particle size and distribution due to formulation temperature were confirmed by the DLS and TEM results.

As has been discussed in previous chapters, parameters that govern whether a product remains suspended for a long period or settles after a while are a combination of particle properties (e.g. density; mass and cross section), the properties of the liquid where particles are dispersed and the external forces affecting the particle. Stokes Law was used to theoretically describe the relation between average particle size and settling time by balancing these parameters in the following relation equation.

$$\nu = \frac{2}{9}\frac{(\rho_p - \rho_f)gr^2}{\eta} \qquad \text{Equation 1}$$

Where, ν is the settling rate, ρ_p and ρ_f are the densities of particle and fluid, respectively, g is the acceleration due to gravity, r is the particle radius and η is the viscosity of the fluid.

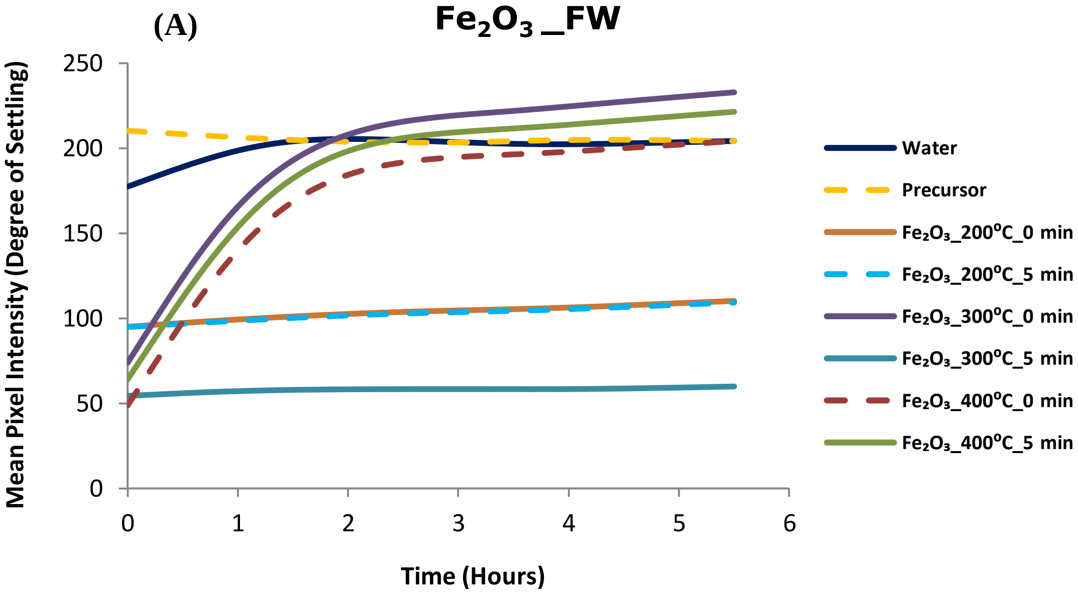

Figure 5.8 (A) FW settling rates plot for Fe_2O_3 samples at different temperatures.

The settling plots, e.g. Figure 5.8, show a slight decrease in the precursor mean pixel value (204) with respect to an initial value (210), although theoretically, this sample should be constant throughout the testing duration. This result can be attributed to the formation of air bubbles (Figure 5.12 (b), sample 2) during the test (after around 0.9 hours) which make the solution appear darker.

Table 5.4 Data extracted from the FW (Figure 5.8) shows the ROI pixel value at settling time.

Solution	Time Settling Ends	Mean Pixel Intensity Value at the End of Settling
Water	-	204
Precursor	-	204
Fe_2O_3_200°C_0 min	5.39	110
Fe_2O_3_200°C_5 min	5.39	109
Fe_2O_3_300°C_0 min	4.91	230
Fe_2O_3_300°C_5 min	5.42	60
Fe_2O_3_400°C_0 min	4.76	201
Fe_2O_3_400°C_5 min	4.87	218

Table 5.4 shows another example using the FW background; pixel values become the closest to the maximum value of white (255), in the grayscale pixel system, with settling. As the samples become clearer after settling, their pixel values should be closest to that of clear water (such as in Fe_2O_3_300°C_0 min, Fe_2O_3_400°C_0 min and Fe_2O_3_400°C_5 min) unlike the unsettled samples which have the lowest pixel values (Fe_2O_3_300°C_5 min).

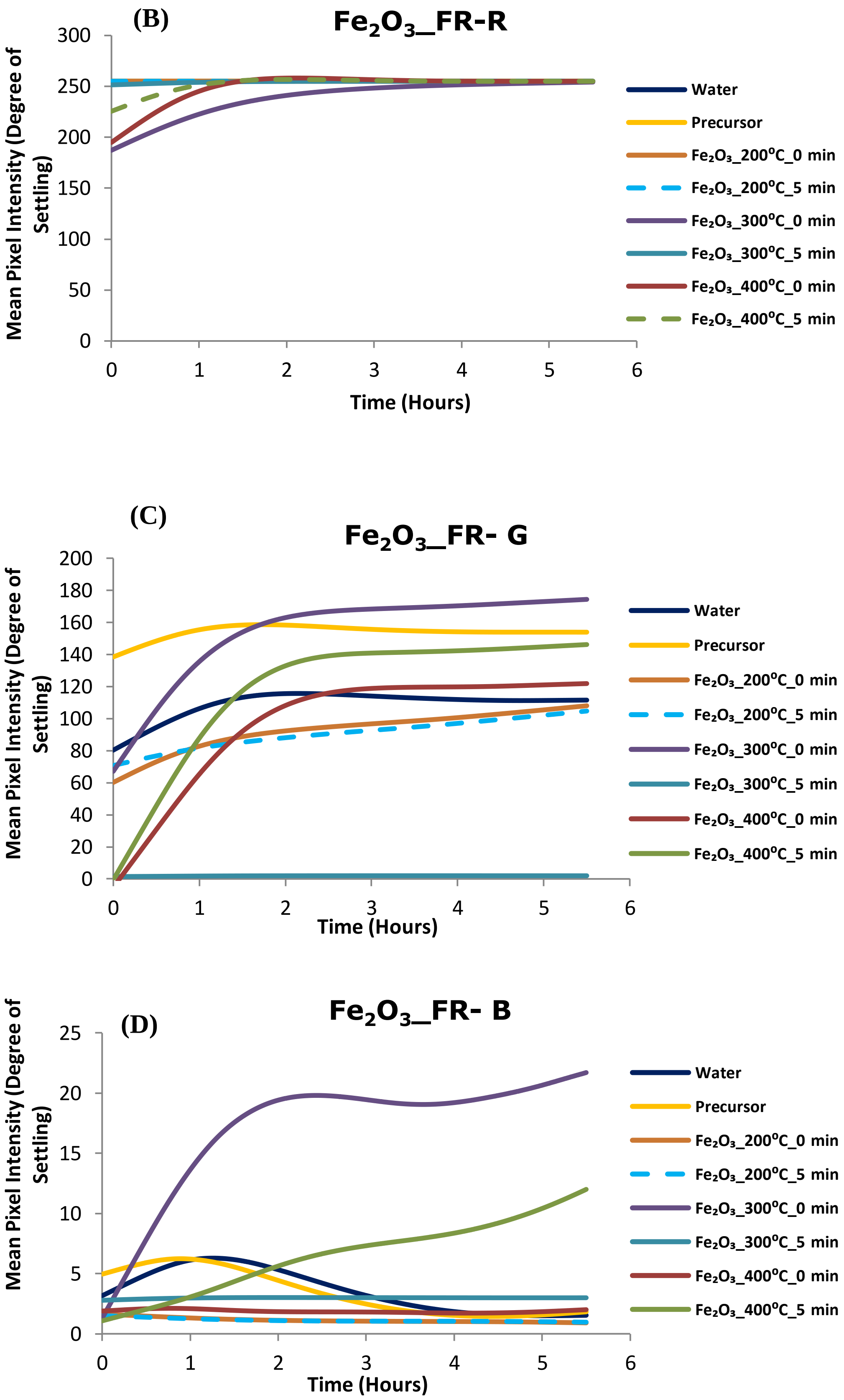

Figure 5.9 FR settling rate plots for Fe_2O_3 samples at different temperatures (B, C and D are for the R, G and B channels, respectively).

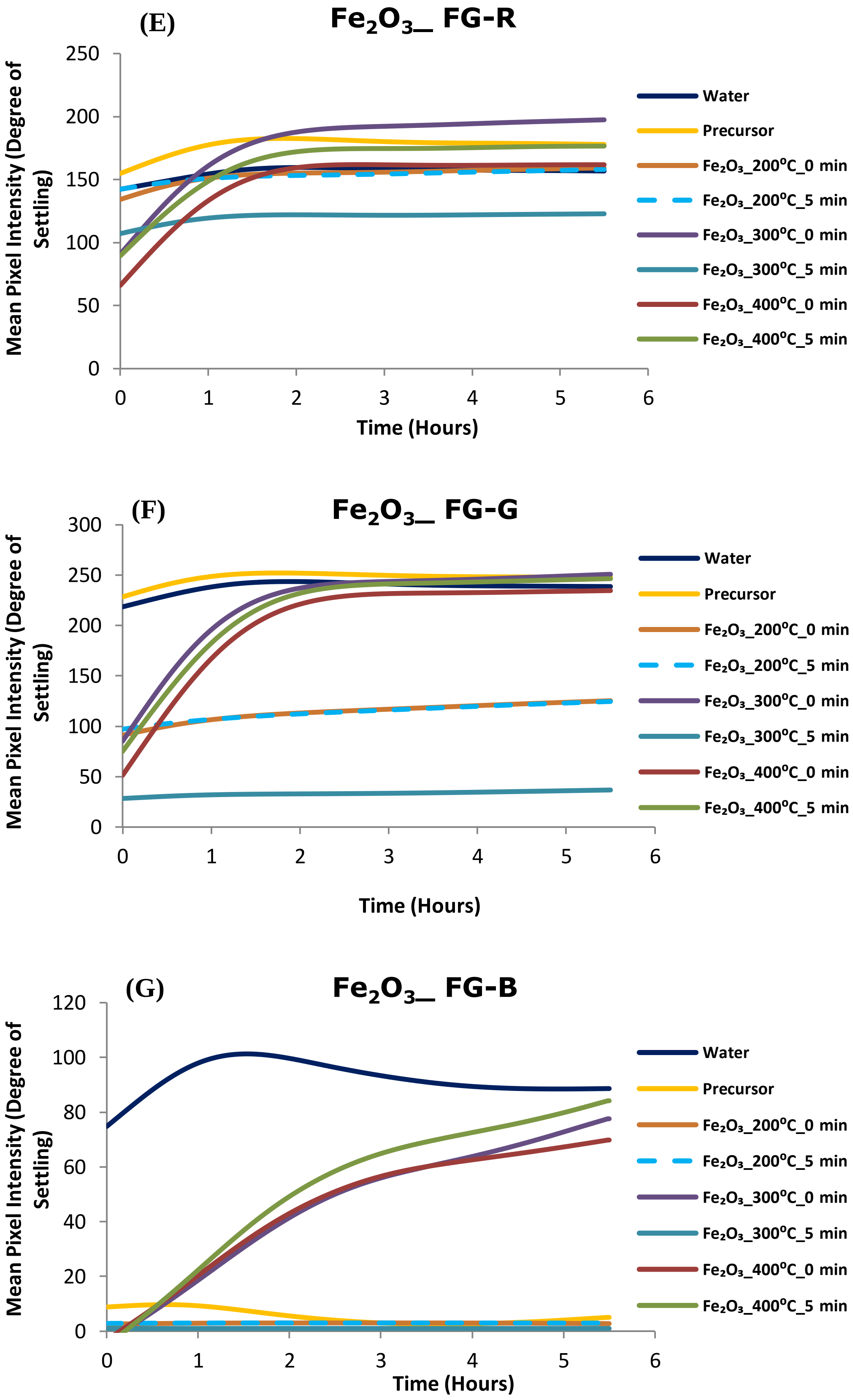

Figure 5.10 FG settling rates plots for Fe_2O_3 samples at different temperatures (E, F and G are for the R, G and B channels, respectively).

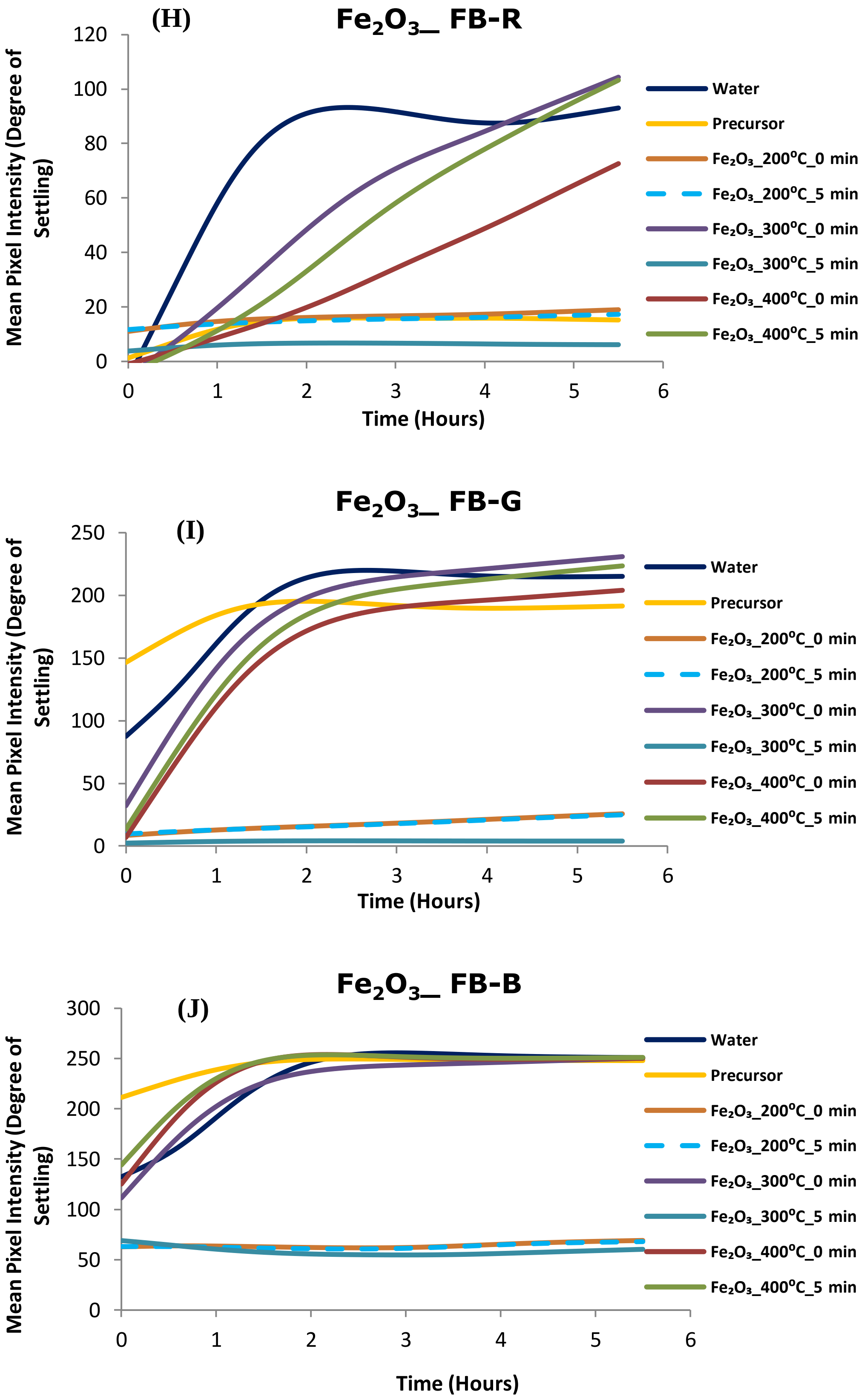

Figure 5.11 FB settling rates plots for Fe_2O_3 samples at different temperatures (H, I and J are for the R, G and B channels, respectively).

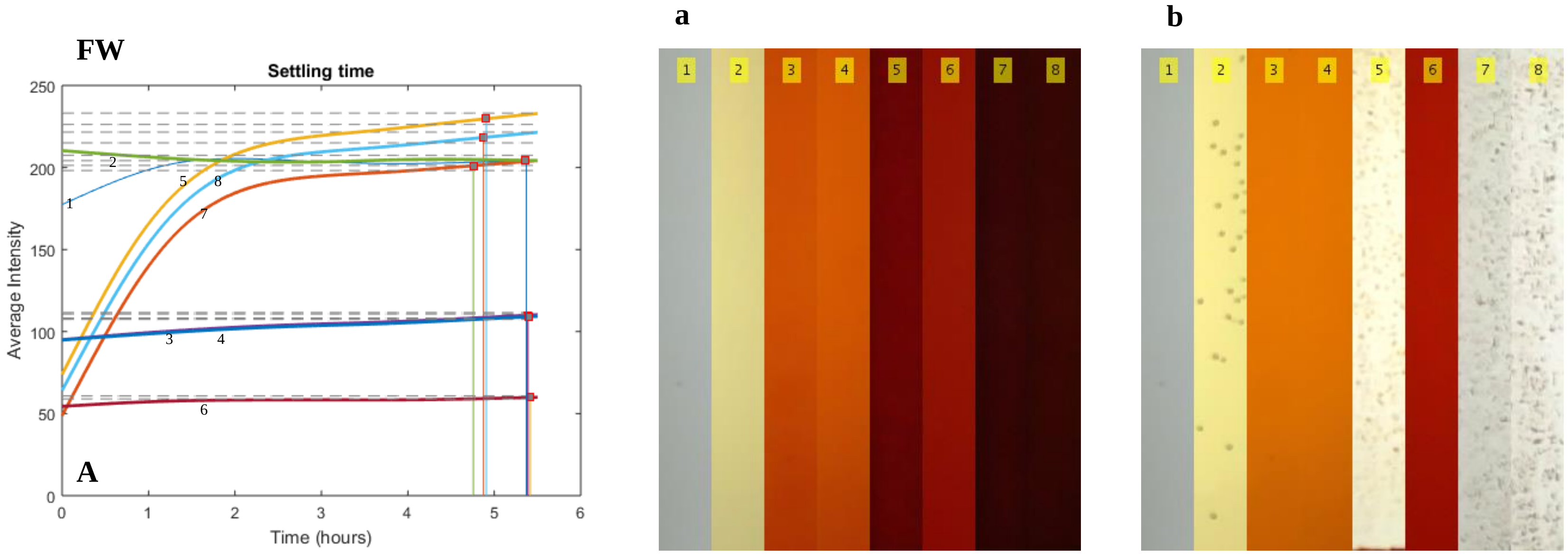

ROI of FW Before Settling

ROI of FW After Settling

Figure 5.12 Settling rates plots for Fe_2O_3 samples at different temperatures for all backgrounds; a, b, c, d, e, f, g & h are ROIs before and after settling and A, B, C, D, E, F, G, H, I & J are settling plots with end of settling calculations.

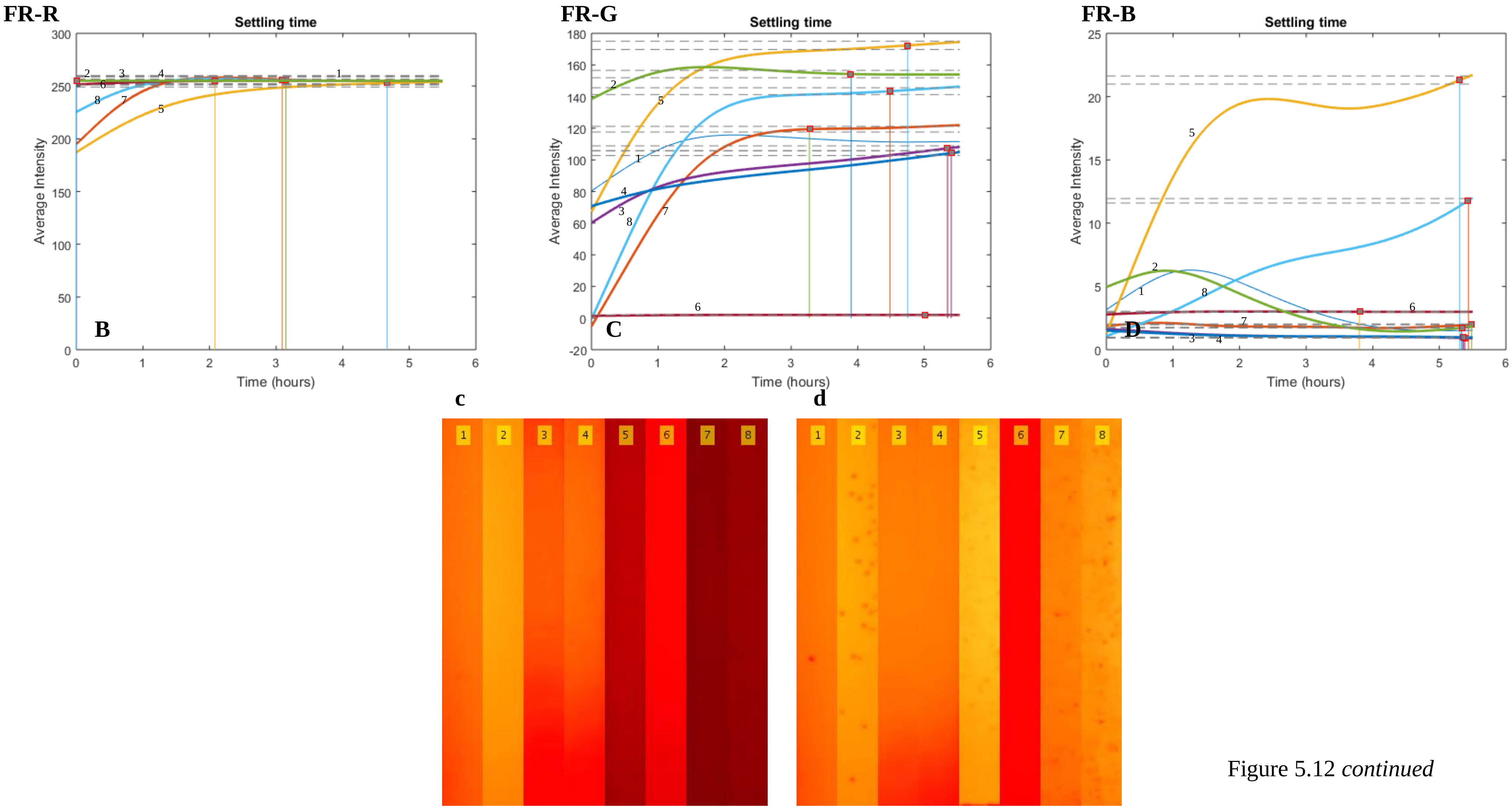

ROI of FR Before Settling

ROI of FR After Settling

Figure 5.12 *continued*

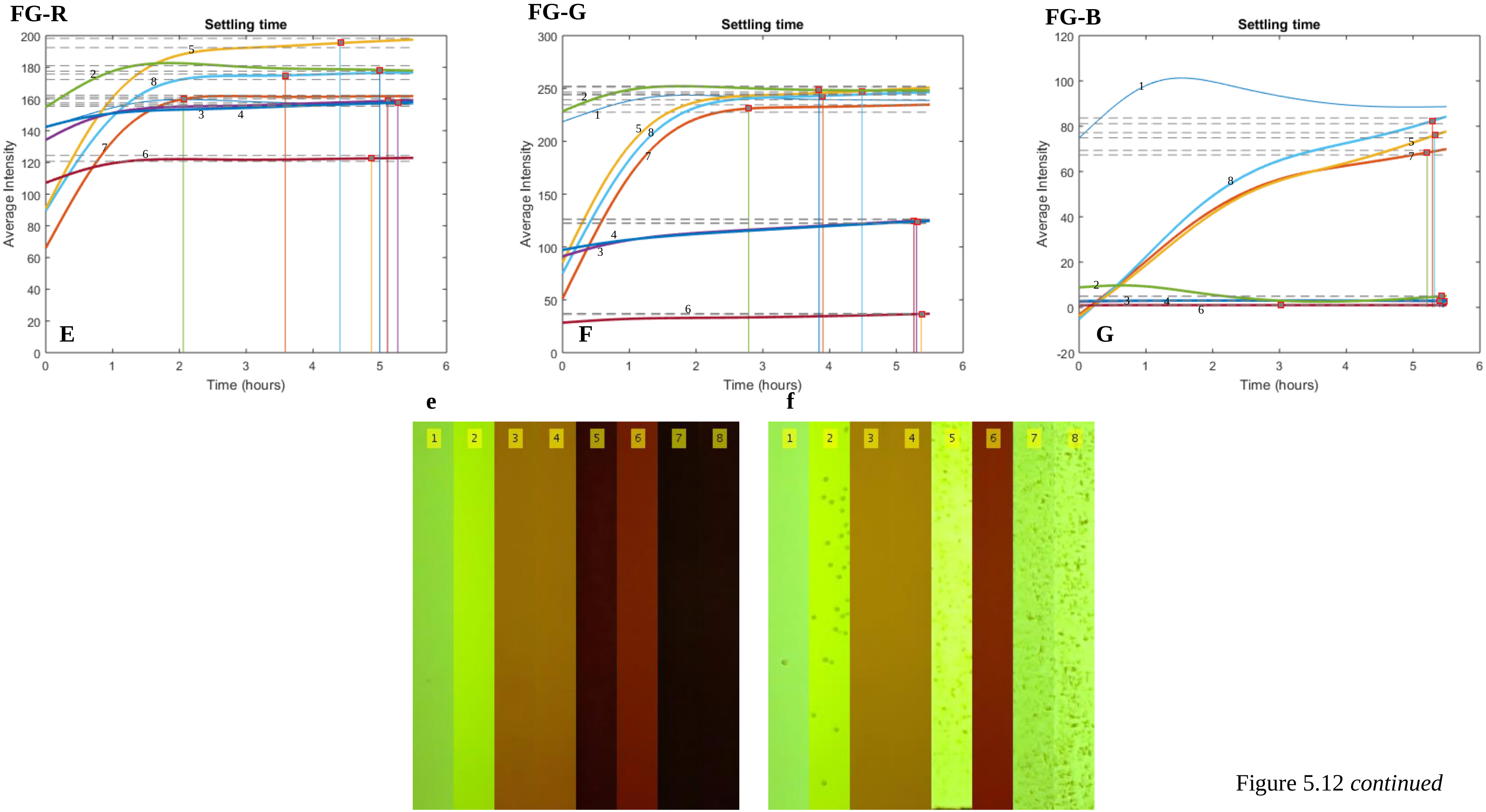

ROI of FG Before Settling

ROI of FG After Settling

Figure 5.12 *continued*

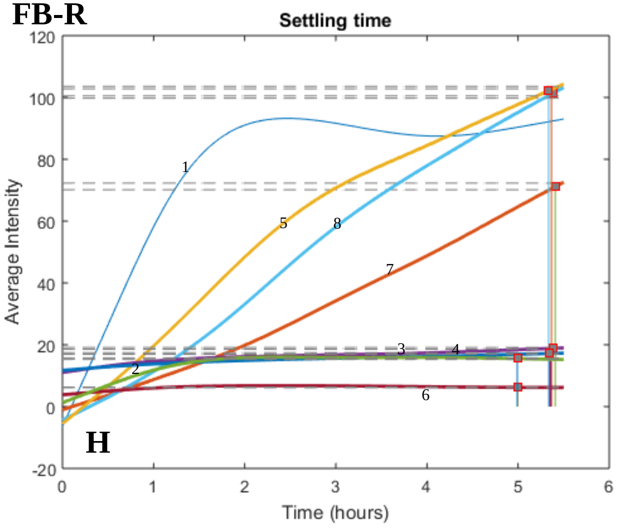

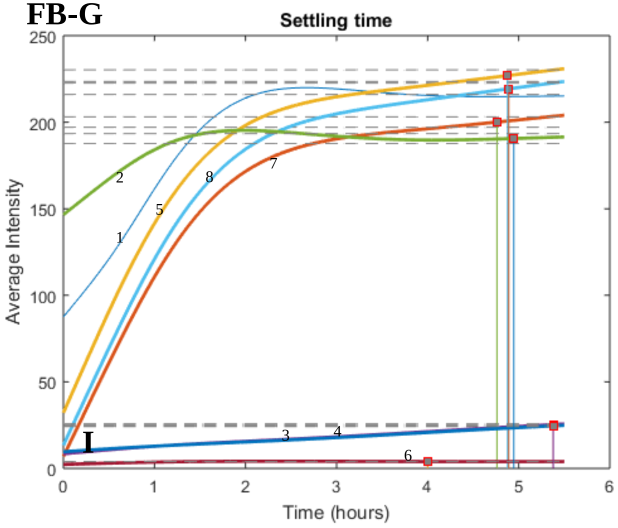

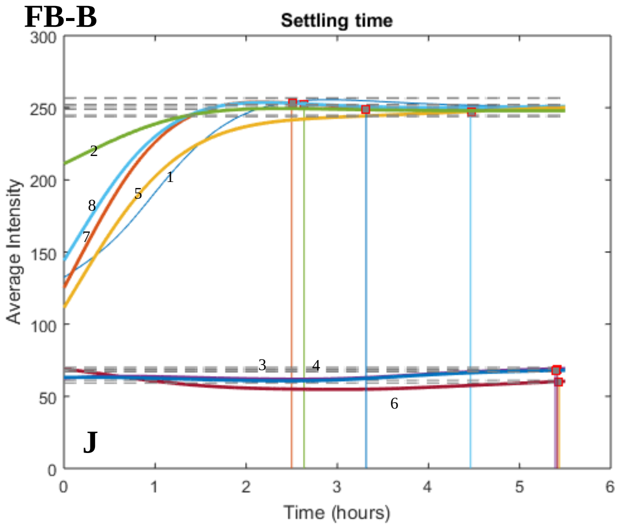

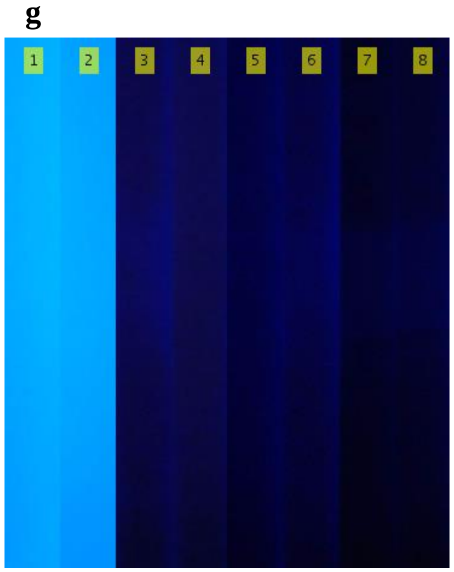

ROI of FB Before Settling

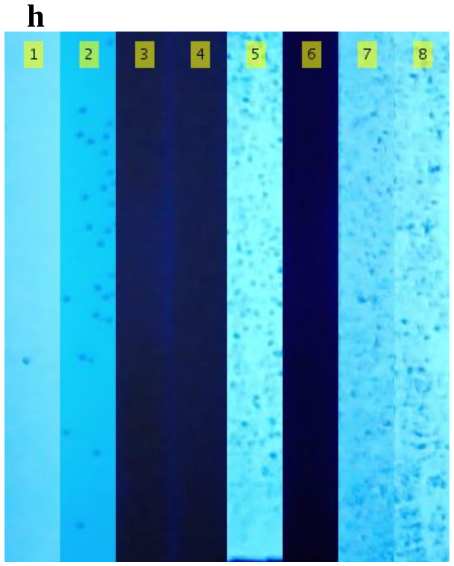

ROI of FB After Settling

Figure 5.12 *continued*

Table 5.5 Settling time calculated based on different backgrounds.

	Settling Time (h)										
Sample with Cuvette No.	**White**	**FR**			**FG**			**FB**			**Theoretically Using Stokes' Equation**$^{\alpha}$
		R	**G**	**B**	**R**	**G**	**B**	**R**	**G**	**B**	
Fe_2O_3_200°C_0 min (3)	5.39	0.00	5.35	5.38	5.12	5.26	5.46	5.36	5.38	5.42	476.67
Fe_2O_3_200°C_5 min (4)	5.39	0.00	5.41	5.36	5.27	5.30	5.40	5.35	5.38	5.39	
Fe_2O_3_300°C_0 min (5)	4.91	4.67	4.75	5.30	4.40	4.48	5.32	5.33	4.88	4.46	1.64
Fe_2O_3_300°C_5 min (6)	5.42	2.08	5.01	3.80	4.87	5.37	3.03	5.00	4.00	5.44	
Fe_2O_3_400°C_0 min (7)	4.76	3.15	3.27	5.49	2.06	2.79	5.21	5.41	4.76	2.64	0.66
Fe_2O_3_400°C_5 min (8)	4.87	3.09	4.48	5.44	3.58	3.90	5.29	5.37	4.89	2.50	
Average	5.12	2.16	4.71	5.13	4.22	4.52	4.95	5.30	4.88	4.31	
SD	0.31	1.87	0.79	0.65	1.22	1.03	0.95	0.15	0.51	1.40	

$^{\alpha}$For Stokes' equation, Fe_2O_3 particle density is 5.26 g/cm^3, and the particle radius is taken from DLS particle size measurements.

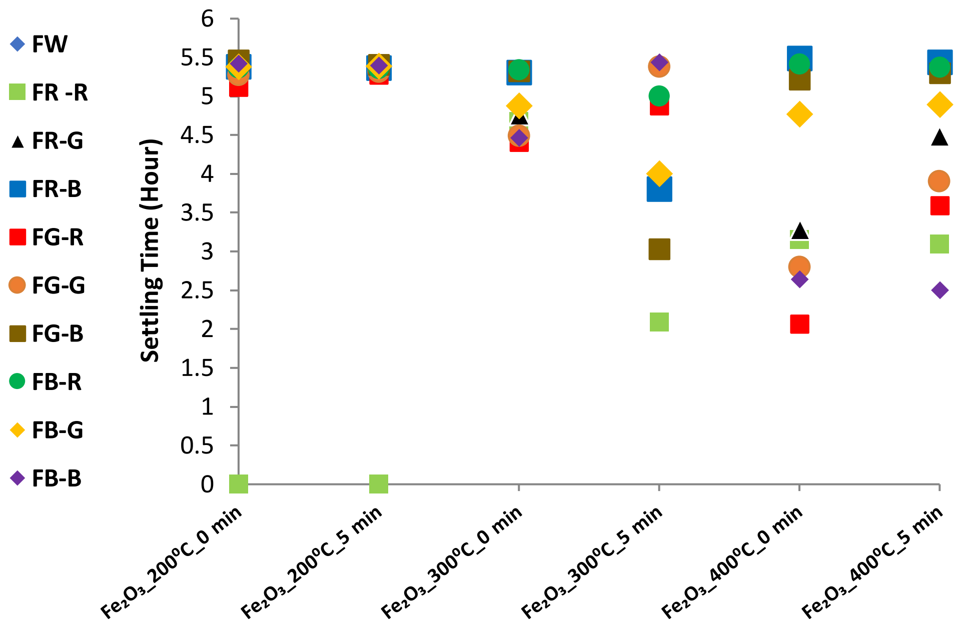

Figure 5.13 Settling time calculated based on different backgrounds.

The four backgrounds; white, red, green, and blue were used to calculate the settling time. However, the colour of the background blends with the colour of the solution, affecting the average intensity of the area inside the cuvettes in the captured images.

In other words, the calculated settling time depends on the colour of the background and which channel, R, G, or B, of the images was considered. Those differences are presented clearly in Table 5.5, which compares between the settling times which have been calculated based on the different backgrounds. In addition, Figure 5.13 illustrates those differences visually. Different backgrounds are used to determine the combination of backgrounds and/or channels that are most sensitive to the solution type.

The obtained settling times from the VIS-3 have been compared to those obtained from Stokes Law (using particles sizes from DLS).

Experimentally, given that the total testing time was 5.5 hours, for the samples that have not settled, such as samples formulated at 200˚C, the obtained settling time value should be the closest to the maximum testing time (i.e. 5.5 hours), which it can be approximated to 'infinity'. Thus, the combination that gives the highest settling time should be the most suitable to describe the settling time for the unsettled (stable) samples and considered the most sensitive to that sample. For this, the settling time for samples at 200°C calculated using the VIS-3 are 5.46 h by FG-B for Fe_2O_3_200˚C_0 min (3), where (3) stands for cuvette number, and 5.41 h by FR-G for Fe_2O_3_200˚C_5 min (4). Furthermore, the settling time using the Stokes approximation for the 200°C sample is the highest (476.67 h) amongst the other samples because the smaller particle sizes correspond to slower settlings. This result can be correlated with the general trend obtained from the VIS-3 for all the backgrounds except for the FR-R, which has the worst sensitivity for the suspended samples, as it gives the lowest settling time values. For the unsettled sample at 300°C collected after 5 min duration, settling time was determined as 5.44 h by FB-B for Fe_2O_3_300˚C_5 min(6).

As for the settled samples, the lowest settling time (fastest settling) was determined for the samples at 400°C with the largest particle size as shown from the DLS and TEM results. The VIS-3 results for this sample were 2.06 h by FG-R and 2.50 h by the FB-B for the Fe_2O_3_400°C_0 min (7) and Fe_2O_3_400°C_5 min (8), respectively. In addition, the result from Stoke's relation is the lowest (0.66 h) compared to the same for the other two samples. Fe_2O_3_300˚C_0 min (5) sample shows a settling behaviour, which has not been observed for the same after 5 min production, which can be attributed to possible instability that occurred in the CHS rig when switching between runs at different temperatures. The settling time for this sample was considered high amongst all the backgrounds, with the lowest at 4.40 h by the FG-R.

These observations in Table 5.5, Figure 5.13 and 5.14 show that the combination of green background with red channel (FG-R) and the combination of the blue background with the blue channel (FB-B) are the most sensitive to the changes in sample type and colour, because they relatively produce the longest settling times for the unsettled samples and the shortest settling times for samples that undergo settling. Moreover, differences between the settling times calculated using these combinations are the largest amongst other combinations, and these differences are indicated by large standard deviation values (1.22 for FG-R and 1.40 for FB-B). This conclusion is after excluding the FR-R because it produces zero settling time values, which are values that correspond to empty cuvettes, indicating its lack of sensitivity.

The white background, however, produces long settling times on average with a very small standard deviation. This small standard deviation makes the proposed system less sensitive to the changes in the intensity of the solutions over time. The lack of sensitivity is because the values extracted from the images of the white background are the average of the three channels; R, G, and B.

The red, green and blue backgrounds have different performances depending on the channel that has been used for calculating the settling times. When the B channel was used, the calculated times were relatively long: 5.13, 4.95 and 4.31 hours on average for the FR-B, FG-B and FB-B backgrounds, respectively.

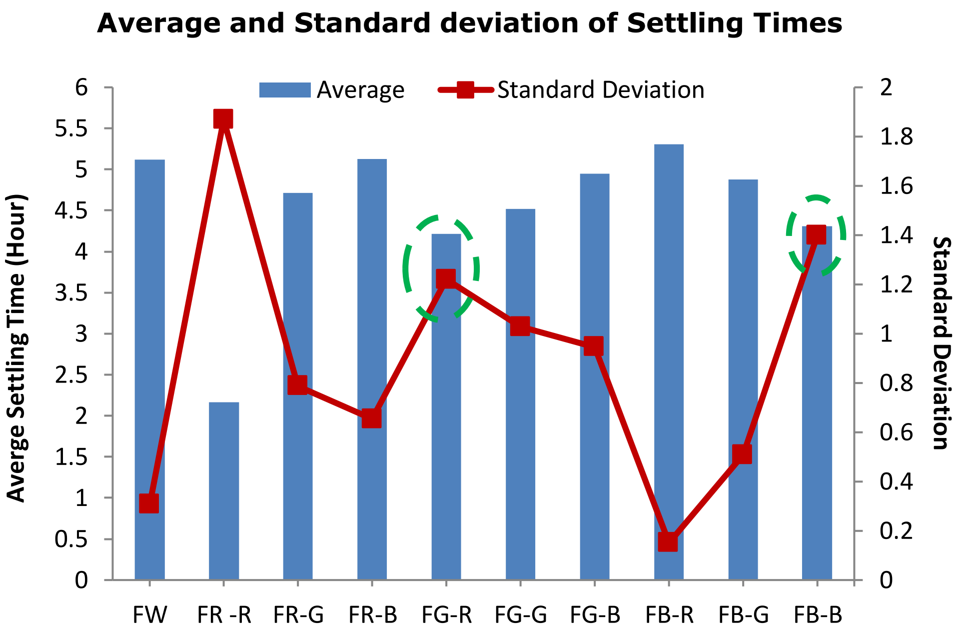

Figure 5.14 Relation between the colour of background-channel and the average and standard deviation of the settling time.

Figure 5.14 illustrates the best selection amongst all backgrounds by showing the relation between the colour of background-channel and the average and standard deviation of the settling time. As mentioned, the green background with the R channel and the blue background with the B channel have the best performances in terms of sensitivity, as indicated by the higher standard deviation, and settling speed, as indicated by the varied settling time that best correlates to the sample behaviour.

5.2.2.2 Colour, transparency and turbidity analysis using the VIS-3

Constant transparency and colour of dispersions with time are indicators of dispersions' stability (de Tercero et al., 2014). Thus, as seen in Tables 5.7 and 5.8, these properties quantified and compared with the same for water and the precursor to confirm the observations in the settling studies.

Letters, thin and thick line backgrounds were used to quantify the transparency of dispersions (see Figures 5.15 and 5.16). Table 5.7 shows that the letter area decreases with increasing solution transparency until it reaches values that are comparable to the values corresponding to water. As a solution is more opaque, it blurs the letters more and causes the letter to cover a larger area in the ROI. In the case of the dispersion formulated at 400 °C, initially, its colour was dark brown which drastically decreases the contrast between the black letter and the very dark solution colour, thus yielding a letter area value of 2034 pixels which is attributed to a very distorted letter, as illustrated in Table 5.7. In contrast, the comparable values of solutions at 200 °C, 300 °C and the precursor with water can confirm that those samples are transparent with different degrees depending on their transparency beside their other properties such as particle size and density.

Figure 5.15 Sample ROIs produced using the letters background at (0 h) testing time. Samples are: 1 water, 2 precursor, 3&4 hematite produced at 200 °C, 5&6 hematite produced at 300 °C and 7&8 hematite produced at 400 °C.

Table 5.6 Stages of letter background image analysing showing the effect of the sample degree of transparency on the calculated letter areas.

Time (h)	**RGB image**	**GREY (complemented)**	**BW**	**Area (pixels^2)**			
0.00861	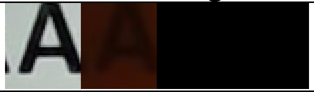			477	2034	0	0
:	:	:	:	:	:	:	:
0.11541	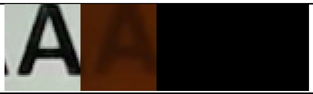	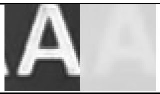		479	1983	0	0
:	:	:	:	:	:	:	:
0.25271	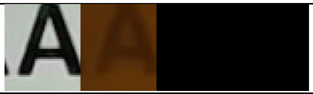	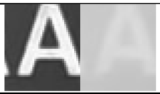		495	909	0	0
:	:	:	:	:	:	:	:
0.31447	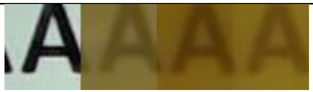			493	776	896	780
:	:	:	:	:	:	:	:
1.4288				500	603	606	608
:	:	:	:	:	:	:	:
2.3741				506	575	569	578
:	:	:	:	:	:	:	:
3.8576				509	553	553	543
:	:	:	:	:	:	:	:
5.5094				514	542	536	538
:	:	:	:	:	:	:	:
6.4047				508	528	537	536

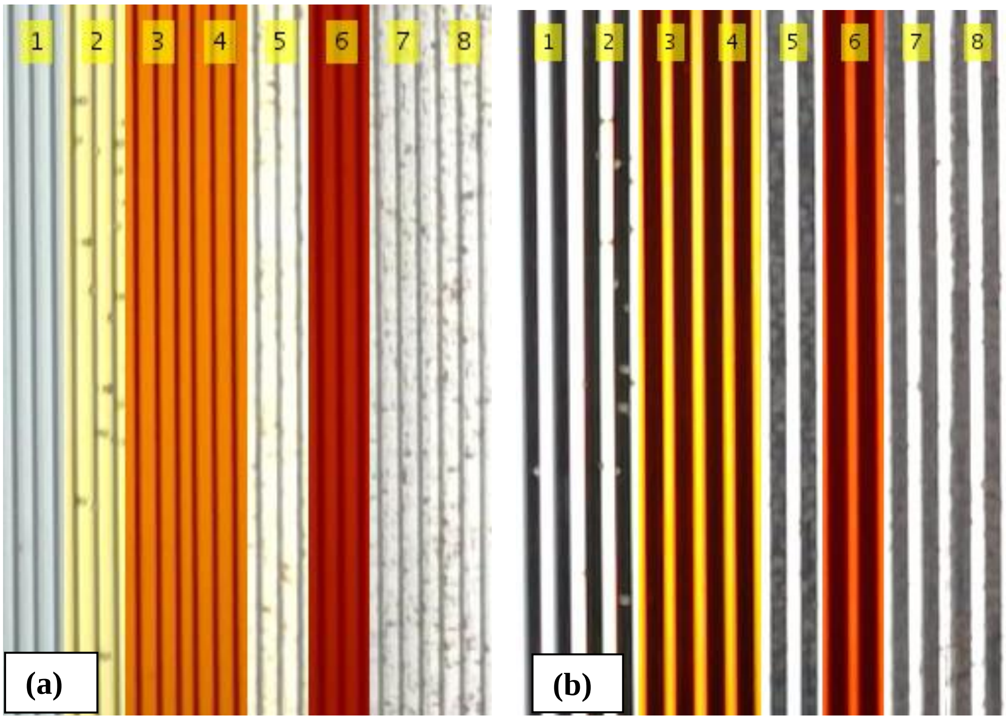

Figure 5.16 Sample ROIs produced using: (a) Thin lines and (b) Thick lines backgrounds at (5.5 h) testing time. Samples are: 1 water, 2 precursor, 3&4 hematite produced at 200 °C, 5&6 hematite produced at 300 °C and 7&8 hematite produced at 400 °C.

Table 5.7 letter areas of samples at time 0 h (before settling) for transparency quantification. Turbidity measurements at 5.5 h (end of testing time) where the lines, with the suspended particles that appeared merged with them, are optically visible.

Samples Names and ROI Numbers (Figures 5.15 and 5.16)	**Particle Size (nm) – TEM**	**Transparency in Terms of Letter Area (Pixel^2) at 0 h**	**Turbidity in Terms of Line Perimeters (Pixel) at 5.5 h**	
			Thin Lines	**Thick Lines**
Water (1)	-	505	836	830
Precursor (2)	-	475	851	833
@200°C (3 or 4)	3.8 ± 0.9	503	836	831
@300 °C (6)	26.5 ± 7	525	847	833
@400 °C (7)	41.5 ± 11.8	2034	892	845

It is worth noting that to ensure the calculated letter area is due to only the sample transparency and not affected by sample colour, the way of image analysing chosen includes transforming the coloured images to grayscale and then thresholding to black and white before determining the letter area (Table 5.6). This effect can be confirmed when comparing the letter areas of water and the yellow colour precursor that are 505 and 475 pixel^2, respectively. The slight deviation in their values (SD=± 21) might be because of the precursor's cuvette position that is, to some extent, in a brighter area than the water's, making the letter look slightly smaller than the water's. The method illustrated in Table 5.6 also measures two extreme values for the letter areas; either 0 in the case of no samples or equal to high value for the highly opaque samples that are blocking the letters; consequently, the calculated area is for the full dark ROI and not for the letter.

Moreover, other properties such as density should also be comparable to that of the reference sample for accurate transparency calculations. The dissolved in the water precursor with a concentration of 0.05 M yields a density of 0.02 g/cm^3 which can also contribute to the difference in letter areas of the two solutions, which become smaller with decreased densities, as demonstrated in Chapter 3. This observation can also be the case for hematite dispersions in water, where the Fe_2O_3 particle density is 5.26 g/cm^3 and might produce more distortion to the letter and, as a result, to the letter area. However, the effect of particle density might only become considerable with the unsettled samples while it can be neglected for the samples that have been settled to show only clear water. Yet, the resulted values in Table 5.7 shows that the area values for the stable dispersions are comparable to the same for water, unlike the value of the precursor, indicating that the density has no effect on the letter size in dispersions. The main factors affecting dispersion transparency are the refractive index (RI) of particles compared to the same for continuous phase (refractive indices should be identical for both for the sample to be transparent) and whether the particle sizes are much smaller than the wavelength of light (Abbott and Holmes, 2013).

To confirm whether a sample contains particles using the VIS-3, the differences between the clear samples and turbid samples were quantified using the thin and thick line backgrounds and compared to that of the water.

Perimeter values were calculated after settling at a point where there were still suspended particles available. Particles appear blended with the lines in the VIS-3 images (Figure 5.16), enlarging the lines perimeter and, as a result, increasing the measured pixel value of perimeter when compared to the same for clear water. This value plus the letter intensity can then provide information about a turbid solution. Conversely, the perimeters or letter intensities of other stable solutions should not change with time (in this case, it is more accurate to compare the dispersion's perimeter for the same sample before and after testing time to determine if there are any changes in turbidity). For this, to ensure accurately comparable results with water, an equal number of lines must be selected within each ROI because the MATLAB code calculates the average perimeter value of all lines inside each ROI.

The results in Table 5.7 show that the perimeter values, from the thick and thin line ROIs of the settled sample within 5.5 hours and with particles still suspended and blended with the line boundaries, are larger than the same from the water, indicating the effect of the presence of particles that enlarged the length of the perimeter. The larger value of the precursor can be attributed to the formation of bubbles after 5.5 hours of testing time, as seen in Figure 5.16 (sample 2). When comparing the results from thin and thick lines, the thin lines background produces more distinct values which can be more useful in describing the samples than the thick lines. This result might be because the latter blocks the presence of most particles available in the sample.

Table 5.8 The VIS-3 results for colour analysis for hematite dispersions using the white, red, green and blue backgrounds.

Samples	**Particle size (nm) -TEM**	**Colour (observed)**	**Colour (Pixel)**									
			FW	**FR**			**FG**			**FB**		
				R	**G**	**B**	**R**	**G**	**B**	**R**	**G**	**B**
Water	-	Colourless	202 ± 5	255 ± 0	110 ± 11	3.4 ± 4	156.4 ± 6	238.6 ± 7	92 ± 13	91.5 ± 16	216.3 ± 4	251.6 ± 0.7
Precursor	-	Light yellow	203.6 ± 4	255 ± 0	155 ± 5	3.2 ± 4	178.5 ± 6	248.8 ± 4	5 ± 9	15.6 ± 3	129.5 ± 5	248 ± 0.1
@200 ˚C	3.8 ± 0.9	Reddish orange	91.9 ± 3	255 ± 0	71.5 ± 2	2.5 ± 0.7	147 ± 0	101 ± 1	3 ± 0	11.5 ± 0.7	9.5 ± 0.7	75 ± 1
@300 °C	26.5 ± 7	Bright red	54.8 ± 1	254.5 ± 1	1.9 ± 0.3	3 ± 0	121.2 ± 3	30 ± 1	1 ± 0	6.5 ± 0.7	4 ± 0.3	58.4 ± 9
@400 °C	41.5 ± 11.8	Dark brown	32.1 ± 0.3	143 ± 7	2.5 ± 0.7	1 ± 0	26.5 ± 2	10 ± 0	3 ± 0	13 ± 0	4.5 ± 0.7	46 ± 0

Table 5.8 shows the colour average and standard deviation values which are taken for duplicate samples at the same temperature before settling (i.e. immediately after introducing the sample to the VIS-3), but the values for water and precursor are the values during the full testing time to account for changes that occur between captures (ideally, their values should be constant, but there are changes due to poor imaging quality, as previously described).

Note that in the colourless solution, the channels that the same as the colour of background has the largest pixel values, indicating that the colourless sample reflects their actual colour. This value can be a full 255 in clearer images.

For this analysis, it was necessary to test many backgrounds to investigate which produce the most sensitive channel to the samples' range of colours that can give significant comparison amongst other channels. (Kohl et al., 2006) demonstrate that because the blue is the complementary colour of yellow, the blue channel is highly sensitive to a single-component yellow-coloured solution compared with the green and red channels.

In the case of the coloured backgrounds (Table 5.8), the results are for the resulted colour after the sample colour is blended with the background colour. The results show that the red, green and blue channel values are significantly different for each background blended with the reddish colour of the samples. For the red background, as can be seen in Table 5.8, the red channel shows no sensitivity for the water, precursor and the sample obtained at 200 °C during the whole testing time. The Green channel was very sensitive to the changes because of consecutive brightness and darkness due to the camera quality in the water sample (SD=11) which is not the case in the other samples that were not affected with the imaging quality and were relatively constant with time potentially because the darker samples compared with water are less affected by the camera adjustment to the environment light. Samples at 200 °C visually had the same colour degree, and the green channel in the red background was sensitive enough to show this with only SD =2 that can be attributed to the imaging quality. The blue channel also shows little sensitivity because the pixel values are closer to 0.

Summary of Fe_2O_3 Work

As the larger particles sediments faster than the smallest size particle, the VIS-3 shows a high settling rate within the samples with the highest temperature. This outcome shows that the results from both commercial techniques of TEM and DLS are consistent with the results from VIS-3.

In all backgrounds, the average pixel values of the grayscale and R, G and B channels increase with settling.

5.3 Magnetite (Fe_3O_4) NPs

5.3.1 Materials and Methods

5.3.1.1 Formulation with CHS rig

Ammonium iron(III) citrate [$C_6H_8O_7.xFe^{3+}. yNH_3$, Sigma Aldrich] and H_2O were used as precursors to produce magnetite (Fe_3O_4) NPs (Figure 5.17).

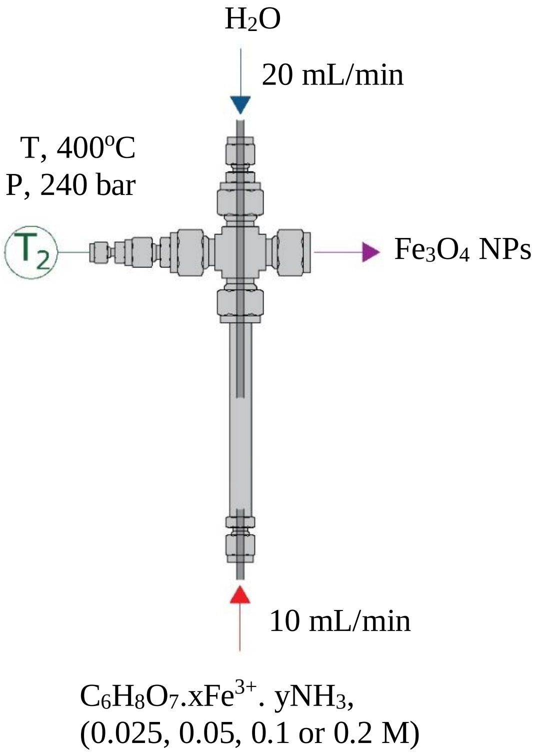

Figure 5.17 supercritical reaction conditions for formulating magnetite dispersions including the use of different metal salt concentrations while fixing other parameters (i.e. mixing point temperature 400 °C, pressure 240 bar, H_2O pumping rate of 20 mL/min downward through the water stream and metal salt with 10 mL/ min upward.

5.3.1.2 Introducing the products to the VIS-3

This work was performed in the same manner as in Section 5.2. The cuvettes were introduced to the VIS-3 from the left to the right immediately after formulation (see Figure 5.20 for the product analysis).

5.3.2 Results and Discussion

DLS Results

Table 5.9 Data produced by DLS instrument for magnetite samples including particle size and zeta potential.

Precursor's Concentration (M)	Z-Ave Size (nm)	PDI	Di90 (nm)	Di50 (nm)	Di10 (nm)	ζ (mV)	Conductivity (mS)
0.025	3049±272.4	0.391	5350	2510	1480	-33.3	1.8
0.05	485.5±17.9	0.364	1340	659	194	-40.6	3.2
0.1	457±6.3	0.284	1290	530	242	-38.2	5.4
0.2	1099± 41.9	0.525	4380	1350	397	-29.1	8.5

The results in Table 5.9 show that the DLS particle size results are comparable to those from TEM (Figure 5.18). Zeta potential values indicate that the samples at 0.05M and 0.1M are the most stable.

TEM Results

From the TEM results, magnetite particle size decreases with increasing precursor's concentration, except for the highest precursor concentration. For the 0.025M and 0.05M samples, there was no significant difference in the mean particle size (both peak and mode are at 10 nm). However, the 0.05M sample contains more particles in the smaller particle size region and less for the larger sizes (seen in the 0.05M histogram in Figure 5.18). Furthermore, TEM images show crystal magnetite particles that have a size of mostly <20nm.

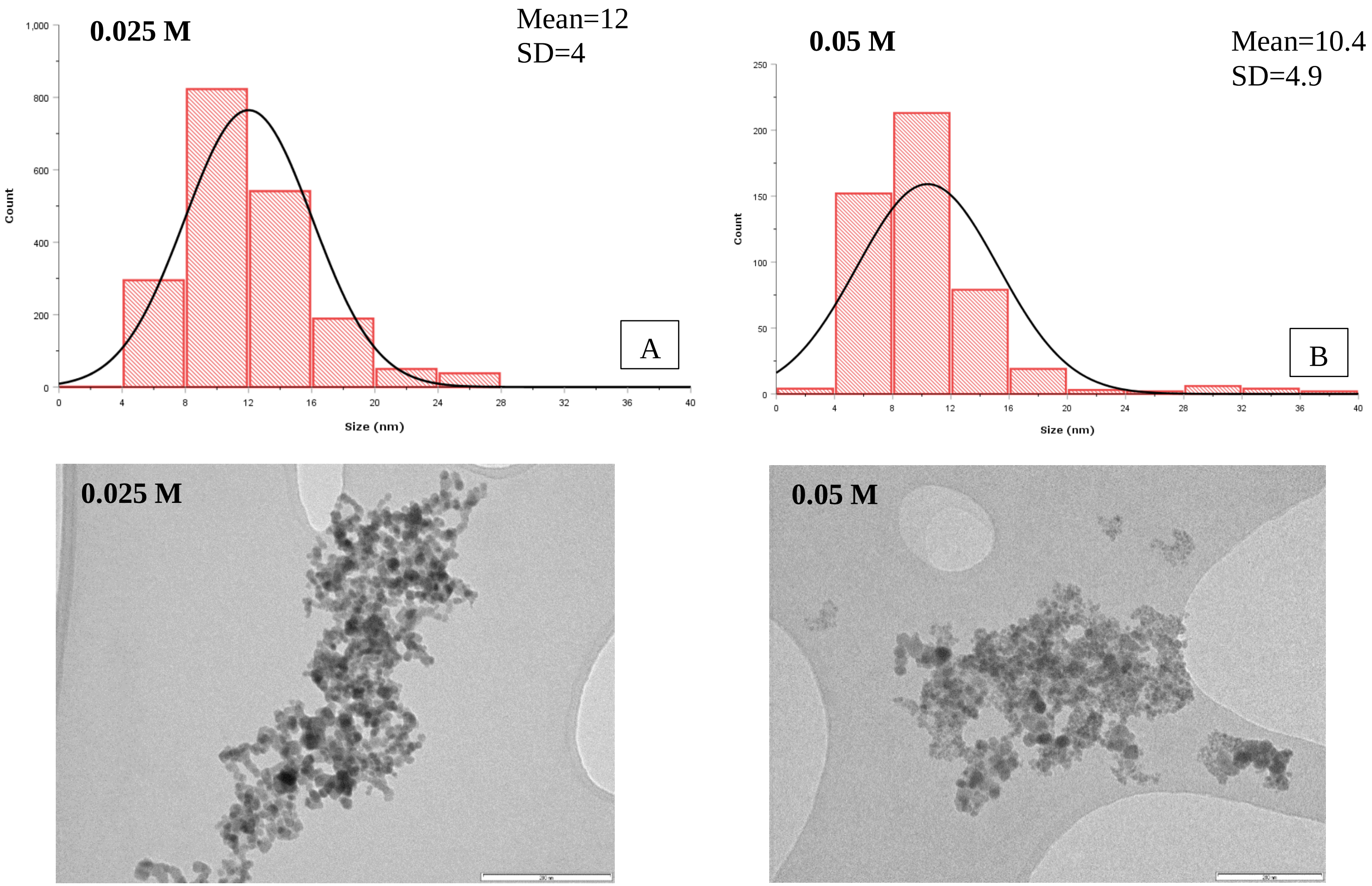

Figure 5.18 TEM images and corresponding size distributions of samples formulated at (A) 0.025, (B) 0.05, (C) 0.1 and (D) 0.2M precursor concentration. Scales in micrographs are all 200 nm.

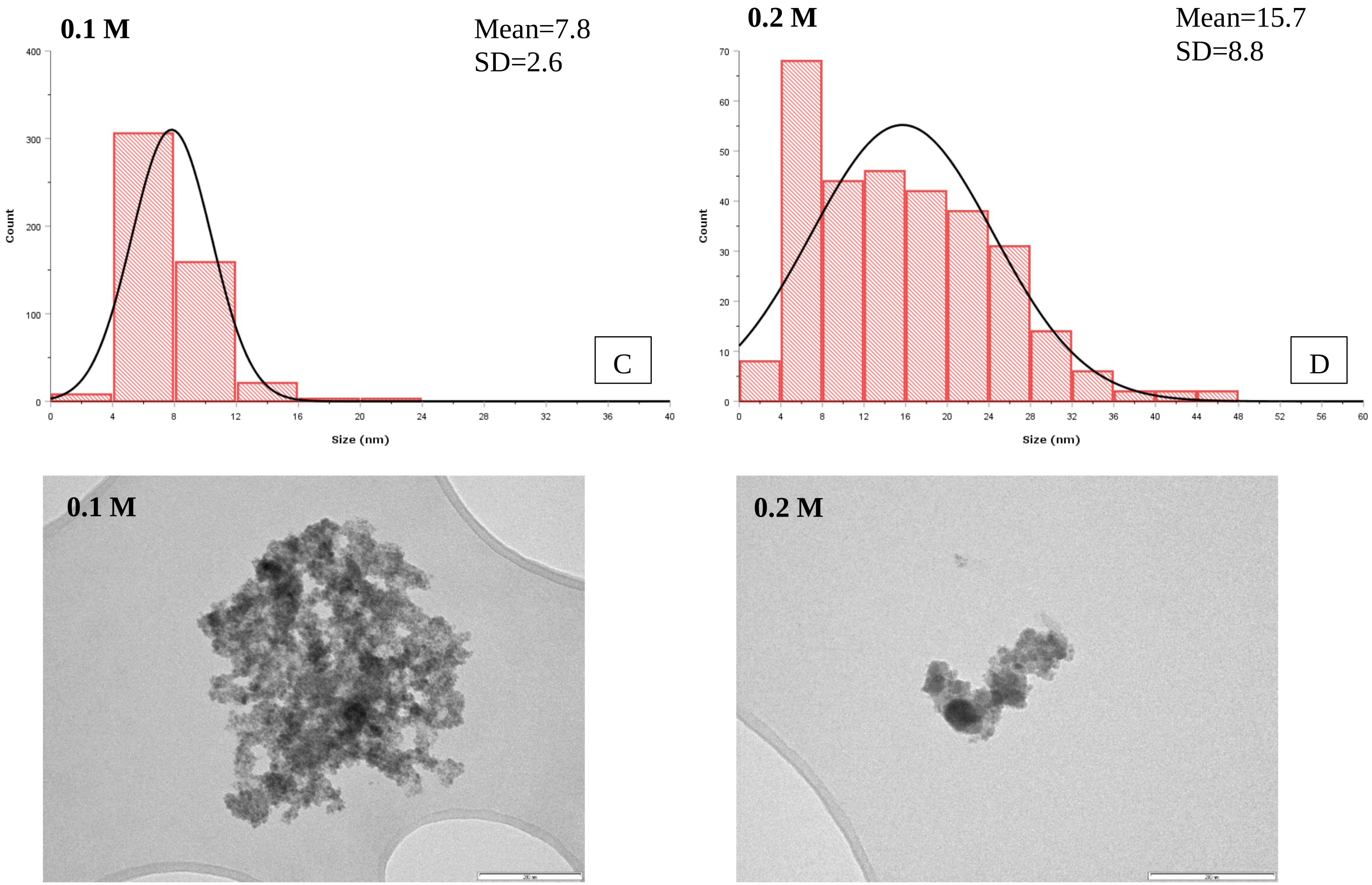

Figure 5.18 *continued*

The VIS-3 Results

Magnetite dispersions were not suitable candidates for the transparency and colour analysis because some undergo rapid settling and others remained unsettled without possible detection to the background characters. Thus, only turbidity (which is possible for the settled samples) and settling studies were presented.

5.3.2.1 Turbidity analysis using the VIS-3

Figure 5.19 depicts a complete settling of Fe_3O_4 _0.025M and Fe_3O_4 _0.2M samples because of the large agglomerations. The agglomeration was quantified using the VIS-3 by measuring the line perimeters for the samples after settling (Table 5.10). The increase in line perimeter pixel values of Fe_3O_4 _0.025M and Fe_3O_4 _0.2M dispersions compared to pure water is due to the blend of dispersion agglomerates with the perimeter in the produced images. Moreover, these results were confirmed by DLS and TEM data by showing larger particle sizes of the Fe_3O_4 _0.025M and Fe_3O_4 _0.2M dispersions compared to the unsettled dispersions (Tables 5.9 and 5.10).

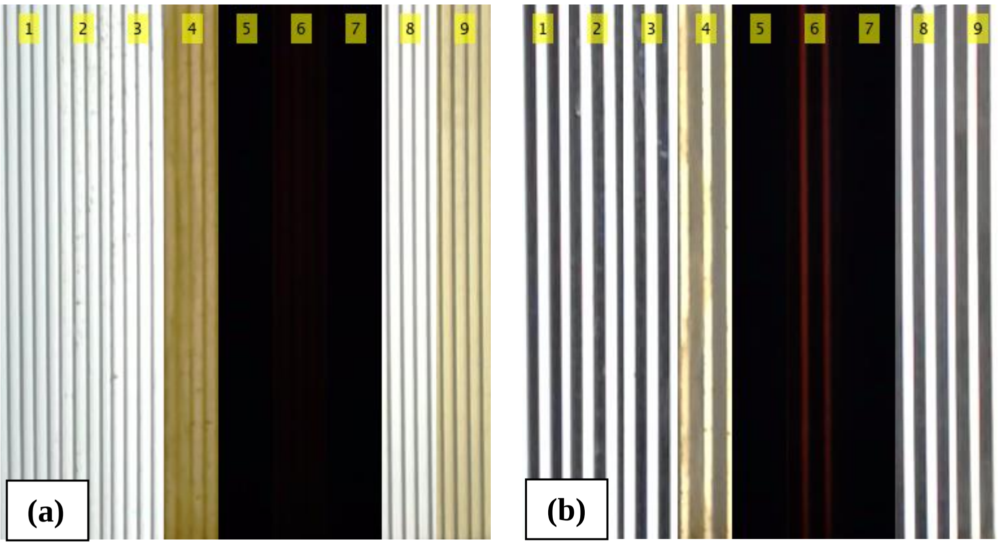

Figure 5.19 Sample ROIs produced using: (a) Thin lines and (b) Thick lines backgrounds at 16h testing time. Samples are: 1 water, 2&3 magnetite_0.025M, 4&5 magnetite_0.05M, 6&7 magnetite_0.1M and 8&9 magnetite_0.2M. (0.025, 0.05, 0.1, 0.2M represent precursor concentrations).

Table 5.10 Turbidity estimation from the VIS-3 using the lines backgrounds.

Sample Names and ROI Numbers (Figure 5.19)	**Particle Size (nm) -TEM**	**Turbidity in Terms of Line Perimeters (Pixel)**	
		Thin Lines	**Thick Lines**
Water (1)	-	770	726
Fe_3O_4 _0.025M (2)	12 ± 4	1203	1417
Fe_3O_4 _0.05M (5)	10.4 ± 4.9	- (unsettled)	- (unsettled)
Fe_3O_4 _0.1M (7)	7.8 ± 2.6	- (unsettled)	- (unsettled)
Fe_3O_4 _0.2M (8)	15.7 ± 8.8	780	730

The results in Figure 5.20 and Table 5.11 indicate that the FR is the most sensitive background because it shows the changes in sample 6 (Fe_3O_4 _0.1M) where no other background could show (as seen in the images in Figure 5.20). Consequently, FR-G gives a settling time of 7.88 h, whereas other backgrounds give almost constant values ~14 and some show no sensitivity (value of 0) (Table 5.11).

In the same manner, from the FR-G combination, the full settling times for samples 2 (Fe_3O_4 _0.025M) and 8 (Fe_3O_4 _0.2M) were 5.87 and 7.59 h, respectively. The faster settling rate can indicate the presence of larger agglomerates in the Fe_3O_4 _0.025M than the Fe_3O_4 _0.2M dispersion.

5.3.2.2 Stability studies using the VIS-3

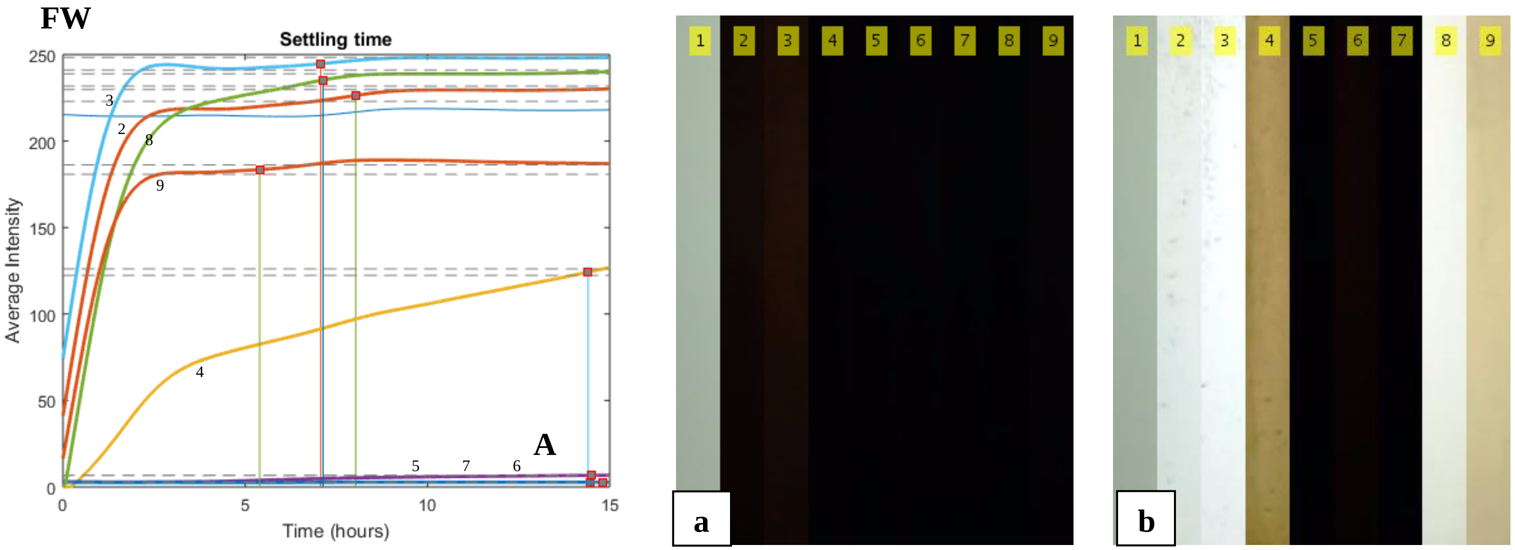

FW Before Settling

FW After Settling

Figure 5.20 Settling rates plots for Fe_3O_4 samples at different precursor concentrations for all backgrounds; a, b, c, d, e, f, g & h are ROIs for all samples before and after settling and A, B, C, D, E, F, G, H, I & J are settling plots with end-of-settling calculations.

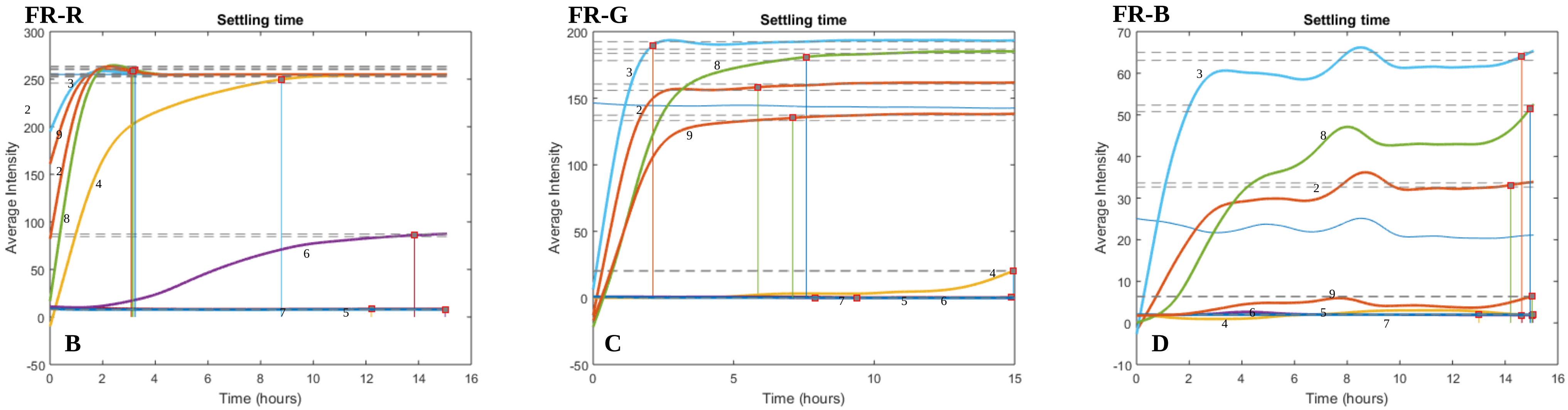

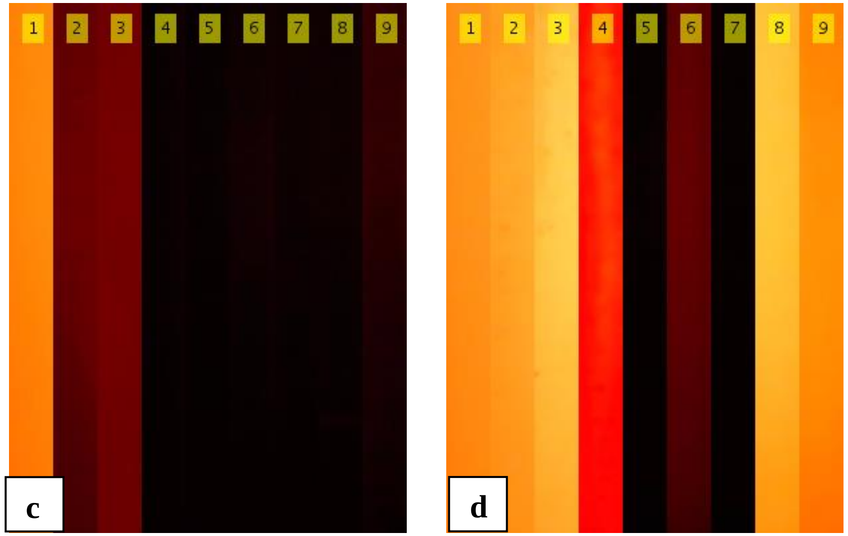

FR Before Settling

FR After Settling

Figure 5.20 *continued*

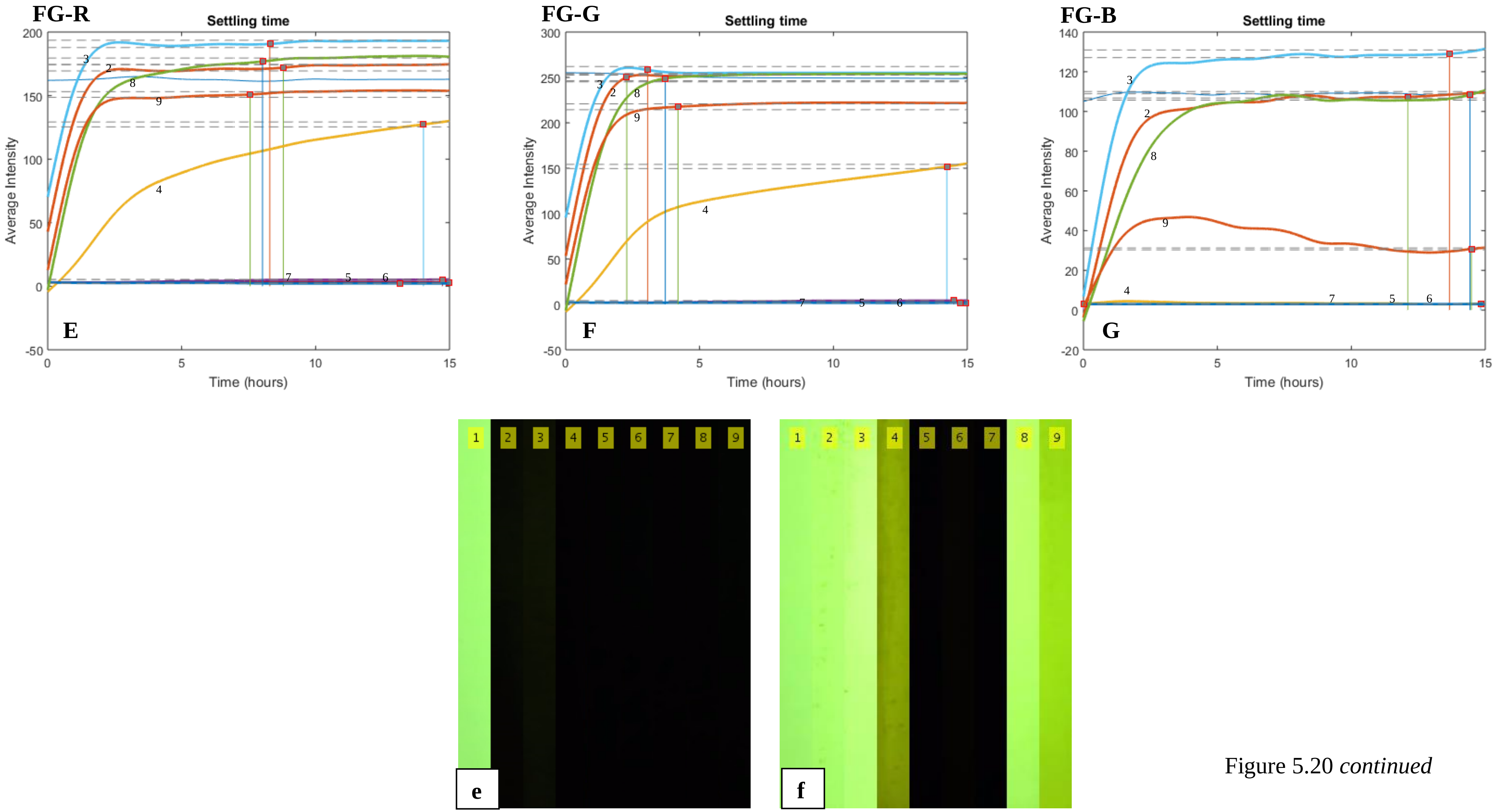

FG Before Settling

FG After Settling

Figure 5.20 *continued*

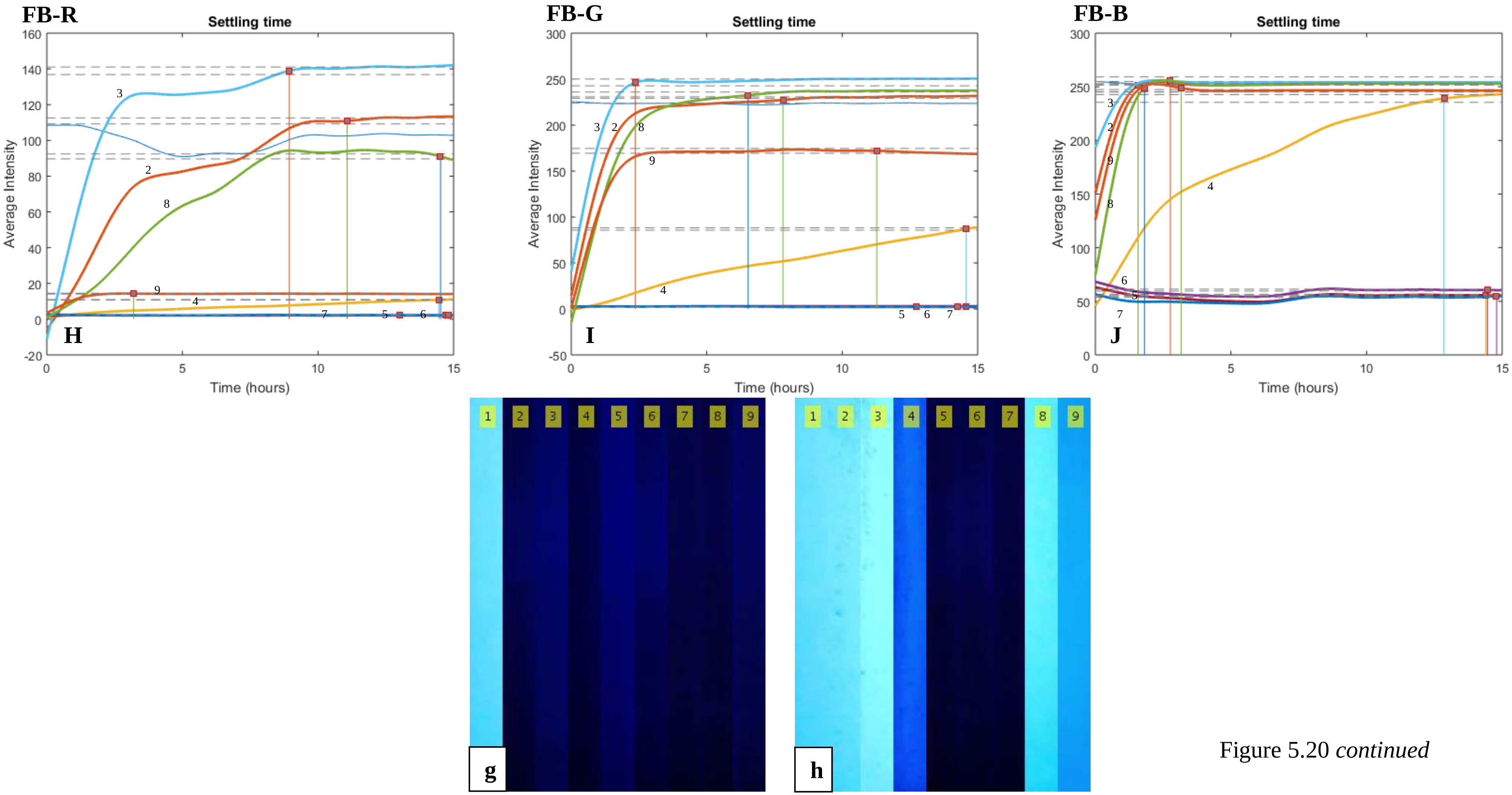

FB Before Settling

FB After Settling

Figure 5.20 *continued*

Table 5.11 Settling times calculated based on different backgrounds.

	Settling Time (h)										
Sample No.	**White**	**FR**			**FG**			**FB**			**Theoretically Using Stokes' Equation**
		R	**G**	**B**	**R**	**G**	**B**	**R**	**G**	**B**	
2	8.03	3.11	5.87	14.21	8.80	2.28	12.11	11.07	7.81	1.57	1.23
3	7.07	3.08	2.13	14.63	8.29	3.06	13.66	8.94	2.36	2.77	
4	14.41	8.79	14.95	15.00	14.03	14.24	14.83	14.45	14.58	12.85	48.65
5	14.45	13.91	14.88	13.01	14.98	14.96	0.00	13.00	14.55	14.39	
6	14.49	13.84	7.88	14.64	14.74	14.50	0.00	14.70	12.73	14.45	54.91
7	14.82	15.00	9.38	15.00	13.14	14.75	0.00	14.80	14.25	14.80	
8	7.14	3.23	7.59	14.95	8.02	3.72	14.43	14.52	6.53	1.81	9.49
9	5.40	3.16	7.10	15.00	7.56	4.20	14.48	3.20	11.28	3.17	
Average	10.73	8.02	8.72	14.55	11.19	8.96	8.69	11.84	10.51	8.23	
SD	4.15	5.52	4.37	0.68	3.30	6.07	7.24	4.07	4.50	6.35	

Settling time using **Stokes' Law**: (Fe_3O_4 particle density $\boldsymbol{\rho_p}$=5 g/ cm^3, water density $\boldsymbol{\rho_f}$=1 g/ cm^3, water viscosity $\boldsymbol{\eta}$ = 0.001 Pa.s and particle radiuses $\boldsymbol{r}$ are taken from DLS results).

$$\boldsymbol{\nu = \frac{2}{9}\frac{(\rho_p - \rho_f)gr^2}{\eta}}$$

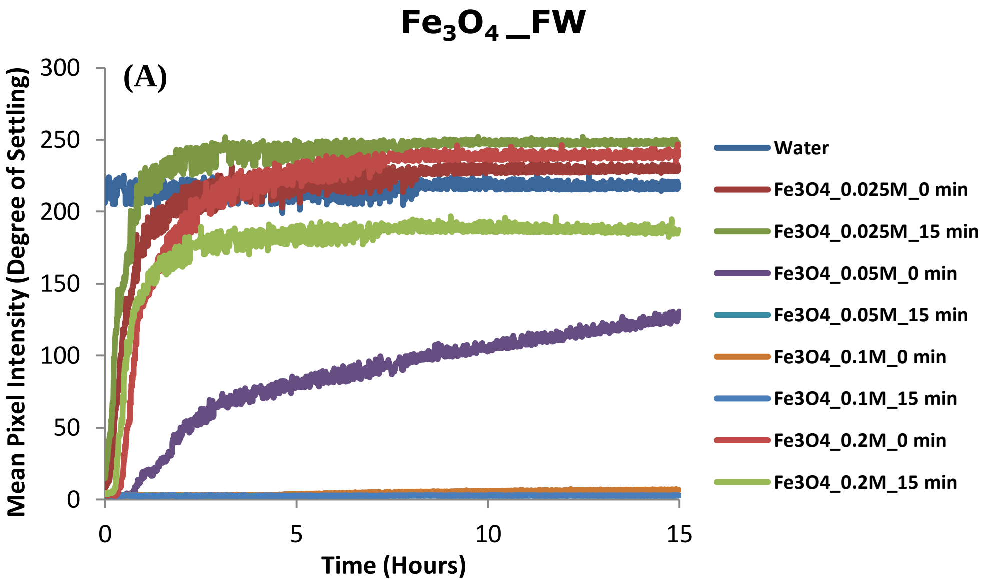

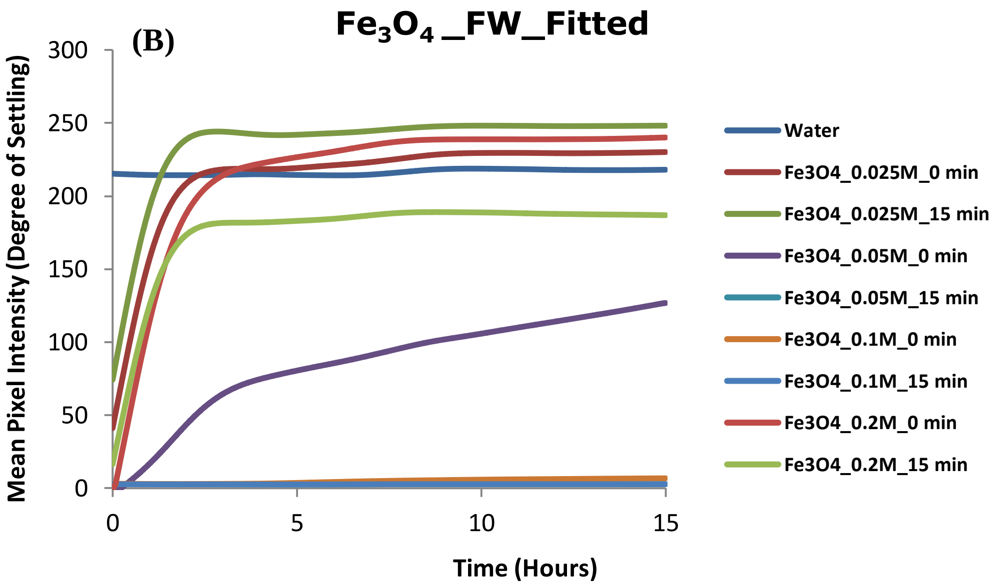

Figure 5.21 Settling plots resulted from analysing the VIS-3 images for magnetite samples for the (A) FW and (B) FW after applying the curve fitting MATLAB function.

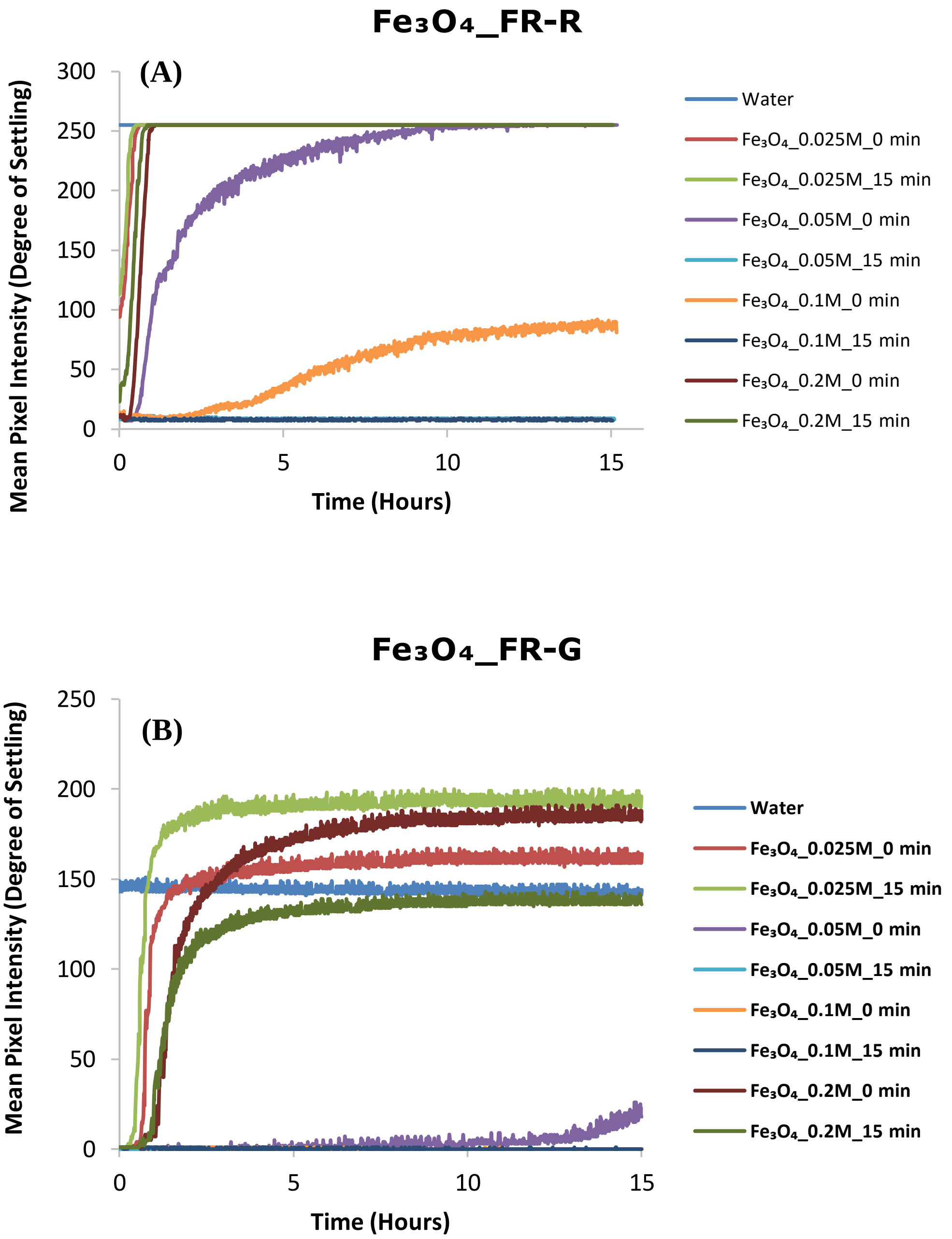

Figure 5.22 Settling plots resulted from analysing the VIS-3 images for magnetite samples for the (A) FR-R and (B) FR-G as an example amongst other backgrounds.

Figures 5.20, 5.21 and 5.22 show that samples are considered fully settled when the mean pixel intensity value is close to that of water (given that the water intensity remains constant with time). Thus, in Table 5.11, the recorded settling times are at that value for each sample. Moreover, for the samples that only partially settled during the testing time, because of a slower settling rate than the other samples and judging by the persistent red colour, the end of settling value to be considered is that at the end of testing time, as shown in Fe_3O_4_0.1M_0 min (6). For the FR-R combination (Figures 5.20 (c and d) and 5.22 (A)), images show different water colours (looks orangish in the FR background), but the MATLAB code does not seem to detect them (as it gives 255 constant value), while sample 4 shows a value of 255 after settling to bright red. Thus, the last settling value that is close to this number is what can be used to calculate settling time. Consequently, the comparison should be with the sample itself before and after settling. Sample 6 is settled but not fully because the images at end of settling show that there are still suspended particles, as evidenced by its lower than water's mean pixel value at the end of the settling test. Samples 8 and 9 have the same settling behaviour as samples 2 and 3, but there are larger agglomerates clearly visible in samples 2 and 3 (insets in Figure 5.20).

5.4 Conclusions

In this chapter, the productions of two iron oxides from different precursors were presented. Hematite shows more stability than magnetite and variations in colours and transparency were observed. The stability behaviour, transparency and colour were quantified and analysed successfully using the VIS-3 system. Exploiting different backgrounds were very useful to capture many features of the dispersions. For example, the backgrounds of the letters were used to identify the sample transparency by showing an increase of letter area (in pixels) with increasing sample's transparency. The perimeters of the thin and thick lines within equal ROIs for all the tested samples was calculated to measure the system's turbidity (i.e. to confirm the presence of large particles). The results show that larger perimeter pixel values indicate more turbid samples, as confirmed with size measurements from TEM and DLS measurements. Furthermore, the variation of colours in the transparent samples were identified using the four coloured backgrounds (white, red, green and blue), and the results are depicted in Table 5.8. Some backgrounds were more sensitive than others in evaluating the colour. While some backgrounds give higher variations in pixel values between samples of different colours, others give constant pixel values such as the FR-R combination and thus such results are eliminated and only the most sensitive combinations are considered.

Chapter 6: Hansen Solubility Parameters by the VIS-3 for Copper with Different Solvents

6.1 Introduction

In general, choosing the ideal solvent for the ideal particle can create a stable dispersion for longer and can also enhance functionality. Furthermore, using different solvents as nanoparticles matrix, in addition to water, can increase the number of dispersants that can be used to stabilise the nanomaterials. This stabilisation can be achieved by determining the types of solvents that can dissolve certain dispersant to be used as a stabiliser (i.e. allow the dispersant’s chain to extend and thus promote steric stabilisation via repulsion). This result is useful when it is necessary to produce nanomaterials with a particular combination of solvent/dispersant rather than others for various reasons such as availability, cost-effectiveness and being environmentally benign.

The Hansen solubility parameters (HSP) theory was used in this work because it comprehensively describes the theory of solubility by covering all the factors affecting the solubility or affinity between the interacting molecules. This theory is based on splitting the cohesion energy into three components, dispersion, polar bonding and hydrogen bonding. Other theories have been always limited to fewer parameters; for example, Hildebrand Solubility relies on one parameter only which is dispersion interaction. Consequently, some of the values used for this single parameter fail to describe certain systems by showing similar values for solvents that successfully dissolve a polymer as well as for solvents that do not. As such, this theory does not fit all available systems. Furthermore, previous methods such as Derjaguin, Landau, Verwey and Overbeek (DLVO) and Zeta potential can give a general idea about steric and electrostatic stabilisation of a solution but not in-depth knowledge about the compatibility between dispersed and dispersing phases.

Thus, the HSP theory established a method to determine the relationships between solvents and solutes, or nanoparticles and solvents, directly or by using a dispersant. HSP is also useful in identifying an unknown material by calculating its solubility behaviour. Furthermore, HSP can be used to estimate the shelf life performance of a system and can also estimate suitable solvents blends to dissolve a polymer or maintain system stability for which one of them would not be suitable on its own (Hansen, 2007). This knowledge is very essential in many applications such as in the coating industry to aid in the selection of solvents and in the characterisation of pigments and fillers and other components of coatings.

HSP for particles in liquids is usually estimated by observing whether this dispersion is sedimented or remains suspended during the desired period. In general, the observations are made either visually or by using a suitable instrument such as UV-visible spectroscopy (Mudunkotuwa and Grassian, 2010). In this chapter, the VIS-3 was used for the first time to observe and quantify the sedimentation behaviour that leads to the calculations of the settling time required to evaluate the HSP, as shown in the following sections.

The HSP method is devised to measure the physical properties of a material that undergoes dispersion, polar and hydrogen bonding and subsequently to compare these three component values for solvents and solutes/dispersed materials. If there are similarities, then the solvents are good to dissolve or disperse those materials. This result was derived from the main solubility principle which is “like seeks like”. The three HSP components (dispersion δ_D, polar δ_P and hydrogen bonding δ_H) are the results of the division of cohesive energy density of a substance. This division enables the quantification of each parameter separately.

1. *Dispersion parameter (δ_D) is used to describe the molecular interactions within non-polar materials based on the Van der Waals forces that govern the intermolecular bonding strength between similar molecules.*

2. *Polar parameter (δ_P) describes the behaviour of polar molecules that possess a lasting dipole moment that causes stronger attractions between molecules.*

3. *Hydrogen bonding parameter (δ_H); in this parameter, δ_H is large for the materials that are strongly hydrogen bond donors, acceptors or both.*

This chapter investigates the number of solvents that can keep the nanoparticle system stabilised without the need for a dispersant.

In this work, dispersions contain solid particles are chosen for HSP measurements. More specifically, this work studies solid surfaces which are not dissolving but rather interact with solvents that are similar in physical properties, thus, slowing down the sedimentation.

For a connection to occur between solvents and material, there should be similarities in the physical properties (dispersion δ_D, polar δ_P and hydrogen δ_H) for both. This matching is correlated based on R_a, as shown in the next section. The HSP theory seeks to measure similarities or differences between key (not necessarily all) components. A material might have similar interactions with some solvents and unique interactions with others. If there are very high differences in energies between two materials such as an organic solvent and inorganic surfaces, then there is not a unique interaction and thus they are not suitable to be characterised by HSP method unless the inorganic surface energy is modified before being introduced to solvents. High affinities can occur between a solvent and a material even if they possess a very different chemical structure.

6.2 Materials and Methods

All materials were obtained from Sigma Aldrich; Copper nitrate [$Cu(NO_3)_2$] in methanol was pumped up-flow and sodium hypophosphite [NaH_2PO_2] in methanol was pumped through the downstream in the CHS rig. The process conditions are shown in Figure 6.1.

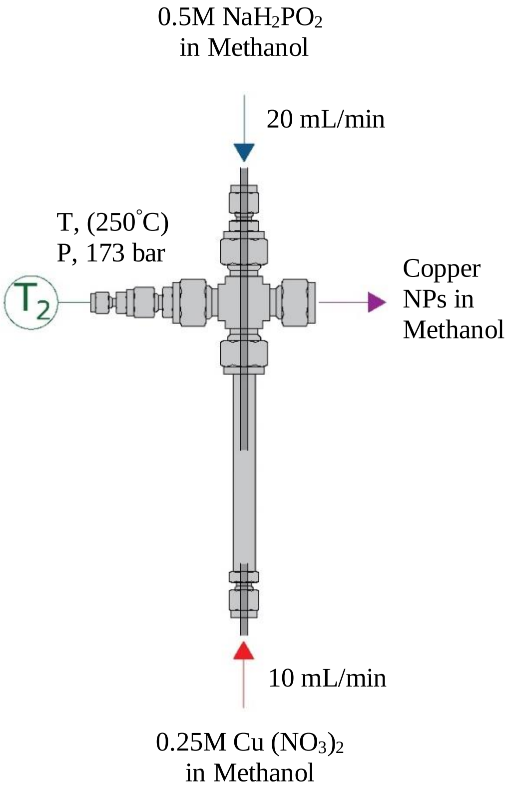

Figure 6.1 Supercritical reaction condition for formulating copper nanoparticles.

6.2.1 Copper Dispersions

Two systems of copper were used:

1. Copper dispersed in different solvents post-production.

Each sample was prepared by adding 9 g solvent to 0.25g copper dispersion, agitated and introduced to the VIS-3.

2. As-synthesised copper in methanol was sonicated at different powers and different sonication durations.

TSC was 7.5 wt.% for each tested sample. The samples as introduced to the VIS-3 from the left to the right were water, non-sonicated sample, other samples were of 50%, 75% and 100% sonication power for 2 min and 100% sonication power for 5, 7.5 and 10 min, respectively.

As described in previous chapters, materials were introduced to the VIS-3 with cuvettes filled from left to the right; however, given that the VIS-3 only accepts 10 samples at a time, four batches for the series of 34 solvents used for the HSP experiments were performed on four consecutive days.

6.2.2 HSP Measurements

The method used to determine the HSP was as follows:

1. The sedimentation time (t_s) was determined using the VIS-3, as shown in Chapter 3.

2. The relative sedimentation time (RST) was determined from the following relation (Equation 6.1):

$$\mathrm{RST} = \mathbf{t_s}(\boldsymbol{\rho}_\mathbf{p} - \boldsymbol{\rho}_\mathbf{s})/\boldsymbol{\eta} \qquad \text{Equation 6.1}$$

Where ρ_p and ρ_s are particle and solvent densities, respectively, and η is the solvent viscosity.

From the RST value, the system can be graded from the best to worst.

3. The system stability, in terms of sedimentation, was graded from 1 to 6 with 1 being the best system (indicating prolonged dispersion of particles in solvents without dissolving the particles) and 6 being the worst (particles completely settling after relatively short RST), as shown in Figure 6.2.

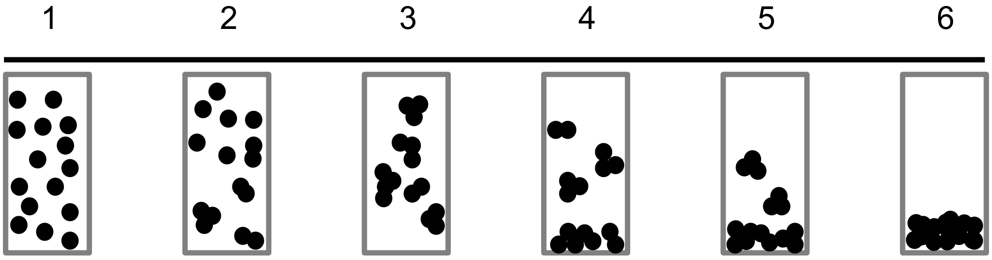

Figure 6.2 Grading the dispersion systems according to their stability behaviour; 1 indicates extreme stability and 6 indicates an extremely unstable system. The grading was done automatically using MATLAB (Chapter 3).

4. HSP was calculated for the unknown copper nanoparticles using the Hansen Solubility Parameters in Practice (HSPiP) software by inputting the resulted grades.

5. From the HSP calculated in (4), the similarity between copper nanoparticles and any solvent in terms of the distance between a material and a solvent, R_a, was determined using Equation 6.2.

$$\mathbf{R_a} = \sqrt{4(\boldsymbol{\delta}_{\mathbf{D1}} - \boldsymbol{\delta}_{\mathbf{D2}})^2 + (\boldsymbol{\delta}_{\mathbf{P1}} - \boldsymbol{\delta}_{\mathbf{P2}})^2 + (\boldsymbol{\delta}_{\mathbf{H1}} - \boldsymbol{\delta}_{\mathbf{H2}})^2} \qquad \text{Equation 6.2}$$

Where δ_D is the dispersive component, δ_P is the polar component and δ_H is the hydrogen bonding components and the subscripts of 1 and 2 represent the solvent and material, respectively. The units of solubility parameters are $MPa^{½}$.

6. The relative energy difference (RED) is determined to normalise the distances.

$$\mathbf{RED= R_a / R_o} \qquad \text{Equation 6.3}$$

Where R_a is the distance between the nanoparticle and the dispersant and R_o is the radius of interaction in the sphere (that contains all the good solvents).

For systems of solvents with nanoparticles only (i.e. without dispersants), it is more convenient to use the similarity parameters term instead of solubility parameters. In addition, the three parameters are reported as [δ_D, δ_P, δ_H].

The list of solvents used in this work and their molecular structure is shown in Section III.1 (Appendix III).

6.3 Results and Discussion

6.3.1 Determining the Solubility Parameters of Copper with Multiple Solvents

Copper nanoparticles were dispersed in different solvents post-production. The products were introduced to the VIS-3 and left for 24 hours for settling measurements. The steps mentioned in Section 6.2.2 are discussed in the following sections.

6.3.1.1 Calculating t_s using the VIS-3

A similar procedure to Chapter 5 was followed in determining the settling time by first identifying the most sensitive combination of the background-channel towards the settling behaviour in the set of samples. Figure 6.3 shows three areas of possible choices (FR-R, FB-R and FB-B). However, by close inspection to the produced data from all three choices, FB-R and FB-B have no sensitivity towards some backgrounds by giving either a value of 0, indicating the sample was not detected or giving very high settling time values for some very fast settling samples such as chloroform and cyclohexane. Thus, the most sensitive combination to be used here is the FR-R.

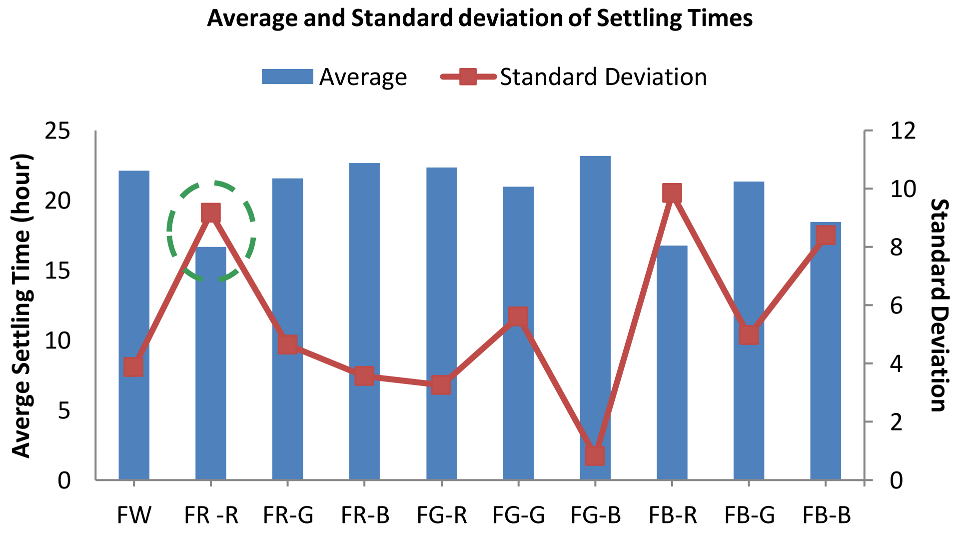

Figure 6.3 The relation between the background combinations and the average and standard deviation of settling time of dispersions in different solvents.

Section III.2 (Appendix III) shows a summary of the settling times produced by all the backgrounds. The error values generated from FB-R and FB-B backgrounds are highlighted with yellow.

The above results were obtained by dividing the 34 solvents used to four groups for the samples to be tested in the VIS-3 (the VIS-3 can accept 10 samples per run). The results are shown in Figures 6.4, 6.5, 6.6 and 6.7.

By viewing the image taken for the first group of samples after 24 hours settling time (Figure 6.4, a), in the first solvent, acetone, the copper remained suspended, but it turned darker and little evaporation occurred during the test time because of acetone's volatility, unlike other dispersions that have similar states but without evaporation, with the copper keeping its rusty colour and not turning blackish in the 3rd solution, acetonitrile. The blackish colour is seen again in the 5th, 1- butanol, 7th, γ -butyrolactone, and 10th, cyclohexanol, solutions.

Benzaldehyde solvent, originally colourless, kept the copper dispersed for up to ~12 hours; then, the copper started to drop out, leaving a light green coloured solution. This result indicates that a solubility occurred for some of the copper particles, leading to a non-pure settling phenomenon. This behaviour was captured in the settling plot (Figure 6.4, b) by showing a lower pixel value curve compared to the dispersions that eventually produced clear solutions after settling; these dispersions were represented by the settling curves in the higher pixel values region in the plot. In the case of benzaldehyde, the settling time was calculated as the time from the point settling commenced until no further settling occurs. For this calculation, the settling must be calculated from after the ~12 hours until the settling ends. For all other solutions, the settling was calculated from the first test moment.

In the n-Butyl Acetate, the 6th cuvette, most of the dispersed copper dropped out instantaneously and the small amount left settled to produce a clear solution after around 3 hours. The trend in the VIS-3 plot showed this by presenting three distinctive areas at the curve, with each area indicating what occurred at each time interval. The same happened with chloroform, the 8th cuvette, and cyclohexane, the 9th, but with the latter, the cuvette wall is left a bit stained with copper particles. It was desired that for such situation, where rapid settling occurs, one plain background design should be used during the test to monitor the changes in fewer time intervals between the successive captured images (e.g. each one second). However, the measurement procedure used in this work requires each group of images of similar backgrounds to be analysed independently, and, as a result, using all ten backgrounds during the test leave a large time gap between the subsequent images of a similar design. For HSP scoring, the t_s is taken to be the time at which settling ends (clear solution) and is equal to 24 hours where no settling occurs.

Some nanodispersions such as n-butyl acetate, chloroform and cyclohexane show a small number of particles suspended after settling ends, potentially indicating that these are smaller size particles and that their mass is lower than that of larger particles that settled faster. Cyclohexane always shows a lower trend (lower pixel values) than n-butyl acetate and chloroform because there is a larger number of particles that remain suspended. This increased number of particles makes the solution looks darker, explaining the lower pixel value (Figure 6.4, b).

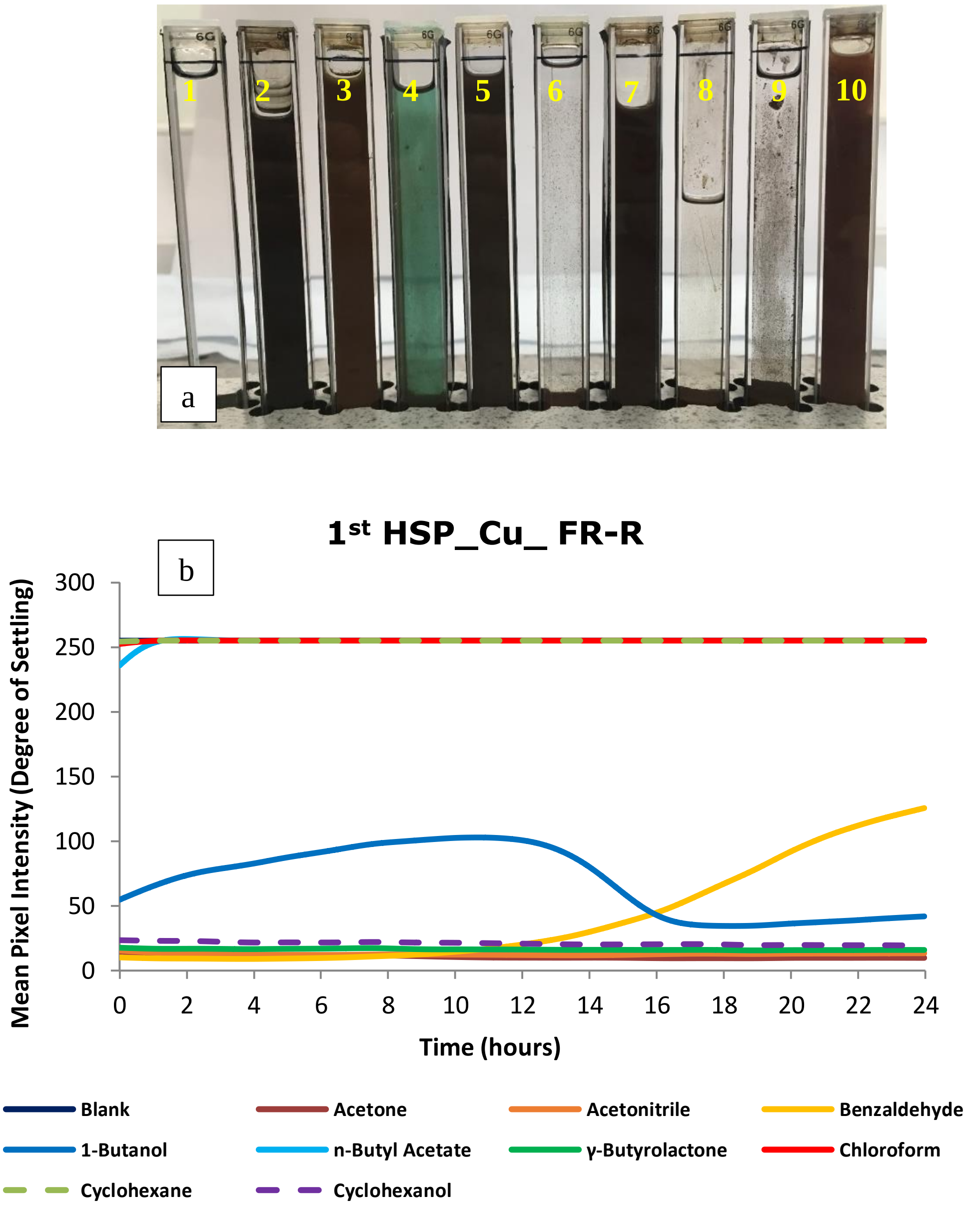

Figure 6.4 First group for Cu-Solvent system: (a) Image of samples at end of settling; from the left to the right: Blank, Acetone, Acetonitrile, Benzaldehyde, 1-Butanol, n-Butyl Acetate, γ-Butyrolactone, Chloroform, Cyclohexane, Cyclohexanol. (b) the settling rates via the VIS-3 method.

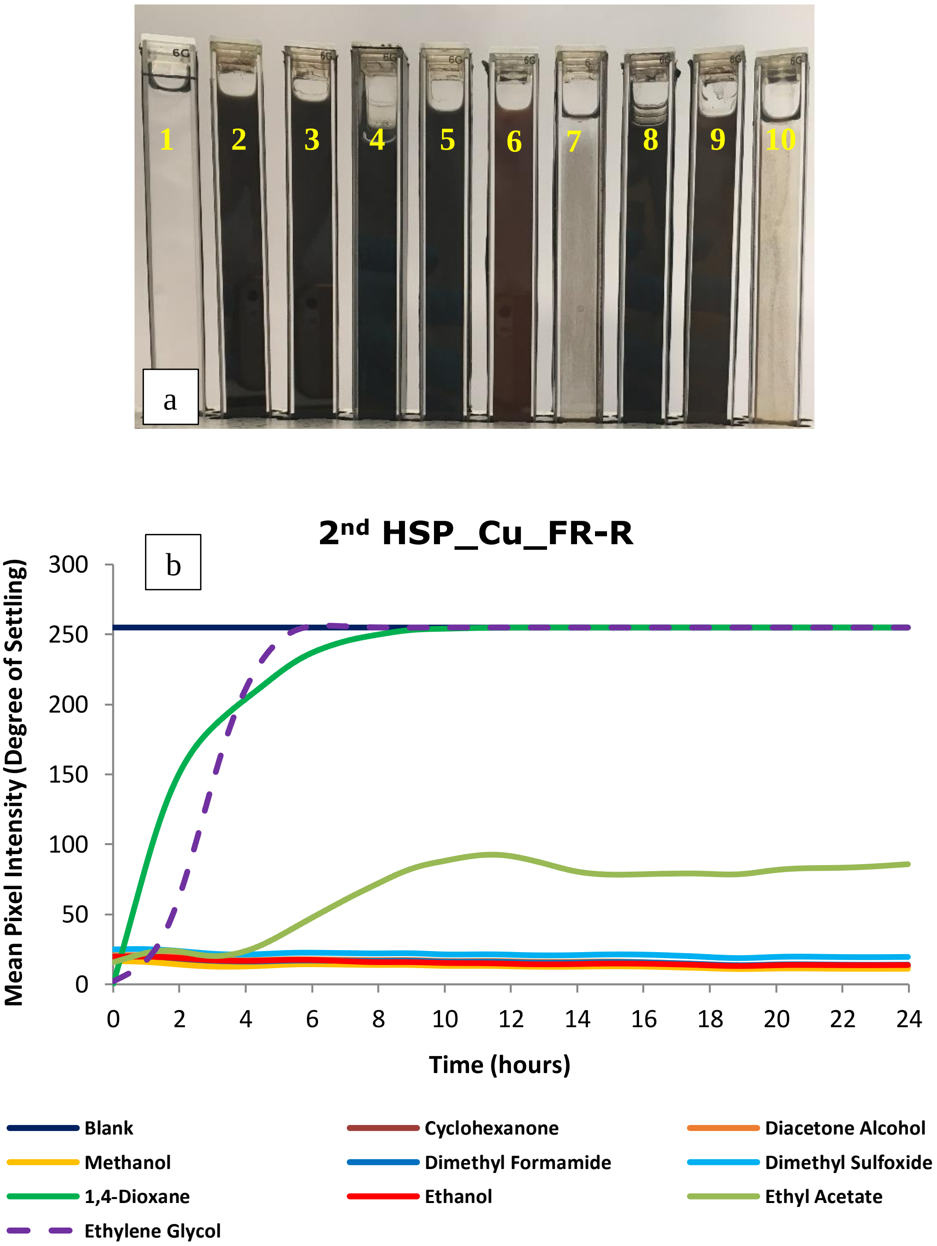

Figure 6.5 Second group for Cu-Solvent system: (a) Image of samples at the end of settling; from the left to the right: Blank, Cyclohexanone, Diacetone Alcohol, Methanol, Dimethyl Formamide, Dimethyl Sulfoxide, 1,4-Dioxane, Ethanol, Ethyl Acetate, Ethylene Glycol. (b) The settling rates via the VIS-3 method.

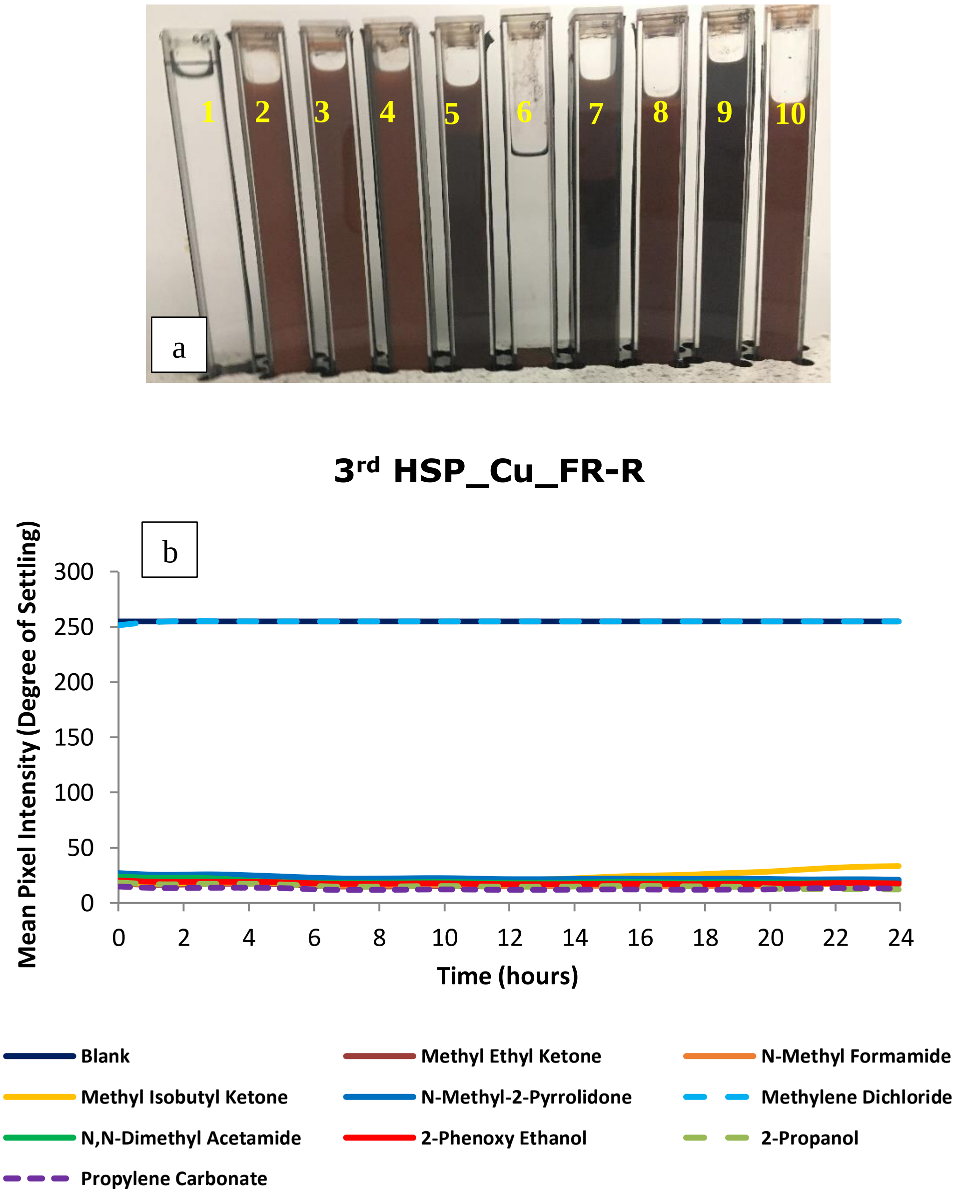

Figure 6.6 Third group for Cu-Solvent system: (a) Image of samples at end of settling; from the left to the right: Blank, Methyl Ethyl Ketone, N-Methyl Formamide, Methyl Isobutyl Ketone, N-Methyl-2-Pyrrolidone, Methylene Dichloride, N,N-Dimethyl Acetamide, 2-Phenoxy Ethanol, 2-Propanol, Propylene Carbonate. (b) The settling rates via the VIS-3 method.

In the second and third group of samples (Figures 6.5 and 6.6), most of the solvents dispersed the copper for the whole testing time (24 hours) except in the 1,4 dioxane, ethylene glycol and methylene dichloride; the samples settle at different rates and clear supernatant is left behind. These results might be because of their lower polarity compared to others, as demonstrated with the HSP measurement in the next sections.

Some of the suspended samples changed from the original copper colour to darker or black. This result might be because of the occurrence of some dissolution within the strong solvents.

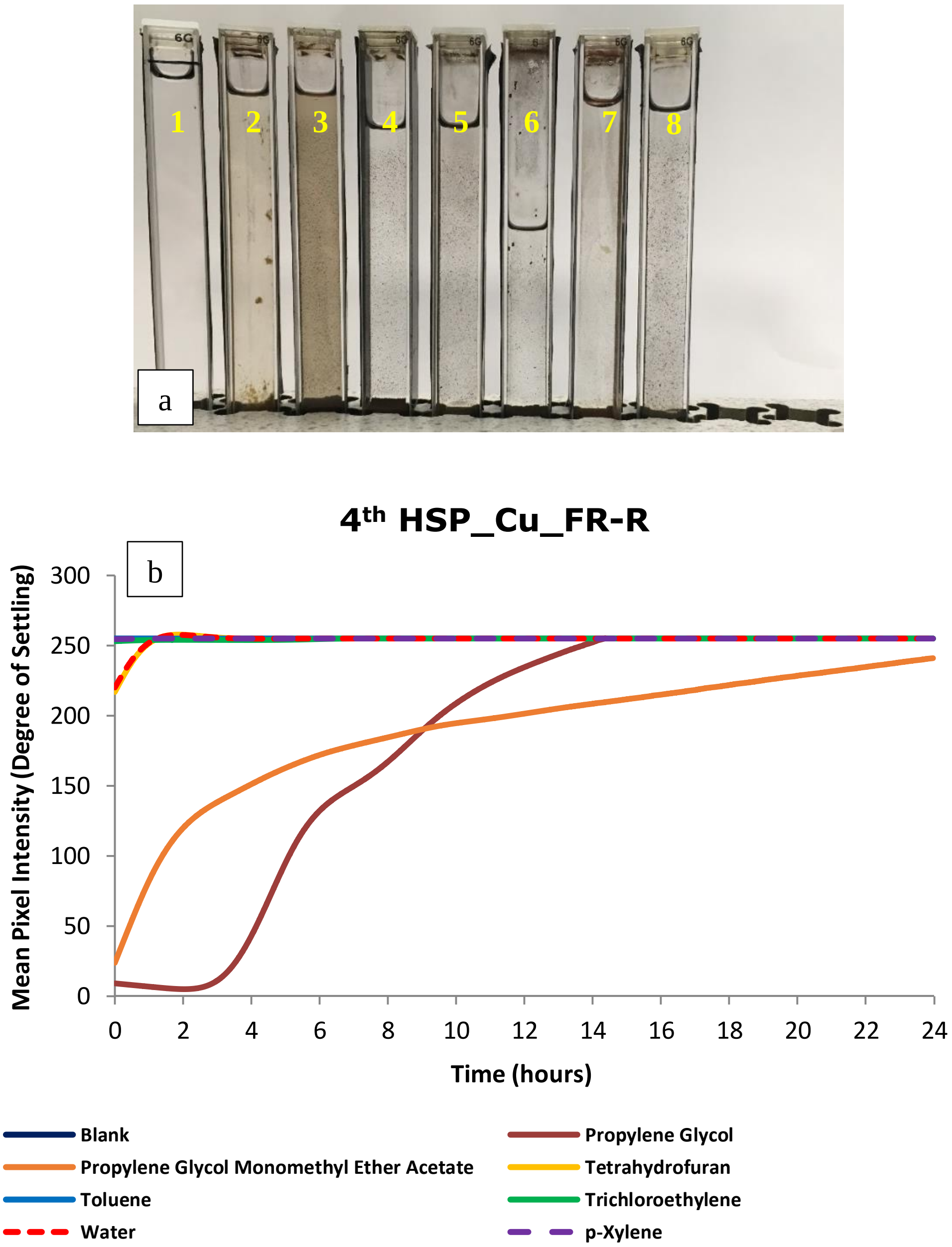

Figure 6.7 Forth group for Cu-Solvent system: (a) Image of samples at end of settling; from the left to the right: Blank, Propylene Glycol, Propylene Glycol Monomethyl Ether Acetate, Tetrahydrofuran, Toluene, Trichloroethylene, Water, p-Xylene. (b) The settling rates via the VIS-3 method.

As shown in Figure 6.7, the fourth group of solvents have caused the particles to completely settle. All the curves in the plot ended up in the high pixel area with different settling behaviour at test starting times differentiated by the rate of settling.

6.3.1.2 RST calculations

To properly compare the sedimentation times for systems of different solvents, the effect of variations in densities and viscosities of different solvents on settling has been eliminated by using Equation 6.1. The resultant RST is purely for particle sedimentations because of gravity. Table 6.1 shows the calculations of RST and the system grading based on it; t_s, RST and HSP grade data are produced automatically using the MAC (Chapter 3) after inputting the viscosity and density values.

Table 6.1 shows that for some solvents, RST values give different indications on settling behaviour than t_s (Section 6.3.1.1). The RST sometimes gives low value for a well-suspended system, as a result, their system grade is 6 and not 1, as seen in 1-butanol situation (Table 6.1). System grading is based on RST values that increase with decreasing RST. This result might contradict with the definition that states that as RST increases more of a solvent adsorbs onto the particle surface (Hansen, 2007). However, this result might also indicate that even though a solvent produces good dispersion in the current experiments, it might not perform well under further processing.

Table 6.1 Calculations of RST and HSP grading. Viscosity is at 25°C and ρ_p is 8.96 g/cm^3.

#	Solvent	η (mPa.s)	ρ (g/cm^3)	t_s (h)	RST	Grade	Status
1	Acetone	0.306	0.971	23.6	616.1	1	Remained suspended/ turned black
2	Acetonitrile	0.369	0.786	23.5	520.5	1	Remained suspended/ kept original copper colour
3	Benzaldehyde	1.39	1.045	23.6	134.4	5	Settled down/green supernatant
4	1-Butanol	2.544	0.81	23.1	74.0	6	Remained suspended/ turned black
5	n-Butyl Acetate	0.685	0.88	3	35.4	6	Settled down/ clear supernatant
6	γ-Butyrolactone	1.738	1.12	23.3	105.1	5	Remained suspended/ turned black
7	Chloroform	0.537	1.492	3	41.6	6	Settled down/ clear supernatant
8	Cyclohexane	0.894	0.779	3	27.5	6	Settled down/ clear supernatant
9	Cyclohexanol	57.5	0.962	20.2	2.8	6	Partial settling/no clear areas
10	Cyclohexanone	2.017	0.947	21.5	85.5	6	Remained suspended/ turned black
11	Diacetone Alcohol	2.798	0.931	21.8	62.6	6	Remained suspended/ turned black
12	Dimethyl Formamide	0.794	0.944	21.4	216.2	4	Remained suspended/ turned black
13	Dimethyl Sulfoxide	1.987	1.1	23.2	91.8	5	Remained suspended/ kept original copper colour
14	1,4-Dioxane	1.177	1.034	8	53.8	6	Settled down/ clear supernatant
15	Ethanol	1.074	0.789	20	152.2	5	Remained suspended/ turned black
16	Ethyl Acetate	0.423	0.902	23.1	439.6	1	Remained suspended/ turned black
17	Ethylene Glycol	16.1	1.113	5.3	2.6	6	Settled down/ clear supernatant
18	Methanol	0.544	0.791	21.5	323.1	3	Remained suspended/ turned black

Table 6.1 (*continued*)

#	Solvent	η (mPa.s)	ρ (g/cm^3)	t_s (h)	RST	Grade	Status
19	Methyl Ethyl Ketone	0.405	0.805	23.4	470.9	1	Remained suspended/ kept original copper colour
20	N-Methyl Formamide	1.746	1.011	23.9	108.6	5	Remained suspended/ kept original copper colour
21	Methyl Isobutyl Ketone	0.545	0.801	23.2	347.2	2	Remained suspended/ kept original copper colour
22	N-Methyl-2-Pyrrolidone	1.65	1.028	23.7	113.9	5	Partial settling/ no clear areas
23	Methylene Dichloride	0.413	1.325	3.6	66.7	6	Settled down/ clear supernatant
24	N,N-Dimethyl Acetamide	1.927	0.937	23.7	98.8	5	Partial settling/ no clear areas
25	2-Phenoxy Ethanol	21.5	1.106	23.8	8.7	6	Remained suspended/ kept original copper colour
26	2-Propanol	2.038	0.785	23.4	93.7	5	Remained suspended/ turned black
27	Propylene Carbonate	2.72	1.189	23.9	68.2	6	Remained suspended/ kept original copper colour
28	Propylene Glycol	40.4	1.036	23.3	4.6	6	Slow settling/ clear supernatant
29	Propylene Glycol Monomethyl Ether Acetate	0.8	0.97	22.8	228	4	Slow settling/ clear supernatant
30	Tetrahydrofuran	0.456	0.899	3	53.4	6	Fast settling/ clear supernatant
31	Toluene	0.56	0.865	0	0	6	Fast settling/ clear supernatant
32	Trichloroethylene	0.545	1.463	6.8	93.9	5	Fast settling/ clear supernatant
33	Water	0.89	1	3	27	6	Fast settling/ clear supernatant
34	p-Xylene	0.34	0.86	3	71.7	6	Fast settling/ clear supernatant

6.3.1.3 Calculating the HSP for copper nanoparticles

The next step is to identify the dispersion, polarity and hydrogen bonding properties for the unknown dispersions based on their behaviours with different solvents of known properties. These solvents with all their chemical and physical properties are available in software known as HSPiP. To obtain the unknown material, the grading produced for copper dispersion with each solvent were inputted to the software and the HSP is then calculated to be [12.1,11.9,8.3] for copper nanoparticles. Furthermore, a three-dimensional (3D) plot showing the HSP space and the interaction radius for the copper that include the good solvents is also generated (Figure 6.8).

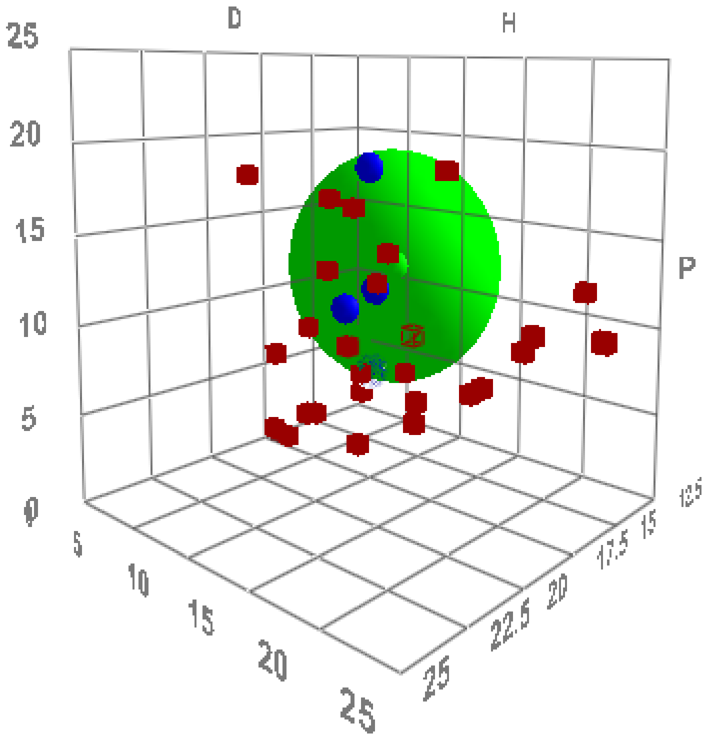

Figure 6.8 Solubility sphere for the copper nanoparticles in different solvents.

Figure 6.8 shows the sphere method used to determine the unknown HSP for a material. The 3D space shows the good solvents in blue markers inside the sphere and bad solvents in red markers outside the sphere. The scattered markers represent the solvents on the boundary between a bad solvents area and a good solvents area. In addition, the green dot in the middle represents the copper. The small sphere radius indicates that most of the solvents used were poor to keep the system stable. The software also confirms the number of good, bad and total solvents and were 6, 28 and 34, respectively.

6.3.1.4 Determining R_a and RED

In the previous step, copper's dispersion δ_D, polar δ_P and hydrogen δ_H components have been determined. These values are inputted to Equation 6.2 to determine R_a and the following Table 6.2 is produced.

Table 6.2 shows a useful feature in the HSP calculations; the distance (R_a) between copper nanoparticles (green dot in the centre of the sphere) and each solvent within the HSP space can be determined separately. If a distance is lower than the sphere radius of interaction (R_o), indicating the space that contains the good solvents as mentioned earlier, then the associated solvent can keep the system stable for a longer period. The RED value can further normalise the relation between R_a and R_o to facilitate describing a system as follows. A solvent with RED equal to 0 means no energy difference; RED less than 1 means high affinity, RED equal or close to 1 corresponds to the boundary conditions (the scattered markers in the sphere, Figure 6.8) and RED greater than 1 expresses low affinity between the interacting materials (Hansen, 2007).

Table 6.2 The HSP of solvents, Grade, R_a and RED calculations. The HSP of copper [12.1,11.9,8.3] and R_o = 9.7 are both obtained from HSPiP.

#	**Solvent**	**δ_D**	**δ_P**	**δ_H**	**Grade**	**R_a**	**RED**
1	Acetone	15.5	10.4	7	1	7.1	0.7
2	Acetonitrile	15.3	18	6.1	1	9.1	0.9
3	Benzaldehyde	19.4	7.4	5.3	5	15.6	1.6
4	1-Butanol	16	5.7	15.8	6	12.5	1.3
5	n-Butyl Acetate	15.8	3.7	6.3	6	11.2	1.2
6	γ-Butyrolactone	18	16.6	7.4	5	12.8	1.3
7	Chloroform	17.8	3.1	5.7	6	14.6	1.5
8	Cyclohexane	16.8	0	0.2	6	17.2	1.8
9	Cyclohexanol	17.4	4.1	13.5	6	14.1	1.5
10	Cyclohexanone	17.8	8.4	5.1	6	12.4	1.3
11	Diacetone Alcohol	15.8	8.2	10.8	6	8.6	0.9
12	Dimethyl Formamide	17.4	13.7	11.3	4	11.2	1.2
13	Dimethyl Sulfoxide	18.4	16.4	10.2	5	13.5	1.4
14	1,4-Dioxane	17.5	1.8	9	6	14.8	1.5
15	Ethanol	15.8	8.8	19.4	5	13.7	1.4
16	Ethyl Acetate	15.8	5.3	7.2	1	10	1.0
17	Ethylene Glycol	17	11	26	6	20.3	2.1
18	Methanol	14.7	12.3	22.3	3	14.9	1.5
19	Methyl Ethyl Ketone	16	9	5.1	1	8.9	0.9
20	N-Methyl Formamide	17.4	18.8	15.9	5	14.8	1.5
21	Methyl Isobutyl Ketone	15.3	6.1	4.1	2	9.6	1.0
22	N-Methyl-2-Pyrrolidone	18	12.3	7.2	5	11.9	1.2
23	Methylene Dichloride	17	7.3	7.1	6	10.9	1.1
24	N,N-Dimethyl Acetamide	16.8	11.5	9.4	5	9.5	1.0
25	2-Phenoxy Ethanol	17.8	5.7	14.3	6	14.3	1.5
26	2-Propanol	15.8	6.1	16.4	5	12.4	1.3
27	Propylene Carbonate	20	18	4.1	6	17.5	1.8
28	Propylene Glycol	16.8	10.4	21.3	6	16.1	1.7
29	Propylene Glycol Monomethyl Ether Acetate	15.6	5.6	9.8	4	9.5	1.0
30	Tetrahydrofuran	16.8	5.7	8	6	11.3	1.2
31	Toluene	18	1.4	2	6	17	1.8
32	Trichloroethylene	18	3.1	5.3	5	15	1.5
33	Water	15.5	16	42.3	6	34.9	3.6
34	p-Xylene	17.8	1	3.1	6	16.6	1.7

The RED values (Table 6.2) show that the best solvent to stabilise copper is acetone as it has the lowest RED. Thus, the HSP calculations shown in Table 6.2 indicate that only eight solvents can keep the system stable, namely: Acetone, acetonitrile, diacetone alcohol, ethyl acetate, methyl ethyl ketone, methyl isobutyl ketone, n,n-dimethyl acetamide and propylene glycol monomethyl ether acetate.

However, as mentioned earlier, the VIS-3 settling results in terms of t_s show different observations than those obtained from the HSP sphere. The results show that the number of solvents that can keep the dispersion suspended for the same amount of time is much more than eight (Figures 6.4, 6.5 and 6.6 show that twenty solvents kept the dispersion stable during the 24h testing time and beyond). The VIS-3 results can still be explained within the HSP values in Table 6.2; The HSP number for cupper surface energy [12.1,11.9,8.3] implies that copper is strongly polar based on its affinity to most of the solvents that have higher polar potential, as follows: n-methyl formamide with the highest δ_p (18.8) followed by acetonitrile, propylene carbonate, γ-butyrolactone, dimethyl sulfoxide, dimethyl formamide, methanol, n-methyl-2-pyrrolidone, n,n-dimethyl acetamide, acetone, methyl ethyl ketone, ethanol, cyclohexanone and diacetone alcohol.

Other good solvents such as 1-butanol, cyclohexanol, 2-phynoxy ethanol and 2-propanol show lower polarity than the above-mentioned solvents; however, this compensated by the higher hydrogen bonding capability can create even stronger dipole interactions with copper nanoparticles.

Furthermore, the reason why some solvents caused unstable systems is either because they have reacted and dissolved the copper such as with benzaldehyde leaving light green supernatant or because they are less polar such as the esters, ethers, alkanes and chlorinated solvents used here. In addition, water is extremely polar, and its molecules are attracted strongly to each other, preventing particles from dispersing within them; thus, the particles settled within a short period.

Dispersion component gives approximately comparable values in general because most of the dispersion interactions are due to van der Waals forces that govern the way this component is determined according to the HSP method.

6.3.2 As-synthesised Copper in Methanol with Sonication

Copper nanoparticles with only methanol were tested separately to investigate the effect of sonication power and period on the resulted dispersions.

First, the settling time was calculated using the VIS-3 system. Figures in Section III.3 (Appendix III) show the results from different backgrounds.

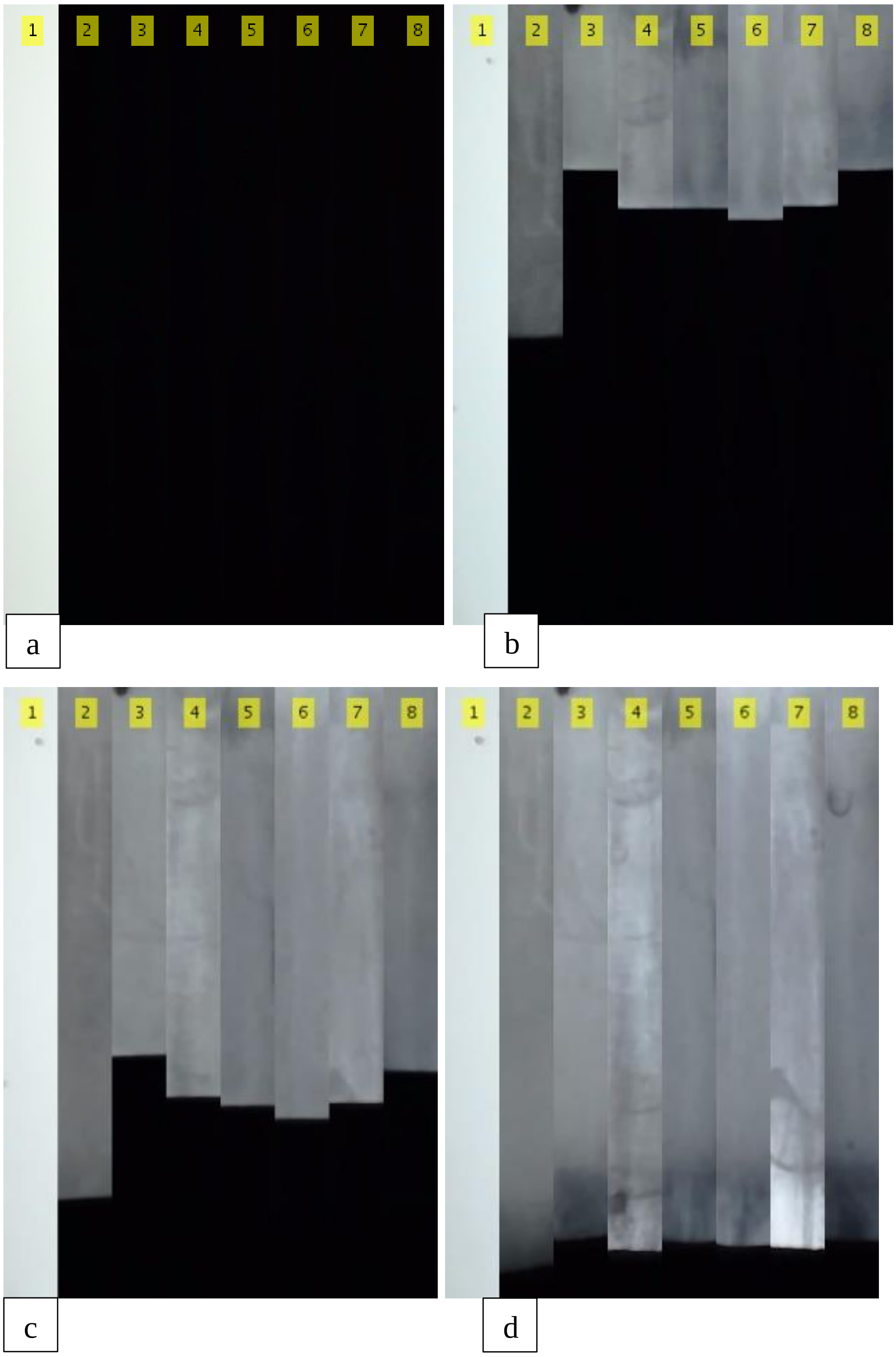

Figure 6.9 The VIS-3 images for sonicated copper settling; samples from the left to the right; Water, Blank (copper dispersion with no sonication), 50% _2 min, 75% _2 min, 100% _2 min, 100% _5 min, 100% _7.5 min, 100% _10 min in: (a) 0 hours, (b) 3.5 hours, (c) 6.5 hours and (d) 24 hours. The percentages indicating sonication power.

Figure 6.9 shows that copper in methanol has fast settled in just 6.5 hours. Furthermore, because of the higher total solid contents (7.5 wt.%) used here, the blank sample was unstable, unlike the sample of copper in methanol in the previous experiment which has lower solid contents (0.03 wt.%). The settling of samples in 24 hours duration is shown in Figure 6.11.

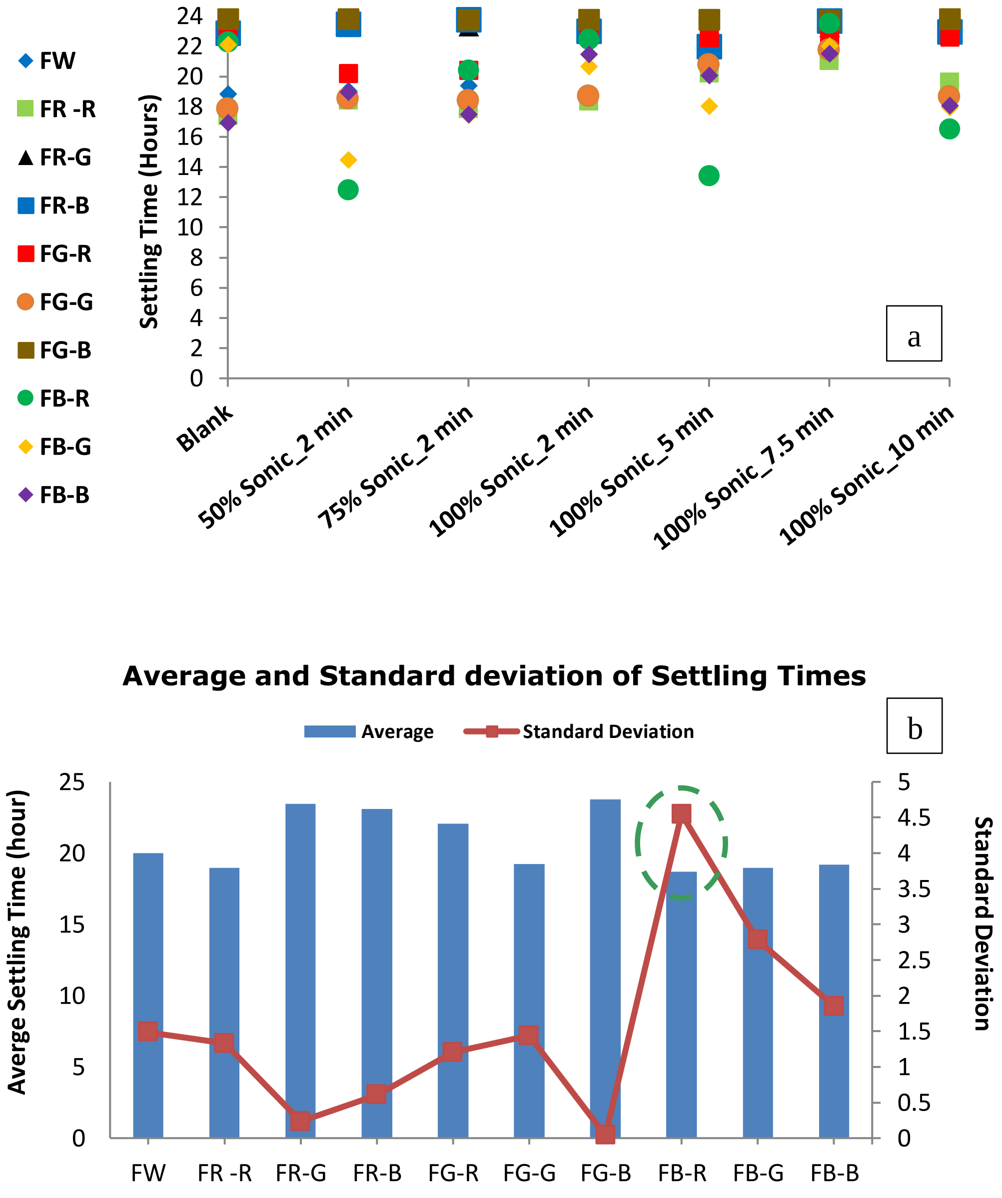

Figure 6.10 Summary of the VIS-3 results using all backgrounds for copper sonication experiments; (a) Settling time and (b) average and standard deviations of settling time. The detailed results are presented in Appendix 2-3.

By using the same strategy to select the background and channel that are most useful to describe a system (Figure 6.10), the calculated t_s from FB-R (Figure 6.11) was used to further calculate the RST and grade the system (Table 6.3).

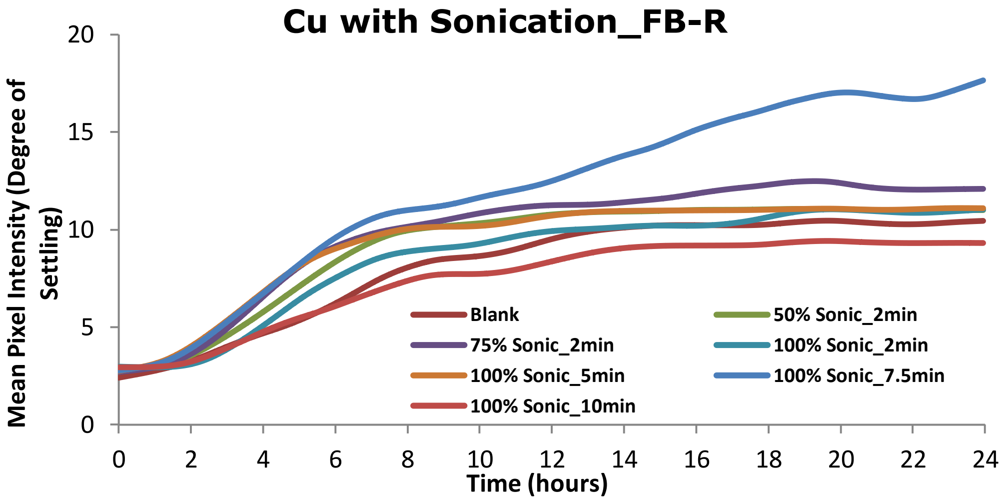

Figure 6.11 The VIS-3 settling plot using FB-R background for copper with sonication.

Figure 6.11 shows that similar settling times have been determined for all samples, indicating that sonication at different conditions made no significant difference in stabilising the solutions. However, some unexpected settling behaviour can be observed as samples sonicated at higher powers settle faster in some samples. This result might be because of agglomeration occurring during sonication that causes particles to become closer to each other and agglomerate because of van der Waals attraction forces. This result has been further confirmed from the grading obtained for these samples (Table 6.3). The grading of 5 and 6 for all the samples indicate quite similar systems in terms of stability.

Table 6.3 solvent is methanol η= 0.544 mPa.s, ρ_s= 0.791 g/cm^3 and copper ρ_p= 8.96 g/cm^3.

Sample	**t_s (h)**	**RST**	**HSP Grade**
Blank	22.3	334.5	5
50% Sonic_2 min	12.5	187.7	6
75% Sonic_2 min	20.4	306.4	5
100% Sonic_2 min	22.4	336.9	5
100% Sonic_5 min	13.4	201.1	6
100% Sonic_7.5 min	23.5	352.9	5
100% Sonic_10 min	16.5	248.1	6

6.4 Conclusions

The HSP can aid the process of choosing the right combination of solvent- dispersant with the optimum concentrations, which can be very useful in the production of nanomaterials using the CHS system. This assistance can improve the quality and stability of products, save time, cost and efforts. To achieve this goal, using the VIS-3 has simplified obtaining the grading system necessary to calculate the HSP data. Furthermore, with using the VIS-3 alone, it was possible to instantly expose some solvents that were not compatible with the copper dispersions, by observing a fast settling in the commencing of the settling test.

For the system tested in this chapter, the aim was to investigate the solvents that can disperse nanoparticles without the need to further chemicals. It was found that there are several solvents that achieve that necessity.

It is worth noting, however, that the obtained HSP for copper dispersions here are for systems that are tested for 24 hours only. These parameters might change with further ageing as the systems that were deemed to be stable for 24 hours might start to encounter sedimentation after a longer time period. Thus, measuring the HSP of such system after additional time periods might be useful for identifying the shelf life behaviour.

In addition, measuring the zeta potential for copper nanoparticle surface can be useful in confirming the encountered settling behaviour. However, the method used in this chapter is to simplify the process of choosing the most desired solvent by using a technique based on well-established prediction rather than comprehensive characterisation that can lead to numerous trial and error experiments.

Lastly, blending two or more poor solvents could produce new solvents capable of dispersing the nanoparticle system. Thus, identifying these poor solvents can also be useful for this purpose. Full automation of this process with the use of robotics, combined with the VIS-3, could also accelerate the process of optimisation for stable dispersions.

Chapter 7: Conclusions and Future Work

This thesis has demonstrated the use of a novel technique to quantify the stability behaviour of different systems. Furthermore, samples with different properties such as colour, transparency and dispersibility were chosen to ascertain the ability of the VIS to characterise such properties. The VIS has been successful in describing many systems as was detailed in the previous chapters and concluded in the following sections.

7.1 The VIS Validation

In Chapter 3, all the possible methods to validate the novel instrument (the Visual Imaging System) were presented. Three designs were explored to minimise the errors occurred during the different stages of development and to maximise the functionality of the VIS. Specifically, issues with the reliability of the obtained data were as a result of the unstable parts in the VIS-1 or due to the quality of images in the VIS-3. Most of the issues were accounted for by using a suitable MATLAB image analysing procedure.

7.2 TiO_2 Stability Studies using the VIS-2

In Chapter 4, the VIS principle was used for the first time to monitor system stability. TiO_2 aqueous dispersion, produced by the University of Nottingham’s CHS rig, was used for this study for its availability and ease of formulation and modification. The dispersions were tested either as produced or after functionalisation (by varying pH and conductivity and using a surfactant with different concentrations). Subsequently, dispersion stability, in terms of sedimentation behaviour, was evaluated by recording the changes in the mean pixel values in correlation with time. The VIS-2 successfully described the dispersions stability by showing an increase in the mean pixel values with time, for the unstable dispersions, which indicates that sedimentation occurs. The results were further confirmed by evaluating the TiO_2 dispersions properties through in-depth characterisations using the SEM, TEM and DLS techniques.

7.3 Iron oxide Dispersions Stability Studies using the VIS-3

Chapter 5 focused on the production of metal oxides using the CHS rig. Using different precursors leads to the formation of different types of metal oxides; Fe_2O_3 from Iron(III) nitrate and Fe_3O_4 from Ammonium iron(III) citrate at similar production conditions. The two iron oxides show different properties in terms of colour, turbidity and stability. Using the VIS-3, it was possible to capture such properties by means of variation in pixel values between different situations. The theories of settling due to the presence of larger particle size samples were confirmed using commercial instruments.

7.4 Solubility Parameters using the VIS-3

In Chapter 6, the HSP were successfully determined using the settling data from the VIS-3 for the first time. As mentioned in Chapter 3, the quantification of settling time was done by first having images of the samples for as long as the user judges it required, then using a custom MATLAB code for automatically processing more than 5000 images at less than 5 second intervals for each sample. After that, the images were analysed for settling time. Previously, this was done either by monitoring the settling visually where a person must be available for manually timing the settling for each sample. This can be impractical and produces quite inaccurate results in addition to the greater efforts which are required. Other methods used are some instrumentation (such as UV-visible spectrophotometer) that are not readily available, expensive and require high training and a relatively longer time for sample preparation in order to use them. Furthermore, all other HSP calculations for the RST and grading the system were automated using a MATLAB and obtained promptly. Thus, the use of the VIS-3 system has highly simplified and expedited obtaining the results from such methods.

7.5 Future work

Possible future plans are as follows:

1. For the stability studies using the VIS, destabilisation in the form of creaming, Figure 7.1 (a), can also be identified and estimated in addition to the sedimentation, by employing the following procedure: using a MATLAB code, the ROIs can be divided into upper and lower halves:. Then, the difference between the average intensity of the halves can be recorded, as shown by Figure 7.1 (b).

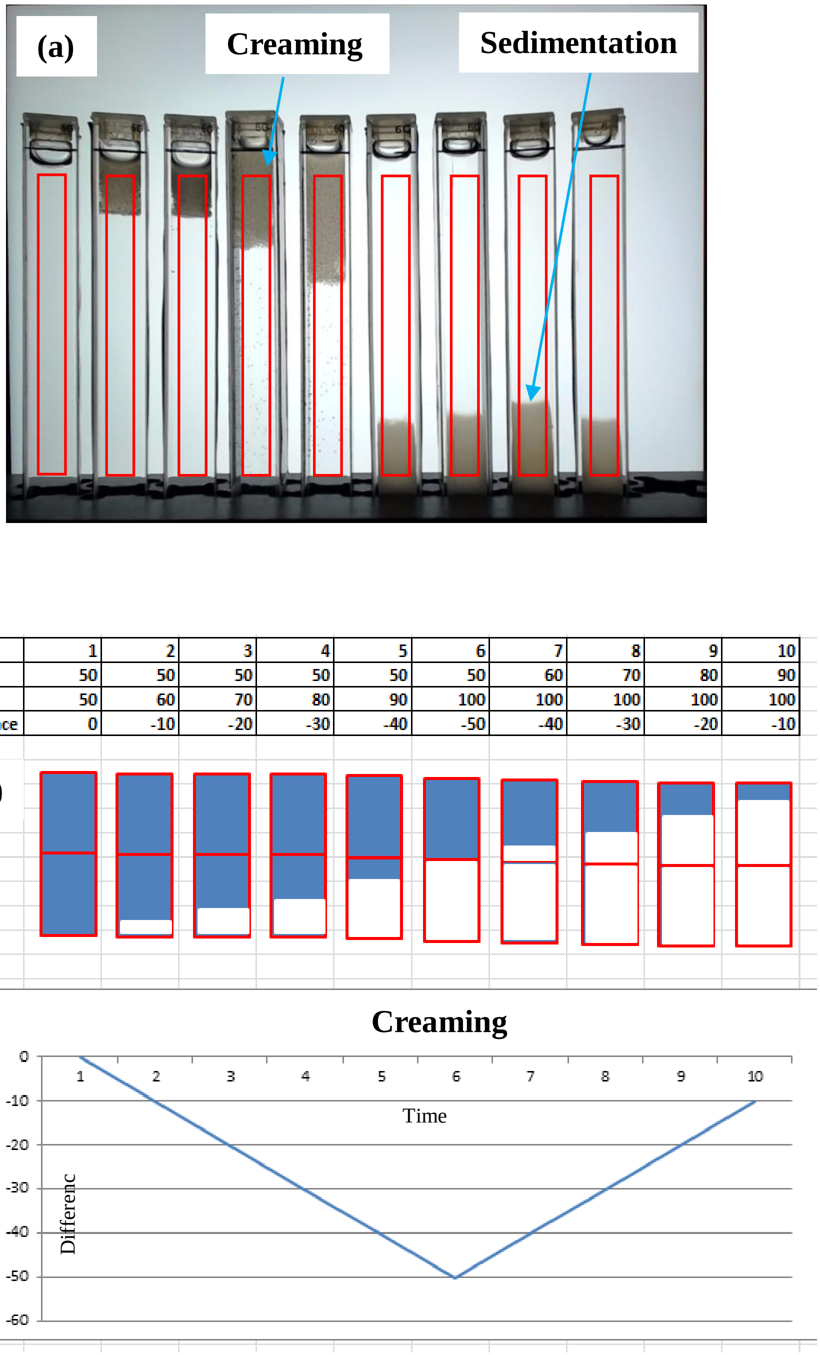

Time	1	2	3	4	5	6	7	8	9	10
Upper	50	50	50	50	50	50	60	70	80	90
lower	50	60	70	80	90	100	100	100	100	100
Difference	0	-10	-20	-30	-40	-50	-40	-30	-20	-10

Figure 7.1 (a) Example image showing creaming and sedimentation of dispersions produced by the University of Nottingham's CHS rig. (b) Example of the suggested measurements to detect and estimate both creaming and sedimentation. Red rectangles indicate the ROIs.

The difference can then be plotted in correlation with the testing time to provide the creaming or sedimentation measurements. Creaming is represented in the chart shown in Figure 7.1 (b). Conversely, in case of sedimentation, the plot would be flipped vertically. In case of stable dispersion, a straight line at 0 value can be obtained.

2. For the HSP studies, solvent blend systems, in order to improve dispersion stability, can be constructed and monitored using the VIS, and a comparison with the pure solvents that have already been measured, so as to determine the best solvent system that can achieve stability for a certain dispersion, can be conducted. Furthermore, the VIS coupled with the HSP method can be used for systems of nanoparticle dispersions that were stabilised by using commercial dispersing additives to provide an estimation of the unknown additive properties. In addition, comparing the performance of different additives to stabilise a dispersion might allow for eliminating the expensive ones and, thus, allow the use of the most economic additive. Therefore, cost benefits to the end-users can be achieved. All the above experiments can be conducted rapidly by testing multiple samples at the same time (up to 10 samples using the VIS-3).

3. Modification of a robotic system that is already available at the University of Nottingham to be used as an automated VIS system to automatically fill in a set of liquid samples with the advantages of real-time monitoring, especially in the application of the HSP method. The HSP measurements can be conducted by filling and mixing different solvents and additives with the targeted sample. Then, the mixed solutions are transferred systematically to the cuvettes that are placed in front of an iPad with a changing background (Figure 7.2). In addition, the automated system can also be used to monitor nanoformulations in real-time the moment that

they are produced by the CHS rig, by continuously extracting the products from the rig and filling the cuvettes within a desired duration.

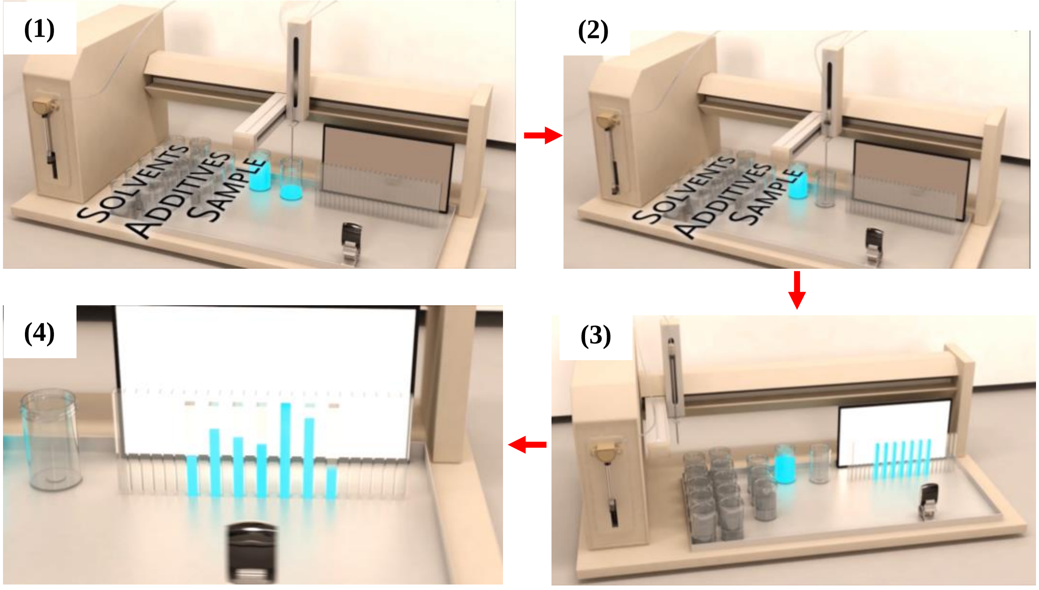

Figure 7.2 Different stages of samples introduced to the automated VIS: (1) sample been mixed with different solvents and additives (2) sample ready to be measured is extracted, (3) cuvettes are filled with samples of varied ratios of solvents and additives, and (4) samples undergo different settling rates.

4. Using the VIS method to characterise transparent polymer nanocomposites before and after a modification to improve their properties. Therefore, the VIS can be expanded to measure transparent solid samples in addition to liquids.

5. General improvement to the image qualities by using a higher quality camera to further confirm the reliability and reproducibility of the resulted data.

6. In addition to monitoring the stability of nanoparticle dispersions produced by the University of Nottingham's CHS rig, the VIS can be used in number of other applications by the determination of sedimentation, creaming or agglomeration in complex systems including: home and personal care (make-up foundation, nail varnish and lipstick), pharmaceutical (emulsions or nanoparticle suspensions that are used as drug carriers), paint and inks, food and beverages (emulsions such as beverages made from milk with different additives and soft drinks), oil and petroleum (in combination with the HSP method, the most suitable additive, to improve the fuel oil quality for example, can be identified) and suspensions (such as metal oxides or carbon nanotubes) that are used as coatings or dispersed in polymers and other materials to enhance their physical, chemical or mechanical properties.

References

ABBOTT, S. & HOLMES, N. 2013. *Nanocoatings: Principles and Practice: From Research to Production*, DEStech Publications, Inc.

ABOU EL-NOUR, K. M. M., EFTAIHA, A., AL-WARTHAN, A. & AMMAR, R. A. A. 2010. Synthesis and applications of silver nanoparticles. *Arabian Journal of Chemistry,* 3**,** 135-140.

ACEVEDO-SANDOVAL, O., ORTIZ-HERNÁNDEZ, E., CRUZ-SÁNCHEZ, M. & CRUZ-CHÁVEZ, E. 2004. El papel de óxidos de hierro en suelos. *Terra Latinoamericana,* 22**,** 485-497.

ADSCHIRI, T., HAKUTA, Y. & ARAI, K. 2000. Hydrothermal synthesis of metal oxide fine particles at supercritical conditions. *Industrial & Engineering Chemistry Research,* 39**,** 4901-4907.

ADSCHIRI, T., HAKUTA, Y., SUE, K. & ARAI, K. 2001. Hydrothermal synthesis of metal oxide nanoparticles at supercritical conditions. *Journal of Nanoparticle Research,* 3**,** 227-235.

ADSCHIRI, T., KANAZAWA, K. & ARAI, K. 1992. Rapid and continuous hydrothermal crystallization of metal oxide particles in supercritical water. *Journal of the American Ceramic Society,* 75**,** 1019-1022.

AGILENT. 2000. *Fundamentals of modern UV-visible spectroscopy, Primer* [Online]. Available: https://www.agilent.com/cs/library/primers/Public/59801397_020660.pdf [Accessed].

AHMAD, J., DESHMUKH, K., HABIB, M. & HAGG, M. B. 2014. Influence of TiO2 Nanoparticles on the Morphological, Thermal and Solution Properties of PVA/TiO2 Nanocomposite Membranes. *Arabian Journal for Science and Engineering,* 39**,** 6805-6814.

AKSOMAITYTE, G., POLIAKOFF, M. & LESTER, E. 2013. The production and formulation of silver nanoparticles using continuous hydrothermal synthesis. *Chemical engineering science,* 85**,** 2-10.

AL-ATTA, A., HUDDLE, T., RODRÍGUEZ, Y. G., MATO, F., GARCÍA-SERNA, J., COCERO, M. J., GOMES, R. & LESTER, E. 2018. A techno-economic assessment of the potential for combining supercritical water oxidation with 'in-situ'hydrothermal synthesis of nanocatalysts using a counter current mixing reactor. *Chemical Engineering Journal,* 344**,** 431-440.

AL-DURI, B., ALSOQYANI, F. & KINGS, I. 2015. Supercritical water oxidation for the destruction of hazardous waste: better than incineration. *Phil. Trans. R. Soc. A,* 373**,** 20150013.

AL-DURI, B., PINTO, L., ASHRAF-BALL, N. & SANTOS, R. 2008. Thermal abatement of nitrogen-containing hydrocarbons by non-catalytic supercritical water oxidation (SCWO). *Journal of Materials Science,* 43**,** 1421-1428.

ALLAKER, R. P. & REN, G. 2008. Potential impact of nanotechnology on the control of infectious diseases. *Transactions of the Royal Society of Tropical Medicine and Hygiene,* 102**,** 1-2.

AMIRI, S. & SHOKROLLAHI, H. 2013. The role of cobalt ferrite magnetic nanoparticles in medical science. *Materials Science and Engineering: C,* 33**,** 1-8.

ANDERSEN, H. L., JENSEN, K. M. O., TYRSTED, C., BOJESEN, E. D. & CHRISTENSEN, M. 2014. Size and Size Distribution Control of gamma-

Fe2O3 Nanocrystallites: An in Situ Study. *Crystal Growth & Design,* 14**,** 1307-1313.

BAI, R. G., MUTHOOSAMY, K., SHIPTON, F. N. & MANICKAM, S. 2017. Acoustic cavitation induced generation of stabilizer-free, extremely stable reduced graphene oxide nanodispersion for efficient delivery of paclitaxel in cancer cells. *Ultrasonics Sonochemistry,* 36**,** 129-138.

BASA, S., MUNIYAPPAN, T., KARATGI, P., PRABHU, R. & PILLAI, R. 2008. Production and in vitro characterization of solid dosage form incorporating drug nanoparticles. *Drug development and industrial pharmacy,* 34**,** 1209-1218.

BERMEJO, M. & COCERO, M. 2006. Supercritical water oxidation: a technical review. *AIChE Journal,* 52**,** 3933-3951.

BEZZI, G., CELOTTI, G., LANDI, E., LA TORRETTA, T., SOPYAN, I. & TAMPIERI, A. 2003. A novel sol–gel technique for hydroxyapatite preparation. *Materials Chemistry and Physics,* 78**,** 816-824.

BHATTACHARJEE, S. 2016. DLS and zeta potential - What they are and what they are not? *Journal of Controlled Release,* 235**,** 337-351.

BHUSHAN, B. 2010. Introduction to nanotechnology. *Springer handbook of nanotechnology***,** 1-13.

BLOOD, P. J., DENYER, J. P., AZZOPARDI, B. J., POLIAKOFF, M. & LESTER, E. 2004. A versatile flow visualisation technique for quantifying mixing in a binary system: application to continuous supercritical water hydrothermal synthesis (SWHS). *Chemical engineering science,* 59**,** 2853-2861.

BRAGG, L. B. & CLARINGBULL, G. F. 1965. *Crystal Structures of Minerals,* London, G. Bell and Sons Ltd.

BREMHOLM, M., FELICISSIMO, M. & IVERSEN, B. B. 2009. Time-Resolved In Situ Synchrotron X-ray Study and Large-Scale Production of Magnetite Nanoparticles in Supercritical Water. *Angewandte Chemie-International Edition,* 48**,** 4788-4791.

BRUNNER, G. 2009. Near and supercritical water. Part II: Oxidative processes. *The Journal of Supercritical Fluids,* 47**,** 382-390.

BURON, H., MENGUAL, O., MEUNIER, G., CAYRE, I. & SNABRE, P. 2004. Optical characterization of concentrated dispersions: applications to laboratory analyses and on-line process monitoring and control. *Polymer International,* 53**,** 1205-1209.

BYRAPPA, K. & ADSCHIRI, T. 2007. Hydrothermal technology for nanotechnology. *Progress in Crystal Growth and Characterization of Materials,* 53**,** 117-166.

CABANAS, A. & POLIAKOFF, M. 2001. The continuous hydrothermal synthesis of nano-particulate ferrites in near critical and supercritical water. *Journal of Materials Chemistry,* 11**,** 1408-1416.

CARAMAZANA-GONZALEZ, P., DUNNE, P. W., GIMENO-FABRA, M., ZILKA, M., TICHA, M., STIEBEROVA, B., FREIBERG, F., MCKECHNIE, J. & LESTER, E. H. 2017. Assessing the life cycle environmental impacts of titania nanoparticle production by continuous flow solvo/hydrothermal syntheses. *Green Chemistry,* 19**,** 1536-1547.

CELIA, C., TRAPASSO, E., COSCO, D., PAOLINO, D. & FRESTA, M. 2009. Turbiscan Lab (R) Expert analysis of the stability of ethosomes (R) and ultradeformable liposomes containing a bilayer fluidizing agent. *Colloids and Surfaces B-Biointerfaces,* 72**,** 155-160.

CHANTARACHINDAWONG, R., LUANGTIP, W., CHINDAUDOM, P., OSOTCHAN, T. & SRIKHIRIN, T. 2012. Development of the scratch resistance on acrylic sheet with basic colloidal silica (SiO2)-methyltrimethoxysilane (MTMS) nanocomposite films by sol-gel technique. *Canadian Journal of Chemical Engineering,* 90**,** 888-896.

CHATURVEDI, S., DAVE, P. N. & SHAH, N. 2012. Applications of nano-catalyst in new era. *Journal of Saudi Chemical Society,* 16**,** 307-325.

CHEN, K. L. & ELIMELECH, M. 2007. Influence of humic acid on the aggregation kinetics of fullerene (C-60) nanoparticles in monovalent and divalent electrolyte solutions. *Journal of Colloid and Interface Science,* 309**,** 126-134.

CHEN, Z., CAO, Y., QIAN, J., AI, X. & YANG, H. 2010. Facile synthesis and stable lithium storage performances of Sn-sandwiched nanoparticles as a high capacity anode material for rechargeable Li batteries. *Journal of Materials Chemistry,* 20**,** 7266-7271.

CLARK, I., DUNNE, P. W., GOMES, R. L. & LESTER, E. 2017. Continuous Hydrothermal Synthesis of Ca 2 Al-NO 3 Layered Double Hydroxides: The Impact of Reactor Temperature, Pressure and NaOH Concentration on Crystal Characteristics. *Journal of Colloid and Interface Science*.

COCHRAN, H., CUMMINGS, P. & KARABORNI, S. 1992. Solvation in supercritical water. *Fluid phase equilibria,* 71**,** 1-16.

CONVERTINO, A., LEO, G., TAMBORRA, M., SCIANCALEPORE, C., STRICCOLI, M., CURRI, M. L. & AGOSTIANO, A. 2007. TiO2 colloidal nanocrystals functionalization of PMMA: A tailoring of optical properties and chemical adsorption. *Sensors and Actuators B-Chemical,* 126**,** 138-143.

COSGROVE, T. 2010. *Colloid Science : Principles, Methods and Applications,* Hoboken, NJ, USA, Wiley-Blackwell.

DASOG, M. & VEINOT, J. G. 2012. Solid-state synthesis of luminescent silicon nitride nanocrystals. *Chemical Communications,* 48**,** 3760-3762.

DE TERCERO, M. D., RODER, C., FEHRENBACHER, U., TEIPEL, U. & TURK, M. 2014. Continuous supercritical hydrothermal synthesis of iron oxide nanoparticle dispersions and their characterization. *Journal of Nanoparticle Research,* 16.

DRONSKOWSKI, R. 2001. The little maghemite story: A classic functional material. *Advanced Functional Materials,* 11**,** 27-29.

DUBEY, S. P., LAHTINEN, M. & SILLANPAA, M. 2010. Green synthesis and characterizations of silver and gold nanoparticles using leaf extract of Rosa rugosa. *Colloids and Surfaces a-Physicochemical and Engineering Aspects,* 364**,** 34-41.

DUNNE, P. W., MUNN, A. S., STARKEY, C. L., HUDDLE, T. A. & LESTER, E. H. 2015. Continuous-flow hydrothermal synthesis for the production of inorganic nanomaterials. *Phil. Trans. R. Soc. A,* 373**,** 20150015.

EDWARDS, H. K., EVANS, E., MCCALDIN, S., BLOOD, P., GREGORY, D. H., POLIAKOFF, M., LESTER, E., WALKER, G. S. & BROWN, P. D. 2006. Hydrothermally synthesised Fe2O3 nanoparticles as catalyst precursors for the CVD production of graphitic nanofibres. EMAG/NANO Conference on Imaging, Analysis and Fabrication on the Nanoscale, Aug 31-Sep 02 2005 Univ Leeds, Leeds, ENGLAND. 195-+.

ELBASUNEY, S. 2012. *Enhanced Flame Retardant Polymer Nanocomposites.* Ph.D., The University of Nottingham.

FANG, Z. 2010. *Rapid Production of Micro- and Nano-Particles Using Supercritical Water,* Berlin, Springer.

FANUN, M. 2008. *Microemulsions: properties and applications*, CRC Press.

FAZIO, S., GUZMAN, J., COLOMER, M., SALOMONI, A. & MORENO, R. 2008. Colloidal stability of nanosized titania aqueous suspensions. *Journal of the European Ceramic Society,* 28**,** 2171-2176.

FEYNMAN, R. P. 2012. There's plenty of room at the bottom: An invitation to enter a new field of physics. *Handbook of Nanoscience, Engineering, and Technology, Third Edition.* CRC Press.

FIGGEMEIER, E., KYLBERG, W., CONSTABLE, E., SCARISOREANU, M., ALEXANDRESCU, R., MORJAN, I., SOARE, I., BIRJEGA, R., POPOVICI, E. & FLEACA, C. 2007. Titanium dioxide nanoparticles prepared by laser pyrolysis: Synthesis and photocatalytic properties. *Applied Surface Science,* 254**,** 1037-1041.

FORMULACTION. 2019. *Turbiscan: the reference technology for dispersion stability analysis* [Online]. Available: http://www.formulaction.com/en/our-solutions/stability-and-shelf-life [Accessed].

GANGULI, A. K., AHMAD, T., VAIDYA, S. & AHMED, J. 2008. Microemulsion route to the synthesis of nanoparticles. *Pure and Applied Chemistry,* 80**,** 2451-2477.

HAKUTA, Y., ONAI, S., TERAYAMA, H., ADSCHIRI, T. & ARAI, K. 1998. Production of ultra-fine ceria particles by hydrothermal synthesis under supercritical conditions. *Journal of materials science letters,* 17**,** 1211-1213.

HALLMANN, S., FINK, M. J. & MITCHELL, B. S. 2011. The mechanochemical formation of functionalized semiconductor nanoparticles for biological, electronic and superhydrophobic surface applications. *Ceramic Trans,* 229**,** 129À142.

HALMANN, M. M. 1996. *Photodegradation of Water Pollutants* London, CRC Press.

HANEMANN, T. & SZABO, D. V. 2010. Polymer-Nanoparticle Composites: From Synthesis to Modern Applications. *Materials,* 3**,** 3468-3517.

HANSEN, C. M. 2007. *Hansen solubility parameters : a user's handbook / Charles M. Hansen,* Boca Raton ; London, Boca Raton ; London : CRC Press.

HAUS, H. A. 1984. *Waves and fields in optoelectronics / Hermann A. Haus,* Englewood Cliffs, N.J. ; London, Englewood Cliffs, N.J. ; London : Prentice-Hall.

HAYNES, W. M. 2011-2012. *CRC Handbook of Chemistry and Physics,* USA, CRC Press, Taylor & Francis Group.

HIEMENZ, P. C. & RAJAGOPALAN, R. 1997. *Principles of Colloid and Surface Chemistry,* CRC press.

HOBBS, H., BRIDDON, S. & LESTER, E. 2009a. The synthesis and fluorescent properties of nanoparticulate ZrO2 doped with Eu using continuous hydrothermal synthesis. *Green Chemistry,* 11**,** 484-491.

HOBBS, H., BRIDDON, S. & LESTER, E. 2009b. The synthesis and fluorescent properties of nanoparticulate ZrO 2 doped with Eu using continuous hydrothermal synthesis. *Green Chemistry,* 11**,** 484-491.

HOLZMANN, D., HOLZINGER, D., HESSER, G., SCHMIDT, T. & KNOR, G. 2013. Long-Term UV-Photoprotection of Transparent Composite Materials Using In-Situ Generated Titanium Dioxide Nanoparticles as Functional Polymer Additives. *Current Nanoscience,* 9**,** 303-307.

HUDDLE, T., AL-ATTA, A., MORAN, S. & LESTER, E. 2017. Pseudo fluid modelling used in the design of continuous flow supercritical water oxidation reactors with improved corrosion resistance. *The Journal of Supercritical Fluids,* 120**,** 355-365.

HUNTER, R. J. 2001. *Foundations of Colloid Science,* USA, Oxford University Press Inc.

IMAI, Y., TERAHARA, A., HAKUTA, Y., MATSUI, K., HAYASHI, H. & UENO, N. 2009. Transparent poly(bisphenol A carbonate)-based nanocomposites with high refractive index nanoparticles. *European Polymer Journal,* 45**,** 630-638.

ISASI-MARÍN, J., PÉREZ-ESTÉBANEZ, M., DÍAZ-GUERRA, C., CASTILLO, J., CORRECHER, V. & CUERVO-RODRÍGUEZ, M. 2009. Structural, magnetic and luminescent characteristics of Pr3+-doped ZrO2 powders synthesized by a sol–gel method. *Journal of Physics D: Applied Physics,* 42**,** 075418.

JAMBOR, J. L. & DUTRIZAC, J. E. 1998. Occurrence and constitution of natural and synthetic ferrihydrite, a widespread iron oxyhydroxide. *Chemical Reviews,* 98**,** 2549-2585.

JAMISON, J. A., KRUEGER, K. M., YAVUZ, C. T., MAYO, J. T., LECRONE, D., REDDEN, J. J. & COLVIN, V. L. 2008. Size-dependent sedimentation properties of nanocrystals. *Acs Nano,* 2**,** 311-319.

JENSEN, K. M. O., ANDERSEN, H. L., TYRSTED, C., BOJESEN, E. D., DIPPEL, A. C., LOCK, N., BILLINGE, S. J. L., IVERSEN, B. B. & CHRISTENSEN, M. 2014. Mechanisms for Iron Oxide Formation under Hydrothermal Conditions: An in Situ Total Scattering Study. *Acs Nano,* 8**,** 10704-10714.

JIANG, J., OBERDORSTER, G. & BISWAS, P. 2009. Characterization of size, surface charge, and agglomeration state of nanoparticle dispersions for toxicological studies. *Journal of Nanoparticle Research,* 11**,** 77-89.

KIM, J., GRATE, J. W. & WANG, P. 2006. Nanostructures for enzyme stabilization. *Chemical Engineering Science,* 61**,** 1017-1026.

KIM, K. M., KIM, H. M., LEE, W. J., LEE, C. W., KIM, T. I., LEE, J. K., JEONG, J., PAEK, S. M. & OH, J. M. 2014. Surface treatment of silica nanoparticles for stable and charge-controlled colloidal silica. *International Journal of Nanomedicine,* 9**,** 29-40.

KLANG, V., MATSKO, N. B., VALENTA, C. & HOFER, F. 2012. Electron microscopy of nanoemulsions: An essential tool for characterisation and stability assessment. *Micron,* 43**,** 85-103.

KOHL, S. K., LANDMARK, J. D. & STICKLE, D. F. 2006. Demonstration of absorbance using digital color image analysis and colored solutions. *Journal of Chemical Education,* 83**,** 644-646.

KRITZER, P., BOUKIS, N. & DINJUS, E. 1999. Factors controlling corrosion in high-temperature aqueous solutions: a contribution to the dissociation and solubility data influencing corrosion processes. *The Journal of supercritical fluids,* 15**,** 205-227.

KUO, C. W. & WEN, T. C. 2008. Dispersible polyaniline nanoparticles in aqueous poly(styrenesulfonic acid) via the interfacial polymerization route. *European Polymer Journal,* 44**,** 3393-3401.

LAACHACHI, A., LEROY, E., COCHEZ, M., FERRIOL, M. & CUESTA, J. M. L. 2005. Use of oxide nanoparticles and organoclays to improve thermal stability and fire retardancy of poly(methyl methacrylate). *Polymer Degradation and Stability,* 89**,** 344-352.

LAAKSONEN, T., LIU, P., RAHIKKALA, A., PELTONEN, L., KAUPPINEN, E. I., HIRVONEN, J., JÄRVINEN, K. & RAULA, J. 2011. Intact nanoparticulate indomethacin in fast-dissolving carrier particles by combined wet milling and aerosol flow reactor methods. *Pharmaceutical research,* 28**,** 2403.

LAGREGA, M. D., BUCKINGHAM, P. L. & EVANS, J. C. 2010. *Hazardous waste management*, Waveland Press.

LEMARCHAND, C., COUVREUR, P., VAUTHIER, C., COSTANTINI, D. & GREF, R. 2003. Study of emulsion stabilization by graft copolymers using the optical analyzer Turbiscan. *International Journal of Pharmaceutics,* 254**,** 77-82.

LERCHE, D. 2002. Dispersion stability and particle characterization by sedimentation kinetics in a centrifugal field. *Journal of Dispersion Science and Technology,* 23**,** 699-709.

LESTER, E., AKSOMAITYTE, G., LI, J., GOMEZ, S., GONZALEZ-GONZALEZ, J. & POLIAKOFF, M. 2012. Controlled continuous hydrothermal synthesis of cobalt oxide (Co3O4) nanoparticles. *Progress in Crystal Growth and Characterization of Materials,* 58**,** 3-13.

LESTER, E. & AZZOPARDI, B. J. 2004. *International Patent Application* UK. patent application PCT/GB2005/000483.

LESTER, E., BLOOD, P., DENYER, J., GIDDINGS, D., AZZOPARDI, B. & POLIAKOFF, M. 2006. Reaction engineering: The supercritical water hydrothermal synthesis of nano-particles. *Journal of Supercritical Fluids,* 37**,** 209-214.

LESTER, E., TANG, S. V. Y., KHLOBYSTOV, A., ROSE, V. L., BUTTERY, L. & ROBERTS, C. J. 2013. Producing nanotubes of biocompatible hydroxyapatite by continuous hydrothermal synthesis. *Crystengcomm,* 15**,** 3256-3260.

LESTER, E. H. & AZZOPARDI, B. J. 2009. Counter current mixing reactor. Google Patents.

LIOU, G.-S., LIN, P.-H., YEN, H.-J., YU, Y.-Y. & CHEN, W.-C. 2010. Flexible Nanocrystalline-Titania/Polyimide Hybrids with High Refractive Index and Excellent Thermal Dimensional Stability. *Journal of Polymer Science Part a-Polymer Chemistry,* 48**,** 1433-1440.

LIU, J., HUANG, X. F., LU, L. J., LI, M. X., XU, J. C. & DENG, H. P. 2011. Turbiscan Lab (R) Expert analysis of the biological demulsification of a water-in-oil emulsion by two biodemulsifiers. *Journal of Hazardous Materials,* 190**,** 214-221.

LORYUENYONG, V., BUASRI, A., POCHANA, J., HOSAWANGWONG, S., THAISAUNG, S. & SOOKSAEN, P. 2013. Synthesis of Anatase TiO2 Nanoparticles by Template Sol–Gel Method and Its Application in Photocatalytic Degradation of Organic Pollutants. *Advanced Science Letters,* 19**,** 2919-2922.

LOU, H. B., WANG, X. D., CAO, Q. P., ZHANG, D. X., ZHANG, J., HU, T. D., MAO, H. K. & JIANG, J. Z. 2013. Negative expansions of interatomic distances in metallic melts. *Proceedings of the National Academy of Sciences of the United States of America,* 110**,** 10068-10072.

LU, A. H., SALABAS, E. L. & SCHUTH, F. 2007. Magnetic nanoparticles: Synthesis, protection, functionalization, and application. *Angewandte Chemie-International Edition,* 46**,** 1222-1244.

LÓPEZ-QUINTELA, M., RIVAS, J., BLANCO, M. & TOJO, C. 2004. Synthesis of nanoparticles in microemulsions. *Nanoscale materials.* Springer.

MACCUSPIE, R. I., ROGERS, K., PATRA, M., SUO, Z. Y., ALLEN, A. J., MARTIN, M. N. & HACKLEY, V. A. 2011. Challenges for physical characterization of silver nanoparticles under pristine and environmentally relevant conditions. *Journal of Environmental Monitoring,* 13**,** 1212-1226.

MALINGER, K. A., MAGUER, A., THOREL, A., GAUNAND, A. & HOCHEPIED, J. F. 2011. Crystallization of anatase nanoparticles from amorphous precipitate by a continuous hydrothermal process. *Chemical Engineering Journal,* 174**,** 445-451.

MALVERNPANALYTICAL. 2019. *Dynamic Light Scattering* [Online]. Available: https://www.malvernpanalytical.com [Accessed].

MARRONE, P. A. & HONG, G. T. 2009. Corrosion control methods in supercritical water oxidation and gasification processes. *The Journal of Supercritical Fluids,* 51**,** 83-103.

MATUSIAK, J. & GRZĄDKA, E. 2017. Stability of colloidal systems - a review of the stability measurements methods. *Annales Universitatis Mariae Curie-Sklodowska,* 72.

MENGUAL, O., MEUNIER, G., CAYRE, I., PUECH, K. & SNABRE, P. 1999a. Characterisation of instability of concentrated dispersions by a new optical analyser: the TURBISCAN MA 1000. *Colloids and Surfaces a-Physicochemical and Engineering Aspects,* 152**,** 111-123.

MENGUAL, O., MEUNIER, G., CAYRE, I., PUECH, K. & SNABRE, P. 1999b. TURBISCAN MA 2000: multiple light scattering measurement for concentrated emulsion and suspension instability analysis. *Talanta,* 50**,** 445-456.

MORI, Y. 2015. Size-Selective Separation Techniques for Nanoparticles in Liquid. *Kona Powder and Particle Journal***,** 102-114.

MUDUNKOTUWA, I. A. & GRASSIAN, V. H. 2010. Citric Acid Adsorption on TiO2 Nanoparticles in Aqueous Suspensions at Acidic and Circumneutral pH: Surface Coverage, Surface Speciation, and Its Impact on Nanoparticle-Nanoparticle Interactions. *Journal of the American Chemical Society,* 132**,** 14986-14994.

MUNN, A., DUNNE, P. W., TANG, S. & LESTER, E. 2015. Large-scale continuous hydrothermal production and activation of ZIF-8. *Chemical Communications,* 51**,** 12811-12814.

NANDA, K., MAISELS, A., KRUIS, F., FISSAN, H. & STAPPERT, S. 2003. Higher surface energy of free nanoparticles. *Physical review letters,* 91**,** 106102.

NANOSENSE. 2006. *Introduction to Nanoscience* [Online]. Available: https://nanosense.sri.com/activities/sizematters/introduction/SM_Lesson1Student.pdf [Accessed].

NEL, A., XIA, T., MADLER, L. & LI, N. 2006. Toxic potential of materials at the nanolevel. *Science,* 311**,** 622-627.

NEOUZE, M.-A. & SCHUBERT, U. 2008. Surface modification and functionalization of metal and metal oxide nanoparticles by organic ligands. *Monatshefte Fur Chemie,* 139**,** 183-195.

NICHOLS, G., BYARD, S., BLOXHAM, M. J., BOTTERILL, J., DAWSON, N. J., DENNIS, A., DIART, V., NORTH, N. C. & SHERWOOD, J. D. 2002. A review of the terms agglomerate and aggregate with a recommendation for nomenclature used in powder and particle characterization. *Journal of Pharmaceutical Sciences,* 91**,** 2103-2109.

NOVO, L. P., BRAS, J., GARCÍA, A., BELGACEM, N. & CURVELO, A. A. 2015. Subcritical water: a method for green production of cellulose nanocrystals. *ACS Sustainable Chemistry & Engineering,* 3**,** 2839-2846.

OGI, T., KAIHATSU, Y., ISKANDAR, F., TANABE, E. & OKUYAMA, K. 2009. Synthesis of nanocrystalline GaN from Ga2O3 nanoparticles derived from salt-assisted spray pyrolysis. *Advanced Powder Technology,* 20**,** 29-34.

ORIEKHOVA, O. & STOLL, S. 2014. Investigation of FeCl3 induced coagulation processes using electrophoretic measurement, nanoparticle tracking analysis and dynamic light scattering: Importance of pH and colloid surface charge. *Colloids and Surfaces a-Physicochemical and Engineering Aspects,* 461**,** 212-219.

ORTS-GIL, G., NATTE, K., DRESCHER, D., BRESCH, H., MANTION, A., KNEIPP, J. & OESTERLE, W. 2011. Characterisation of silica nanoparticles prior to in vitro studies: from primary particles to agglomerates. *Journal of Nanoparticle Research,* 13**,** 1593-1604.

PANKHURST, Q. A., CONNOLLY, J., JONES, S. K. & DOBSON, J. 2003. Applications of magnetic nanoparticles in biomedicine. *Journal of Physics D-Applied Physics,* 36**,** R167-R181.

PARIDA, G., CHAIRA, D., CHOPKAR, M. & BASU, A. 2011. Synthesis and characterization of Ni-TiO2 composite coatings by electro-co-deposition. *Surface & Coatings Technology,* 205**,** 4871-4879.

PARK, S. 2009. Preparation of iron oxides using ammonium iron citrate precursor: Thin films and nanoparticles. *Journal of Solid State Chemistry,* 182**,** 2456-2460.

PARTELI, E. J. R., SCHMIDT, J., BLUMEL, C., WIRTH, K. E., PEUKERT, W. & POSCHEL, T. 2014. Attractive particle interaction forces and packing density of fine glass powders. *Scientific Reports,* 4**,** 7.

PASHLEY, R. & KARAMAN, M. 2005. *Applied colloid and surface chemistry,* John Wiley & Sons.

PEDROTTI, F. L. S. J., PEDROTTI, L. M. & PEDROTTI, L. S. 2007. *Introduction to Optics,* New Jersey, Prentice Hall.

PELIN, I. M., MAIER, S. S., CHITANU, G. C. & BULACOVSCHI, V. 2009. Preparation and characterization of a hydroxyapatite-collagen composite as component for injectable bone substitute. *Materials Science & Engineering C-Materials for Biological Applications,* 29**,** 2188-2194.

PREETZ, C., HAUSER, A., HAUSE, G., KRAMER, A. & MADER, K. 2010. Application of atomic force microscopy and ultrasonic resonator technology on nanoscale: Distinction of nanoemulsions from nanocapsules. *European Journal of Pharmaceutical Sciences,* 39**,** 141-151.

RAHMAN, S., NADEEM, K., ANIS-UR-REHMAN, M., MUMTAZ, M., NAEEM, S. & LETOFSKY-PAPST, I. 2013. Structural and magnetic properties of ZnMg-ferrite nanoparticles prepared using the co-precipitation method. *Ceramics International,* 39**,** 5235-5239.

SAMPATHKUMARAN, E. V., MUKHERJEE, K., IYER, K. K., MOHAPATRA, N. & DAS, S. D. 2011. Magnetism of fine particles of Kondo lattices, obtained by high-energy ball-milling. *Journal of Physics: Condensed Matter,* 23**,** 094209.

SATHIYA, C. K. & AKILANDESWARI, S. 2014. Fabrication and characterization of silver nanoparticles using Delonix elata leaf broth. *Spectrochimica Acta Part a-Molecular and Biomolecular Spectroscopy,* 128**,** 337-341.

SCHWARTZ, W. 1980. S. Yariv and H. Cross, Geochemistry of Colloid Systems. XII + 450 S., 86 Abb., 32 Tab. Berlin—Heidelberg—New York 1979. Springer-Verlag. DM 110,00. *Zeitschrift für allgemeine Mikrobiologie,* 20**,** 300-300.

SENTHILKUMAAR, S. & SELVI, R. T. 2008. Synthesis and characterization of one dimensional ZnS nanorods. *Synthesis and Reactivity in Inorganic, Metal-Organic, and Nano-Metal Chemistry,* 38**,** 710-715.

SHQAU, K. 2005. Electrosteric dispersants used in colloidal processing of ceramics. *Group of Inorganic Materials Science. Columbus: The Ohio State University*.

SHRIVER, D. F., ATKINS, P. W. & LANGFORD, C. H. 1994. *Inorganic Chemistry* Oxford, Oxford University Press.

SIERRA-PALLARES, J., MARCHISIO, D. L., ALONSO, E., PARRA-SANTOS, M. T., CASTRO, F. & COCERO, M. J. 2011. Quantification of mixing efficiency in turbulent supercritical water hydrothermal reactors. *Chemical engineering science,* 66**,** 1576-1589.

SOHRABNEZHAD, S. & VALIPOUR, A. 2013. Synthesis of Cu/CuO nanoparticles in mesoporous material by solid state reaction. *Spectrochimica Acta Part A: Molecular and Biomolecular Spectroscopy,* 114**,** 298-302.

SUE, K., SUZUKI, M., ARAI, K., OHASHI, T., URA, H., MATSUI, K., HAKUTA, Y., HAYASHI, H., WATANABE, M. & HIAKI, T. 2006. Size-controlled synthesis of metal oxide nanoparticles with a flow-through supercritical water method. *Green Chemistry,* 8**,** 634-638.

SUN, L. M., ZHANG, C. L. & LI, P. 2012. Characterization, Antibiofilm, and Mechanism of Action of Novel PEG-Stabilized Lipid Nanoparticles Loaded with Terpinen-4-ol. *Journal of Agricultural and Food Chemistry,* 60**,** 6150-6156.

SUN, Y., DEAC, A. & ZHANG, G. G. Z. 2019. Assessing Physical Stability of Colloidal Dispersions Using a Turbiscan Optical Analyzer. *Molecular Pharmaceutics,* 16**,** 877-885.

SUTTIPONPARNIT, K., JIANG, J., SAHU, M., SUVACHITTANONT, S., CHARINPANITKUL, T. & BISWAS, P. 2011. Role of Surface Area, Primary Particle Size, and Crystal Phase on Titanium Dioxide Nanoparticle Dispersion Properties. *Nanoscale Research Letters,* 6.

TAGUCHI, M., TAKAMI, S., ADSCHIRI, T., NAKANE, T., SATO, K. & NAKA, T. 2011. Supercritical hydrothermal synthesis of hydrophilic polymer-modified water-dispersible CeO2 nanoparticles. *Crystengcomm,* 13**,** 2841-2848.

TAKAMI, S., SUGIOKA, K.-I., TSUKADA, T., ADSCHIRI, T., SUGIMOTO, K., TAKENAKA, N. & SAITO, Y. 2012. Neutron radiography on tubular flow reactor for hydrothermal synthesis: In situ monitoring of mixing behavior of supercritical water and room-temperature water. *The Journal of Supercritical Fluids,* 63**,** 46-51.

TAKENAKA, N., SUGIMOTO, K., TAKAMI, S., SUGIOKA, K., TSUKADA, T., ADSCHIRI, T. & SAITO, Y. 2013. Application of neutron radiography to flow visualization in supercritical water. *7th International Topical Meeting on Neutron Radiography (Itmnr-7),* 43**,** 264-268.

THIEBAUT, B. 2011. Flame Spray Pyrolysis: A Unique Facility for the Production of Nanopowders. *Platinum Metals Review,* 55**,** 149-151.

THUAN, N. C., PHONG, P. T. & PHUC, N. X. 2009. Magnetic properties of La0. 7Ca0. 3MnO3 nanoparticles prepared by reactive milling. *Journal of Alloys and Compounds,* 479**,** 828-831.

TIGHE, C. J., CABRERA, R. Q., GRUAR, R. I. & DARR, J. A. 2013. Scale up production of nanoparticles: continuous supercritical water synthesis of Ce–Zn oxides. *Industrial & Engineering Chemistry Research,* 52**,** 5522-5528.

TSANTILIS, S. & PRATSINIS, S. E. 2004. Soft- and hard-agglomerate aerosols made at high temperatures. *Langmuir,* 20**,** 5933-5939.

UDO SCHWERTMANN, R. M. C. 1991. *Iron oxides in the laboratory,* Wiley-VCH.

VICENT, M., SANCHEZ, E., SANTACRUZ, I. & MORENO, R. 2011. Dispersion of TiO2 nanopowders to obtain homogeneous nanostructured granules by spray-drying. *Journal of the European Ceramic Society,* 31**,** 1413-1419.

WANG, F. D., RICHARDS, V. N., SHIELDS, S. P. & BUHRO, W. E. 2014. Kinetics and Mechanisms of Aggregative Nanocrystal Growth. *Chemistry of Materials,* 26**,** 5-21.

WEINGÄRTNER, H. & FRANCK, E. U. 2005. Supercritical water as a solvent. *Angewandte Chemie International Edition,* 44**,** 2672-2692.

WEIR, A., WESTERHOFF, P., FABRICIUS, L., HRISTOVSKI, K. & VON GOETZ, N. 2012. Titanium Dioxide Nanoparticles in Food and Personal Care Products. *Environmental Science & Technology,* 46**,** 2242-2250.

WILLARD, M., KURIHARA, L., CARPENTER, E., CALVIN, S. & HARRIS, V. 2004. Chemically prepared magnetic nanoparticles. *International materials reviews,* 49**,** 125-170.

WOO, S. H., LEE, M. K. & RHEE, C. K. 2007. Sedimentation properties of TiO2 nanoparticles in organic solvents. *Nanocomposites and Nanoporous Materials,* 119**,** 267-270.

XU, F. 2018. Review of analytical studies on TiO2 nanoparticles and particle aggregation, coagulation, flocculation, sedimentation, stabilization. *Chemosphere,* 212**,** 662-677.

YANG, H., TENG, F., WANG, P., TIAN, B., LIN, X., HU, X., ZHANG, L., ZHANG, K., ZHANG, Y. & TANG, X. 2014. Investigation of a nanosuspension stabilized by Soluplus (R) to improve bioavailability. *International Journal of Pharmaceutics,* 477**,** 88-95.

YETTER, R. A., RISHA, G. A. & SON, S. F. 2009. Metal particle combustion and nanotechnology. *Proceedings of the Combustion Institute,* 32**,** 1819-1838.

YUAN, Y., GAO, Y. X., ZHAO, J. & MAO, L. 2008. Characterization and stability evaluation of beta-carotene nanoemulsions prepared by high pressure homogenization under various emulsifying conditions. *Food Research International,* 41**,** 61-68.

ZHAO, Q., LI, Y. J., CHAI, X. L., ZHANG, L. F., XU, L. Z., HUANG, J. H., NING, P. & TIAN, S. L. 2019. Interaction of nano carbon particles and anthracene with pulmonary surfactant: The potential hazards of inhaled nanoparticles. *Chemosphere,* 215**,** 746-752.

ZHAO, X., LV, L., PAN, B. C., ZHANG, W. M., ZHANG, S. J. & ZHANG, Q. X. 2011. Polymer-supported nanocomposites for environmental application: A review. *Chemical Engineering Journal,* 170**,** 381-394.

Appendices

Appendix I: MATLAB codes

I. 1 Image capturing in greyscale

```
% MATLAB Code for Image Taking

clear all % Clears out your MATLAB workspace
clc
%startLoop = tic;

loopcounter = 0; % Defines the initial loop counter as zero
time = 0; % Defines the initial time as zero
loopendtime = input(' Please enter the amount of hours you would like the experiment to run for: '); % Allows the user to type in for many hour the experiment is to be carried out
cycletime = input(' Please enter the number of seconds between pictures:  ')

% The following section sets all the necessary camera settings to "manual"
% mode and defines them to certain values, which I considered to be ideal
    imaqreset
    vid = videoinput('winvideo', 1, 'RGB24_1920x1080'); % Sets the video input source to Logitech webcam
    src = getselectedsource(vid);
    vid.FramesPerTrigger = 1;
    vid.ReturnedColorspace = 'grayscale'; % Sets camera settings to black & white
    %vid.ROIPosition = [1162 802 55 30];
    src.BacklightCompensation = 'off';
    src.Brightness = 100;
    src.Contrast = 175;
    src.ExposureMode = 'auto';
    %src.ExposureMode = 'manual';
    %src.Exposure = -1;
    src.FocusMode = 'manual';
    src.Focus = 25;
    src.Saturation = 0;
    src.Sharpness = 242;
    src.WhiteBalanceMode = 'manual';
    src.WhiteBalance = 6500;

% The following section consists of a "while" loop
while time < loopendtime % This loop keeps on repeating itself until the time the experiment has been running for equals the time previously defined as loopendtime

    startIteration = tic;
    loopcounter = loopcounter + 1
```

```
   % The following section takes the image.
   start(vid); % Starts image acquisition
   stoppreview(vid); % Stops image acquisition
   filename = sprintf('Image%d.tif', loopcounter); % Defines the filename for the
image taken. The "sprintf" function continuously adds the current loopcounter to the
image name to make sure the previous image is not being overwritten.
   %imshow(filename); %If you would like the image to be displayed for each loop,
delete the "%" infront of "imshow(filename);"
   image = getdata(vid); % Aquired the image taken
   imwrite(image, filename); % Saves the image under the priviously defined
"filename"
   %Timestamp=[d.datenum]



   pause(cycletime);
   % If you would like the loop at pause at this point for a
   %certain amount of time, delete the "%" in front of "pause(5);" and type
   %in instead of "5" the amount of seconds you would like the loop to
   %pause for. This increases the time interval between the individual
   %images and hence decreases the amount of memory required.

   % The following section adds up the amount of time the individual
   % loops take. This time is then converted from seconds into hours.
   % This value is then saved as a timestamp for each loop and
   % corresponding image in a separate CSV file, called time.csv
   endIteration = toc(startIteration)
   endIteration = (endIteration/3600);
   time = time + endIteration
   dlmwrite('time.csv',time,'-append');

end
%endLoop = toc(startLoop)
```

I. 2 Image capturing in RGB

```
clear all % Clears out your MATLAB workspace
clc
%startLoop = tic;

loopcounter = 0;
time = 0;
loopendtime = input(' Please enter the amount of hours you would like the experiment
to run for: ');
cycletime = input(' Please enter the number of seconds between pictures:  ')

   imaqreset
   vid = videoinput('winvideo', 1, 'RGB24_1920x1080');
```

```
    src = getselectedsource(vid);
    vid.FramesPerTrigger = 1;
    vid.ReturnedColorspace = 'rgb';
    %vid.ROIPosition = [1162 802 55 30];
    src.BacklightCompensation = 'off';
    src.Brightness = 100;
    src.Contrast = 175;
    src.ExposureMode = 'auto';
    %src.ExposureMode = 'manual';
    %src.Exposure = -1;
    src.FocusMode = 'manual';
    src.Focus = 25;
    src.Saturation = 128;
    src.Sharpness = 242;
    src.WhiteBalanceMode = 'manual';
    src.WhiteBalance = 6500;

% The following section consists of a "while" loop
while time < loopendtime % This loop keeps on repeating itself until the time the experiment has been running for equals the time previously defined as loopendtime

    startIteration = tic;
    loopcounter = loopcounter + 1

    % The following section takes the image.
    start(vid); % Starts image acquisition
    stoppreview(vid); % Stops image acquisition
    filename = sprintf('Image%d.tif', loopcounter); % Defines the filename for the image taken. The "sprintf" function continuously adds the current loopcounter to the image name to make sure the previous image is not being overwritten.
    %imshow(filename); %If you would like the image to be displayed for each loop, delete the "%" infront of "imshow(filename);"
    image = getdata(vid); % Acquired the image taken
    imwrite(image, filename); % Saves the image under the previously defined "filename"
    %Timestamp=[d.datenum]

    pause(cycletime);
    endIteration = toc(startIteration)
    endIteration = (endIteration/3600);
    time = time + endIteration
    dlmwrite('time.csv',time,'-append');

end
%endLoop = toc(startLoop)
```

I. 3 Analysing image letters (AIL) code

```
clear all;
clc;


filename=uigetfile('*.tif','Select image file for analysis...');
w=imread(filename)
BW=w>20;
BW=imcomplement(BW);
stats=regionprops(BW,w,'all');
Title=input('Choose a title:  ','s')
setname= [Title '.jpg'];
imshow(w);figure(gcf);
hold on

 for i=1:numel(stats)

rectangle('Position',[stats(i).BoundingBox(1),stats(i).BoundingBox(2),stats(i).BoundingBox(3),stats(i).BoundingBox(4)],'EdgeColor','r')
 end
 hold off

  set(gcf, 'PaperPositionMode', 'manual');
    set(gcf, 'PaperUnits', 'points');
    set(gcf, 'PaperPosition', [0 0 1920 1080]);
    print ('-djpeg', setname);
close all;

 data=zeros(numel(stats),10);
 data(:,1)=1:numel(stats)

for i=1:numel(stats)
    data(i,2)=stats(i).Centroid(1)
    data(i,3)=stats(i).Centroid(2)
    data(i,4)=stats(i).Area
    data(i,5)=stats(i).BoundingBox(1);
    data(i,6)=stats(i).BoundingBox(2);
    data(i,7)=stats(i).BoundingBox(3);
    data(i,8)=stats(i).BoundingBox(4);
    data(i,9)=stats(i).Perimeter;
    data(i,10)=numel(stats(i).PixelList);
end

Headers={'Element' 'Centroid x' 'Centroid y' 'Area' 'BBx' 'BBy' 'BBw' 'BBh'
'Perimeter' 'Num. pixels'}
Dataout=[Headers;num2cell(data)];

setname= [Title '.xlsx'];
xlswrite(setname, Dataout)
```

```
%winopen(setname)
```

I. 4 Analysing image colours (AIC) code

```
close all
clear all

file=uigetfile({'*.tif';'*.jpg';'*.*'},'Image Selector');

Col_hor=17;
Col_vert=30;
ROI=0.35;

num_sq=Col_hor*Col_vert;

im=imread(file);
h=figure();
imshow(im);
[x, y] = getpts(h);
x1=sort([x(1),x(2)]);
xs1=x1(2);
x1=x1(1);
x2=sort([x(3),x(4)]);
xs2=x1(1);
x2=x2(2);
y1=sort([y(1),y(4)]);
ys1=y1(2);
y1=y1(1);
y2=sort([y(2),y(3)]);
ys2=y2(1);
y2=y2(2);

new_x=(x-x1)+1
new_y=(y-y1)+1


im3=imcrop(im,[x1,y1,x2-x1,y2-y1]);
[h,w,~]=size(im3);
figure();
imshow(im3);
hold on
plot([new_x;new_x(1)],[new_y;new_y(1)],'r','LineWidth',2);
 fp =
[new_x(1),new_y(1);new_x(2),new_y(2);new_x(3),new_y(3);new_x(4),new_y(4)]
 mp = [1,1;1,h;w,h;w,1]
tform = fitgeotrans(fp,mp,'projective')
```

```
im4 = imwarp(im3, tform);
h2=figure();
imshow(im4);
rect = getrect(h2);

Vert_sep = (rect(4))/(Col_hor-1)
Hor_sep = (rect(3))/(Col_vert-1)

mid_pnts=zeros(Col_vert*Col_hor,2)

for a=1:Col_vert
    for b=1:Col_hor
        mid_pnts(b+((a-1)*Col_hor),2)=floor(((a-1)*Hor_sep)+rect(1));
        mid_pnts(b+((a-1)*Col_hor),1)=floor(((b-1)*Vert_sep)+rect(2));
        %mid_pnts(b+((a-1)*Col_vert),2)= (floor((b-1)/Col_hor)*Hor_sep)+rect(1);
        %mid_pnts(b+((a-1)*Col_hor),1)= rect(1)+((b-1)*Vert_sep)
    end
end
mid_pnts2=[mid_pnts(:,2),mid_pnts(:,1)];
hold on
plot(mid_pnts(:,2),mid_pnts(:,1),'*','Color','blue')

sq_size=floor(Vert_sep*ROI);
sq_lbl = strtrim(cellstr(num2str((1:num_sq)')));

Aves=[];
for n=1:num_sq
    rectangle('Position',[floor(mid_pnts(n,2)-(sq_size*0.5)),floor(mid_pnts(n,1)-
(sq_size*0.5)),sq_size,sq_size],'FaceColor','r');
    text(floor(mid_pnts(n,2)-(sq_size*0.5)),floor(mid_pnts(n,1)-(sq_size*0.5)),
sq_lbl(n),'color','w');
    Mini_squ=imcrop(im4,[floor(mid_pnts(n,2)-(sq_size*0.5)),floor(mid_pnts(n,1)-
(sq_size*0.5)),sq_size,sq_size]);
    Mini_r=Mini_squ(:,:,1);
    Mini_g=Mini_squ(:,:,2);
    Mini_b=Mini_squ(:,:,3);

Col_aves=[round(mean2(Mini_r)),round(mean2(Mini_g)),round(mean2(Mini_b))];
    Aves=[Aves;Col_aves];
end

headers={'Square #', 'Red Value', 'Green Value', 'Blue Value'}

table=[headers;sq_lbl,num2cell(Aves)]

figure (3);
%set(gca,'position',[0 0 1 1],'units','normalized')
%print('-dpng','-r300', img);
foldername2=pwd;
fname=[foldername2 '/' file];
```

```
fname=strrep(fname, '.tif', '_3_legend.jpg');
hgexport(gcf, fname, hgexport('factorystyle'), 'Format', 'jpeg');

close;

fname2=[file];
fname2=strrep(fname2, '.tif', '_Colour_Analysis.xlsx');

Excel = actxserver('Excel.Application');
set(Excel,'Visible',1);
Workbooks = Excel.Workbooks;
Workbook = invoke(Workbooks, 'Add');
Sheets = Excel.ActiveWorkBook.Sheets;
Sheet1 = get(Sheets, 'Item', 1);
Sheet1.Activate;
Shapes = Sheet1.Shapes;
Shapes.AddPicture([fname] ,0,1,250,20,600,335);
Activesheet = Excel.Activesheet;
Alphabet = 'ABCDEFGHIJKLMNOPQRSTUVWXYZ';
tab_size=size(table);
ex_cell_range=['A1:',Alphabet(tab_size(2)),num2str(tab_size(1))];
ActivesheetRange = get(Activesheet,'Range',ex_cell_range);
set(ActivesheetRange, 'Value', table);
ActivesheetRange.Select;
invoke(Excel.Selection.Columns,'Autofit');
Workbook.SaveAs([cd '\' foldername2 '\' fname2])
invoke(Workbook, 'Close');
invoke(Excel, 'Quit');
delete(Excel);
```

I. 5 Reference point analysing code

```
clear all;
close all;
files = dir('*.tif');
ref=imread('ref.tif');
a=numel(files);
%b = waitbar(0,'Process running...');
foldername='Aligned';
pro_foldername=[foldername '/Alignment_processing'];
mkdir(foldername);
mkdir(pro_foldername);

for k=1:a
im=imread(files(k).name);
imshow(im);
```

```
fname=[pro_foldername '/' files(k).name];
fname=strrep(fname, '.tif', '_1_original.jpg');
hgexport(gcf, fname, hgexport('factorystyle'), 'Format', 'jpeg');
close;

BW_ref=rgb2gray(ref);
BW_im=rgb2gray(im);
ptsOriginal  = detectSURFFeatures(BW_ref);
ptsDistorted = detectSURFFeatures(BW_im);
[featuresOriginal,   validPtsOriginal] = extractFeatures(BW_ref,  ptsOriginal);
[featuresDistorted, validPtsDistorted] = extractFeatures(BW_im, ptsDistorted);
index_pairs = matchFeatures(featuresOriginal, featuresDistorted);
matchedPtsOriginal  = validPtsOriginal(index_pairs(:,1));
matchedPtsDistorted = validPtsDistorted(index_pairs(:,2));
figure;
showMatchedFeatures(BW_ref,BW_im,matchedPtsOriginal,matchedPtsDistorted);
title('All Matched SURF points');

fname=[pro_foldername '/' files(k).name];
fname=strrep(fname, '.tif', '_3_matchedSURFpoints.jpg');
hgexport(gcf, fname, hgexport('factorystyle'), 'Format', 'jpeg');
close;

[tform,inlierPtsDistorted,inlierPtsOriginal] =
estimateGeometricTransform(matchedPtsDistorted,matchedPtsOriginal,'projective');
figure; showMatchedFeatures(BW_ref,BW_im,inlierPtsOriginal,inlierPtsDistorted);
title('Matched inlier points');

fname=[pro_foldername '/' files(k).name];
fname=strrep(fname, '.tif', '_4_inlierSURFpoints.jpg');
hgexport(gcf, fname, hgexport('factorystyle'), 'Format', 'jpeg');
close;

outputView = imref2d(size(BW_ref));
Ir = imwarp(im, tform, 'OutputView', outputView);
figure; imshow(Ir); title('Recovered image');

fname=[pro_foldername '/' files(k).name];
fname=strrep(fname, '.tif', '_2_resolvedimage.jpg');
hgexport(gcf, fname, hgexport('factorystyle'), 'Format', 'jpeg');
close;

Old_filename=files(k).name;
New_filename=strrep(Old_filename, '.tif', '_ALIGNED.tif');
New_filename=[foldername '/' New_filename];
imwrite(Ir, New_filename);
end

%COLOUR SQUARES
```

```
close all;
iptsetpref('ImshowBorder','tight');

%SETTINGS:

Col_hor=30;
Col_vert=17;
reg_width=0.5;
reg_height=0.5;


%SETTINGS END

foldername2='Colour_processed';
mkdir(foldername2);

files=dir('Aligned/*.tif');
a=numel(files);

for g=1:a

readfile=['Aligned/' files(g).name];
im=imread(readfile);
%Red=im(:,:,1);
%Green=im(:,:,2);
%Blue=im(:,:,3);
BW=rgb2gray(im);
[imx,imy]=size(BW);
BW2=BW>5;
BW2=imcomplement(BW2);
stats=regionprops(BW2,'all');
imshow(im);figure(gcf);
hold on;

[k,~]=size(stats);
aspects=[];
for n=1:k
    temp1=[n,(stats(n).BoundingBox(3)/stats(n).BoundingBox(4))];
    if(stats(n).Area>500) & temp1(2)>0.9 & temp1(2)<1.1
    aspects=[aspects;temp1];
    end
end

P1=aspects(1,1)
P2=aspects(2,1)
P3=aspects(end-1,1)
P4=aspects(end,1)

if stats(P1).BoundingBox(2)>stats(P2).BoundingBox(2)
```

```
     tempP=P1
     P1=P2
     P2=tempP
 end

  if stats(P3).BoundingBox(2)>stats(P3).BoundingBox(2)
     tempP=P3
     P3=P4
     P4=tempP
  end

   if stats(P3).BoundingBox(2)>stats(P4).BoundingBox(2)
     tempP=P3
     P3=P4
     P4=tempP
  end


Point1=[stats(P1).BoundingBox(1)+stats(P1).BoundingBox(3),stats(P1).BoundingBox(2)+stats(P1).BoundingBox(4)]
Point2=[stats(P2).BoundingBox(1)+stats(P2).BoundingBox(3),stats(P2).BoundingBox(2)]
Point3=[stats(P3).BoundingBox(1),stats(P3).BoundingBox(2)+stats(P3).BoundingBox(4)]
Point4=[stats(P4).BoundingBox(1),stats(P4).BoundingBox(2)]

m=0;
for i=aspects(:,1)'
    m=m+1;

rectangle('Position',[stats(i).BoundingBox(1),stats(i).BoundingBox(2),stats(i).BoundingBox(3),stats(i).BoundingBox(4)],'EdgeColor','r')
 end
 %hold off;

 if Point1(2)>Point2(2)
     temppoint=Point1
     Point1=Point2
     Point2=temppoint
 end

  if Point3(2)>Point4(2)
     temppoint=Point3
     Point3=Point4
     Point4=temppoint
  end


scatter(Point1(1),Point1(2),'d','r');
scatter(Point2(1),Point2(2),'d','r');
```

```
scatter(Point3(1),Point3(2),'d','r');
scatter(Point4(1),Point4(2),'d','r');

%l1x=[Point1(1),Point3(1)];
%l1y=[Point1(2),Point3(2)];
%annotation('line',l1x,l1y)

Xs=[Point1(1),Point3(1),Point4(1),Point2(1),Point1(1)];
Ys=[Point1(2),Point3(2),Point4(2),Point2(2),Point1(2)];
figure(1);
plot(Xs,Ys,'r','LineWidth',2);

figure(1)
hold on;
Unc_crop=imcrop(im,[Point1(1),Point1(2),Point3(1)-Point1(1),Point2(2)-
Point1(2)]);
Unc_BW=rgb2gray(Unc_crop);
Unc_BW2=Unc_BW>100;
Unc_BW2=imcomplement(Unc_BW2);
Unc_BW2=imfill(Unc_BW2,'holes');
%imshow(Unc_BW2);
stats2=regionprops(Unc_BW2,'Centroid','BoundingBox','Area');


[k,~]=size(stats2)
aspects2=[];
for n=1:k

temp2=[n,(stats2(n).BoundingBox(3)/stats2(n).BoundingBox(4)),stats2(n).Centroid(
1),stats2(n).Centroid(2)];
   if stats2(n).Area>500 & temp2(2)>0.9 & temp2(2)<1.1
   aspects2=[aspects2;temp2];
   end
end
asp=aspects2(1,1);
sq_size=[stats2(asp).BoundingBox(3),stats2(asp).BoundingBox(4)];

fname=[foldername2 '/' files(g).name];
fname=strrep(fname, '_ALIGNED.tif', '_1_ROI.jpg');
hgexport(gcf, fname, hgexport('factorystyle'), 'Format', 'jpeg');
close;


figure(2);
hold on;
imshow(Unc_BW2);
m=0;
for i=aspects2(:,1)'
   m=m+1;
```

```
rectangle('Position',[stats2(i).BoundingBox(1),stats2(i).BoundingBox(2),stats2(i).Bo
undingBox(3),stats2(i).BoundingBox(4)],'EdgeColor','r')
end

%z = extractfield(stats2, 'Centroid');
%z2=reshape(z,2,[])';
min_x=min(aspects2(:,3));
max_x=max(aspects2(:,3));
min_y=min(aspects2(:,4));
max_y=max(aspects2(:,4));
[tu,~]=size(aspects2);
add=zeros(1,tu)'
aspects2=[aspects2,add]
aspects2(1,5)=(aspects2(1,3))
for k=2:tu;
    if aspects2(k,3)<(aspects2(k-1,5)+5);
        aspects2(k,5)=(aspects2(k-1,5));
    else
        aspects2(k,5)=(aspects2(k,3));
    end




end
[m,n]=size(Unc_BW2);

%bottom=find(aspects2(:,4)>max_y-25);
%bottom=aspects2(bottom,:);
%left=find(aspects2(:,3)<min_x+25);
%left=aspects2(left,:);

aspects3=[aspects2,aspects2(:,5)*m+aspects2(:,4)];
aspects4=sortrows(aspects3,6);
[tur,~]=size(aspects4);
aspects5=[linspace(1,tur,tur)',aspects4];
lbl = strtrim(cellstr(num2str((1:tur)')));
text(aspects5(:,4), aspects5(:,5), lbl(:),'color','r');

Vert_sep=[];
Hor_sep=[];
Bottoms=[];


for i=2:tur
if aspects5(i,5)-aspects5(i-1,5)<sq_size(2)*2 & aspects5(i,5)-aspects5(i-1,5) > 0;
        Vert_sep=[Vert_sep,aspects5(i,5)-aspects5(i-1,5)];
    end;
```

```
if aspects5(i,6)-aspects5(i-1,6)>0;
        Hor_sep=[Hor_sep,aspects5(i,6)-aspects5(i-1,6)];
        Bottoms=[Bottoms;aspects5(i-1,2),aspects5(i-1,4),aspects5(i-1,5)];
end

end

Vert_ave=mean(Vert_sep);
Hor_ave=mean(Hor_sep);

mid_pnts=[];

for a=0:Col_hor-1
    for b=0:Col_vert-1
        mid_pnts=[mid_pnts; Bottoms(1,2)+a*Hor_ave, Bottoms(1,3)-b*Vert_ave];
    end
end

%rb=imread('ref_bacon.tif');
%figure(3);


%Squares=[mid_pnts(:,1)-(sq_size(1)/2),mid_pnts(:,2)-(sq_size(2)/2)];

%Squares=[Squares(:,1)+Point1(1),Squares(:,2)+Point1(2)];
%plot(Squares(:,1),Squares(:,2),'r+');

%for i=1:(numel(Squares)/2)
%
rectangle('Position',[Squares(i,1),Squares(i,2),sq_size(1),sq_size(2)],'FaceColor','k')
%end

%truesize(figure(3));
%f=getframe(gcf);
%new=f.cdata;
%imwrite(new,'Squ.tif');

%BW5=imadjust(Unc_BW);
%BW5=imadjust(Unc_BW,[0.5 0.8],[]);
%BW5 = edge(BW5,'canny');
%BW3=imfill(BW5,'holes');
%imshow(BW3);
%se = strel('diamond',0.5);
%BW4=imdilate(BW3,se);
%figure(2), imshow(BW4);

fname=[foldername2 '/' files(g).name];
fname=strrep(fname, '_ALIGNED.tif', '_2_threshold_detected.jpg');
hgexport(gcf, fname, hgexport('factorystyle'), 'Format', 'jpeg');
close;
```

```
figure(3);
imshow(Unc_crop);
hold on;
plot(mid_pnts(:,1),mid_pnts(:,2),'r+');

Squares=[mid_pnts(:,1)-(sq_size(1)*reg_width/2),mid_pnts(:,2)-
(sq_size(2)*reg_height/2)]
[num_sq,~]=size(Squares);
wh=[sq_size(1)*reg_width,sq_size(2)*reg_height]

sq_lbl = strtrim(cellstr(num2str((1:num_sq)')));


Aves=[];
for i=1:(numel(mid_pnts)/2)
    xy=Squares(i,1:2);
    rectangle('Position',[xy(1,1),xy(1,2),wh(1,1),wh(1,2)],'FaceColor','r');
    text(xy(1,1)-(sq_size(1)*reg_width/2),xy(1,2)-(sq_size(2)*reg_height/2),
sq_lbl(i),'color','w');
    Mini_squ=imcrop(Unc_crop,[xy(1,1),xy(1,2),wh(1,1),wh(1,2)]);
    Mini_r=Mini_squ(:,:,1);
    Mini_g=Mini_squ(:,:,2);
    Mini_b=Mini_squ(:,:,3);

Col_aves=[round(mean2(Mini_r)),round(mean2(Mini_g)),round(mean2(Mini_b))];
    Aves=[Aves;Col_aves];
end

headers={'Square #', 'Red Value', 'Green Value', 'Blue Value'}

table=[headers;sq_lbl,num2cell(Aves)]

figure (3);
%set(gca,'position',[0 0 1 1],'units','normalized')
%print('-dpng','-r300', img);

fname=[foldername2 '/' files(g).name];
fname=strrep(fname, '_ALIGNED.tif', '_3_legend.jpg');
hgexport(gcf, fname, hgexport('factorystyle'), 'Format', 'jpeg');

close;

fname2=[files(g).name];
fname2=strrep(fname2, '_ALIGNED.tif', '_Colour_Analysis.xlsx');

Excel = actxserver('Excel.Application');
set(Excel,'Visible',1);
Workbooks = Excel.Workbooks;
```

```
Workbook = invoke(Workbooks, 'Add');
Sheets = Excel.ActiveWorkBook.Sheets;
Sheet1 = get(Sheets, 'Item', 1);
Sheet1.Activate;
Shapes = Sheet1.Shapes;
Shapes.AddPicture([pwd '\' fname] ,0,1,250,20,600,335);
Activesheet = Excel.Activesheet;
Alphabet = 'ABCDEFGHIJKLMNOPQRSTUVWXYZ';
tab_size=size(table);
ex_cell_range=['A1:',Alphabet(tab_size(2)),num2str(tab_size(1))];
ActivesheetRange = get(Activesheet,'Range',ex_cell_range);
set(ActivesheetRange, 'Value', table);
ActivesheetRange.Select;
invoke(Excel.Selection.Columns,'Autofit');
Workbook.SaveAs([cd '\' foldername2 '\' fname2])
invoke(Workbook, 'Close');
invoke(Excel, 'Quit');
delete(Excel);

end

%close all;
```

I. 6 Analysing settling rates (ASR) code

```
close all
clear all % Clears out your MATLAB workspace
clc

%Sample locations
Smpl_1 = [14 200 60 650]
Smpl_2 = [172 200 60 650]
Smpl_3 = [324 200 60 650]
Smpl_4 = [473 200 60 650]
Smpl_5 = [609 200 60 650]
Smpl_6 = [740 200 60 650]
Smpl_7 = [867 200 60 650]
Smpl_8 = [996 200 60 650]
Smpl_9 = [1122 200 60 650]
Smpl_10 = [1251 200 60 650]
Smpl_11 = [1387 200 60 650]
Smpl_12 = [1530 200 60 650]
Smpl_13 = [1685 200 60 650]
Smpl_14 = [1835 200 60 650]



Runname=input ('Enter experiment name and/or date   ', 's');
Outputname=[Runname ' - White Background.xlsx'];
```

```
Timefile = uigetfile('*.csv','Select the CSV file containing the image capture times...')
time=csvread(Timefile);
TemplateXLSX = uigetfile('*.xlsx','Select the desired excel template file...')
copyfile(TemplateXLSX,Outputname)
Imfolder = uigetdir('','Select directory containing TIF images for processing')
Imfolder=[Imfolder '\*.tif']
files = dir(Imfolder); %Replace 'photo*.tif' with relevant name and Frames 1 with
foldername

%Sample detection
Frame=imread(files(1).name);
Sample_truth=[];
for k = 1:14
    K=num2str(k)
    str=['Smpl_' K]
    unc=eval(str)
    Detect=imcrop(Frame, unc)
    Avedetect=mean(Detect(:))
    if Avedetect > 150
        Sample_truth(k,1)=0
    else
        Sample_truth(k,1)=1
    end
end

Totaverage=time
Cumaverage=[];
a=numel(files);
b = waitbar(0,'Process running...');
% The following section consists of a "while" loop

for k = 1:numel(files) %For the number of different frames...
    Frame=imread(files(k).name);
    %Frame=rgb2gray(Frame);
    Curaverage = [];

    %1
    j=1
    if Sample_truth(j,1)==1
    Smpl = imcrop(Frame,Smpl_1); % Crops the image to the specified region of
interest
    %figure(1);
    %imshow(croppedimage); % If you would like the cropped image to be displayed,
delete the "%" infront of "imshow(croppedimage);"
    Smpl = double(Smpl); % Changes the format of the image values
    average = mean(Smpl(:));
    else
        average = NaN;
    end
    Curaverage(1,j) = average;
```

```
    %Totaverage = [Totaverage average];
    % Saves the average intensity and adds it to a CSV file
    %a = csvread('y1.csv');
    %figure(2);
    %plot(a);
    %hold off;
    % If you would like the average intensities to be continuously plotted by Matlab,
delete the "%" infront of "1=csvread('y1.csv');" and the "%" infront of "plot(1);" and
the the "%" infront of "hold off;"

    %2
    j=2
    if Sample_truth(j,1)==1
    Smpl = imcrop(Frame,Smpl_2); % Crops the image to the specified region of
interest
    %imshow(croppedimage); % If you would like the cropped image to be displayed,
delete the "%" infront of "imshow(croppedimage);"
    Smpl = double(Smpl); % Changes the format of the image values
    average = mean(Smpl(:)); % Averages all the pixel intensities within the region of
interest
    else
        average = NaN;
    end
    Curaverage(1,j) = average;

    %3
    j=3
    if Sample_truth(j,1)==1
    Smpl = imcrop(Frame,Smpl_3);
    Smpl = double(Smpl);
    average = mean(Smpl(:));
    else
        average = NaN;
    end
    Curaverage(1,j) = average;

    %4
    j=4
    if Sample_truth(j,1)==1
    Smpl = imcrop(Frame,Smpl_4);
    croppedimage = double(Smpl);
    average = mean(Smpl(:));
    else
        average = NaN;
    end
    Curaverage(1,j) = average;

    %5
    j=5
```

```
    if Sample_truth(j,1)==1
    Smpl = imcrop(Frame,Smpl_5);
    Smpl = double(Smpl);
    average = mean(Smpl(:));
    else
        average = NaN;
    end
    Curaverage(1,j) = average;

    %6
    j=6
    if Sample_truth(j,1)==1
    Smpl = imcrop(Frame,Smpl_6);
    Smpl = double(Smpl);
    average = mean(Smpl(:));
    else
        average = NaN;
    end
    Curaverage(1,j) = average;

    %7
    j=7
    if Sample_truth(j,1)==1
    Smpl = imcrop(Frame,Smpl_7);
    Smpl = double(Smpl);
    average = mean(Smpl(:));
    else
        average = NaN;
    end
    Curaverage(1,j) = average;


    %8
    j=8
    if Sample_truth(j,1)==1
    Smpl = imcrop(Frame,Smpl_8);
    %croppedimage = imcrop(image,[1204 328 55 553]); % Crops the image to the
specified region of interest
    Smpl = double(Smpl);
    average = mean(Smpl(:));
    else
        average = NaN;
    end
    Curaverage(1,j) = average;

    %9
    j=9
    if Sample_truth(j,1)==1
    Smpl = imcrop(Frame,Smpl_9);
```

```
    %croppedimage = imcrop(image,[1340 279 63 670]); % Crops the image to the
specified region of interest
    Smpl = double(Smpl);
    average = mean(Smpl(:));
    else
        average = NaN;
    end
    Curaverage(1,j) = average;

    %10
    j=10
    if Sample_truth(j,1)==1
    Smpl = imcrop(Frame,Smpl_10);
    %croppedimage = imcrop(image,[1476 279 63 670]); % Crops the image to the
specified region of interest
    Smpl = double(Smpl);
    average = mean(Smpl(:));
    else
        average = NaN;
    end
    Curaverage(1,j) = average;

    %11
    j=11
    if Sample_truth(j,1)==1
    Smpl = imcrop(Frame,Smpl_11);
    %croppedimage = imcrop(image,[1617 279 63 670]); % Crops the image to the
specified region of interest
    Smpl = double(Smpl);
    average = mean(Smpl(:));
    else
        average = NaN;
    end
    Curaverage(1,j) = average;

    %12
    j=12
    if Sample_truth(j,1)==1
    Smpl = imcrop(Frame,Smpl_12);
    %croppedimage = imcrop(image,[1753 279 63 670]); % Crops the image to the
specified region of interest
    Smpl = double(Smpl);
    average = mean(Smpl(:));
    else
        average = NaN;
    end
    Curaverage(1,j) = average;

    %13
    j=13
```

```
    if Sample_truth(j,1)==1
    Smpl = imcrop(Frame,Smpl_13);
    %croppedimage = imcrop(image,[1923 279 63 670]); % Crops the image to the specified region of interest
    Smpl = double(Smpl);
    average = mean(Smpl(:));
    else
        average = NaN;
    end
    Curaverage(1,j) = average;

    %14
    j=14
    if Sample_truth(j,1)==1
    Smpl = imcrop(Frame,Smpl_14);
    %croppedimage = imcrop(image,[2098 279 63 670]); % Crops the image to the specified region of interest
    Smpl = double(Smpl);
    average = mean(Smpl(:));
    else
        average = NaN;
    end
    Curaverage(1,j) = average;

    Curaverage=Curaverage';
    Cumaverage=[Cumaverage Curaverage];

    waitbar(k/a,b);
end


Cumaveragesm=Cumaverage;

for s=1:14

    if (Cumaveragesm(s,1)>0)
    Cumaveragesm(s,:)=smooth(Cumaveragesm(s,:),0.05,'moving');
    end

end

Cumaverage=Cumaverage';
Cumaveragesm=Cumaveragesm';

[tcropn,~]=size(Cumaverage);
tcrop=time
tcrop(tcropn+1:end)=[];
figure(3);
hold on;
for p=1:14
```

```
  if (Cumaverage(1,p)>0)
      plot(tcrop,Cumaverage(:,p))
  end
end
for p=1:14
  if (Cumaveragesm(1,p)>0)
      plot(tcrop,Cumaveragesm(:,p),'r')
  end
end
Setname = [Runname '.jpg']
title(Runname,'FontSize', 30,'fontWeight','bold')
xlhand = get(gca,'xlabel')
set(xlhand,'string','Time (Hours)','fontsize',25)
xlhand = get(gca,'ylabel')
set(xlhand,'string','Mean Inensity (Degree of Settling)','fontsize',25)
set(gca,'fontsize',20)
    set(gcf, 'PaperPositionMode', 'manual');
    set(gcf, 'PaperUnits', 'points');
    set(gcf, 'PaperPosition', [0 0 1920 1080]);
    print ('-djpeg', Setname)
    close(3)

Prenorm=Cumaveragesm;
normval=min(Cumaveragesm(1,:));
norms=Cumaveragesm(1,:)-normval;
[m,~]=size(Cumaveragesm)
norms=repmat(norms,m,1)
Cumaveragesm=Cumaveragesm-norms
[m,~]=size(Cumaveragesm);
[t,~]=size(time);
if m<t
    time(m+1:end,:)=[];
else
    time(end+1:m,:)=NaN;
end
Table=[time Cumaveragesm];
Table=num2cell(Table);
Churned=Table(1:5:end,:);
Headers = {'Time' 'Sample 1' 'Sample 2' 'Sample 3' 'Sample 4' 'Sample 5' 'Sample 6'
'Sample 7' 'Sample 8' 'Sample 9' 'Sample 10' 'Sample 11' 'Sample 12' 'Sample 13'
'Sample 14'};
Table= [Headers; Table];
Churned=[Headers; Churned];

Prenorm= [time Prenorm]
Prenorm=num2cell(Prenorm);
Prenormchurn=Prenorm(1:5:end,:);
Prenorm= [Headers; Prenorm];
Prenormchurn= [Headers; Prenormchurn];
```

```
xlswrite(Outputname,Prenorm,4);
xlswrite(Outputname,Prenormchurn,3);
xlswrite(Outputname,Table,2);
xlswrite(Outputname,Churned,1);
close all;
winopen(Outputname)
clear all;
```

I. 7 The background classification code

```
clear
close all
clc

load Trained_symbol.mat


mkdir Output-1
mkdir Output-2
mkdir Output-3
mkdir Output-4
mkdir Output-5
mkdir Output-6
mkdir Output-7
mkdir Output-8
mkdir Output-9
mkdir Output-10
mkdir Output-11
mkdir Output-12


dirPath = uigetdir();
files = dir([dirPath '/*.tif']);
% read directory




%
% sort by number
for i = 1:size(files, 1)
    index = str2double(regexp(files(i).name, '[0-9]+', 'match'));
    files(i).datenum = index;
end
[~, fi] = sort([files.datenum]);
files = files(fi);
```

```
I = imread(horzcat(dirPath,'\',files(1).name));


figure, imshow(I);


h = imrect;
%r  = msgbox('Select the number of the background. Make sure that the whole circle
is inside the box then double click inside the box when you finish.');
position(1,1:4) = wait(h);
position = round(position);
close all

Selected = I(position (2):position (2)+position (4)-1,position (1):position
(1)+position (3),:);
Roi = 1-( im2bw(imadjust(rgb2gray(Selected))));

Sum = sum(Roi);

j = 1;
while Sum(j) == 0
    j = j+1;
end
x_min = j;

j = length(Sum);
while Sum(j) == 0
    j = j-1;
end
x_max = j;

Sum2 = sum(Roi,2);

i = 1;
while Sum2(i) == 0
    i = i+1;
end
y_min = i;

i = length(Sum2);
while Sum2(i) == 0
    i = i-1;
end
y_max = i;

%Crop = Roi(y_min:y_max, x_min:x_max);
position2(1) = position(1)+x_min+20;
position2(2) = position(2)+y_min+20;
position2(3) = 49;%x_max - x_min+40;
position2(4) = 50;%y_max - y_min+40;
```

```
H = waitbar(0,'Initializing waitbar...');
for i = 1:size(files,1)
   rgb = imread(horzcat(dirPath,'\',files(i).name));
   Roi_crop = imadjust(rgb2gray(rgb(position2 (2):position2 (2)+position2 (4)-
1,position2 (1):position2 (1)+position2 (3),:)));
   imshow (imresize(Roi_crop,2))
   Name= horzcat('.\','image.bmp');
   imwrite(Roi_crop,Name);
   imds = imageDatastore({Name});
   Predicted = double(classify(convnet,imds));

   OUt (i) = Predicted;
   copyfile ((horzcat(dirPath,'\',files(i).name)), horzcat('Output-
',num2str(Predicted)));

   waitbar(i / size(files,1))
   perc = fix( i/size(files,1)*100);
   waitbar(perc/100,H,sprintf(horzcat('processing  %d%% .....'),perc))
end
close (H)
close all
```

I. 8 The training code

```
clear
close all
clc

load imds_sym.mat
imds.Labels = categorical(imds.Labels);
digitData = imds;
Cl = 11; %number of classes
img = readimage(digitData,1);
[m n o] = size(img) % size of input image

trainingNumFiles = 33;
rng(1) % For reproducibility
[trainDigitData,testDigitData] = splitEachLabel(digitData, ...
            trainingNumFiles,'randomize');

layers = [imageInputLayer([m n o])
         convolution2dLayer(5,100)
         reluLayer
         maxPooling2dLayer(2,'Stride',2)
         fullyConnectedLayer(Cl) % number of classes
         softmaxLayer
         classificationLayer()];
```

```
options = trainingOptions('sgdm','MaxEpochs',25, ...
    'InitialLearnRate',0.0001);

convnet = trainNetwork(trainDigitData,layers,options);

YTest = classify(convnet,testDigitData);
TTest = testDigitData.Labels;


L = length(YTest);
A = zeros(Cl,L);
B = zeros(Cl,L);

for i = 1: L
    a = TTest(i);
    A(a,i) = 1;

    b = YTest(i);
    B(b,i) = 1;
end

plotconfusion(A,B)

accuracy = sum(YTest == TTest)/numel(TTest)
```

I. 9 Rejecting unusable images code

```
% this code selects the best images for analysis
clear
close all
clc


th = 2;    %threshold
Num_Cuv = 1;
Imfolder1 = uigetdir('','Select directory containing TIF images for processing');
Imfolder2=[Imfolder1 '\*.tif'];
files = dir(Imfolder2); %Replace 'photo*.JPG' with relevant name and Frames 1 with foldername
% sort by number
for i = 1:size(files, 1)
    index = str2double(regexp(files(i).name, '[0-9]+', 'match'));
    files(i).datenum = index;
end
```

```
[~, fi] = sort([files.datenum]);
files = files(fi);


Cuv = 1: Num_Cuv;

options.Interpreter = 'tex';
% Include the desired Default answer
options.Default = 'No. Already selected.';
% Use the TeX interpreter in the question
qstring = 'Do you want to select ROI inside the cuvette that contains water?';
choice = questdlg(qstring,'Boundary Condition',...
    'Yes','No. Already selected.',options);


if strcmp (choice,'Yes')
    F = 1;
    while (F == 1)
        f = files(length(files));
        path = [Imfolder1 '\' f.name];
        rgb = imread(path);
        [position,startY,endY, startX,endX] =  Select_ROI (rgb,Num_Cuv);

        options.Interpreter = 'tex';
        % Include the desired Default answer
        options.Default = 'No';
        % Use the TeX interpreter in the question
        qstring = 'Do you want to reselect ROI ?';
        choice = questdlg(qstring,'Boundary Condition',...
            'Yes','No',options);
        if strcmp (choice ,'No')
            F = 0;
            position (:,1) = position (:,1)+round(startX);
            position (:,2) = position (:,2)+round(startY);
            bound = [startY,endY, startX,endX];
            save position.mat position
            save bound.mat bound
        end
        close (1)
    end
else
    load position.mat
    load bound.mat
    position = position (Cuv,:);
end



Font = 16;% text font used during ROI displaying
```

```
Sample_size = 3*ones(1,Num_Cuv);

Smpl = position;
av = Smpl(:,3);
Xp = (Cuv'-1).*av + (av-Font)/2;
Loc = horzcat(Xp, 30*ones(1,Num_Cuv)'); %position of numbers in ROIs display


data = {};
tsIndex = [];
NuFiles = size(files, 1);


for i =  1: NuFiles % range of images (original value = 1)
   f = files(i);
   path = [Imfolder1 '\' f.name]
   rgb = imread(path);
   tsIndex = str2double(regexp(f.name, '[0-9]+', 'match'));
   [crgb] = get_ROI (rgb,position);
   R = crgb(:,:,1);
   G = crgb(:,:,2);
   B = crgb(:,:,3);
   info(i,1:5) = [i tsIndex mean(R(:)) mean(G(:)) mean(B(:))];
end


H = histogram(info(:,3),7);
V =  H.Values;
Max = find(V ==max(V));
Bin = H.BinEdges;
Width = H.BinWidth*th;
Rlim = Bin(Max)+Width;
Llim = Bin(Max)-Width;

Ind1 = (info(:,3) > Llim & info(:,3) <Rlim);

H = histogram(info(:,4),7);
V =  H.Values;
Max = find(V ==max(V));
Bin = H.BinEdges;
Width = H.BinWidth*th;
Rlim = Bin(Max)+Width;
Llim = Bin(Max)-Width;

Ind2 = (info(:,4) > Llim & info(:,4) <Rlim);

H = histogram(info(:,5),8);
V =  H.Values;
Max = find(V ==max(V));
Bin = H.BinEdges;
```

```
Width = H.BinWidth*th;
Rlim = Bin(Max)+Width;
Llim = Bin(Max)-Width;

Ind3 = (info(:,5) > Llim & info(:,5) <Rlim);

AND = Ind1 & Ind2 & Ind3;

Ind = info(AND,1);

Folder = horzcat(Imfolder1, '\Good');
mkdir (Folder)
for i = 1: length(Ind)
    %File = horzcat(
  copyfile(horzcat(Imfolder1,'\','Image',num2str(info(Ind(i),2)),'.tif'), Folder);
end
```

I. 10 Entering experiment details code

```
clear
close all
clc

HEADERS = {'Time' 'Sample 1' 'Sample 2' 'Sample 3' 'Sample 4' 'Sample 5' 'Sample 6' 'Sample 7' 'Sample 8' 'Sample 9' 'Sample 10'};

Runname = input ('Enter experiment name and/or date   ', 's');
Outputname_R=[Runname ' -Blue background_R channel.xlsx'];
Outputname_G=[Runname ' -Blue background_G channel.xlsx'];
Outputname_B=[Runname ' -Blue background_B channel.xlsx'];


Num_Cuv = input ('How many cuvettes do you have in this experiment ?   ', 's');
Num_Cuv = str2num(Num_Cuv);

[Timefile, Path1] = uigetfile('*.csv','Select the CSV file containing the image capture times...');
time=csvread(horzcat(Path1,Timefile));

TemplateXLSX_1 = 'RED CHANNEL TEMPLATE v1.0.xlsx';
TemplateXLSX_2 = 'GREEN CHANNEL TEMPLATE v1.0.xlsx';
TemplateXLSX_3 = 'BLUE CHANNEL TEMPLATE v1.0.xlsx';


Imfolder1 = uigetdir('','Select directory containing TIF images for processing');
Imfolder2=[Imfolder1 '\*.tif'];
```

```
files = dir(Imfolder2); %Replace 'photo*.JPG' with relevant name and Frames 1 with
foldername
% sort by number
```

I. 11 The selection tool code

```
function [position,startY,endY, startX,endX]  = Select_ROI (rgb,Num_Cuv)

[startY,endY, startX,endX] = find_boundries (rgb);
I =  rgb(startY:endY, startX:endX, 1:3);
figure (1), imshow(I);
h = imrect;
position(1,1:4) = wait(h);

for i = 2: Num_Cuv
    h = imrect(gca,[position(1,1:4)]);
    position(i,1:4) = wait(h);

end
position = round (position);

position = sortrows(position, 1);
position (:,2) = max(position (:,2));
position (:,3) = min(position (:,3));
position (:,4) = min(position (:,4));

Image_ROI = insertShape(I,'Rectangle',position ,'LineWidth',3, 'Color','red');
imshow (Image_ROI)

 end
```

I. 12 The cuvette detection code

```
function [cuv_rgbs] = get_ROI8 (I,position,Cuv,bound)

startY = bound (1);
endY = bound (2);
startX = bound (3);
endX = bound (4);

position2 = position;
position2 (:,1) = position (:,1)-round(startX);
position2 (:,2) = position (:,2)-round(startY);

rgb =  I(startY:endY, startX:endX, 1:3);
HSV = rgb2hsv(rgb);
```

```
Q = rgb(1:220, position2 ((1),1):position2 ((1),1)+ position2 ((1),3)-1, 1:3);
%figure; imshow(Q)

hsv = rgb2hsv(Q);

v = hsv(:,:,3);
%figure;imshow(v);%

Sum = sum(v,2);
%figure;plot(Sum);
i = find(Sum == max(Sum));






i = max(i);
cuv_rgbs = {};
[h, w, ~] = size(rgb);
H = 1- HSV(i+15:i+45,:,3);% it depebds on the position of the covettes
% figure; imshow (H);

Ref = zeros(1,w);
for C = 1:Cuv;
   Ref(position2((C),1):position2((C),1)+position2((C),3)-1) =
ones(1,position2((C),3));
end

Sum = sum(H);

Max_value = max(Sum(10:140))-min(Sum);

vs_treshold = Max_value*.5; % based on experimental data
x_filter = Sum > vs_treshold;

A = x_filter ;
x_filter = x_filter & Ref;


show_figure = 0;
if show_figure == 1
   figure
   subplot(2,2,1), plot(Sum)
   subplot(2,2,2), plot(A)
   subplot(2,2,3),  plot(Ref)
   subplot(2,2,4),  plot(x_filter)
end
```

```
Bound =  Find_Bound (x_filter);
B = size(Bound,1);

for k = 1: size(position,1)
    Temp = [zeros(1,startX) x_filter];
    si = zeros(1,length(Temp));
    st = position (k,1);
    sp = position (k,1)+position (k,3);
    si(st:sp) = 1;
    s2 = si& Temp;
   %figure;
   %subplot(2,2,1), plot(Temp)
   %subplot(2,2,2), plot(si)
   %subplot(2,2,3),  plot(s2)
   D = sum(s2);
   %[k  D position(1,3)*.55]
   if D > 22

        cuv_rgb = I(position (k,2):position (k,2)+ position (k,4)-1, position
((k),1):position ((k),1)+ position ((k),3)-1, 1:3);
        %position (Cuv(k),2)
        %size(cuv_rgb)
   else
       cuv_rgb = zeros( position (k,4),position (k,3),3);
   end
   cuv_rgbs = [cuv_rgbs; {cuv_rgb}];


end





end

function [Bound] = Find_Bound (x)

 L = length (x);

 i = 1;
 k = 1;
 Bound=[];
 while i < L
     if x(i) == 1
         S = i;
         E = i;
         F = 1;
```

```
        while F == 1 && i < L
            i = i + 1;
            if x(i) == 1
                E = i;
            else
                F = 0;
                Bound (k,:) = [S E];
                k = k + 1;

            end
        end
    end
    i = i + 1;
end

end
```

I. 13 The data extraction code (white background)

```
files = dir(Imfolder2); %Replace 'photo*.JPG' with relevant name and Frames 1 with
foldername
% sort by number
for i = 1:size(files, 1)
    index = str2double(regexp(files(i).name, '[0-9]+', 'match'));
    files(i).datenum = index;
end
[~, fi] = sort([files.datenum]);
files = files(fi);


Cuv = 1: Num_Cuv;

options.Interpreter = 'tex';
% Include the desired Default answer
options.Default = 'No. Already selected.';
% Use the TeX interpreter in the question
qstring = 'Do you want to select ROI ?';
choice = questdlg(qstring,'Boundary Condition',...
    'Yes','No. Already selected.',options);


if strcmp (choice,'Yes')
    F = 1;
    while (F == 1)
        f = files(length(files));
        path = [Imfolder1 '\' f.name];
        rgb = imread(path);
        [position,startY,endY, startX,endX] =  Select_ROI (rgb,Num_Cuv);
```

```
        options.Interpreter = 'tex';
        % Include the desired Default answer
        options.Default = 'No';
        % Use the TeX interpreter in the question
        qstring = 'Do you want to reselect ROI ?';
        choice = questdlg(qstring,'Boundary Condition',...
            'Yes','No',options);
        if strcmp (choice ,'No')
            F = 0;
            position (:,1) = position (:,1)+round(startX);
            position (:,2) = position (:,2)+round(startY);
            bound = [startY,endY, startX,endX];
            save position.mat position
            save bound.mat bound
        end
        close (1)
    end
else
    load position.mat
    load bound.mat
    position = position (Cuv,:);
end




Font = 16;% text font used during ROI displaying
Sample_size = 3*ones(1,Num_Cuv);

Smpl = position;
av = Smpl(:,3);
Xp = (Cuv'-1).*av + (av-Font)/2;
Loc = horzcat(Xp, 30*ones(1,Num_Cuv)'); %position of numbers in ROIs display

data = {};
tsIndex = [];
NuFiles = size(files, 1);
Cumaverage = [ NaN NaN NaN NaN NaN NaN NaN NaN NaN NaN];
Cumaverage = repmat(Cumaverage,NuFiles,1);

outputVideo = VideoWriter(fullfile(Imfolder1,'Out1.avi'));
outputVideo.FrameRate = 10;
open(outputVideo)


for i =  1:  NuFiles % range of images (original value = 1)
    f = files(i);
    path = [Imfolder1 '\' f.name]
    rgb = imread(path);
    tsIndex = [tsIndex str2double(regexp(f.name, '[0-9]+', 'match'))];
```

```
    %[crgb] = get_ROI (rgb,position);
    [crgb] = get_ROI6 (rgb,position,Num_Cuv,bound);

    preview_rgb = [];
    Size_crgb = size(crgb, 1);
    for j = 1:Size_crgb
        [samples, preview_crgb] = get_samples(crgb{j});

        data{i, j} = samples;
        %preview_crgb = crgb{j};

        Cumaverage (i,Cuv(j)) = mean(preview_crgb(:));
        preview_rgb = [preview_rgb preview_crgb];
    end
    RGB =
insertText(preview_rgb,Loc(1:Size_crgb,:),Cuv(1:Size_crgb),'AnchorPoint','LeftBott
om','FontSize',Font);
    imshow(RGB);
    FrameWidth = length(Cuv)*Smpl(1,3);
    if FrameWidth ~= size(RGB,2)
        RGB(:,size(RGB,2)+1:FrameWidth,:) = 0;
    end


    writeVideo(outputVideo,RGB)
end
close(outputVideo)
time = time(tsIndex);
imshow(get_color_distance_map(data));
```

I. 14 The data extraction code (coloured background)

```
files = dir(Imfolder2); %Replace 'photo*.JPG' with relevant name and Frames 1 with
foldername
% sort by number
for i = 1:size(files, 1)
    index = str2double(regexp(files(i).name, '[0-9]+', 'match'));
    files(i).datenum = index;
end
[~, fi] = sort([files.datenum]);
files = files(fi);


Cuv = 1: Num_Cuv;

options.Interpreter = 'tex';
% Include the desired Default answer
options.Default = 'No. Already selected.';
```

```
% Use the TeX interpreter in the question
qstring = 'Do you want to select ROI ?';
choice = questdlg(qstring,'Boundary Condition',...
    'Yes','No. Already selected.',options);


if strcmp (choice,'Yes')
    F = 1;
    while (F == 1)
        f = files(length(files));
        path = [Imfolder1 '\' f.name];
        rgb = imread(path);
        [position,startY,endY, startX,endX] =  Select_ROI (rgb,Num_Cuv);

        options.Interpreter = 'tex';
        % Include the desired Default answer
        options.Default = 'No';
        % Use the TeX interpreter in the question
        qstring = 'Do you want to reselect ROI ?';
        choice = questdlg(qstring,'Boundary Condition',...
            'Yes','No',options);
        if strcmp (choice ,'No')
            F = 0;
            position (:,1) = position (:,1)+round(startX);
            position (:,2) = position (:,2)+round(startY);
            bound = [startY,endY, startX,endX];
            save position.mat position
            save bound.mat bound
        end
        close (1)
    end
else
    load position.mat
    load bound.mat
    position = position (Cuv,:);
end

Font = 16;% text font used during ROI displaying
Sample_size = 3*ones(1,Num_Cuv);

Ns = position;
av = Ns(:,3);
Xp = (Cuv'-1).*av + (av-Font)/2;
Loc = horzcat(Xp, 30*ones(1,Num_Cuv)'); %position of numbers in ROIs display


data = {};
tsIndex = [];
NuFiles = size(files, 1);
```

```
outputVideo = VideoWriter(fullfile(Imfolder1,'Out1.avi'));
outputVideo.FrameRate = 10;
open(outputVideo)

%% prepare Excel file
Smpl = zeros(Num_Cuv,4);
sq_lbl = strtrim(cellstr(num2str((1:Num_Cuv)')));
Empty ={" " " "}; Dataout = Empty;

Excel = actxserver('Excel.Application');
set(Excel,'Visible',1);
Excel.DisplayAlerts = false;
Workbooks = Excel.Workbooks;
Workbook = invoke(Workbooks, 'Add');
Sheets = Excel.ActiveWorkBook.Sheets;
Sheet1 = get(Sheets, 'Item', 1);
Sheet1.Activate;
Shapes = Sheet1.Shapes;
Alphabet = 'ABCDEFGHIJKLMNOPQRSTUVWXYZ';
Aves=[];

%% SAMPLE LOCATIONS
Cumaverage_R = [ NaN NaN NaN NaN NaN NaN NaN NaN NaN NaN];
Cumaverage_R = repmat(Cumaverage_R,NuFiles,1);
Cumaverage_G = [ NaN NaN NaN NaN NaN NaN NaN NaN NaN NaN];
Cumaverage_G = repmat(Cumaverage_G,NuFiles,1);
Cumaverage_B = [ NaN NaN NaN NaN NaN NaN NaN NaN NaN NaN];
Cumaverage_B = repmat(Cumaverage_B,NuFiles,1);

for i =  1: NuFiles
   f = files(i);
   path = [Imfolder1 '\' f.name]
   rgb = imread(path);
   tsIndex = [tsIndex str2double(regexp(f.name, '[0-9]+', 'match'))];
   [crgb] = get_ROI4 (rgb,position,Num_Cuv,bound);

   preview_rgb = [];
   Size_crgb = size(crgb, 1);


   for j = 1:Size_crgb

      [samples, preview_crgb] = get_samples(crgb{j});

      Cuv_r= preview_crgb(:,:,1);
      Cuv_g= preview_crgb(:,:,2);
      Cuv_b= preview_crgb(:,:,3);
      Colours_avg                                    =                                    [i,
round(mean2(Cuv_r)),round(mean2(Cuv_g)),round(mean2(Cuv_b))];
      Cumaverage_R (i,Cuv(j)) = round(mean2(Cuv_r));
```

```
        Cumaverage_G (i,Cuv(j)) = round(mean2(Cuv_g));
        Cumaverage_B (i,Cuv(j)) = round(mean2(Cuv_b));

        Aves = [Aves;Colours_avg];
        preview_rgb = [preview_rgb preview_crgb];
    end


        K=num2str(i);

    RGB = insertText(preview_rgb,Loc(1:Size_crgb,:),Cuv(1:Size_crgb),'AnchorPoint','LeftBottom','FontSize',Font);
    imshow(RGB);
    FrameWidth = length(Cuv)*Ns(1,3);
    if FrameWidth ~= size(RGB,2)
        RGB(:,size(RGB,2)+1:FrameWidth,:) = 0;
    end
        writeVideo(outputVideo,RGB)
end
close(outputVideo)
```

I. 15 The data extraction code (stripes & letters)

```
files = dir(Imfolder2); %Replace 'photo*.JPG' with relevant name and Frames 1 with foldername
% sort by number
for i = 1:size(files, 1)
    index = str2double(regexp(files(i).name, '[0-9]+', 'match'));
    files(i).datenum = index;
end
[~, fi] = sort([files.datenum]);
files = files(fi);


Cuv = 1: Num_Cuv;

options.Interpreter = 'tex';
% Include the desired Default answer
options.Default = 'No. Already selected.';
% Use the TeX interpreter in the question
qstring = 'Do you want to select ROI ?';
choice = questdlg(qstring,'Boundary Condition',...
    'Yes','No. Already selected.',options);


if strcmp (choice,'Yes')
    F = 1;
```

```
    while (F == 1)
        f = files(length(files));
        path = [Imfolder1 '\' f.name];
        rgb = imread(path);
        [position,startY,endY, startX,endX] =  Select_ROI (rgb,Num_Cuv);

        options.Interpreter = 'tex';
        % Include the desired Default answer
        options.Default = 'No';
        % Use the TeX interpreter in the question
        qstring = 'Do you want to reselect ROI ?';
        choice = questdlg(qstring,'Boundary Condition',...
            'Yes','No',options);
        if strcmp (choice ,'No')
            F = 0;
            position (:,1) = position (:,1)+round(startX);
            position (:,2) = position (:,2)+round(startY);
            bound = [startY,endY, startX,endX];
            save position.mat position
            save bound.mat bound
        end
        close (1)
    end
else
    load position.mat
    load bound.mat
    position = position (Cuv,:);
end




Font = 16;% text font used during ROI displaying
Sample_size = 3*ones(1,Num_Cuv);

Ns = position;
av = Ns(:,3);
Xp = (Cuv'-1).*av + (av-Font)/2;
Loc = horzcat(Xp, 30*ones(1,Num_Cuv)'); %position of numbers in ROIs display


data = {};
tsIndex = [];
NuFiles = size(files, 1);

outputVideo = VideoWriter(fullfile(Imfolder1,'Out1.avi'));
outputVideo.FrameRate = 10;
open(outputVideo)

%% prepare Excel file
```

```
Smpl = zeros(Num_Cuv,4);
sq_lbl = strtrim(cellstr(num2str((1:Num_Cuv)')));
Empty ={" " " "}; Dataout = Empty;

Excel = actxserver('Excel.Application');
set(Excel,'Visible',1);
Excel.DisplayAlerts = false;
Workbooks = Excel.Workbooks;
Workbook = invoke(Workbooks, 'Add');
Sheets = Excel.ActiveWorkBook.Sheets;
Sheet1 = get(Sheets, 'Item', 1);
Sheet1.Activate;
Shapes = Sheet1.Shapes;
Alphabet = 'ABCDEFGHIJKLMNOPQRSTUVWXYZ';

%% SAMPLE LOCATIONS
Cumaverage_1 = [ NaN NaN NaN NaN NaN NaN NaN NaN NaN NaN];
Cumaverage_1 = repmat(Cumaverage_1,NuFiles,1);
Cumaverage_2 = [ NaN NaN NaN NaN NaN NaN NaN NaN NaN NaN];
Cumaverage_2 = repmat(Cumaverage_2,NuFiles,1);
Cumaverage_3 = [ NaN NaN NaN NaN NaN NaN NaN NaN NaN NaN];
Cumaverage_3 = repmat(Cumaverage_3,NuFiles,1);

for i =  1: NuFiles
    f = files(i);
    path = [Imfolder1 '\' f.name]
    rgb = imread(path);
    tsIndex = [tsIndex str2double(regexp(f.name, '[0-9]+', 'match'))];
    %[crgb] = get_ROI (rgb,position);
    [crgb] = get_ROI6 (rgb,position,Num_Cuv,bound);

    preview_rgb = [];
    Size_crgb = size(crgb, 1);

    for j = 1:Size_crgb

        [samples, preview_crgb] = get_samples(crgb{j});
        Selected_region =  255-rgb2gray(preview_crgb);
        %ALL_letters_GRAY = [ALL_letters_GRAY Gray_letter];
        level = graythresh(Selected_region);
        BW_letter = im2bw(Selected_region,level);
        SUM = sum(~BW_letter(:));
        %w = rgb2gray(preview_crgb); bw =  w<128;
        stats=regionprops(BW_letter,'Area','BoundingBox','Perimeter');
         if i == NuFiles
           INFO{j} = stats;
        end
        Aves=[]; mont={};
        data=zeros(numel(stats),10);
        data(:,1)=1:numel(stats);
```

```
    All_rect_im4 = [0 0 0 0 0];
    All_rect_Cuv = [0 0 0 0 0];

    AR = 0;
    TH = 0;
    PR = 0;
    k = 0;

    for c = 1:numel(stats)

      if stats(c).Area(:)>900 && stats(c).Area(:)<1300
          k = k + 1;
          color_rect = stats(c).BoundingBox(:);
          area = stats(c).Area(:);
          Perimeter = stats(c).Perimeter(:);
          %color_rect_im4 = [Smpl(i,1)+color_rect(1),Smpl(i,2)+
color_rect(2),color_rect(3),color_rect(4)];
          %rectangle('Position',color_rect_im4,'EdgeColor','r')

          % collect/analyse the data
          Data_avg =[data(c), area, color_rect(3) Perimeter];
          AR = AR + area;
          TH = TH + color_rect(3);
          PR = PR + Perimeter;
          Aves=[Aves; Data_avg];
          %All_rect_im4(j,:) = color_rect_im4;
          %All_rect_Cuv(j,:) = color_rect;

      end
    end
    if SUM ~= 0

      Cumaverage_1 (i,Cuv(j)) = (AR/k);
      Cumaverage_2 (i,Cuv(j)) = (TH/k);
      Cumaverage_3 (i,Cuv(j)) = (PR/k);
    else
      Cumaverage_2 (i,Cuv(j)) = 0;
      Cumaverage_1 (i,Cuv(j)) = 0;
      Cumaverage_3 (i,Cuv(j)) = 0;
    end
    preview_rgb = [preview_rgb preview_crgb];

    tab_size=size(Dataout);
    Image = {'Image_' i '' ''};
    Sample ={'Smpl_' j '' ''};
    Headers ={'Strip #', 'Area', 'Thickness' 'Perimeter'};
    Dataout =[Dataout;Image;Sample;Headers;num2cell(Aves);Empty];
K=num2str(i);

    strtrim(cellstr(num2str((1:numel(All_rect_im4(:,1)))')));
```

```
        Smpl(i,1)+All_rect_im4(:,3)/2,All_rect_im4(:,2)-Smpl(i,2)+All_rect_im4(:,4)/2,
stripe_lbl(:),'color','b','FontSize', 6);
        'Format', 'jpeg');

    end
    RGB =
insertText(preview_rgb,Loc(1:Size_crgb,:),Cuv(1:Size_crgb),'AnchorPoint','LeftBott
om','FontSize',Font);
    imshow(RGB);
    FrameWidth = length(Cuv)*Ns(1,3);
    if FrameWidth ~= size(RGB,2)
        RGB(:,size(RGB,2)+1:FrameWidth,:) = 0;
    end

    writeVideo(outputVideo,RGB)
end
close(outputVideo)
```

I. 16 Exporting the results as excel files code

```
time = time(tsIndex);

O1 = horzcat(Imfolder1, '\', Runname,'_Excel_1');
O2 = horzcat(Imfolder1, '\', Runname,'_Excel_2');
mkdir (O1)
mkdir (O2)

copyfile(TemplateXLSX_1,horzcat(O1,'\',Outputname_1));
copyfile(TemplateXLSX_2,horzcat(O1,'\',Outputname_2));
copyfile(TemplateXLSX_3,horzcat(O1,'\',Outputname_3));

copyfile(TemplateXLSX_1,horzcat(O2,'\',Outputname_1));
copyfile(TemplateXLSX_2,horzcat(O2,'\',Outputname_2));
copyfile(TemplateXLSX_3,horzcat(O2,'\',Outputname_3));

Outputname_11 = horzcat(O1,'\',Outputname_1);
Gen_plot_2 (Outputname_11,Cumaverage_1,time,Cuv,Runname,HEADERS);
Outputname_21 = horzcat(O1,'\',Outputname_2);
Gen_plot_2 (Outputname_21,Cumaverage_2,time,Cuv,Runname,HEADERS);
Outputname_31 = horzcat(O1,'\',Outputname_3);
Gen_plot_2 (Outputname_31,Cumaverage_3,time,Cuv,Runname,HEADERS);

Outputname_12 = horzcat(O2,'\',Outputname_1);
Gen_plot_3 (Outputname_12,Cumaverage_1,time,Cuv,Runname,O2,'Average Area
(Pixel)',HEADERS);
Outputname_22 = horzcat(O2,'\',Outputname_2);
Gen_plot_3 (Outputname_22,Cumaverage_2,time,Cuv,Runname,O1,'Average
Thickness (Pixel)',HEADERS);
```

```
Outputname_32 = horzcat(O2,'\',Outputname_3);
Gen_plot_3            (Outputname_32,Cumaverage_3,time,Cuv,Runname,O2,'Average
Perimeter (Pixel)',HEADERS);


figure('Position',get(0,'ScreenSize'))
imshow(rgb);

for IN = 1 : length (INFO)
   stats = INFO{IN};
   for st = 1:numel(stats)
      if  stats(st).Area(:)>900 && stats(st).Area(:)<1300
         stats(st).Area
         rectangle('Position',[position(IN,1)+stats(st).BoundingBox(1),position(IN,2)+
stats(st).BoundingBox(2),stats(st).BoundingBox(3),stats(st).BoundingBox(4)],'Edge
Color','r')
      end
   end
end
fname=[Imfolder1 '\' 'ROI.bmp'];
hgexport(gcf, fname, hgexport('factorystyle'), 'Format', 'bmp');
close;

fname2=([Imfolder1 '\' 'Output.xlsx']);
Excel = actxserver('Excel.Application');
Excel.DisplayAlerts = false;
set(Excel,'Visible',1);
Workbooks = Excel.Workbooks;
Workbook = invoke(Workbooks, 'Add');
Sheets = Excel.ActiveWorkBook.Sheets;
Sheet1 = get(Sheets, 'Item', 1);
Sheet1.Activate;
Shapes = Sheet1.Shapes;
Shapes.AddPicture(fname ,0,1,500,20,600,335); % col row width length


%fname3=strrep(fname, '.tif', '_Manual_VStrThin.xlsx');
Activesheet = Excel.Activesheet;
Alphabet = 'ABCDEFGHIJKLMNOPQRSTUVWXYZ';
tab_size=size(Dataout);
ex_cell_range=['A1:',Alphabet(tab_size(2)),num2str(tab_size(1))];
ActivesheetRange = get(Activesheet,'Range',ex_cell_range);
set(ActivesheetRange, 'Value', Dataout);
ActivesheetRange.Select;
invoke(Excel.Selection.Columns,'Autofit');
Workbook.SaveAs([Imfolder1 '\' 'Output.xlsx'])
invoke(Workbook, 'Close');
invoke(Excel, 'Quit');
delete(Excel);
```

I. 17 The curve fitting code

```
clear
close all
clc


Imfolder1 = uigetdir('','Select directory containing the Excel files for processing');
Imfolder2=[Imfolder1 '\*.xlsx'];
files = dir(Imfolder2); %Replace 'photo*.JPG' with relevant name and Frames 1 with foldername


%[FileName,PathName] = uigetfile('*.xlsx','Select the file to analyze');
%filename = horzcat(PathName,FileName);

for u = 1:size(files,1)
    FileName = files(u,1).name;
    PathName = files(u,1).folder;
    filename = horzcat(PathName,'\',FileName)
    num = xlsread(filename,'Full Raw Data');
    [num2,txt,raw]= xlsread(filename,'Full Raw Data','A1:K1');
    k = 0;
    for i = 1:10
        H = txt{i};
        if length (H)>6
            s = H(1:6);
            if ~isequal(s,'Sample')
                k = k + 1;
            end
        else
             k = k + 1;
        end
    end

    L = size(num,1);

    for j = 2:k
        i = L;
        p = 0;
        while  isnan(num(i,j)) & i>=1
            i = i -1;
            p = p + 1;
        end

        M(j) = p;
    end
    m = max(M);
    %L = L-m;
```

```
for j =2:k
    i = 1;
    while  (num(i,j)==0) & i<=L
        i = i +1;
    end

    N(j) = i-1;
end
MAX = max(N);
new_size = L-MAX-m-2;
num2(1:new_size,1)= num(1:new_size,1);
for j = 2:k
    num2(1:new_size,j)= num(1+N(j):N(j)+new_size,j);
end
num3 = num2;
for j= 2:k
    V = num2(:,j);
    G = V>0;
    [Bound] = Find_Bound (~G)
    %sum(Bound(:));
    if sum(Bound(:))>0
        for c = 1:size(Bound,1)
            Up = Bound(c,1)-1;
            Low = Bound(c,2)+1;
            Missed = Low-Up;
            Dif = (V(Low)-V(Up))/Missed;

            for b = Up+1:Low-1
                V(b-1)+Dif;
                V(b) = V(b-1)+Dif;
            end
        end
    end
    num3(:,j) = V;
end

num4=num3;
X = num4(:,1);
%figure;
for j=2:k
    Y =  num3(:,j);
    [myFit,g1,o1] = fit(X,Y,'smoothingspline','SmoothingParam',.1);
    YHat = myFit(X);
    num4(:,j) = YHat;
    %subplot(k-1,1,j-1)
    %plot(Y)
    %hold on
    %plot(YHat);
end
out1 = [txt(1:k);num2cell(num4)];
```

```
    out2 = [txt(1:k);num2cell(num3)];

    %filename2 = 'fitted curve.xlsx';
    warning('off','MATLAB:xlswrite:AddSheet')
    xlswrite(filename,out2,'Full Raw Data (Modified)','A1');
    xlswrite(filename,out1,'fitted curve','A1');
end
```

I. 18 Settling time calculation code

```
clear
close all
clc

[FileName,PathName] = uigetfile('*.xlsx','Select the file to analyze');
filename = horzcat(PathName,FileName);
[num,Header] = xlsread(filename,'fitted curve');
%[num2,txt,raw]= xlsread(filename,'Full Raw Data');

 [Sz, C] = size(num);

t = num(1:Sz,1);
y = num(1:Sz,2);
%y2 = round(y/5)*5
S = stepinfo(y,t);

plot(t,y)
hold on
Out = [];
k = 1;
for i = 3: C

    y = num(1:Sz,i);
    %y2 = round(y/5)*5
    S = stepinfo(y,t);

    plot(t,y,'LineWidth',2)
    hold on
    t2 = [S.SettlingTime ;S.SettlingTime ];

    Time = abs(t-S.SettlingTime);
    Set = find(min(Time) == Time);
    Out(k,1:2) = [S.SettlingTime y(Set)];
    k = k + 1;
    L = [0; y(Set)];
    Up = (y(Set)*1.015)*(ones(1,Sz));
    Down = (y(Set)*.985)*(ones(1,Sz));
    plot(t,Up,'--','Color',[0.5,0.5,0.5])
```

```
    plot(t,Down,'--','Color',[0.5,0.5,0.5])
    plot(t2,L)
    plot(t(Set),y(Set),'--gs',...
    'LineWidth',1,...
    'MarkerSize',7,...
    'MarkerEdgeColor','r',...
    'MarkerFaceColor',[0.5,0.5,0.5]);
    hold on


end
title ('Settling time');
ylabel('Average Intensity') % x-axis label
xlabel('Time (hours)') % y-axis label
fname=[PathName '\"Settling time.tif'];
hgexport(gcf, fname, hgexport('factorystyle'), 'Format', 'tiff');


x = [Header(3:end)' num2cell(Out)];
header = {'Cuvette','Time','Value'};
output = [header; x];
warning('off','MATLAB:xlswrite:AddSheet');
xlswrite(filename,output,'Settling time','A1');
```

I. 19 The HSP code

```
clear
close all
clc

PathName = uigetdir('','Select directory containing the analysis files');
Imfolder2=[PathName '\*.xlsx'];
files = dir(Imfolder2); %Replace 'photo*.JPG' with relevant name and Frames 1 with foldername

[FileName,Path] = uigetfile('*.xlsx','Select the file containing Viscosity and Density');
filename = horzcat(Path,FileName);
[Data,txt,raw] = xlsread(filename);
pp = str2num(input ('Enter the value of pp ?   ', 's'));

List={};
for i = 1:size(files, 1)
    f = files(i);
    filename = [PathName '\' f.name];

    [num,Header] = xlsread(filename,'fitted curve');
```

```
%[num2,txt,raw]= xlsread(filename,'Full Raw Data');

  [Sz, C] = size(num);

t = num(1:Sz,1);
y = num(1:Sz,2);
%y2 = round(y/5)*5
S = stepinfo(y,t);

plot(t,y)
hold on
Out = [];
k = 1;
for i = 3: C

y = num(1:Sz,i);
%y2 = round(y/5)*5
S = stepinfo(y,t);

plot(t,y,'LineWidth',2)
hold on
t2 = [S.SettlingTime ;S.SettlingTime ];

Time = abs(t-S.SettlingTime);
Set = find(min(Time) == Time);
Out(k,1) = [S.SettlingTime ];
k = k + 1;
L = [0; y(Set)];
Up = (y(Set)*1.015)*(ones(1,Sz));
Down = (y(Set)*.985)*(ones(1,Sz));
plot(t,Up,'--','Color',[0.5,0.5,0.5])
plot(t,Down,'--','Color',[0.5,0.5,0.5])
plot(t2,L)
plot(t(Set),y(Set),'--gs',...
'LineWidth',1,...
'MarkerSize',7,...
'MarkerEdgeColor','r',...
'MarkerFaceColor',[0.5,0.5,0.5]);
hold on


end
title ('Settling time');
ylabel('Average Intensity') % x-axis label
xlabel('Time (hours)') % y-axis label
fname=[PathName '\''Settling time.tif'];
hgexport(gcf, fname, hgexport('factorystyle'), 'Format', 'tiff');


x = [Header(3:end)' num2cell(Out)];
```

```
    List = vertcat(List,x);
    header = {'Cuvette','Time'};
    output = [header; x];
    warning('off','MATLAB:xlswrite:AddSheet');
    xlswrite(filename,output,'Settling time','A1');
end


Final(1,1:14) = raw(1,1:14);
for i = 1: size(List,1)
    Sol = List (i,1);
    for j = 2: size(raw,1)
        S = raw (j,1);
        if isequal(Sol,S)
            Temp = raw(j,1:14);
            ts = List {i,2};
            Temp {1,6} = ts;
            n = Temp {1,2};
            ps = Temp {1,4};
            Temp {1,8} = ts* (pp-ps)/n;
            Final = vertcat (Final,Temp);
        end
    end
end

RST = cell2mat(Final (2:end,8));
MIN = min(RST);
MAX = max (RST);
Range = MAX-MIN;
DIV = Range /6;
i = 1:5;
b = DIV*i+MIN;
for i = 1:length(RST)
    if RST (i) < b(1)
        Final{i+1,9}= 6;
    elseif RST (i) < b(2)
        Final{i+1,9} = 5;
    elseif RST (i) < b(3)
         Final{i+1,9} = 4;
    elseif RST (i) < b(4)
         Final{i+1,9} = 3;
    elseif RST (i) < b(5)
        Final{i+1,9} = 2;
    else
        Final{i+1,9} = 1;
    end
end
filename = horzcat(PathName,'\','RST.xlsx');
xlswrite(filename,Final,'RST','A1');
```

Appendix II

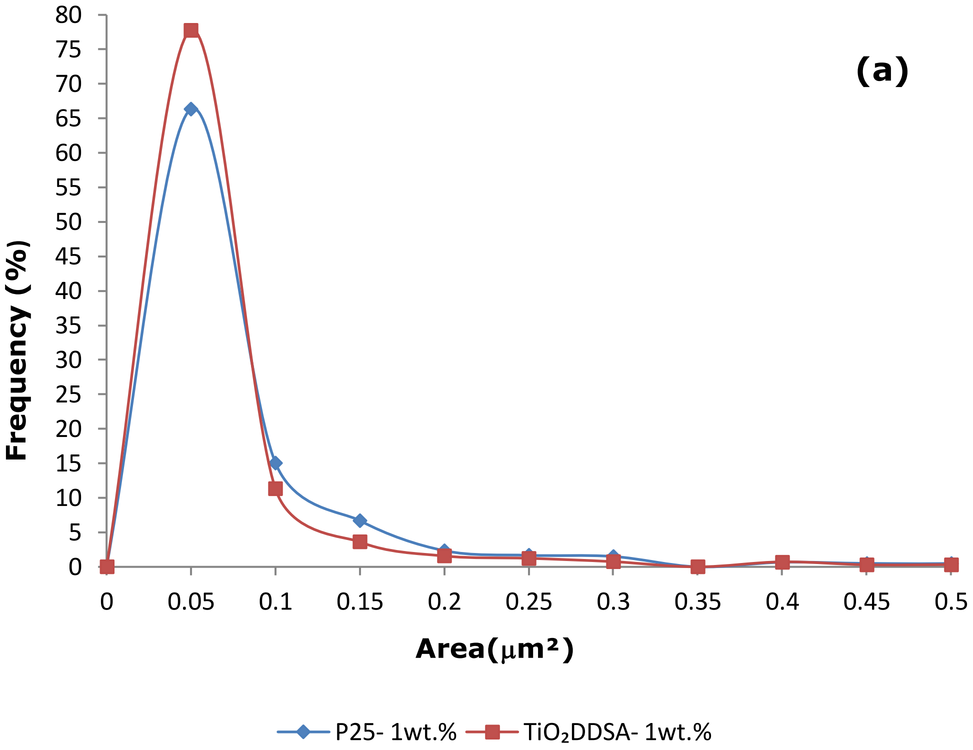
(a)
Frequency (%)
0
5
10
15
20
25
30
35
40
45
50
55
60
65
70
75
80
Area(μm²)
0
0.05
0.1
0.15
0.2
0.25
0.3
0.35
0.4
0.45
0.5
P25- 1wt.%
TiO₂DDSA- 1wt.%

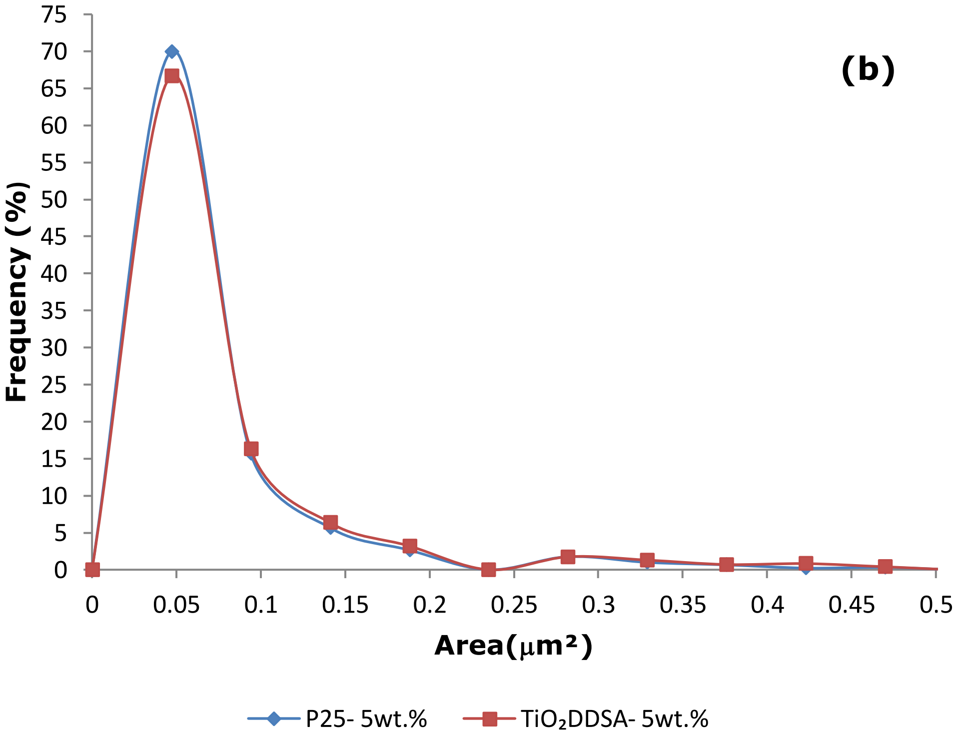
(b)
Frequency (%)
0
5
10
15
20
25
30
35
40
45
50
55
60
65
70
75
Area(μm²)
0
0.05
0.1
0.15
0.2
0.25
0.3
0.35
0.4
0.45
0.5
P25- 5wt.%
TiO₂DDSA- 5wt.%

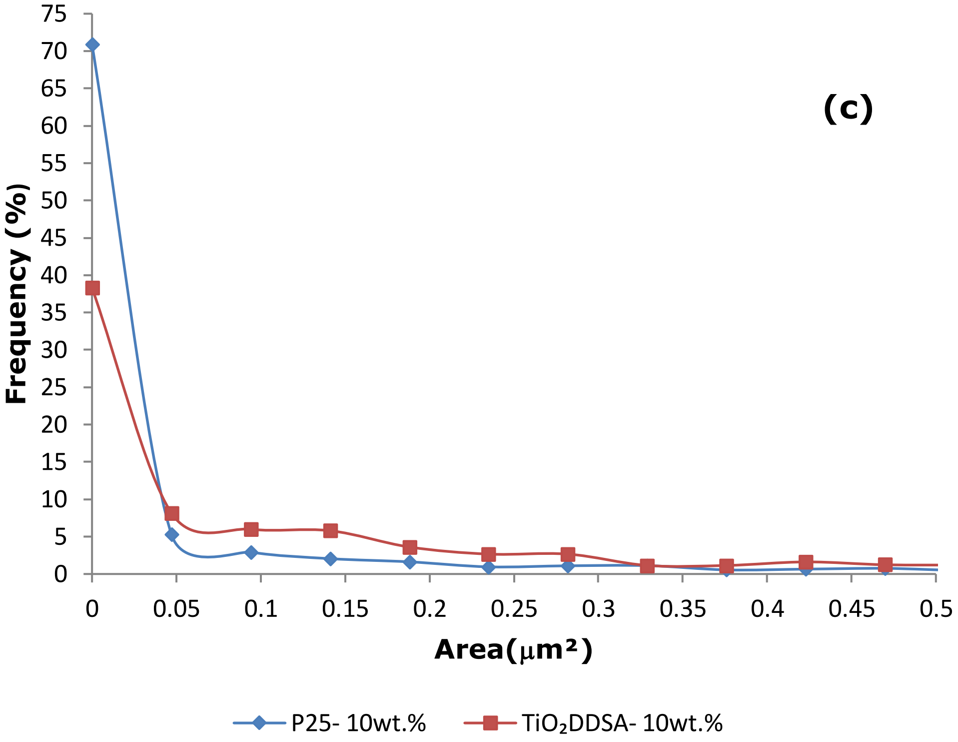

II. 1 Area distribution for different concentrations of TiO_2 and TiO_2DDSA NPs, obtained using image J, from the SEM micrographs for the surfaces of the corresponding epoxy resin blocks.

The curves in Section II.1 (a, b and c) show the NP agglomerate areas occupied by TiO_2 NPs before and after modification within a polymer matrix (epoxy resin) for: (a) 1 wt.%, (b) 5 wt.% and (c) 10 wt.% of TiO_2 and TiO_2DDSA NPs, respectively. All the samples of the three concentrations show the presence of particle areas of a desired nanometre scale (10-100 nm). Samples of 1 wt.% and 10 wt.% of TiO_2DDSA NPs show a higher frequency of 50 nm^2 NPs than the same concentrations of the unmodified TiO_2 as shown in Section II.1 (a & c). However, 5% samples show the opposite (b).

Appendix III

Solvent	Molecular Structure
Acetone	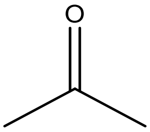
Acetonitrile	$H_3C-C\equiv N$
Benzaldehyde	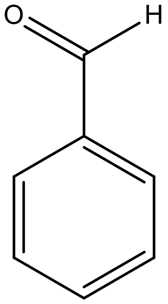
1-Butanol	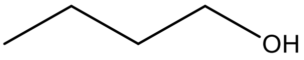
n-Butyl Acetate	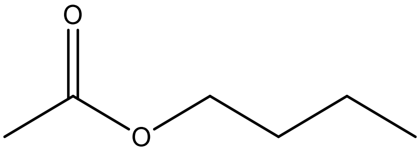
γ-Butyrolactone	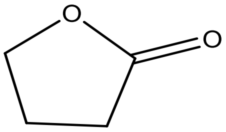
Chloroform	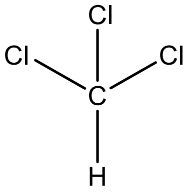
Cyclohexane	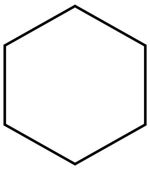

Cyclohexanol	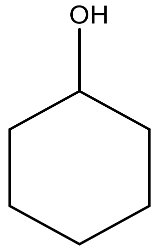
Cyclohexanone	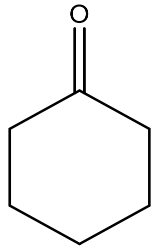
Diacetone Alcohol	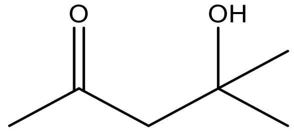
Dimethyl Formamide	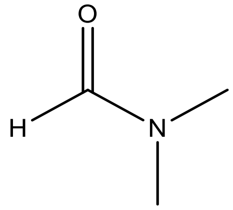
Dimethyl Sulfoxide	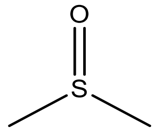
1,4-Dioxane	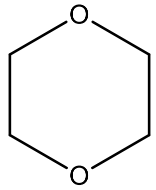
Ethanol	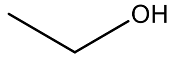
Ethyl Acetate	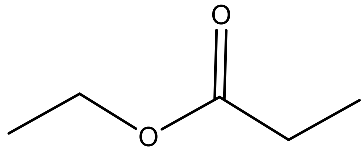
Ethylene Glycol	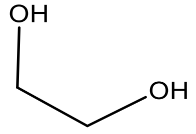
Methanol	H_3C-OH

Methyl Ethyl Ketone	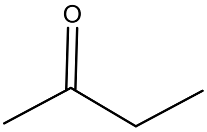
N-Methyl Formamide	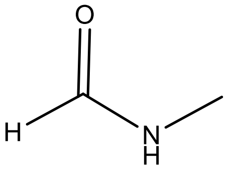
Methyl Isobutyl Ketone	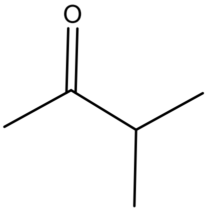
N-Methyl-2-Pyrrolidone	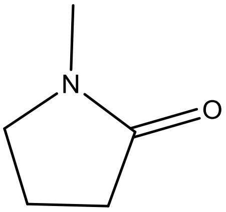
Methylene Dichloride	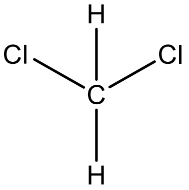
N,N-Dimethyl Acetamide	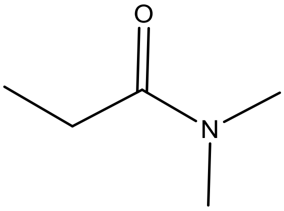
2-Phenoxy Ethanol	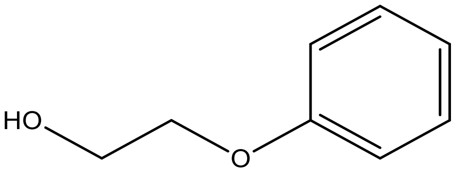
2-Propanol	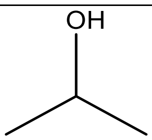
Propylene Carbonate	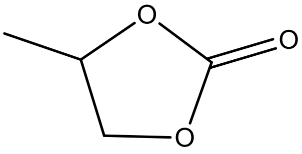

Propylene Glycol	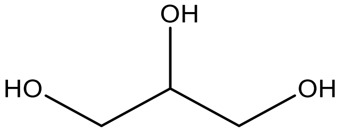
Propylene Glycol Monomethyl Ether Acetate	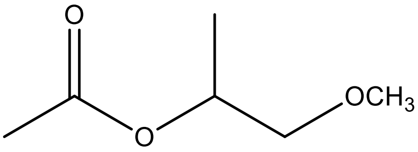
Tetrahydrofuran	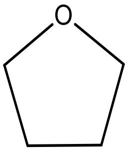
Toluene	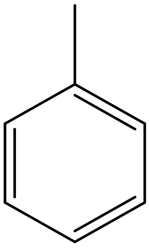
Trichloroethylene	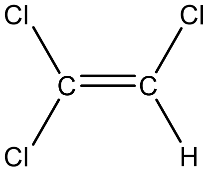
Water	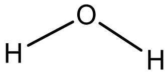
p-Xylene	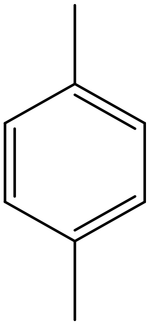

III.1 Molecular structure for the solvents used in this chapter.

Solvent	**FW**	**FR -R**	**FR-G**	**FR-B**	**FG-R**	**FG-G**	**FG-B**	**FB-R**	**FB-G**	**FB-B**
Acetone	22.6	23.6	16.9	23.0	23.7	22.6	23.8	23.8	23.0	23.8
Acetonitrile	22.6	23.5	18.0	23.5	21.9	23.9	23.9	0.0	23.4	23.8
Benzaldehyde	23.8	23.6	23.8	23.9	23.9	23.8	23.8	23.6	23.7	23.7
1-Butanol	23.5	23.1	23.9	23.8	23.8	23.8	23.8	0.0	23.8	23.8
n-Butyl Acetate	19.6	3.0	20.3	23.5	23.4	6.8	22.7	23.6	11.6	13.2
γ-Butyrolactone (GBL)	23.9	23.3	22.9	23.8	23.3	23.9	23.9	0.0	21.6	23.8
Chloroform	20.5	3.0	19.7	23.6	23.6	13.0	23.4	23.6	22.3	23.4
Cyclohexane	23.0	3.0	23.7	23.8	23.8	22.7	23.9	23.6	23.5	23.5
Cyclohexanol	23.5	20.2	23.8	23.8	22.1	23.7	23.8	23.8	23.7	23.8
Cyclohexanone	23.8	21.5	23.7	19.4	23.6	23.3	23.3	23.9	23.5	23.9
Diacetone Alcohol	23.8	21.8	22.4	23.3	21.9	19.4	21.8	23.8	23.4	23.9
Dimethyl Formamide (DMF)	23.6	21.4	23.8	23.4	23.5	23.4	23.8	23.0	23.2	23.9
Dimethyl Sulfoxide (DMSO)	23.8	23.2	23.9	23.8	23.5	22.7	23.6	5.1	23.7	23.9
1,4-Dioxane	22.4	8.0	23.3	23.9	21.0	22.2	23.1	23.9	23.1	9.8
Ethanol	23.8	20.0	23.8	23.5	23.1	23.4	23.0	5.7	23.5	23.9
Ethyl Acetate	22.4	23.1	23.7	23.6	23.6	23.5	23.1	4.6	23.8	21.6
Ethylene Glycol	18.3	5.3	21.3	23.9	14.1	18.2	22.6	23.5	20.8	4.5
Methanol	23.8	21.5	22.8	23.5	23.4	20.7	20.3	23.9	22.9	23.9
Methyl Ethyl Ketone (MEK)	23.8	23.4	23.2	22.3	23.6	23.8	23.7	23.8	23.5	23.8
N-Methyl Formamide	23.8	23.9	22.9	23.9	23.2	23.7	23.8	20.7	22.3	23.8
Methyl Isobutyl Ketone (MIBK)	23.8	23.2	23.9	23.8	23.1	23.7	23.8	23.8	22.3	23.8
N-Methyl-2-Pyrrolidone (NMP)	23.7	23.7	23.8	23.9	23.7	23.6	23.2	5.1	23.7	23.8
Methylene Dichloride (Dichloromethane)	21.1	3.6	23.0	22.1	23.5	22.8	23.0	23.5	23.7	3.2
N,N-Dimethyl Acetamide	23.8	23.7	23.7	23.9	23.2	23.5	23.1	5.3	21.9	23.8
2-Phenoxy Ethanol	23.9	23.8	21.4	23.9	23.5	23.6	23.6	0.0	23.7	23.8

2-Propanol	23.8	23.4	21.7	23.6	21.5	23.7	23.7	23.7	23.7	23.8
Propylene Carbonate	23.9	23.9	23.1	23.8	23.0	23.7	22.6	23.8	22.9	23.8
Propylene Glycol	23.3	23.3	23.7	23.6	23.5	23.3	23.7	22.4	23.6	8.8
Propylene Glycol Monomethyl Ether Acetate	23.1	22.8	23.6	3.3	23.3	22.7	23.5	3.2	23.4	22.6
Tetrahydrofuran (THF)	9.1	3.0	6.6	22.1	6.8	4.5	21.7	22.5	8.2	3.2
Toluene	23.5	0.0	23.4	23.5	23.6	21.4	23.5	23.5	23.4	3.2
Trichloroethylene	23.0	6.8	21.9	22.9	23.3	22.7	23.1	22.6	8.4	8.1
Water	6.6	3.0	2.7	21.3	20.6	2.6	21.5	3.1	5.1	3.2
p-Xylene	23.3	3.0	22.9	21.7	23.1	23.2	23.1	23.5	20.7	3.2
Average	22.1	16.7	21.6	22.7	22.3	21.0	23.2	16.8	21.3	18.5
Standard Deviation	3.9	9.2	4.6	3.6	3.3	5.6	0.8	9.8	5.0	8.4

III.2 Settling time (t_s) for copper with multiple solvents calculated based on different backgrounds.

III.3 The VIS-3 results for sonicated copper by using different backgrounds.

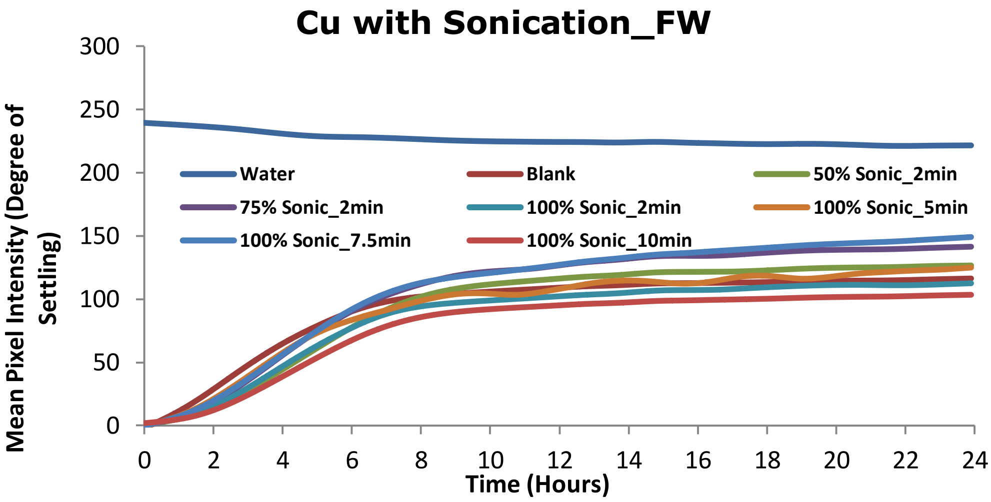

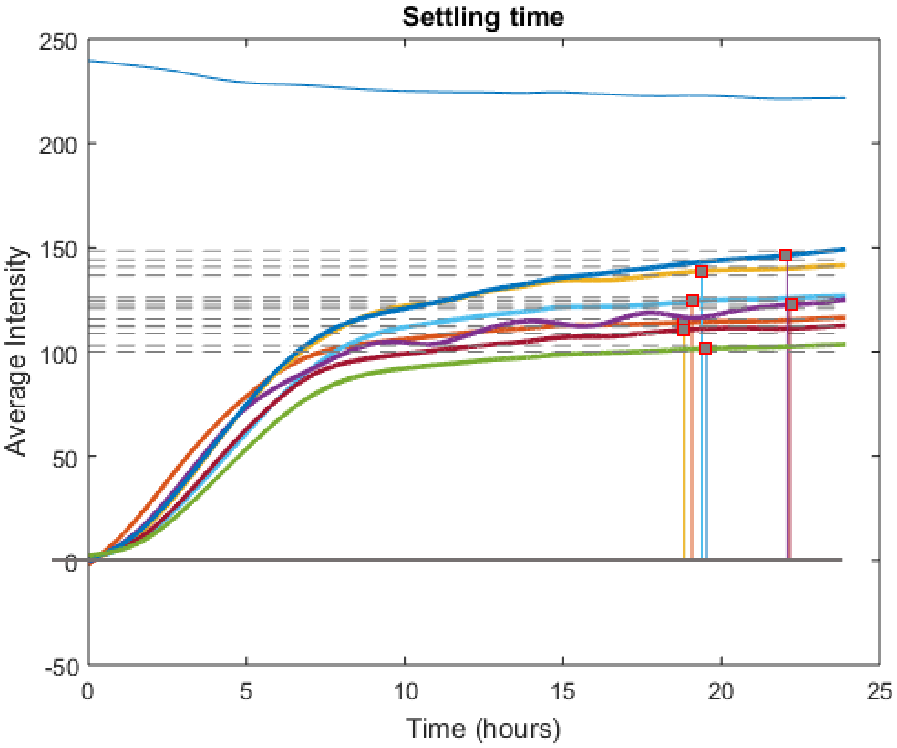

Full white background with settling time calculations.

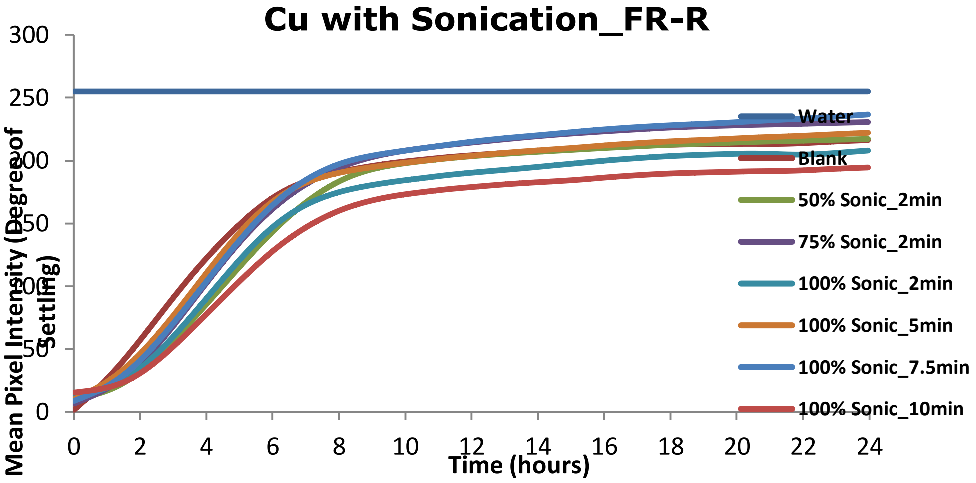

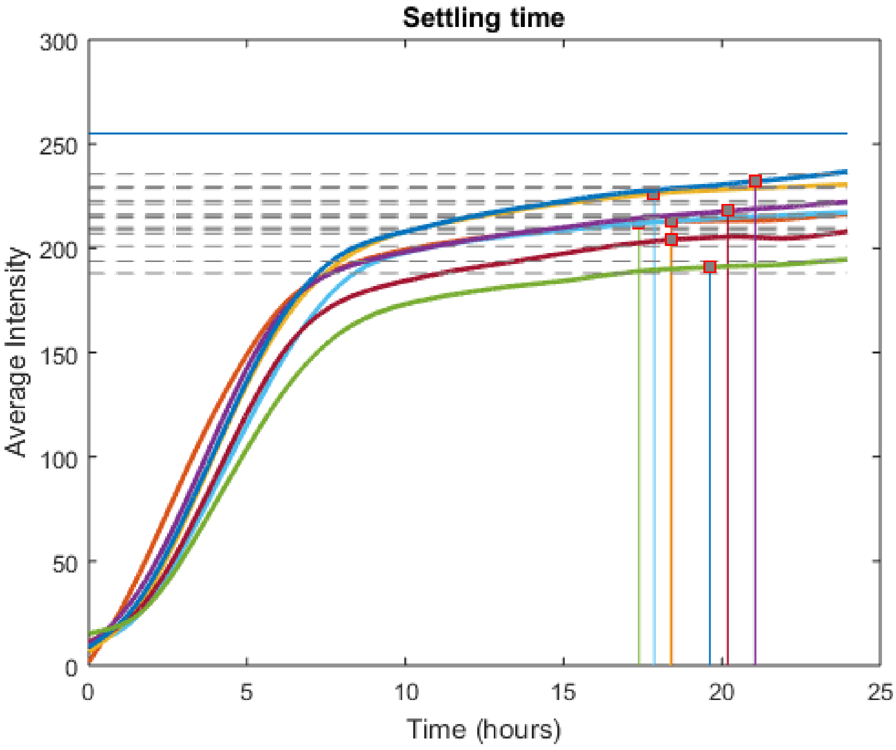

FR-R background with settling time calculations.

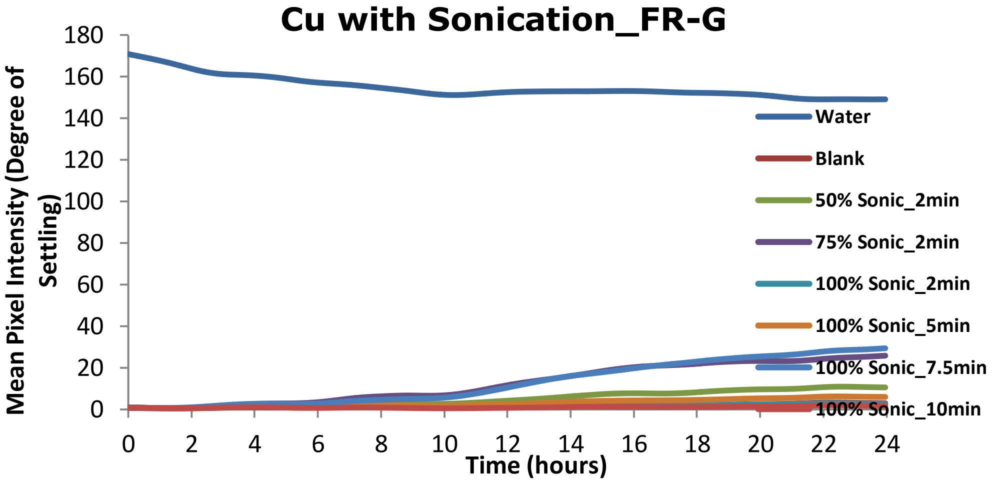

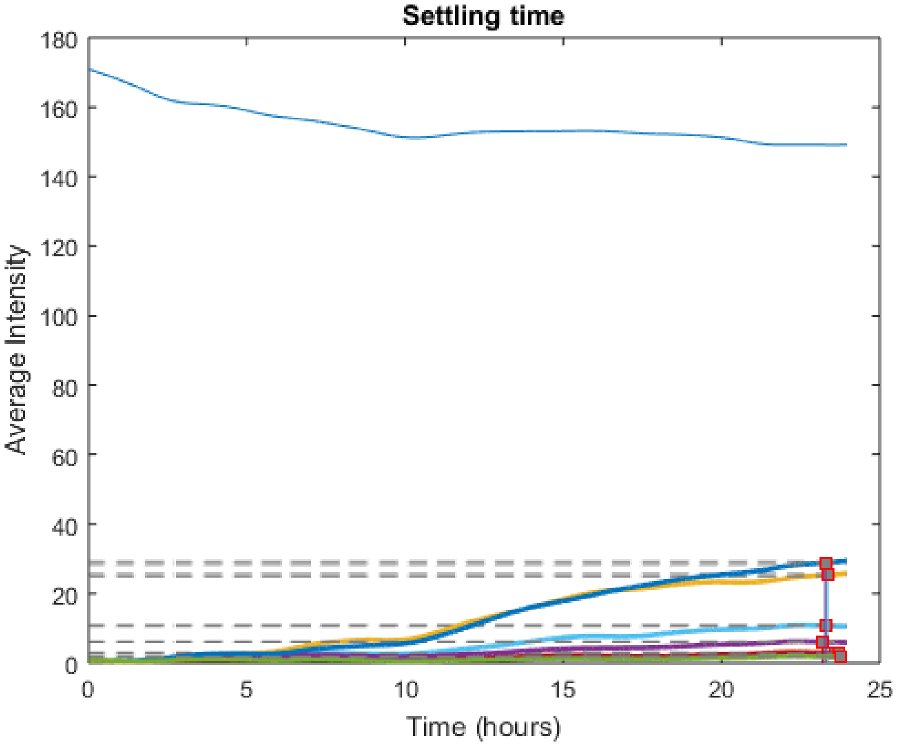

FR-G background with settling time calculations.

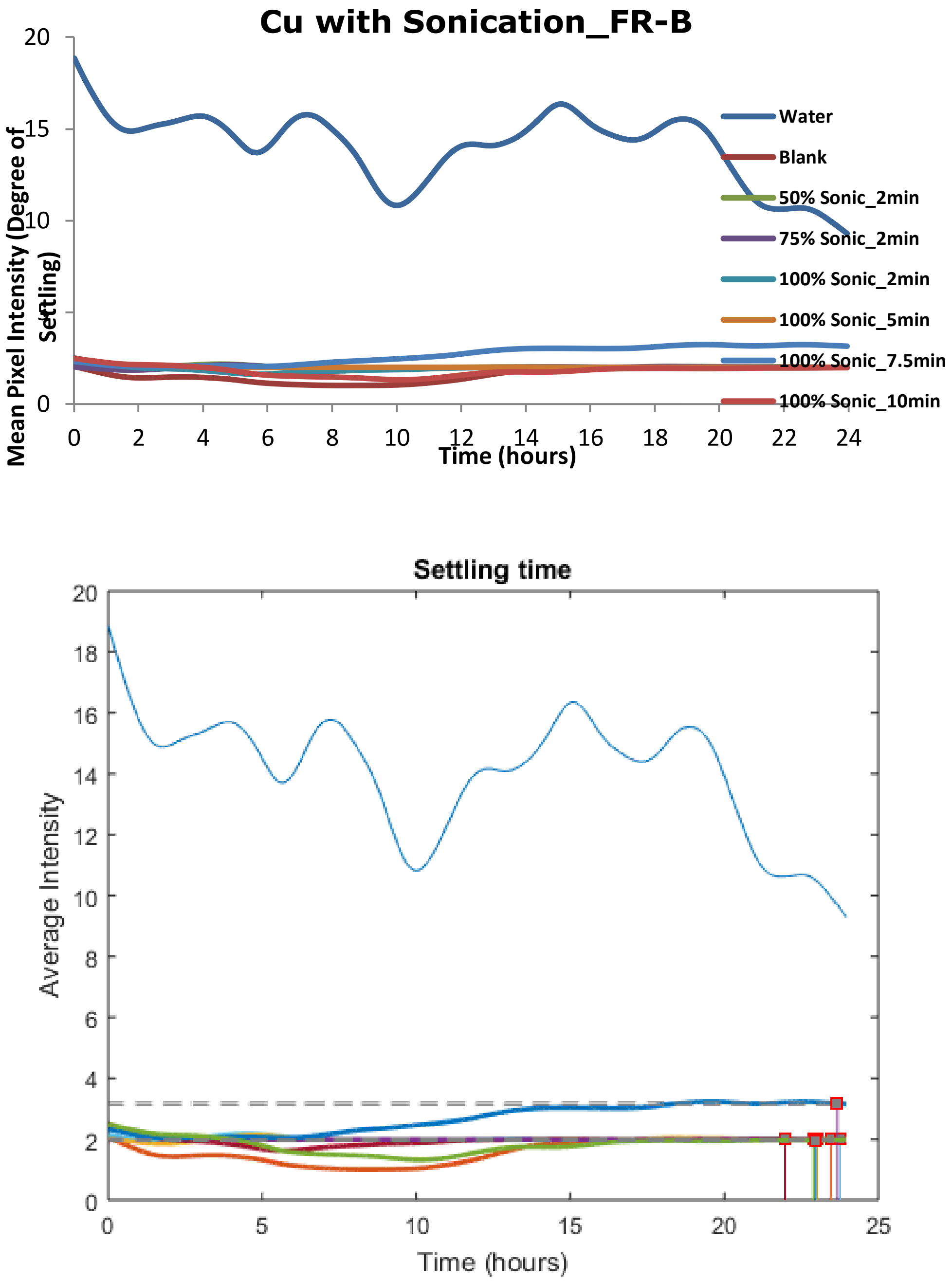

FR-B background with settling time calculations.

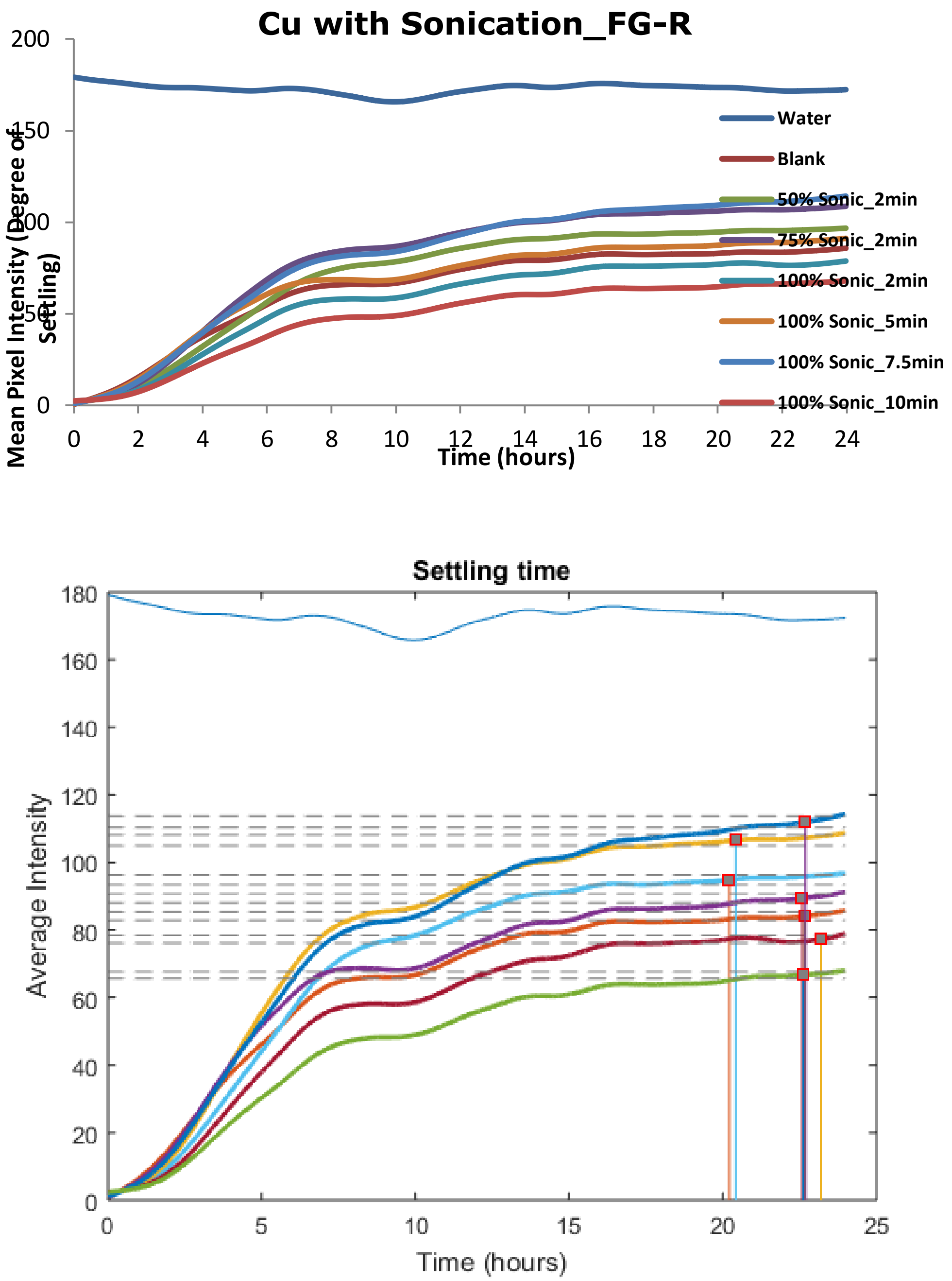

FG-R background with settling time calculations.

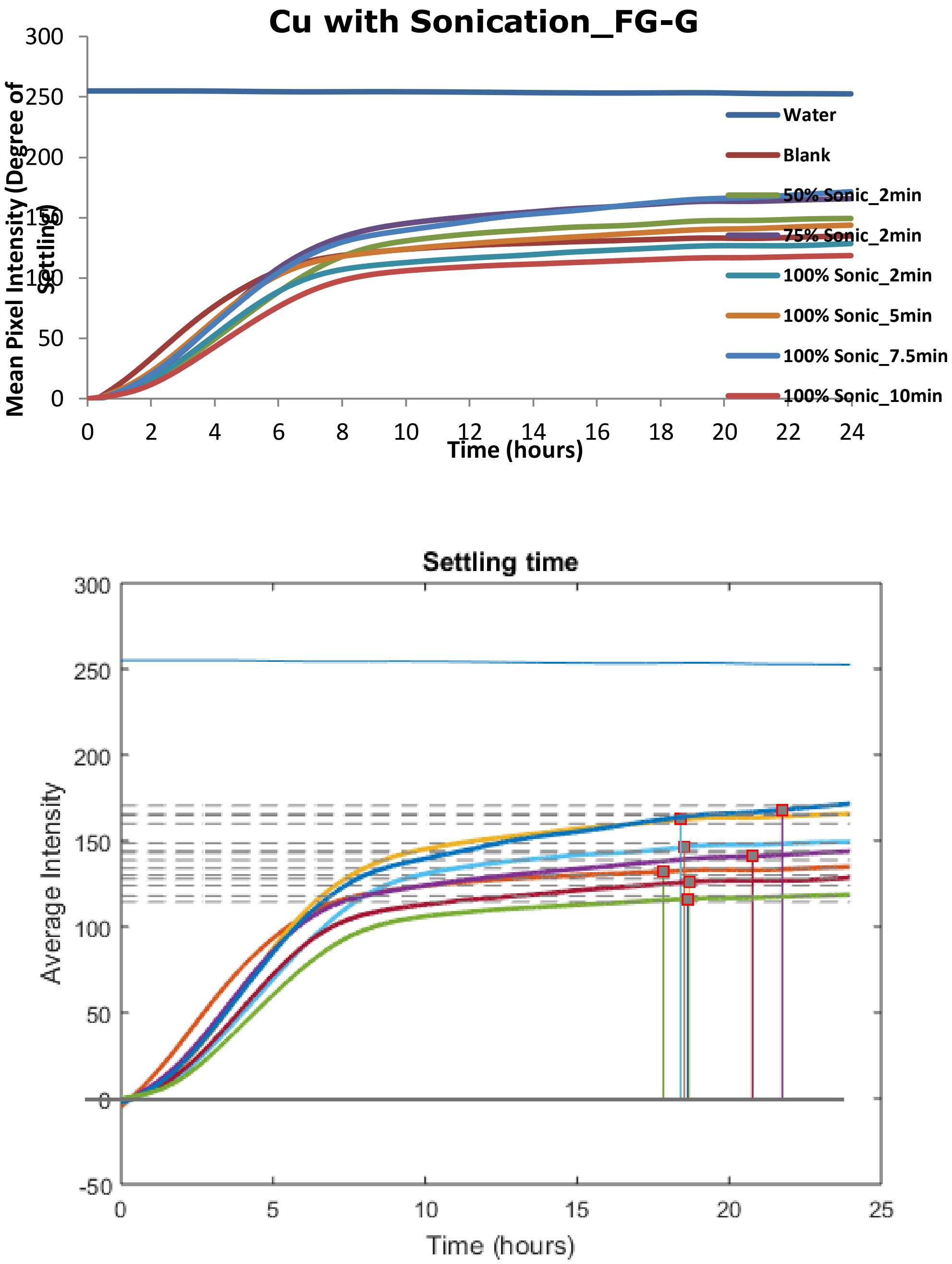

FG-G background with settling time calculations.

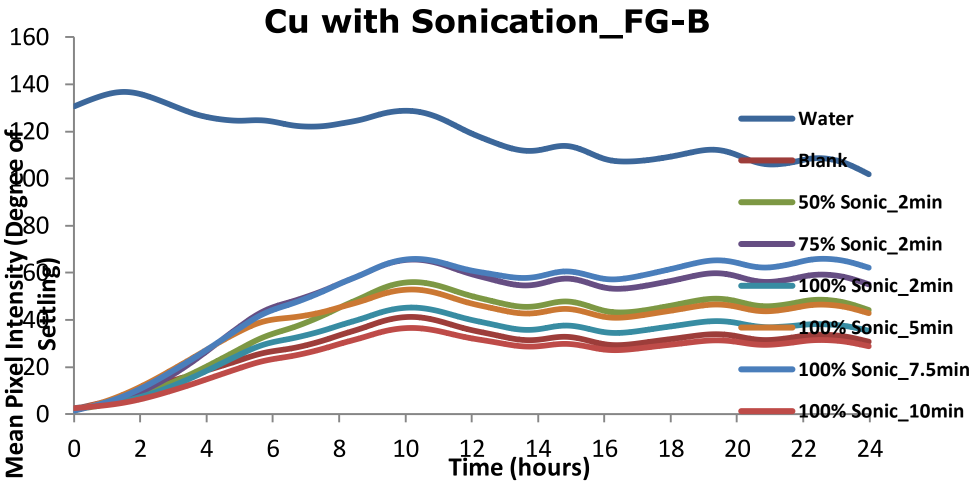

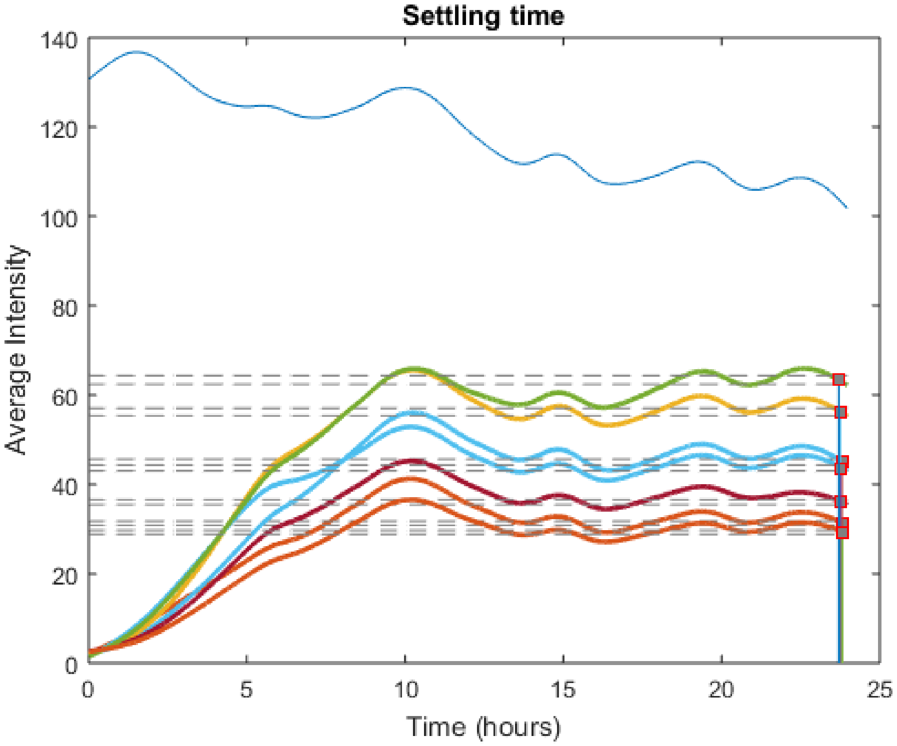

FG-B background with settling time calculations.

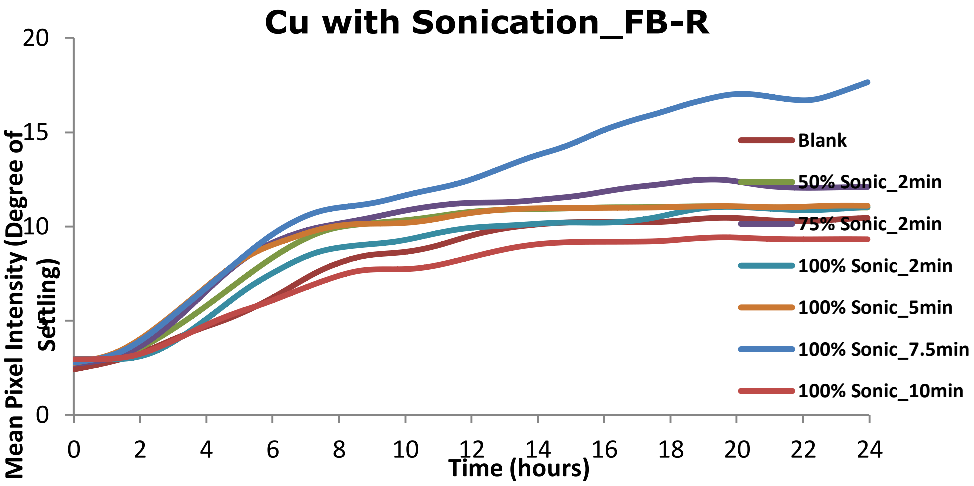

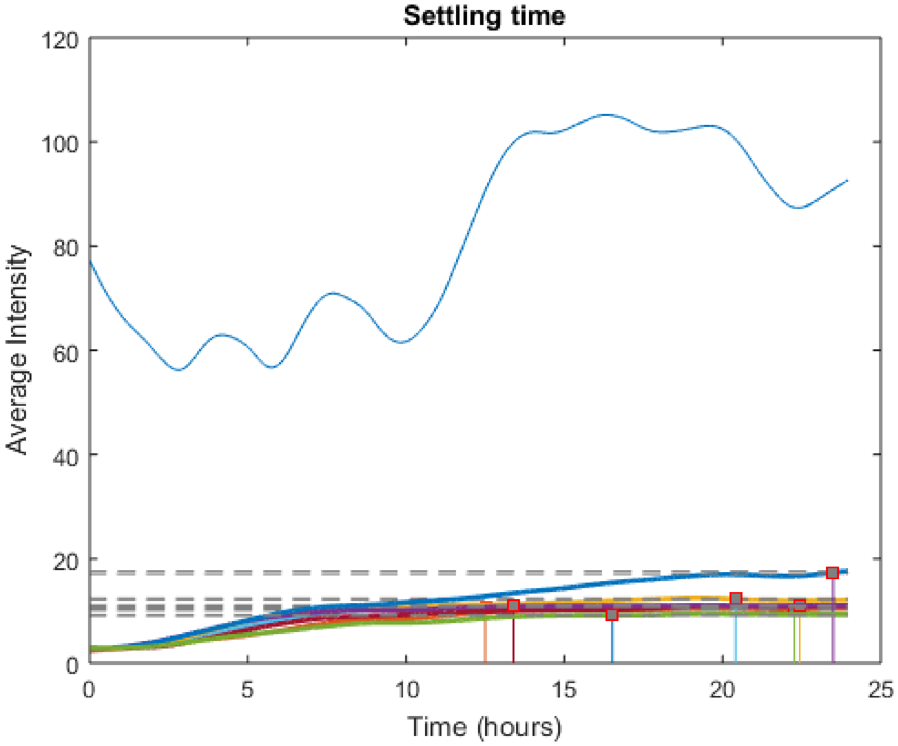

FB-R background with settling time calculations.

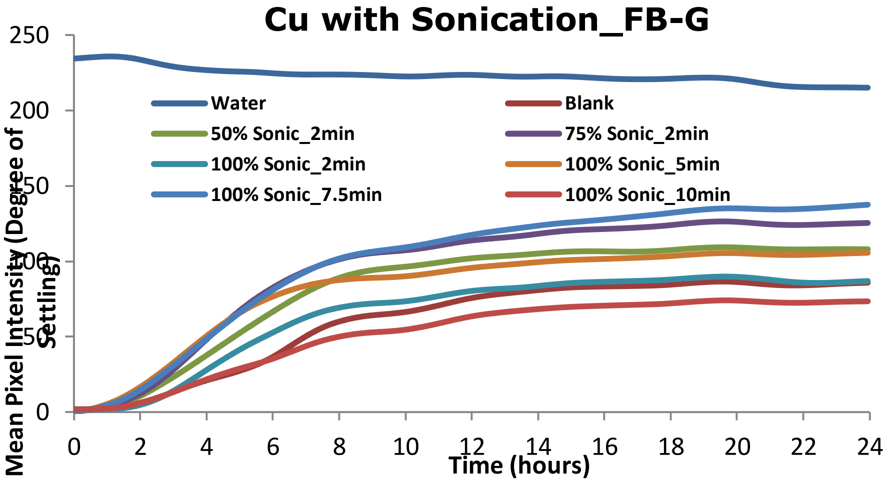

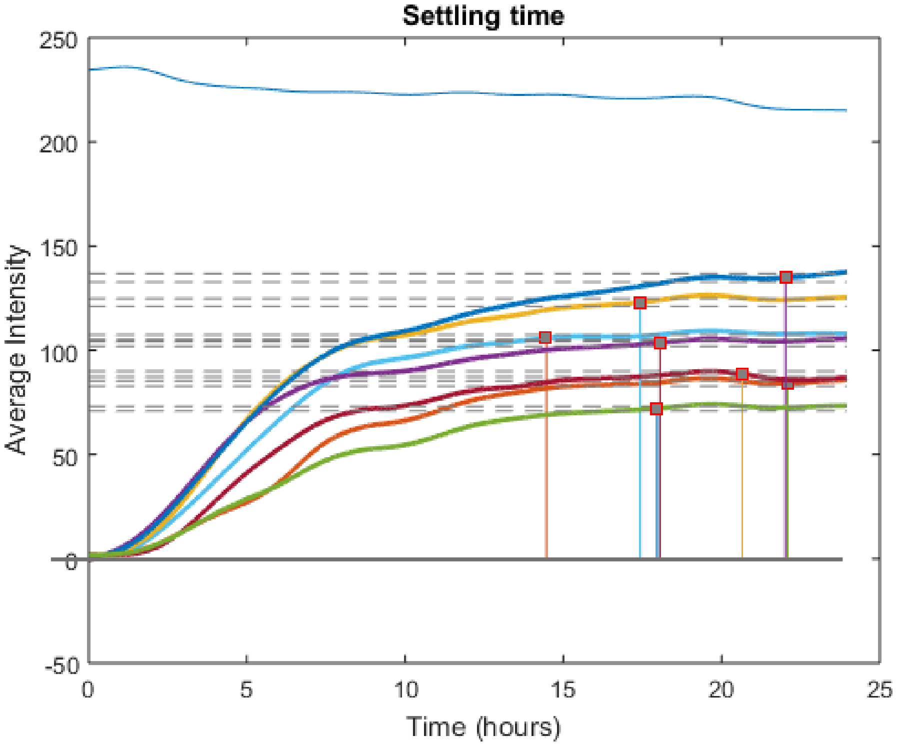

FR-G background with settling time calculations.

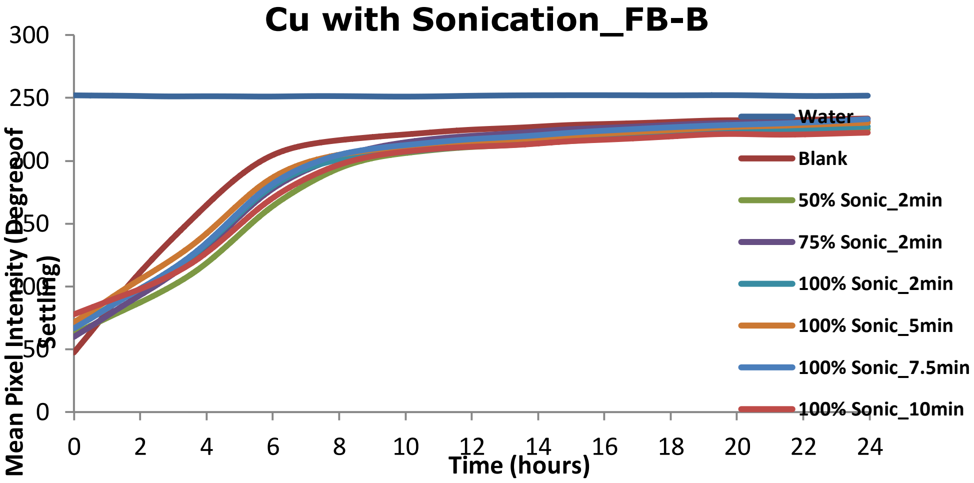

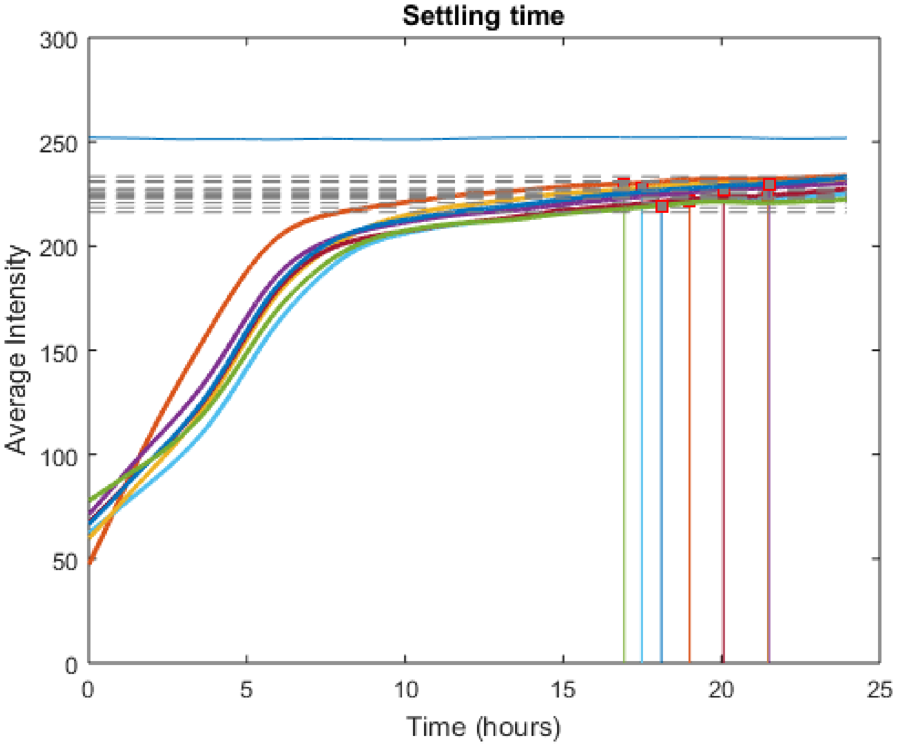

FB-B background with settling time calculations.